A Multiscale Study on Fatigue Mechanism and Life Estimation on Welded Joints of Orthotropic Steel Decks

Benjin Wang

Promotors: Prof. H. De Backer, PhD, Prof. A. Chen, PhD
Doctoral thesis submitted in order to obtain the academic degrees of
Doctor of Civil Engineering (Ghent University) and
Doctor of Engineering (Tongji University)

GHENT
UNIVERSITY

Department of Civil Engineering
Head of Department: Prof. P. Troch, PhD
Faculty of Engineering and Architecture

Department of Bridge Engineering
Head of Department: Prof. L. Sun, PhD
College of Civil Engineering

Academic year 2016 - 2017

ISBN 978-94-6355-034-5
NUR 956
Wettelijk depot: D/2017/10.500/69

Examination board:

Chair:	
Prof. Lewei Tong	Tongji University
Co-chair:	
Prof. Luc Taerwe	Ghent University
Supervisors:	
Prof. Airong Chen	Tongji University
Prof. Hans De Backer	Ghent University
Faculty reading committee:	
Prof. Pengfei He	Tongji University
Prof. Guoqiang Li	Tongji University
Prof. Bohumil Culek	University of Pardubice
Prof. Wim De Waele	Ghent University
Other members:	
Dr. Ken Schotte (secretary)	Ghent University

Tongji University
College of Civil Engineering

Department of Bridge Engineering
Siping Road 1239
200092 Shanghai
China

Tel.: +86 021 6598 1871
Fax.: +86 021 6598 4211

Ghent University
Faculty of Engineering and Architecture

Department of Civil Engineering
Technologiepark 904
9052 Zwijnaarde
Belgium

Tel.: +32 9 264 54 89
Fax.: +32 9 264 58 37

PREFACE

This thesis gives a conclusion to my five-year Ph.D. study, which seems to be a long journey with complex feelings and emotions in my life. It is a journey consists of successes and failures, bitterness and happiness, self-doubts and insistence, all of which grinded me physically and mentally on both academic and living aspects, and finally lead me here. Even not as perfect in every aspect, I am still grateful for the endeavors I contributed and some fortunes I got, that makes me stick to the plan, never lose my faith during these years, and finally complete the journey. It will be a treasure that I can always rediscover the value and a memory that I can always recall, with expectations to explore more of myself.

Hence, for the guidance to me on this journey, I will firstly express my gratitude to my supervisors, Prof. Airong Chen and Assoc. Prof. Dalei Wang in Tongji University, and Prof. Hans De Backer in Ghent University. Thanks to your trusts, encouragements, and most importantly, the exceptional patience for me. Your valuable insights also enlightened me on many aspects, and deserves my most sincere thanks.

Heartfelt gratitude to my parents, my wife, and my son, who had provided the most unselfish supports during these years, and helped me to find the willpower on getting over all difficulties. I apologize for my absence when studying aboard, but I do felt your unconditional love more strongly during that period, and it provided me extra encouragements to finish the research. I truly wish to land my every step with you in the future.

I would like to address my thanks to Dr. Wim Nagy, my colleague in Ghent University, for the work you did on the fatigue test and the discussions we had, and to Dr. Xiaoyi Zhou, my former colleague in Tongji University, for the suggestions and helps you provides and for the collaborations we had. I am also quite grateful to Prof. Bohumil Culek and Prof. Eva Schmidova in University of Pardubice, Czech Republic, for their academic and technical guidance for the fatigue test.

Sincere thanks to Prof. Philippe Van Bogaert, Prof. Peter Troch, Prof. Luc Taerwe, Prof. Pengfei He, Assoc. Prof. Rujin Ma, Assoc. Prof. Xin Ruan, Dr. Xu Jiang, Dr. Kai Wu, Dr. Zichao Pan, Dr. Xi Tu, for showing me the academic elegance and the scientific standards of excellence. All the recommendations you provided, no matter intentionally or unintentionally, has directed me on the way of my research work, and will always benefit me in the future career.

I also want to thank all colleagues I have been worked with, i.e. colleagues in the research group of Bridge Design Method and Process, Tongji University, and the research group of Road Bridge and Tunnel, Ghent University, for all the supports, helps, and friendships.

Wish you all the best!

Benjin Wang

August, 2017

SUMMARY

Orthotropic steel deck is widely used for long-span bridges due to the extraordinary mechanical and economical performances. However, fatigue crack often starts to emerge on welded joints of orthotropic steel decks that has been put into service for about ten years, and severely affects the severability and durability. The practical experiences on large-scale engineering projects show that the traditional ways of fatigue performance evaluation, i.e. macroscopic fatigue tests and numerical simulations, are essentially phenomenological and regardless of fatigue mechanism for not taking the effects in meso- or micro- scale into account. As a result, they are either unable to achieve consistent results, or not always on the safe side for the design, leading to premature fatigue damage on welded joints, and subsequent cost in a considerable amount on management, maintenance or, in the worst case, the re-build of structures. To solve that problem, this thesis is endeavored to study the fatigue behavior, mechanism, and life estimation on welded joints of orthotropic steel decks, in which the process-oriented fatigue test, mesoscopic characteristics of material, multiscale numerical simulations should be focused on.

For the first step, the fatigue test was conducted to small-scale specimens of a typical orthotropic steel deck. A line load was applied to better simulate the effect of vehicles running over it, and the boundary conditions were carefully designed as a critical factor on small-scale tests. To get more information about the fatigue crack growth process, the beach marks were produced by applying cyclic loadings with different types and stress ranges during the test, which indicated the crack sizes and crack growth rates in different stages. As a result, the rib-to-deck weld toe crack was observed on all specimens, and caused the final failure of them. The fractographic and metallographic analyses on the region of interest were given afterwards, pointing out that the coarse grained heat-affected-zone is fragile under cyclic loadings, as the intergranular crack occurs primarily there. It can be inferred that the depth of this sub-zone can be taken as the initial crack depth. However, as a sub-zone exists along the entire longitudinal direction, it is hardly an indicator of the initial crack length. Besides, weld defects were occasionally addressed by scanning electron microscope in the observation. According to a preliminary analysis on crack growth rate, it showed the necessity on studying the early-stage crack problem that affected by material heterogeneities like weld defects, in a numerical way with respect to the randomness of them.

Consequently, a program of extended finite element method was developed using MATLAB, with consideration of random weld defects. Additionally, to be feasible on the representative volume elements extracted from rib-to-deck welded joints, a level-set function was built for easily modelling the weld toe flank angles. As the geometries are independent to meshes, the program enables to build models that are free for re-mesh, providing great benefits to the evaluation of random weld defects when solving a big number of cases. With this program, a homogenization method was proposed based on the concept of equivalent crack growth length. Numerical examples showed its applicability on early-stage cracks, as the relatively small crack growth rate in that stage will only lead to tiny errors. Then the main factors that affect crack growth were addressed by parametric analyses. The results of this homogenization method showed large standard deviations of the effects from weld defects, which could be important for structures in a much larger scale. However, given the lack of knowledge on the sizes, numbers and spatial distributions of weld defects, it is only possible to conduct the homogenization with some reasonable assumptions.

Afterwards, the multiscale study was carried out in correspondence with the fatigue test, using the numerical tools achieved before. Two different multiscale methods were built with respect to the detailed fatigue crack growth process. The comparison of them implied that the non-concurrent multiscale method, with a full independent mesoscopic model, is of great efficiency without losing accuracy, and thus is applied to reproduce the crack growth process in the test. Accordingly, different stages in crack growth were addressed, and the material constants in the stable crack growth stage, were achieved by data fitting. The values conformed with the ones provided in standards and specifications for crack grows in Paris region, and thus can obtain results with acceptable accuracy. However, the material constants in Stage I, which is for relatively low stress intensity factors, was not clear enough as the fatigue test cannot provide more information on the crack growth rates in this stage.

Finally, the multiscale method was introduced into case studies on three projects, including the Millau Viaduct in southeast France, the KW5 Bridge on Albert Canal, Belgium, and the Runyang Yangtze River Bridge in China. The three case studies estimated the fatigue life based on traffic flows that are: i) measured in Europe in a short term; ii) recommended by Eurocode; iii) measured in China in a long term, thus presented the extensive feasibility of this multiscale method. Specifically, the fatigue life was calculated by two parts, i.e. the macro crack initiation life and macro crack growth life. The former one was given in a probabilistic way for the sake of the randomness induced by the initial crack depth

and other weld defects, as investigated in the above works. Whilst the latter one was provided in a deterministic way as the influence factors were of less scatter or not so critical then. The results suggested that the traffic flow on the Millau Viaduct was much lighter or easier than that on the Runyang Yangtze River Bridge. Hence, the fatigue problem will not be a concern for Millau Viaduct in decades. In contrast, the Runyang Yangtze River Bridge may suffer from fatigue damage in less than ten years. In addition, the case study on KW5 Bridge implied that the traffic load recommended by Eurocode was not a proper option when using fracture mechanics to evaluate the fatigue performance. The main reason is that the traffic volume consists of heavy vehicles only, and thus is quite large and design-oriented. Hence, the fatigue life obtained for KW5 Bridge was too short and unrealistic. To sum up, the study showed its feasibility by applying on the actual projects under various conditions, and the life estimation results are of acceptable accuracy when traffic flow is measured in a relatively long term. The obtained results are in a probabilistic form, and will provide valuable information to making maintenance strategies for bridges, such as the schedule of the visual inspections and further retrofitting works.

SAMENVATTING

Orthotrope stalen brugdekken worden veel gebruikt voor lange overspanningen vanwege de buitengewone mechanische en economische prestaties. Echter, vermoeiingsscheuren ontstaan vaak vroeg in een van de vele lasverbindingen van orthotrope stalen dekken en dit zelfs voor ze 10 jaar in dienst zijn, wat ernstige gevolgen heeft voor de betrouwbaarheid en duurzaamheid. De praktische ervaringen met grootschalige engineering projecten hebben aangetoond dat de traditionele manieren om het vermoeiingsgedrag te evalueren, dit wil zeggen macroscopische vermoeiingstests en numerieke simulaties, in wezen fenomenologisch zijn, en dus onafhankelijk van het eigenlijke vermoeiingsmechanisme, en dus niet in staat om rekening te houden met de effecten op meso- of microschaal. Als gevolg daarvan zijn ze ofwel niet in staat om consistente resultaten te bereiken, of niet altijd voldoende veilige, wat leidt tot voortijdige vermoeiingsschade aan lasnaden. De daaropvolgende kosten vormen een aanzienlijk bedrag en hebben impact op het beheer, het onderhoud of, in het ergste geval, de reconstructie van structuren. Om dat probleem op te lossen, wordt in dit scriptie getracht het vermoeiingsgedrag en het mechanisme voor lasverbindingen in orthotrope stalen dekken, met behulp van procesgerichte vermoeiingstesten, de mesoscopische kenmerken van materiaal en een multiscale numerieke simulatie te bestuderen.

Voor de eerste stap werden de vermoeiingstesten op kleinschalige specimens uitgevoerd, typisch voor orthotrope stalen dekken. Een lijnlast werd gebruikt om het effect van voertuigen die over het dek rijden te simuleren en de randvoorwaarden werden zorgvuldig ontworpen, wat een kritische factor is voor kleinschalige proeven. Om meer informatie over de vermoeiingsweerstand te krijgen, werden beach marks aangebracht door het aanbrengen van cyclische belastingen met verschillende spanningsniveaus en vormen tijdens de test, waarbij de scheurafmetingen bestudeerd kunnen worden en de scheurgroei in verschillende stadia opgevolgd. Als resultaat werden scheuren aan de lasteen waargenomen bij alle proefstukken, die verantwoordelijk waren voor het falen van de proef. De fractografische en metallografische analyse van het scheuroppervlak wees erop dat de grofkorrelig sublaag in de door warmte beïnvloede zones kwetsbaar wordt onder cyclische belasting, de intergranulaire scheur ontstaat voornamelijk op die locatie. De initiële scheurdiepte kan worden afgeleid uit de diepte van deze sublaag. Echter, als een laag in de lengterichting bestaat, is het moeilijk ze als een indicator van de oorspronkelijke scheurlengte te aanvaarden. Daarnaast werden lasfouten soms ook

bestudeerd door een rasterelektronenmicroscoop. Uit een voorlopige analyse van de scheurgroeisnelheid bleek de noodzaak voor het bestuderen van de beginnende scheur op basis van de materiële heterogeniteiten zoals lasfouten op een numerieke wijze noodzakelijk, rekening houdens met hun willekeurige natuur.

Ten tweede, werd een programma met de uitgebreide eindige elementen methode (XFEM) ontwikkeld met behulp van MATLAB, met inachtneming van willekeurige lasfouten. Bovendien, om haalbaar te zijn voor de representatieve volume elementen, onttrokken aan de verstijver-aan-dekplaat lasverbinding, werd een specifieke functie ontwikkeld voor het eenvoudig modelleren van de flankhoeken van de lasteen. Omdat de geometrieën onafhankelijk zijn van het elementennet, heeft het programma blijkbaar een voordeel doordat makkelijk het elementennet kan aanpassen, wat heel handig is wanneer willekeurige lasfouten beoordeeld dienen te worden voor het oplossen van een groot aantal gevallen. Met dit programma werd een homogenisatie-methode voorgesteld, gebaseerd op het concept van equivalente scheurgroei lengte. Numerieke voorbeelden toonden de toepasbaarheid ervan op scheuren in een vroeg stadium aan, omdat de relatief kleine groeisnelheid van de scheur in dat stadium alleen maar zal leiden tot kleine fouten. De parametrische analyse duidde de belangrijkste invloedsfactoren aan. De resultaten hadden grote standaardafwijkingen voor wat betreft de effecten van lasdefecten, wat belangrijk kan zijn voor macroscopische structuren. Echter, gezien het gebrek aan kennis over de echte maten, grootte en ruimtelijke verdelingen van de lasfouten, kon de homogenisering alleen worden gedaan gebaseerd op een aantal redelijke veronderstellingen.

Vervolgens werd een multiscale studie uitgevoerd op basis van de vermoeiingstestresultaten en de numerieke gereedschappen die hierboven ontwikkeld werden. Twee verschillende multiscale-methodes werden ontwikkeld voor wat betreft het gedetailleerde groeiproces van de vermoeiingsscheur. De vergelijking van beide impliceerde dat het niet-gelijktijdige model, met een volledige onafhankelijke mesoscopisch model, een grote efficiëntie heeft, zonder verlies van nauwkeurigheid en aldus in staat om het scheurgroeiproces te reproduceren van de tests. Op die manier werden verschillende stadia van scheurgroei bestudeerd evenals de materiaalconstanten in Fase II, wat het stadium is waarin de scheur stabiel groeit, met behulp van data fitting. De waarden bleken in overeenstemming te zijn met de waarden die in normen en specificaties voor scheurgroei in de Paris-regio vermeld worden, en dus kan de methode resultaten bereiken met een aanvaardbare nauwkeurigheid. De materiaalconstanten in Fase I, zijnde het stadium met relatief lage spanningsintensiteitsfactoren, waren niet

duidelijk genoeg in de vermoeiingstest aangezien die geen informatie geven over de scheurgroeisnelheden in dit stadium.

Ten slotte werd de multiscale methode geïntroduceerd in case studies voor drie projecten: het viaduct van Millau in het zuidoosten van Frankrijk, de KW5 Brug over het Albertkanaal in Antwerpen, België, en de Runyangbrug over de Yangtze in China. De drie casestudies hebben het vermoeidheidsleven geschat op basis van de verkeersstromen die zijn: i) in korte tijd in Europa gemeten; ii) aanbevolen door Eurocode; iii) op lange termijn in China gemeten, dus de uitgebreide haalbaarheid van deze multiscale methode voorgesteld. De vermoeiingslevensduur werd berekend in twee delen, d.w.z. de macro scheurinitiatie levensduur en de macro scheurgroei levensduur. Eerstgenoemde werd bestudeerd op een probabilistische wijze omwille van de willekeur geïnduceerd door de initiële scheur diepte en de andere lasfouten, zoals onderzocht in de bovengenoemde studie. De laatstgenoemde werd bestudeerd op een deterministische wijze aangezien de invloedsfactoren veel minder willekeurig zijn. De resultaten suggereerden dat de doorstroming van het verkeer op het viaduct van Millau veel lichter en makkelijker was dan die op het Runyangbrug. Daarom zal het vermoeiingsprobleem niet voorkomen voor het Viaduct van Millau in de eerste tientallen jaren, terwijl de Runyangbrug daarentegen last kan hebben van vermoeiing in minder dan tien jaar. Daarnaast bleek de verkeersbelasting aanbevolen door de Eurocode geen goede optie wanneer breukmechanica toegepast wordt om de vermoeiingsprestaties te evalueren, omwille van het gebruik van grote en ontwerp-georiënteerde verkeersvolumes. Vandaar dat de levensduur verkregen voor de KW5 brug te kort en onrealistisch bleek. Kortom, de studie toonde de haalbaarheid voor het toepassen op concrete projecten aan, en de resultaten van de levensbeschatting zijn van aanvaardbare nauwkeurigheid wanneer de verkeersstroom op een relatief lange termijn wordt gemeten. De verkregen resultaten zijn in een probabilistische vorm, en zullen waardevolle informatie verstrekken om onderhoudsstrategieën voor bruggen te maken, zoals het schema van de visuele inspecties en aanpassingswerken uit te voeren.

X

NOMENCLATURE

a	crack length
a_0	initial crack length
a_c	homogenization coefficient of Paris constant
a_d	crack length that can be detected, i.e. initial length of a marco-crack
$\boldsymbol{a_I}$	enriched degrees of freedom
$B(x)$	crack-tip enrichment function
C	Paris constant
C_0	original value of Paris constant
C_{eff}	effective Paris constant
C_k	cycle count
da/dN	crack growth rate
D_t	damage induced by test truck
D_y	damage per year
E_I	elastic modulus of inclusions
E_M	elastic modulus of matrix
E_S	elastic modulus of steel
F	shape factor for calculating K
F_b	shape factor for bending stress
$H(x)$	Heaviside enrichment function
K	stress intensity factor
K_I	Mode-I stress intensity factor
K_{II}	Mode-II stress intensity factor
ΔK_{eff}	effective stress intensity factor range
ΔK_{th}	threshold value of stress intensity factor range
$\overline{\Delta K}$	representative SIF range between two beach marks
L_d	data length of the wheel loads in days
m	Paris exponent
n_I	number of inclusions
n_P	number of pores
n_d	number of defects
N_{base}	regular fatigue cycle numbers in the test
$N_{beachmark}$	beach mark cycle numbers in the test
N_d	fatigue life in days
N_y	fatigue life in years
$N_I(x)$	shape function in the traditional FEM
P_{base}	regular fatigue cycle loading range in the test
$P_{beachmark}$	minimum beach mark cycle loading in the test
P_{max}	maximum regular fatigue cycle loading in the test
P_{min}	minimum regular fatigue cycle loading in the test
P_j	possibility for each location
P_l	percentage of different types of lorries
P_M	Poisson's ratio of matrix

P_I	Poisson's ratio of inclusions
P_{max}	maxiregular fatigue cycle loading in the test
$P_{beachmark}$	beach mark cycle loading in the test
R	stress ratio
r_p	plastic area around crack tip
$sign(x)$	sign function
S_d	size of defects
T_y	total volume of lorries per year and per slow lane
$\boldsymbol{u(x)}$	displacement field
$\boldsymbol{u_I}$	traditional degrees of freedom
w_l	ratio of the standard lorry weight to the test truck weight
W	thickness of deck plate

Greek symbols

λ_I	volume fraction of inclusions
λ_P	volume fraction of pores
θ_c	crack growth angle
σ_{nom}	nominal stress
σ_y	yield stress
μ	beach mark cycle parameter
Ω	entire domain
Ω_d	enriched domain
$\phi(x)$	enrichment function
$\Psi(x)$	inclusion enrichment function
ζ_I	level set value for the material interface.
$r,\ \theta$	coordinates based on the crack-tip polar coordinate system

ABBREVIATIONS

CV	coefficient of variance
CGR	crack growth rate
DOF	degree of freedom
EDS	energy dispersive spectroscopy
FEM	finite element method
HAZ	heat-affected-zone
LEFM	linear elastic fracture mechanics
MCGL	macro-crack growth life
MCIL	macro-crack initiation life
NDT	non-destructive test
OSD	orthotropic steel deck
PM	parental material
PUM	partition of unity method
RVE	representative volume element
SD	standard deviation
SEM	scanning electron microscope
SIF	stress intensity factor
WM	welding material
XFEM	extended finite element method

CONTENTS

LIST OF FIGURES

LIST OF TABLES

CHAPTER 1

INTRODUCTION

1.1. General introduction

The orthotropic steel deck (OSD) is a frequently-used structure type for constructing bridges. This kind of structure was firstly built in 1950s, originated from the stiffened steel plates used in deck in shipbuilding. Benefitted by the development of high-strength steel and weld technologies, it became a very common structure type in bridge constructions, as it can save up to 50% steel consuming compared to pre-war bridges (Kolstein, 2007). Fig. 1-1 and Fig. 1-2 presented the bridges with OSDs with respect to countries and spans, respectively. Accordingly, OSD had a lot of applications on small-span bridges. However, even not obvious on the figures, OSD is certainly the favorite design for large-span bridges world-widely, for example, the Second Bosphorus Bridge in Turkey, the Great Belt Bridge in Denmark, the Millau Viaduct in France, etc. As the infrastructures developed rapidly in recent decades in China, a lot of large-span bridges with OSDs emerged, such as the ones crossing big rivers including Runyang Yangtze River Bridge, Sutong Yangtze River Bridge, Taizhou Yangtze River Bridge, Shanghai Yangtze River Tunnel and Bridge etc., and the ones crossing sea including Hangzhou Bay Bridge, Qingdao Bay Bridge, etc.

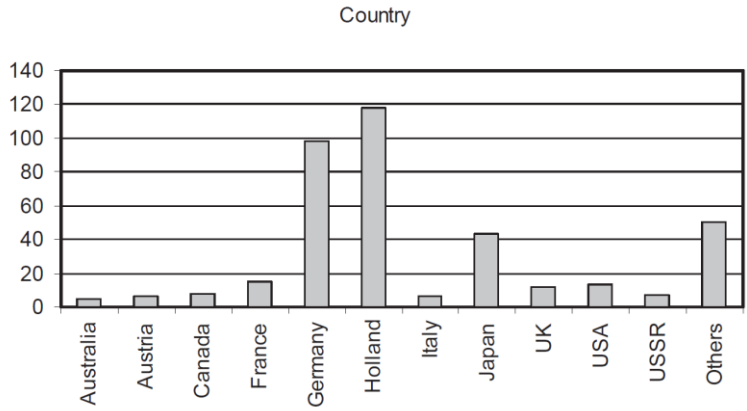

Fig. 1-1 Number of bridges with orthotropic decks identified in each country (Kolstein, 2007)

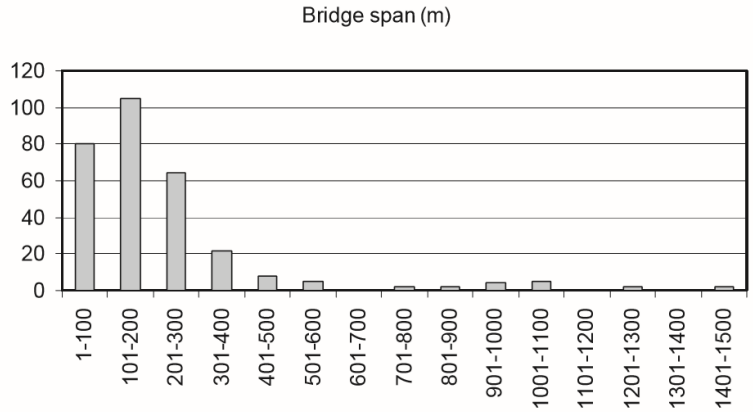

Fig. 1-2 Bridge spans of bridges with OSDs (Kolstein, 2007)

As the large-span bridges are always located at vital positions for the entire transportation systems, the durability design or life-cycle design is often laid great importance on. Even so, OSD turns to be a fatigue-prone structure type as documented all over the world, such as the Severn Bridge in Great Britain, the Haseltal and Sinntal viaducts in Germany (Wolchuk, 1990), the Second Van Brienenoord Bridge in Netherland (Maljaars et al. 2012), the Hanshin Expressway in Japan (Okura et al., 1989), and the Willamsburg Bridge in the United States (Tsakopoulos and Fisher, 2003), etc. Causes were found from different perspectives, like the short influence line that lead to high cycle numbers (Nunn and Cuninghame, 1974), the misalignments in terms of construction (Tong and Shen, 1998), the severe overloading in terms of management, etc. These studies could benefit solving fatigue problems in separated aspects, but are still incapable of fatigue evaluation and life prediction since the fatigue mechanism on OSDs were not comprehensively considered.

Therefore, due to the inexperience in the stage of manufacture, construction, and management, the actual fatigue performance of OSDs may not be satisfied, even though they were designed with fatigue cautions. Given the fast pace of massive constructions of China, the seeds of fatigue issues on these bridges might have been sowed in a more severe amount. Some of the recently-exposed fatigue problems on existing OSDs were undoubtedly premature, and greatly reduced the serviceability and durability of bridges.

1.2. Literature review

1.2.1. Fatigue design method

Ever since the Silver Bridge collapse in 1967 due to the fatigue failure on its eye bar, fatigue design becomes a necessity for steel bridges. As for OSDs, the development on fatigue design mainly focuses on two parts: 1) the design theories based on the fatigue performance of material itself; 2) the vehicle loads on different type of bridges.

1.2.1.1. Fatigue design theories

a) Infinite life design

The target of infinite life design is to reduce the stress range on fatigue-prone details to be small enough, thus the components and the whole structure could have an infinite fatigue life. As regular S-N curves show, the fatigue life may not be affected by the stress range when it is smaller than the fatigue limit, which leads to the infinite life. For an infinite life design, the design equation is as follows,

$$\Delta\sigma_{max} \leq [\Delta\sigma_L] \tag{1-1}$$

where $\Delta\sigma_{max}$ is the maximum stress range, $[\Delta\sigma_L]$ is the fatigue limit.

It is obvious that the infinite life design will be too conservative and thus sacrifice the economic efficiency. In addition, some studies on fatigue and fracture for high-strength steels starts to challenge the existence of fatigue limit (Suresh, 1998), which holds that there is no obvious fatigue limit on S-N curves. Sonsino (2007a) also proposed similar ideas for the cases of jointed components, material in high temperatures and corrosive environments. The infinite life design is, therefore, more of a way on designing irreplaceable components in some industries, but not an option for large-scale civil engineering projects.

b) Safe life design

Safe life design is to provide sufficient ability to resist fatigue failure for the structure during its design life. It is developed from infinite life design method, thus they both use nominal stresses as the basic design parameter following S-N curves. The difference is that the safe life design considers the fatigue resistance with respect to the stress range. That means the fatigue performance is evaluated by calculating the damage induced by the stress ranges higher than the fatigue limit. The damage is usually accumulated linearly according to Miner's Rule,

$$D = \sum n_i/N_i \tag{1-2}$$

where D is the damage; n_i is the applied stress cycles; N_i is the stress cycles at failure; the subscript i refers to the corresponding stress ranges. Therefore, the safe life design is much more economic than infinite life design, which make it the most common method to design engineering structures such as OSDs.

c) Damage tolerance design

The concept of damage tolerance design was firstly proposed in the aircraft industry, which attempted to take initial defects and maintenance into account in the design phase. The design aims to evaluate the residual life by recognizing the damages in maintenance, thus requires consideration of three factors: the residual strength, crack growth life, and damage detection. The residual strength analysis is to determine the allowable damage and to ensure the structure keeps the capability to resist fracture. The crack growth life provides the time for the current crack grows to the critical size, according to which the inspection periods could be determined. Finally, the damage detection guarantees the cracks or other defects can be detected before they start to jeopardize the structure safety and serviceability.

Combined with the fracture mechanics, damage tolerance design considers the ability of fracture resistance effectively, and thus is feasible on preventing fracture of the structure, especially the brittle fracture on key components. Therefore, it is helpful to use damage tolerance design when the aforementioned three factors are achievable, as demonstrated by examples in industries like aircraft, marine (Lassen and Sorensen, 2002) and automotive (Mahadevan and Ni, 2003). However, it is not yet conducted on OSDs due to the difficulties in fatigue-oriented inspections in bridge engineering during the whole service life. The main reason could be attributed to the difference in scale between fatigue cracks and structures, which requires high precision and a gigantic amount of work for inspection.

1.2.1.2. Vehicle loads

Vehicle loads are the main cause of the stress ranges applied on welded joints of OSDs. It can vary from the bridge sites, vehicle types, and the traffic volume increase when looking into long-term effects like fatigue. Therefore, the vehicle loads defined in standards or codes are often based on the statistical analyses on domestic transportation status, and may differ with each other.

British standards BS 5400 (BSI, 2000) defines a standard vehicle for fatigue design, while the Japanese Bridge Fatigue Design Recommendation and AASHTO LRFD (AASHTO, 2012) provide a similar way for regular fatigue load. Furthermore, for the OSDs and the wearing surfaces on them, a refined loading pattern is also recommended by AASHTO LRFD, which is apparently another

proof that the fatigue on OSDs should be paid extra attention to. In Eurocode 1 (NBN, 2004), a detailed work is conducted as the fatigue load is divided into five different types, with respect to different design concept. For instance, Fatigue Load Models 1 and 2 are for infinite life design, while Fatigue Load Models 3, 4 and 5 are for fatigue life assessment according to fatigue strength curves, following the way of safe life design.

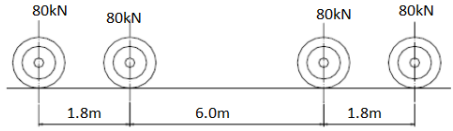

Fig. 1-3 Standard vehicle for fatigue design in BS 5400

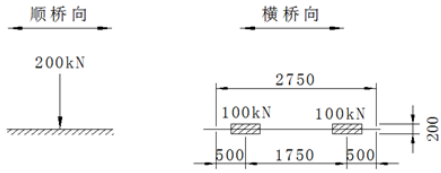

Fig. 1-4 T-loading in Japanese Bridge Fatigue Design Recommendation

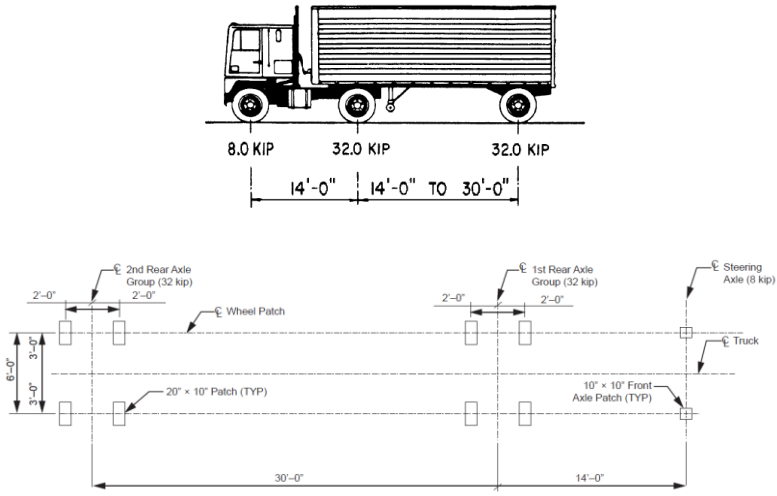

Fig. 1-5 Design truck and the refined loading pattern for OSDs in AASHTO

According to these standards and recommendations, the vehicle types, axial weights on each lane are significant factors for fatigue performance of OSDs. It illustrates the necessity to consider the realistic traffic volumes and related parameters for the specific bridge. Wang et al. (2005) proposed a three-dimensional nonlinear model based on data from Weigh-In-Motion (WIM) systems to analyze fatigue damages on steel bridges, with a case study on one specific site on the I-75 in the United States. Ji et al. (2012) generated a random traffic flow model based on traffic data from the toll system, and analyzed the traffic-induced stresses on the steel deck of a suspension bridge on the Yangtze River combined with the finite element model.

Furthermore, the specific wheel location, rather than the vehicle distribution on different lanes, is quite crucial on this issue, especially for OSDs whose fatigue is mainly caused by local load effects. Almost all the standards or codes, including BS 5400 (BSI, 2000), AASHTO LRFD (AASHTO, 2012), Eurocode 1 (NBN, 2004), uses a normal distribution assumption for the transverse in-lane position of vehicles, as shown in Fig. 1-6 a). Nevertheless, it is just a simplification and thus may not be accurate and not necessarily conservative for fatigue of different bridges. In Japanese Recommendation, a quasi-normal distribution was adopted based on measured data, see Fig. 1-6 b). Zhou et al. (2015) investigated the effect of transverse in-lane position based on WIM system, and proposed that it follows Gumbel distribution, instead of the commonly-used normal distribution.

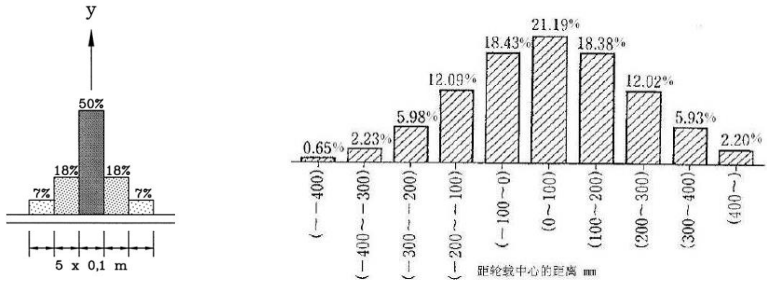

a) Eurocode 1 b) Japanese Recommendation

Fig. 1-6 Frequency distribution of transverse location of central line of vehicle

1.2.2. Fatigue-prone details on orthotropic steel decks

The earliest researches on fatigue of OSDs can be traced back to 1967, when fatigue cracks, and brittle fractures in some cases, were found on the welded joints of highway and railway bridges in the United States (Fisher, 1970, 1979, 1989).

According to the results from on-site investigations and full-scale fatigue tests, it is believed that the stress range is the most significant factor that affects the fatigue life. In addition, the fatigue failure behaviors of 22 steel bridges were analyzed, showing the relationships between fatigue and parameters like crack sizes, weld geometries and fracture toughness.

In 1970s, fatigue cracks were found on the Severn Bridge, a suspension bridge with an 11-mm thick deck plate and 6-mm thick trapezoidal ribs. According to Wolchuk (1990), three kinds of cracked details were found: a) welded attachments; b) rib-to-cross-beam welds; c) rib-to-deck welds. The Humen Bridge in China, which is put into service in 1997, suffered from fatigue cracks on its OSD since 2003. The investigation found cracks on deck plate, rib-to-deck welded joints and rib-to-diaphragm welded joints, as shown in Fig. 1-8. According to a summarizing study on fatigue cracks on OSDs of Hanshin Highway Bridges in Japan, four typical locations that crack occurs were stated with respective proportion: a) rib-to-deck welds (9.7%); b) longitudinal ribs butt welds (3.6%); c) welds that connecting vertical web stiffener and deck plate (20.9%); d) rib-to-diaphragm welds (56.3%) (Zeng, 2011). Therefore, the studies on fatigue on OSDs are usually based on different details rather than the whole structure.

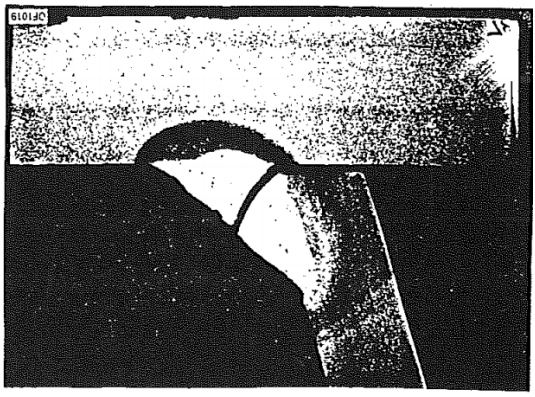

Fig. 1-7 Rib-to-deck weld fracture in Severn Bridge (Wolchuk, 1990)

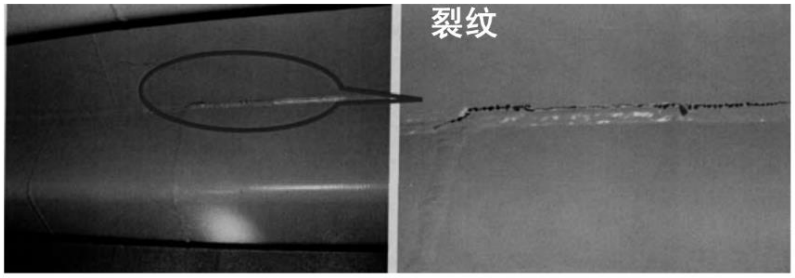

a) Rib-to-deck weld crack

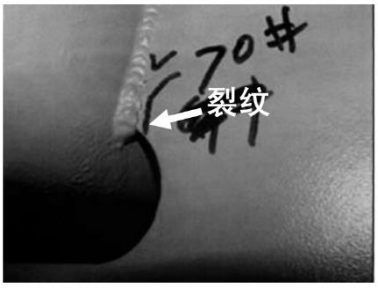

b) Rib-to-diaphragm weld crack

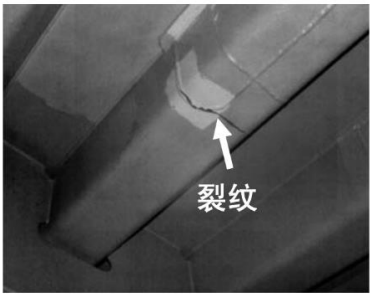

c) Longitudinal ribs butt weld crack

Fig. 1-8 Fatigue cracks on Humen Bridge

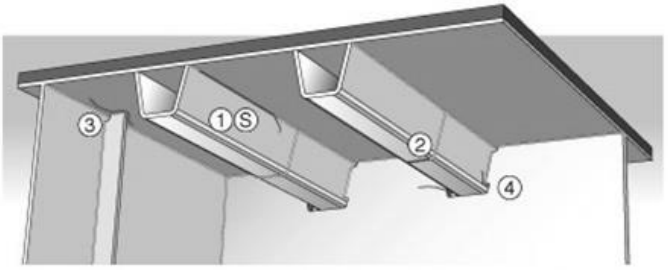

①Rib-to-deck welds

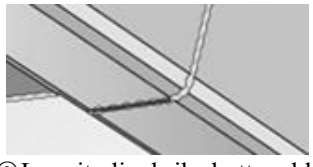

②Longitudinal ribs butt welds

③Vertical stiffener and deck welds

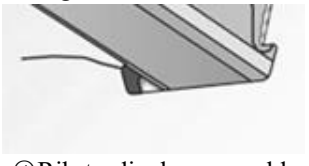

④Rib-to-diaphragm welds

Fig. 1-9 Four typical cracks on OSD on Hanshin Highway Bridges

1.2.2.1. Rib-to-deck welded joints

Among all types of cracks on OSDs, crack on rib-to-deck welded joints is regarded as the most harmful one, as it goes through the deck plate and results in larger deflection and local failure of the pavements. The aforementioned Humen Bridge was one of the victims of it, and was eventually out of service even after several retrofitting works. Another instance is the Second Van Brienenoord Bridge in Netherlands, which was built and put into service in 1990. Fatigue damages started to bother it after seven years, and led to severe reduction of serviceability and consequent repairing works of this bridge. The investigation showed that the typical crack is crack initiated from the rib-to-deck weld root and went through the deck plate, as shown in Fig. 1-10 (Maljaars et al., 2012).

Wang and Feng (2009) showed that the rib-to-deck welded joints cracked in the following three ways: a) weld toe crack that goes through the longitudinal rib; b) weld toe crack that goes through the deck plate; c) weld root crack go through the weld throat. While according to Zeng (2011), other types of weld root crack that goes through the deck plate (CR-D-6 and CR-D-8 in Fig. 1-11) were also stated.

De Backer et al. (2007) conducted a strain measurement to investigate the stress concentration on this detail, achieved results validated by comparison with that from Finite Element Method (FEM) models. With this measuring system, different pavements on OSDs were studied afterwards, indicating a possible 20% to 30% reduction of stresses (De Backer et al., 2008a). They also proposed an analytical way to calculate the internal forces (De Backer et al., 2008b).

Xiao et al. (2006, 2008) studied different types of cracks around rib-to-deck welds based on the Kinuura Bridge in Japan. By comparing the experimental results with the Linear Elastic Fracture Mechanics (LEFM) solutions, it is claimed that the welded joint will have low fatigue strength if the fusion zone is too small. By using FEM on OSDs, it was also found that the out-of-plane momentum is the main reason of the high local stress in this detail, and thus suggested to enlarge the wheel contact area, or use deck plates with bigger thickness, to improve the fatigue performance.

Nagy et al. (2015b, 2016) evaluated the fatigue behavior of rib-to-deck welded joints using LEFM and eXtended finite element method (XFEM), obtained the crack path at the weld root in a more realistic way. By comparing the crack growth curves for random and fixed load sequences, it is implied that the load sequence will not affect the crack length at the final stage.

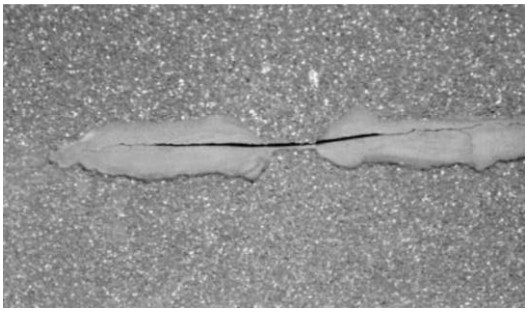

Fig. 1-10 The though-crack in the Second Van Brienenoord Bridge (Maljaars et al., 2012)

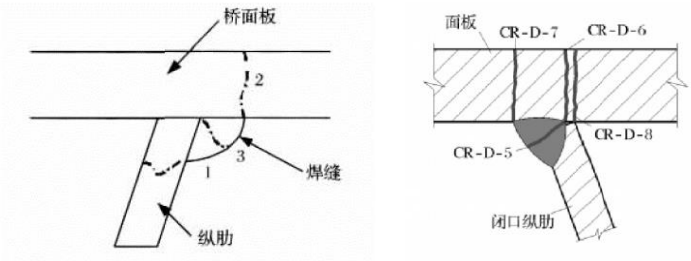

a) Wang and Feng (2009) b) Zeng (2011)

Fig. 1-11 Different types of crack on rib-to-deck welded joints

As the lack-of-penetration is the main cause of root cracks on this detail, it is always believed that more penetration to weld root could be effective on preventing crack initiation from weld root and growth through weld throat. But according to some recent studies (Ya and Yamada, 2008, Sim and Uang, 2012), specimens with full penetration are of slightly lower fatigue strength than those with 80% penetration. Kanimura et al. (2016) investigated the rib-to-deck weld root cracks with tests on specimens with different weld penetration rates and stress ratios, and confirmed the benefits of penetration rate slightly lower than 100%, e.g. 80%, on fatigue strength. In addition, the tensile mean stress, was emphasized for its effect on root crack initiation.

1.2.2.2. Rib-to-diaphragm welded joints

Rib-to-diaphragm welded joint is a quite, if not the most, fatigue-prone detail according to the given proportions of detected cracks as mentioned before, i.e. 56.3%.

The common way in early design of OSDs is to weld the longitudinal ribs to diaphragms directly, without setting up cut-outs on diaphragms, which means the

longitudinal ribs were interrupted. This design, as applied by the Severn Bridge, may result in severe out-of-plane distortion, help crack starting from the bottom of the longitudinal ribs. Therefore, current fatigue design suggests using cut-outs on this detail, while the shape of the cut-outs became another issue on fatigue design afterwards. The widely-used type of cut-outs are in elliptical shape, as suggested in Japanese recommendation and Eurocode for highway bridges, see Fig. 1-12. For railway bridges, a novel design, named Haibach cut-out, is recommended by Eurocode, which can reduce the stress concentration and improve the fatigue performance on rib-to-diaphragm welded joints.

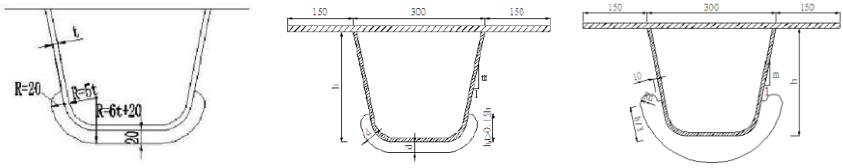

a) Japanese Recommendation | b) Eurocode for highway bridges | c) Eurocode for railway bridges

Fig. 1-12 Cut-out shapes in different specifications

Nevertheless, the stress concentration induced by the cut-out still exists, leading to cracks at the bottom weld toe of rib-to-diaphragm welded joints. Tsakopoulos and Fisher (2003) studied the plan of replacement of the OSD on Williamsburg Bridge with fatigue tests, and compared to other designs suggested by AASHTO LRFD. It was proposed that by using thicker diaphragms, the in-plane stresses can be reduced without increasing out-of-plane stresses. Zhang et al. (2015) conducted full-scale fatigue tests on this detail, and analyzed it with hot-spot stress method and notch stress method, concluding that the fatigue performance is still determined by the out-of-plane distortion of ribs.

Provided that the rib-to-deck welded joints and rib-to-diaphragm welded joints are both lacking of fatigue resistance, the detail at the intersection of them, as Qian and Abruzzese (2009) called rib-to-diaphragm-to-deck plate (RDDP), should be paid extra attention to on fatigue issues. Kolstein (2007) presents a typical example of cracked RDDP, as given in Fig. 1-13. Another instance of Jiangyin Yangtze River Bridge is shown in Fig. 1-14. Zhou (2010) summarized the procedure of the crack propagation at RDDP, divided it into three phases (see Fig. 1-15): i) crack initiation at RDDP; ii) crack grows perpendicularly, and go through the deck plate; iii) crack grows longitudinally. It is also suggested that the phase ii and iii may proceed simultaneously, resulting in dangerous invisible long cracks.

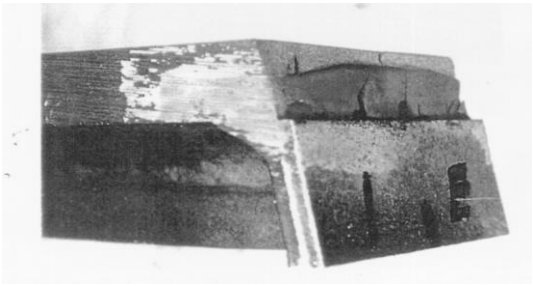

Fig. 1-13 Typical crack at RDDP welded joint (Kolstein, 2007)

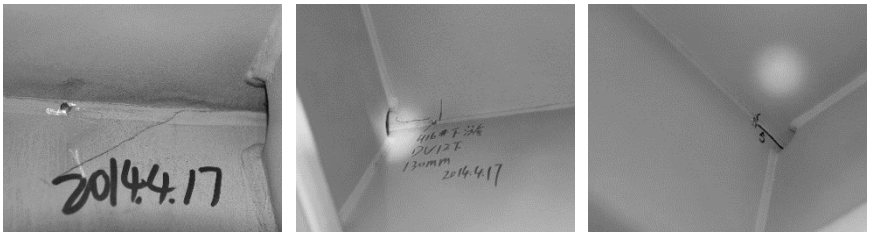

Fig. 1-14 RDDP cracks on Jiangyin Yangtze Bridge, China

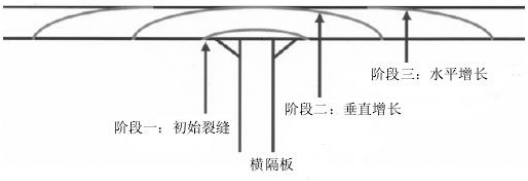

Fig. 1-15 Three stages of RDDP crack growth (Zhou, 2010)

1.2.2.3. Longitudinal rib welded joints

Longitudinal ribs used to be connected with butt welding, which is convenient to construct, but vulnerable to fatigue damages. The main reason is the relatively low quality of on-site welded joints, which may result in defects such as the misalignment. Tong and Shen (1998, 2000) evaluated the on-site butt weld joints of longitudinal ribs and claimed that the misalignment is an important factor to the fatigue performance. It was found that the misalignment might reach 30% of the thickness of ribs, which will greatly reduce the fatigue life. Besides, the over-head welding is also regarded as a significant cause for low welding qualities.

Therefore, the butt welding is not the preferred way of connecting longitudinal ribs recently. More bridges with OSDs attempted to improve the design of this

detail using high strength bolt connection, or to retrofit this detail with it. It is proven that this type of connection is easy to construct by machinery ways, and thus provides stable and better connection quality and fatigue performance. Fig. 1-16 presented an example of the Third Yangtze Bridge in Nanjing (Feng, 2009).

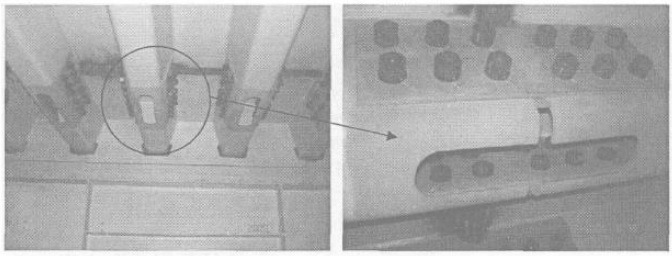

Fig. 1-16 The high strength bolt connection of longitudinal ribs (Feng, 2009)

1.2.3. Weld fatigue

1.2.3.1. Fatigue strength classification and evaluation

In the scope of weld fatigue study, the early indicative works were focused on fatigue strength classification for different weld types (Gurney 1979, 1991). The accomplished researches successively helped to develop British Standard BS 5400, which provides different fatigue categories according to weld types, as shown in Fig. 1-17. Similarly, the existing specifications or codes about weld fatigue also use the weld type classification for fatigue design of welds. Note that when using the classifications to evaluate the fatigue life, the reference stress ranges could be determined in different ways as follows.

a) Nominal stress method

Nominal stress method is the starting point of stress-based fatigue evaluation, and is quite practical as it developes with long-term experiences in practice. It assumes that the fatigue strength is related to the remote stress of region of interest. For simple components, nominal stress can be obtained by linear elastic analytical models, while for complex structures, a relatively coarse finite element model would suffice as well.

b) Hot-spot stress method

Hot-spot stress method develops from nominal stress method, with the main idea to take the key position as the “hot-spot” to evaluate the fatigue strength. It calculates the hot-spot stress by extrapolating from stresses at another two or three spots. It usually considers the geometrical stress concentration by linear extrapolation, whilst the non-linear stress peak might be ignored. The spots whose

stresses to be measured or calculated could vary from different recommendations or standards. Hot-spot stress method is commonly applied by fatigue evaluation or prediction on welded joints of OSDs. Zhou (2003) analyzed the fatigue performance of key components of Tsing-Ma Bridge in Hong Kong, China, using hot-spot stresses method. The relationship between the hot-spot stress and nominal stress was addressed, and the stress concentration factor was achieved.

c) Notch stress method

Due to the presence of macroscopic notch in the vicinities of welded joints, and the possible weld defects such as pores, inclusions, slag etc., the analysis on weld fatigue strength often turns into fatigue evaluations with respect to notch effects. Radaj (1997) proposed the concept of fictitious notch for the short gaps or cracks in welded joints, and validated by applying on a cruciform welded joint. Afterwards, the effective notch stress method based on the fictitious notch was put forward and became widely-accepted. It was also recommended by International Institute of Welding (IIW) (Hobbacher, 2008), suggesting a weld toe/root notch with a 1mm radius should be adopted in fatigue evaluations (see Fig. 1-18). Studies on notch fatigue (Radaj et al., 2009, Berto and Lazzarin, 2010) showed that the results are sensitive to the detailed geometries, such as the notch tip radius and the opening angle. However, the size of this fictitious notch is still under discussion. Vogt et al. (2012) believed that a notch with a 0.3mm radius will lead to better accuracy according to test results, whilst Schijve (2012) suggested that it should be dependent on the weld bead height, and the ratio of notch radius to weld bead height should equal 0.1. These discussions show that more researches on this issue is still needed to cut down the safety margin and/or to improve the current fatigue design method. Apart from that, the concept of notch stress also helped to develop the Notch Stress Intensity Factor (NSIF) for fatigue evaluation (Atzori et al., 2008, Lazzarin et al., 2010).

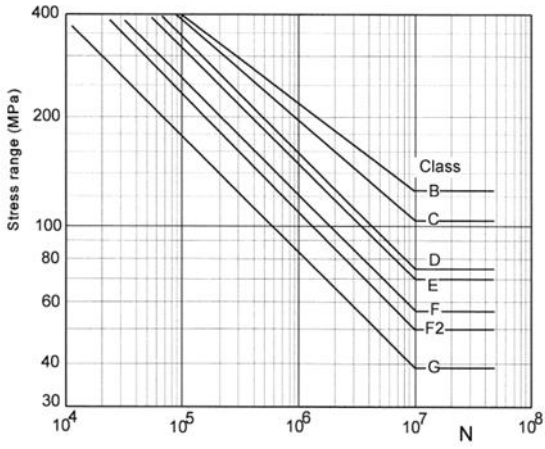

Fig. 1-17 Different categories of fatigue strength (Gurney, 1979)

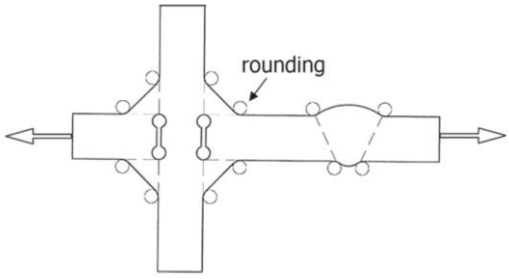

Fig. 1-18 The fictitious notches in Effective Notch Stress Method (Hobbacher, 2008)

Benefited by the development of computation abilities nowadays, the hot-spot stress method and notch stress method were applied more and more in realistic projects. Fricke et al. (2012) studied the fatigue on fillet welds with hot-spot stress method and effective notch stress method, obtained similar results with both methods. Aygül et al. (2012, 2013) built the model of OSDs with FEM, and compared the results to that from full-scale tests. Then the fatigue lives were calculated by nominal stress method, hot-spot stress method and effective notch stress method, and the feasibility of the three method on this issue were provided.

Even though the stress-based fatigue evaluation method were proven to be effective in practice, they were still empirical and required large amount of fatigue tests for a specific project. As the welding techniques developed and the fatigue mechanism in welded joints better revealed, the simple way of fatigue strength

classification appeared to be outdated in recent years. More researches started to investigate and evaluate fatigue based on its mechanism, which is more relevant to the mesoscopic or microscopic structures of welded joints, and the effect of residual stresses.

1.2.3.2. Weld defects

The weld defect is always regarded important on fatigue strength. In the early stage, the macroscopic weld defects, especially the geometries that may lead to stress concentration, were the main concerns back then. Gurney (1979) tested the butt welds of different weld toe flank angles and weld toe radius. They are both seemed sensitive to the fatigue strength, especially for high cycle fatigue issues, as shown in Fig. 1-19. Therefore, by grinding the weld toe, even may introduce undercuts on welds, the fatigue life will be largely prolonged.

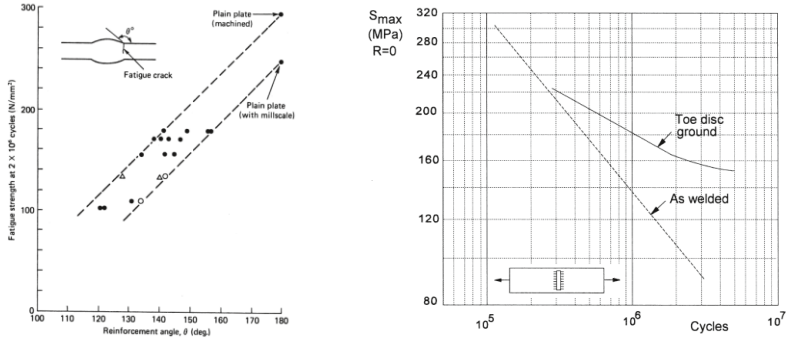

Fig. 1-19 The effect of weld toe flank angle and weld toe radius (Gurney,1979)

Miki et al. (1993, 2001) listed five kinds of defects in welded joints that are widely-accepted to have significant effects on the fatigue performance, i.e. cracks (CR), incomplete penetration (IP), lack of fusion (LOF), slag inclusions (SI) and blowholes (BH) in Fig. 1-20. By evaluating the fatigue strength of fillet welds and butt welds with defects, it can be stated that the shape, size and location of the defects are the key contributing factors to the fatigue performance. In fact, with the development of welding technologies and non-destructive testing (NDT), such large weld defects in Fig. 1-20 became rare in practice, whilst the defects in meso-scale or even micro-scale were the main source of the fatigue cracks. A recent and updated summary on the possible scales of defects a component subjected to cycling loads based on existing examples was provided by Zerbst et al. (2012), as shown in Fig. 1-21. It should be noted that the scales of defects, such as flaws, pores, inclusions, were all beyond the scope of NDT, thus might exist in the welded

joints that do meet to criteria of weld specifications, and affect the fatigue strength of the structures eventually.

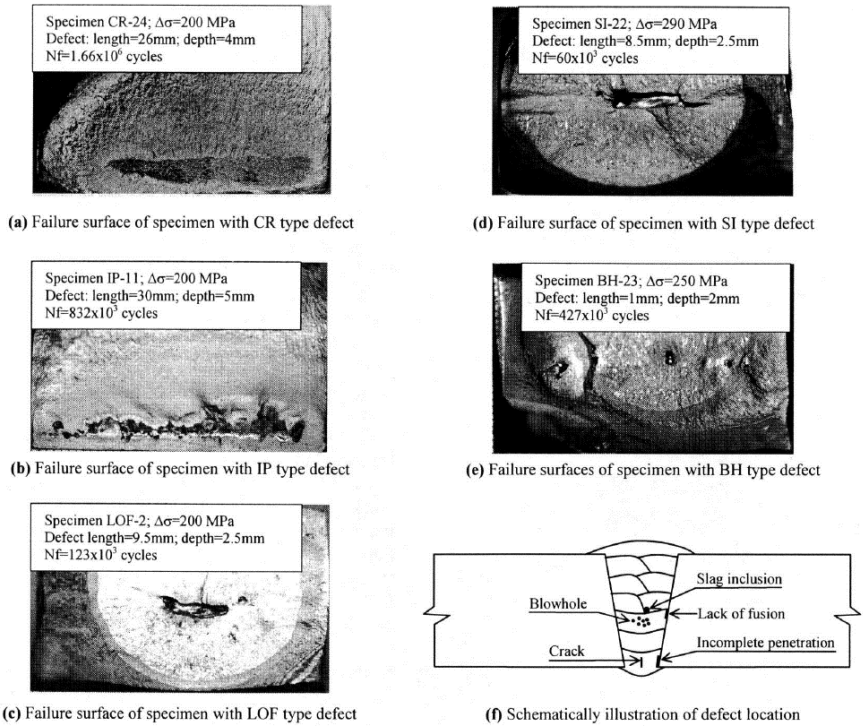

Fig. 1-20 Typical weld defects on fracture surfaces (Miki et al., 2001)

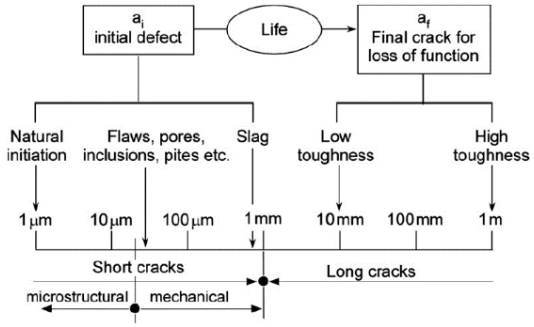

Fig. 1-21 Length scales of the life cycle of a component subjected to cyclic loading (Zerbst et al., 2012)

1.2.3.3. Heat-Affected Zone

Heat-affected zone (HAZ), as the transition area between base material and welding material, is believed to be an important feature that affects fatigue strength of welded joints. Due to the welding process, mechanical characteristics of the materials in HAZ are different from that of parental material (PM) and welding material (WM). From a metallographic perspective, the essential cause is the difference of microstructures in HAZ. Remes et al. (2012) compared the grain size in PM, and in HAZ of submerged-arc welding and laser hybrid welding, as shown in Fig. 1-22.

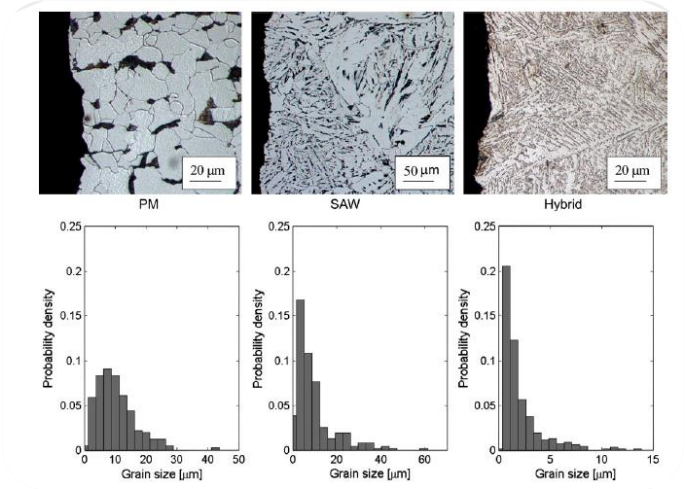

Fig. 1-22 The grain size of parent metal (PM), HAZ of submerged-arc welding (SAW), and HAZ of laser hybrid welding (Hybrid) (Remes et al., 2012)

According to Fig. 1-22, it is easy to find that inside the HAZ of SAW, the grain size could vary due to the different distances to the weld central line. Ramazani et al. (2013) investigated the HAZ of gas metal arc welding (GMAW), demonstrated the microstructures of sections of different distances (see Fig. 1-23). Therefore, HAZ could be divided it into several sub-zones, in which the microstructures always vary from each other because of the different compositions of ferrite, martensite, bainite and pearlite etc. Lee et al. (2000) tested the welded joints with post-weld treatment, analyzed the fracture toughness of the HAZ. The results showed that the fracture toughness of WM is better than other parts. Inside HAZ, the acicular ferrite zone has better fracture toughness, while the worst one is the sub-zone consisting of coarse grains of bainite.

Since the different types of grains will present different hardness in macro-scale, studies on HAZ were often based on hardness. Hertelé et al. (2014) presented the hardness distribution of a typical butt weld HAZ, as shown in Fig. 1-24. Remes (2008) attempted to divide HAZ of laser welded joint into four sub zones, and studied the crack growth in it with respect to material properties according to hardnesses.

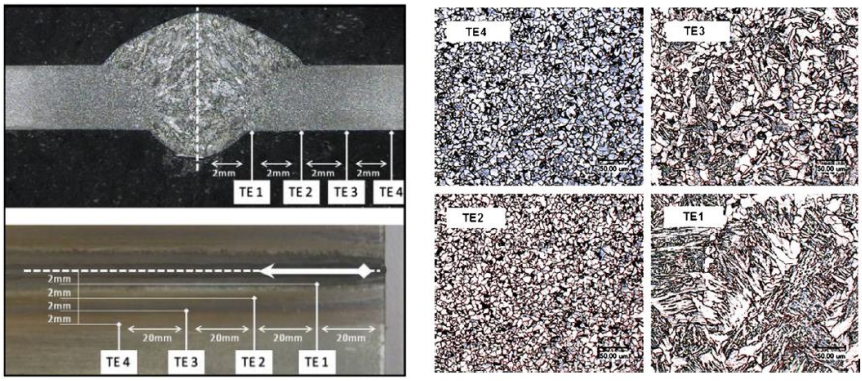

Fig. 1-23 Microstructures in sections of different distances of HAZ (Ramazani et al., 2013)

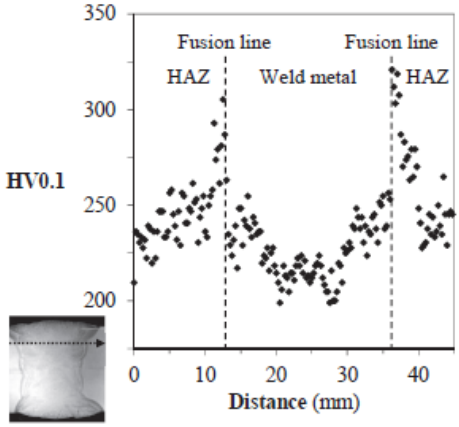

Fig. 1-24 Hardness of a typical butt welded joint (Hertelé et al., 2014)

1.2.3.4. Residual stresses

Generally speaking, residual stresses in welded joints are mainly produced by thermal strains in welding process, and will be particularly harmful when tensile

residual stresses exist at the weld toe (Schijve, 2001, Radaj, 2003). Different experimental methods can be applied to measure the residual stresses, and were mostly adequate and accurate on condition that proper care is taken according to the standards, such as ASTM E837-13a (ASTM International, 2013). Zerbst et al., (2014) summarized the previous works and demonstrated the residual stress distributions of a butt welded joint, as shown in Fig. 1-25.

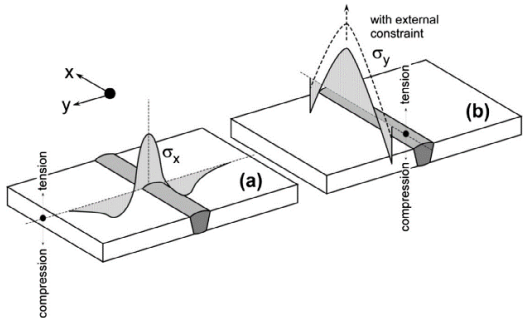

Fig. 1-25 Schematic welding residual stress distributions in a butt joint (Zerbst et al., 2014)

In terms of the effect on crack growth, the residual stress is believed to act in a similar way of mean stress, which means it will change stress intensity factor range and stress ratio, and may interact with the plasticity induced crack closure (Beghini et al., 1994). Therefore, residual stress has drawn attention of the industry when investigating the fatigue performance of OSDs. Beghini et al., (1997) studied the fatigue life of OSDs using weight functions that are capable of considering the residual stresses. The results suggested that the effect is dependent on the manufacturing process, and can be beneficial under certain conditions. It proved that some post-weld treatments can provide practical solutions for this issue by releasing tensile residual stresses and/or introducing compressive residual stresses. Cheng et al., (2003) studied the residual stress of the welded joints and the fatigue performance after using two different post-weld treatments: ultra-sonic impact treatment (UIT) and shot peening treatment. The results showed that UIT produced larger area of compression stress, and was useful to stop the initiation and early-stage growth of fatigue cracks. Roy et al. (2003) also confirmed the improvement on fatigue strength of welded joints using UIT, and emphasized its effect on reducing the micro-discontinuities of welded joints and subsequent increasing crack growth threshold.

On the other hand, the knowledge about the residual stress distribution of as-welded joints is equally important, since the majority of existing OSDs did not employ the post-weld treatments that can release residual stresses in a considerable way. Nagy et al., (2015a) conducted a hole-drilling measurement on welded joints of OSD, mainly focused on the weld toe part due to the limitation of possible site to drill the hole. For the weld root part, Kainuma et al. (2016) measured the residual stresses using cutting and magnetostriction method. However, given the difficulty in measuring the residual stresses for welded structure with complex geometries, especially when a non-destructive way is required, the numerical simulation ways were developed as an applicable way to predict and evaluate residual stresses. Based on the measurement mentioned before, Nagy (2017) further calculated the residual stress distribution around rib-to-deck welded joints by numerical simulation, and the results were validated by comparing with the test results. Lindgren (2001a, 2001b, 2001c) summarized the methods on welding simulation, and established a model incorporating with other methods in engineering. Barsoum and Barsoum (2009) proposed an FEM way to simulate welding process with access to prediction of the residual stresses. The prediction was validated by comparing the crack propagation path calculated by fracture mechanics and that from fatigue tests.

1.2.4. Fatigue behavior and prediction

Classical fatigue evaluation and prediction were established by stress-life relationship, i.e. S-N curves, as given in Fig. 1-17. This method only defines the fatigue failure point for materials, therefore lead to insufficient knowledge on the fatigue mechanism. Consequently, efforts were made on investigating the progress of fatigue to reveal the mechanisms.

1.2.4.1. Typical stages of fatigue behavior

The entire fatigue progress is often divided into four stages according to the different behaviors and mechanisms: i) crack nucleation and initiation; ii) short crack growth; iii) long crack growth; iv) final fracture (Chen, 2002, Lee, 2005). In practice, fatigue life spent in Stage i and ii is recognized as crack initiation life, and that in Stage iii and iv as crack propagation life. In terms of the number of cycles consumed till final fracture, the fatigue can be divided into high-cycle fatigue and low-cycle fatigue. In high-cycle fatigue, the elastic deformation is dominant since the plastic zone around crack tip is quite small, and the crack initiation life occupies the majority of the whole life, with the proportion about 80% or more according to some studies (Yang et al. 1997). Whilst in low-cycle fatigue, elastoplastic

deformation is dominant, and crack initiation life is relatively short, leading to a total number of cycles below 10^4 - 5×10^4.

In fatigue studies, especially the high-cycle fatigue, the final fracture stage, also known as the unstable growth stage, is often quite short and thus can be ignored. For the other three stages, Fig. 1-26 provided a clear demonstration. If the initial crack is not the case, the crack will initiate because of the formation of persistent slip band due to micro-stress concentration. It propagates in a microstructural way after initiation, i.e. in the short crack growth stage, and then gradually turns to propagate in a mechanical way, i.e. in the long crack growth stage. In fact, there is no clear boundary between these two stages, but according to previous works (Chen, 2010), the size of short crack is around 0.1 ~ 1.0 mm, and crack with size beyond that range is regarded as long crack. This conclusion made an accordance with Fig. 1-21 as well. Therefore, for the weld fatigue issues, the understanding of the fatigue behaviors in short crack growth stage and long crack growth stage is of higher value than that in the crack initiation stage. It is because the weld defects are quite possible to act as the source of initial cracks, since their sizes are apparently larger than that of persistent slip bands.

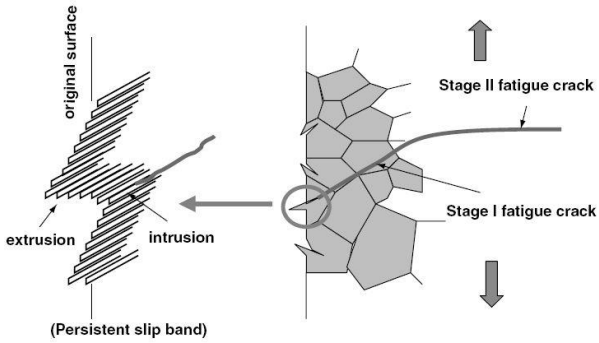

Fig. 1-26 Fatigue behavior of a thin plate under cyclic tensile stress (Lee, 2005)

1.2.4.2. Paris law

The development of fracture mechanics brands a new period for fatigue study, especially for the part of steady long crack propagation. One of the fundamental and most significant studies is conducted by Paris and Erdogan (1963), which obtained the crack growth rate (CGR) curve by testing the propagation of a central crack on aluminum plate. Accordingly, the Paris law that fit part of the curve, i.e. the Paris region, was put forward as follows:

$$\frac{da}{dN} = C(\Delta K)^m \tag{1-3}$$

where a is the crack length and N is the number of load cycles; $\Delta K = K_{max} - K_{min}$, is the stress intensity factor (SIF) range; C *and* m are the Paris constant and exponent, respectively, and are usually experiment-based. Paris then presented the crack growth rate curve for A533 steel, which also fit the Paris law, as shown in Fig. 1-27.

Even though Paris law is widely applied in engineering projects, such as the aforementioned Damage Tolerance Design, it only fits part of the CGR curve, and is affected by the way of load applying. Hence various modified form of Paris law has been put forward. Foreman proposed the following form of Paris law that could be applied to the fast propagation phase:

$$\frac{da}{dN} = \frac{C(\Delta K)^m}{(1-R)K_C - \Delta K} \tag{1-4}$$

where K_C is the fracture toughness. Walker proposed a modified Paris law that is able to take stress ratio R into account:

$$\frac{da}{dN} = C(1-R)^m (K_{max})^n \tag{1-5}$$

Elber (1971) observed the crack closure in fatigue crack propagation, which means the crack tip starts to close before the unloading of tensile stress. The reason is that the elastic area will add an extra compression force to the plastic zone around the crack tip when unloading, thus lead to the crack closure phenomenon. Consequently, an effective SIF range ΔK_{eff} is suggested to be taken into account. by the Paris law as follows:

$$\frac{da}{dN} = C(\Delta K_{eff})^m \tag{1-6}$$

and a closure coefficient U is introduced:

$$U = \Delta K_{eff}/\Delta K \tag{1-7}$$

Schijve (1981) studied the effect of stress ratio R on this closure coefficient based on tests on 2024-T3 aluminum alloy, and proposed a parabolic formula to quantify the effect with good accuracy. Another similar idea is to introduce the threshold of SIF range ΔK_{th} into Paris law (Donalure, 1972):

$$\frac{da}{dN} = C(\Delta K - \Delta K_{th})^m \tag{1-8}$$

or another form that considers fracture toughness:

$$\frac{da}{dN} = C\left(\frac{\Delta K - \Delta K_{th}}{K_C - K_{max}}\right)^m \tag{1-9}$$

The Paris law with respect to the threshold value is also adopted in NASGRO model for fatigue life predictions, and applied to various industries (Jones et al., 2015).

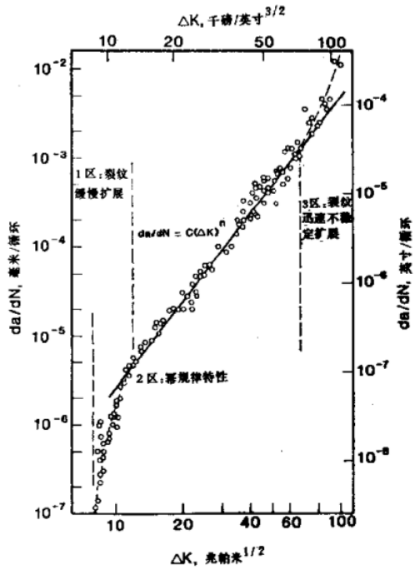

Fig. 1-27 The crack growth rate for A533 steel (R=0.1) (Wang & Chen, 2009)

1.2.4.3. Short crack propagation

As mentioned before, no clear boundary can be addressed between short and long cracks. It is, however, can be generally distinguished for the sake of different behaviors. Miller (1993) indicated that the thresholds of micro-crack and mechanical crack were different, and Microscopic Fracture Mechanics (MFM) and Elastic-Plastic Fracture Mechanics (EPFM) should be applied. A similar idea was proposed by Zerbst et al. (2014) that three stages for short crack initiation and propagation before it turns to long crack were defined. It suggests that even for a short crack, the behavior might vary because of the different sizes comparing to the grains. Only when the crack length exceeds a certain value, it starts to grow mechanically, thus can be described by continuum fracture mechanics. As defects included in engineering materials is often large enough, they could be treated conservatively as mechanically short cracks.

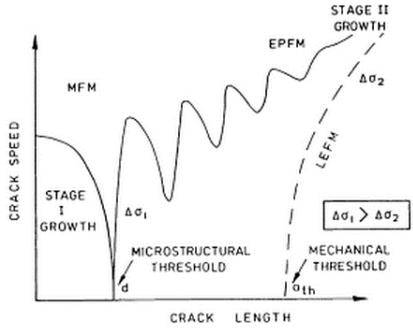

Fig. 1-28 Different fatigue thresholds d and a_{th} (Miller, 1993)

Unlike the cases of long cracks, the plastic area in the vicinity of short crack tip is relatively larger, that the behavior is more elastoplastic, and the propagation will not be in a steady way. And if the size of short crack is in the same magnitude of grain size, the plastic area, as well as the crack growth, will be influenced by the microstructures. Therefore, the LEFM may not be applicable to short crack propagation, and efforts on predicting the short crack propagation life were made in various ways. Theory of Critical Distance (Susmel and Taylor, 2007, 2010, 2012, Taylor, 2010) was one of the most practical models, in which the microstructural features are considered by introducing a critical distance that relates to material itself. With respect to the yield area around the crack tip, Remes et al. (2012, 2013) used the Manson-Coffin damage model in a characteristic length that is close to the maximum grain size, and simulated the propagation of a crack starting from a micro-notch on a butt welded joint. Similarly, the Generalized Paris Law (GPL) proposed by Pugno et al. (2006) and Unified Two-parameter Growth (UniGrow) model (Mikheevskiy et al. 2009, 2011, 2015) both attempted to introduce parameters that are related to microstructure of material, and were validated by experiments. Another novel method that showed potential on this issue is the Peridynamics. Its inherent advantage on fracture simulations and calculation of multiscale problems has drawn lots of attentions as well (Silling and Askari, 2005, 2014).

1.3. Problems and Objectives

Based on the above literature review, the problems in the scope of fatigue on OSDs can be summarized as follows:

1) Mesoscopic or microscopic structures of welded joints

As explained in Section 1.2.3, existing knowledge on the mesoscopic and microscopic structures of welded joints of OSDs is insufficient. Although the heterogeneity in materials induced by welding process, as well as different types of weld defects, were addressed for typical welded joints, the practical way for large-scale civil engineering projects like OSDs were to employ the fictitious defects at present. Due to the limitations of NDT technologies, few studies showed the specific features of meso- or micro-structure for OSDs as well. Consequently, their effect to fatigue performance of OSDs were not comprehensively considered.

2) Numerical simulation of crack propagation

Although the fatigue test on specimens is the most reliable and preferred way to investigate the fatigue performance of OSDs, the numerical simulation is still valuable when crack propagation is considered. Nonetheless, the numerical way to reproduce the critical stage of short crack propagation is still missing, especially when the weld defects are taken into account. It is more of a case that dominated by uncertainties, and requires an adequate and effective numerical method.

3) Multiscale method

The multiscale problem arises when looking into the big gap in scale between the tiny initial crack and the huge engineering work. For OSDs, the complexity of the structure itself and the randomness in vehicle loads present the necessity to build a proper multiscale method to calculate the entire process of fatigue crack growth on OSDs. It should be noted that there is no widely-accepted boundary between micro-, meso- and macro- scales when speaking of the fatigue on OSDs. In this study, the meso-scale refers to the scale in which the short crack grows in a mechanical way, while the smaller scale being the microscopic one and the larger scale being the macroscopic one. In that case, Fig. 1-21 could provide some knowledges or references.

With respect to the problems exist, this dissertation is supposed to achieve the following objectives:

1) To conduct the process-oriented fatigue tests on specimens of OSDs, revealing the relation between the microstructure and crack propagation behavior through fracture surface analyses;
2) To build the mesoscopic model to simulate the initial crack growth with consideration of uncertainties induced by weld defects and weld geometries;
3) To propose a method with multiscale concerns that links the mesoscopic model to the macroscopic one, and thus the random traffic loads can be taken into account;

4) To estimate the fatigue life of OSDs in a probabilistic context with respect to randomness from both the material itself and the loading.

Based on these objectives, a brief flowchart for this study can be given in Fig. 1-29. Accordingly, the thesis is organized as follows. Chapter 2 illustrates the process-oriented fatigue test, in which the fatigue behavior is investigated with fractographic and metallographic analysis. Based on the observation, Chapter 3 & 4 presents the principle and method of the numerical tool to build the mesoscopic model in a probabilistic context. Chapter 5 shows the way of establishing the multiscale method, and the validation/calibration of it based on the fatigue test. Afterwards, Chapter 6 introduces the random vehicle loading into the multiscale method, and estimates the fatigue life for actual projects.

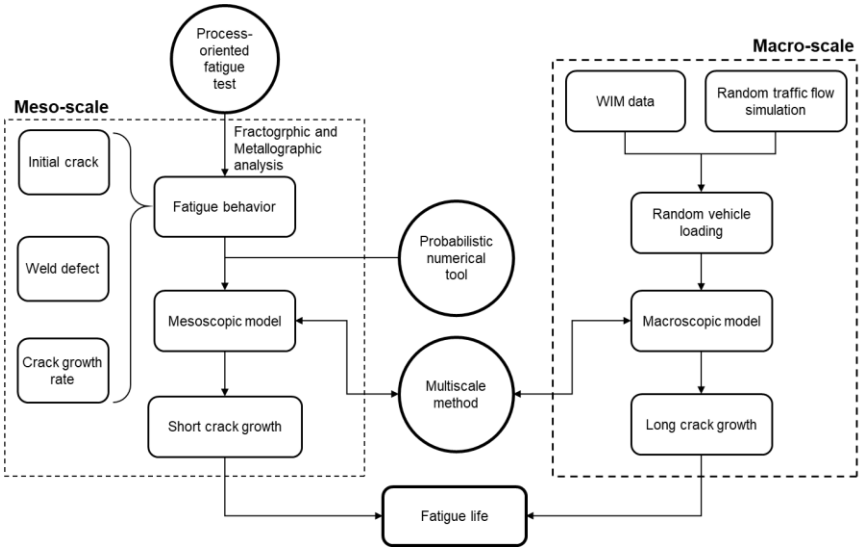

Fig. 1-29 A brief flowchart of this study

CHAPTER 2

FATIGUE TESTS AND MICROSTRUCTURE ANALYSIS

This chapter is based on:

Nagy, W., Wang, B., Culek, B., Van Bogaert, Ph., and De Backer, H., Experimental fatigue assessment of the stiffener-to-deck plate connection in orthotropic steel decks. *International Journal of Steel Structures (accepted)*

2.1. Introduction

In order to evaluate the fatigue strength of rib-to-deck welded joint of OSDs, the fatigue test should always be considered as the first option since it is the most convincing way. Kolstein (2007) summarized 245 fatigue tests on rib-to-deck welded joints of OSDs in the period of 1974 ~ 2000, and the stress-life relations were obtained and compared with the S-N curves in Eurocode. These tests were mainly carried out on small-scale specimens. The earliest example was provided by Maddox (1974), as shown in Fig. 2-1a. As the small-scale specimen is not exactly the real case, several series of test setups were conducted with variation of boundary conditions and loading positions, for generating similar stress status on deck plate and/or stiffeners. In recent years, more fatigue tests were carried out on full-scale specimens, which consist of several longitudinal stiffeners and at least two crossbeams (Tsakopoulos and Fisher, 2005; Sim et al., 2009; Kainuma et al., 2016). Benefited by the larger scale of specimens, these tests had more realistic boundary conditions, and the loadings were mainly applied via a pad to simulate the load dispersion effect of pavements, as shown in Fig. 2-1b.

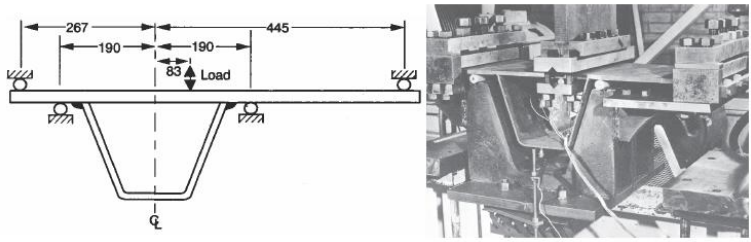

a) small scale specimen (Maddox, 1974)

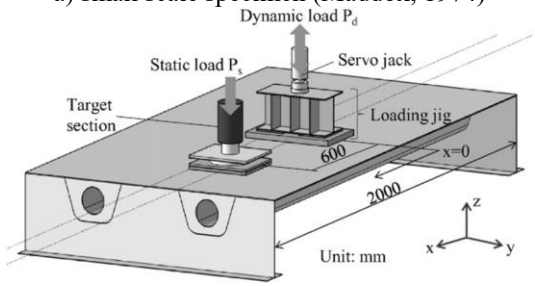

b) full scale specimen (Kainuma et al., 2016)

Fig. 2-1 Fatigue test schemes (unit: mm)

For most fatigue studies on OSDs, the classical stress-life relation, namely the S-N curve, is adopted. It is undoubtedly effective as recommended by most of the standards or specifications on fatigue strength evaluation. However, the S-N curve

only indicates the point when the specimen fails. As a phenomenological way, it is incapable of looking into the entire process of fatigue crack growth and the fatigue mechanism, apparently. This will inevitably lead to inaccuracies on estimating fatigue life in practice due to variation of other parameters. Furthermore, as there is a large number of welded joints on OSDs, the uncertainties introduced by welding process could be quite important, especially for the microscopic or mesoscopic crack in such a high-cycle fatigue. Once the uncertainties are taken into account, this way will be ineffective on this issue, since there is always limitation on the number of specimens.

Therefore, to better understand the entire process of fatigue crack growth and the scatter in fatigue test results, using some other method like fracture mechanics may provide valuable knowledge to assess the fatigue life. Since there is rare information available on crack growth process on rib-to-deck welded joints of OSDs, a fatigue test designed with respect to that is quite needed.

2.2. Test scheme

For the purpose of understanding the crack growth process on welded joints of OSDs, it is preferred that the fatigue tests can be repeated as many times as possible, so that the uncertainties could be better evaluated. In that case, fatigue test on small-scale specimens is a better option than on full-scale ones for cost concerns. Besides, the fractographic and metallographic analyses should be applied on the specimens to provide more details. Eventually, the fatigue tests were carried out in a recently-built laboratory in the University of Pardubice, Czech Republic, which is specialized in both performing fatigue tests and fractographic and metallographic analyses. The general view of this laboratory is shown in Fig. 2-2.

Fig. 2-2 Laboratory of the Educational and Research Center in Transport, University of Pardubice, Czech Republic (photo by Wim Nagy)

2.2.1. Test specimens and boundary conditions

For a test on the small-scale specimens, the boundary conditions need to be checked if they reproduce the similar stress concentrations at the same locations as in the reality. On the other hand, the possibility of realizing the boundary conditions in the laboratory will be considered as well.

In the first place, a full-scale model of an OSD was taken as a reference, as shown in Fig. 2-3. It is an OSD with 15-mm-thick deck plate and 6-mm-thick trapezoidal stiffeners. The span length between two diaphragms is 4 m. The trapezoidal stiffeners are 275 mm in height, and the width is 300 mm at the top and 150 mm at the soffit.

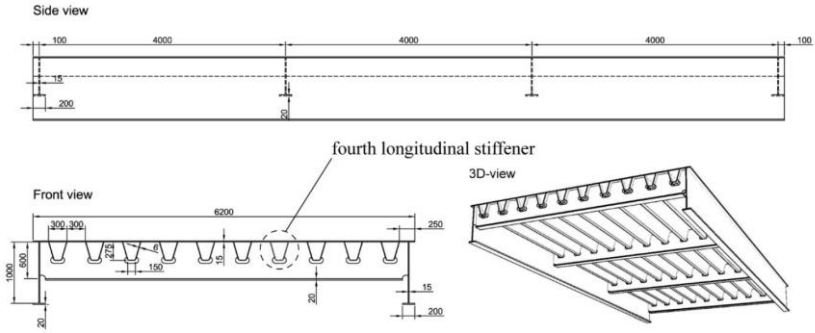

Fig. 2-3 Full-scale reference model of an OSD

Afterwards, the fourth longitudinal stiffener, which is the one nearest to the left wheel of the truck on slow lane, was selected to be the critical component. The small-scale specimen around it was modeled using FEM. The stresses at the weld toe and root of the rib-to-deck welded joint of this model were calculated and compared with that from the reference model. More details on the reference model can be found in (Nagy et al., 2016). Eventually, by comparing the ratio between stresses at the toe and root, and with compromises to the test conditions in the laboratory, the final test specimen and the boundary conditions were decided, as shown in Fig. 2-4.

The design of specimen consisted of a trapezoidal stiffener and a deck plate, with an out-of-plane length of 400 mm. It was simply supported at the distance between longitudinal stiffeners, i.e. 300mm, to the concerned welded joint, and fixed at the distance of 150 mm to the welded joint on the other side. The load was a line load applied at the distance of 80 mm to the left of the welded joint. Eventually, due to the inevitable difference between design and implementation,

the length of the specimens was actually 370 mm, and the distance between the loading location and the welded joint was 70 mm.

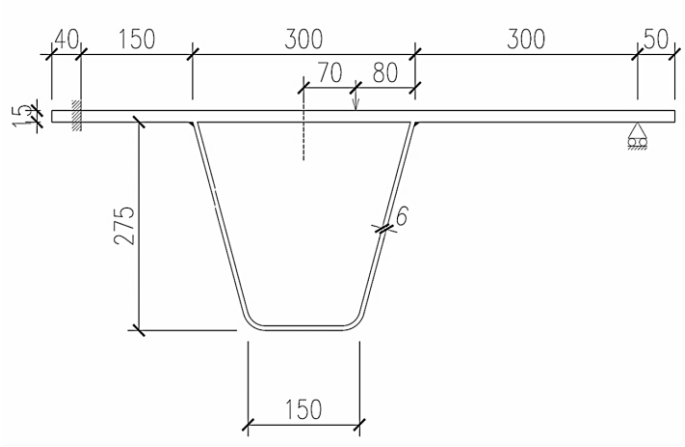

a) basic scheme (unit: mm)

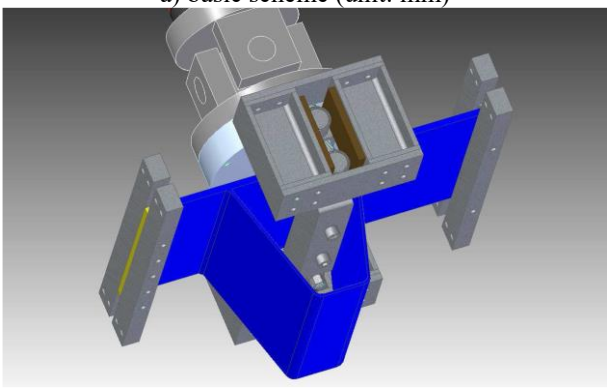

b) 3D visualization in the laboratory

Fig. 2-4 Test specimens and boundary conditions

2.2.2. Manufacturing specimens

According to the common way of OSD production, the test specimens were welded by submerged arc welding (SAW) using an electric arc beneath a bed of granulated flux. To manufacture small-scale specimens with comparable weld qualities, two 4-meter-long specimens were produced firstly, and then cut into smaller pieces with equal length for each.

Given that there were two rib-to-deck welded joints on the specimens, the welding process could be done separately or simultaneously. In both way, tack welding was applied initially to prevent the thermal deformations from being too

large. More details can be found in (Nagy et al., 2017). The welding parameters were summarized in Table 2-1. It should be noted that wire angle, which is the angle from the wire to the vertical direction, was designed differently for the two specimens. Consequently, it produced different weld geometries as shown in the next section.

Table 2-1 Summary of welding parameters

Welding sequence	Separate	Simultaneous
Welding machine	Semi-automatic	Automatic
Description	Twin wire	Single wire
Current (A)	600 - 700	500 - 600
Wire feed speed (m/min)	0.71	2.0 – 2.5
Voltage (V)	28 – 32	25 – 26
Travel speed (mm/min)	700 – 900	550 – 650
Arc energy (kJ/mm)	1.2 – 1.7	1.3 – 1.8
Distance electrode to work piece (mm)	10 – 20	10 – 20
Wire angle θ	30°	25°

2.2.3. Data collection

As one of the most important concern of this study is the crack growth process, the fatigue test attempted to generate information about the fatigue fracture as much as possible. A common way to monitor the fatigue crack growth is the Crack Tip Opening Displacement (CTOD) (ASTM International, 2015). However, for a specimen of OSD, it is difficult to make an initial notch or crack, and the complex geometry of the specimen is not preferred by CTOD measurement as well. Fortunately, as beach mark is always observed on the fatigue fracture surface (Witek, 2009), it could provide an alternative method. The only concern is that according to some of the fatigue tests on OSDs (Ya et al., 2011, Kainuma et al., 2016), the beach marks obtained were either with limited quantities, or can hardly be identified visually.

Therefore, it was planned to apply loading sequences designed for this fatigue test specifically, which can help to produce clear beach marks on the fracture surface. A way of designing these loading sequences were proposed by Schepens and Laseure (2015), given as follows,

$$\begin{cases} \frac{N_{beachmark}}{N_{base}} = 0.5 \\ \mu = \frac{P_{max} - P_{beachmark}}{P_{max} - P_{min}} = 0.4 \end{cases} \tag{2-1}$$

where $N_{beachmark}$, N_{base}, $P_{beachmark,}$ P_{max} and P_{min} were defined in Fig. 2-5. The value of μ is recommended to be 0.4 to keep the variable amplitude effect from affecting the regular fatigue behavior significantly. However, it does not

necessarily achieve good beach marks with the equation above. Some attempts were inevitable to find the best way to tune the beach mark technique during the test.

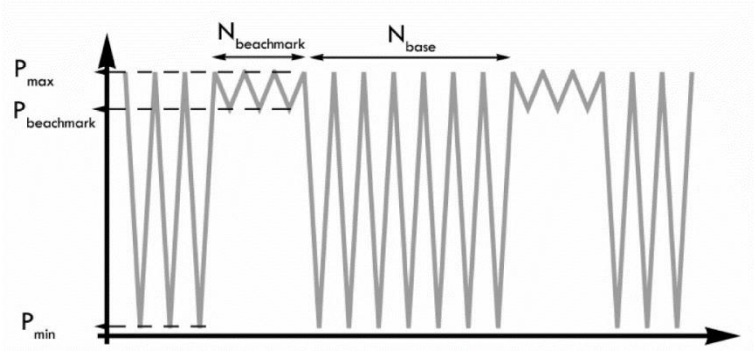

Fig. 2-5 Load parameters in a beach marks signal (Schepens and Laseure, 2015)

In addition, the strain gauges were also installed to collect the data during the test. The strain gauges should be placed on the top and bottom of the deck plate at the corresponding locations, which enables us to determine the membrane stresses and bending stresses. The summary of the strain gauge locations was given in Fig. 2-6. As can be expected, the stress/strain gradient near the weld toe and root were quite high, and more strain gauges should be placed around. For the sake of the close distances between these measuring points (2 mm), the strain gauge group (1-KY11-2/120) were adopted, whilst regular strain gauges (1-LY41-3/350) were used for the other measuring points. The specifications of the strain gauges were provided in Table 2-2.

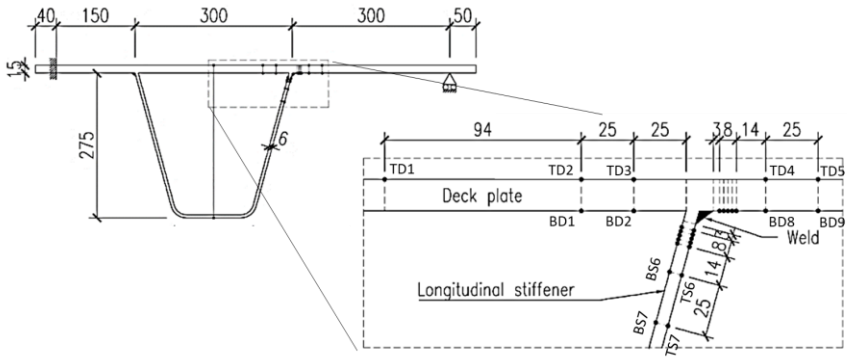

Fig. 2-6 Strain gauge locations at the stiffener-to-deck plate test specimen

Table 2-2 Parameters of strain gauges for the test specimens

Type	1-LY41-3/350	1-KY11-2/120
Layout	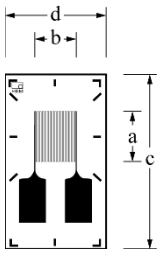	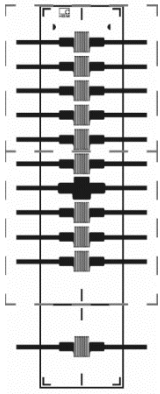
Measuring grid length (a)	3 mm	1.5 mm
Measuring grid width (b)	2.5 mm	1.3 mm
Pitch	-	2 mm
Resistance	350 Ω	120 Ω

2.3. Fatigue test

2.3.1. Test setups

The tests were conducted with a hydraulic jack system supported by a heavy steel framework, and the supporting system of the specimen (see Fig. 2-4) was fixed by a triangular-shaped steel body, as shown in Fig. 2-7. The fixed support of the specimen was realized by bolt connection to two rectangular steel bars (see Fig. 2-8 a), while the simple support was by two bars with steel rolls whose diameters were 20 mm (see Fig. 2-8 b). The hydraulic jack system was horizontally fixed by cylindrical supports, and the load was applied by two loading beams on top and bottom of the deck plate. To avoid cutting the deck plate, the contact surfaces of loading beams were curved in a radius of 50 mm, as shown in Fig. 2-9. In that way, the load on the specimen could be a line loading and always applied vertically.

Fig. 2-7 The supporting triangular-shaped body

a) fixed support

b) roller support

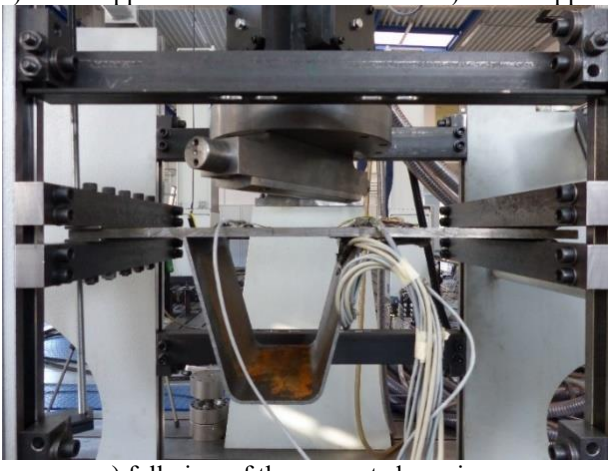

c) full view of the supported specimen

Fig. 2-8 Supports of the specimens

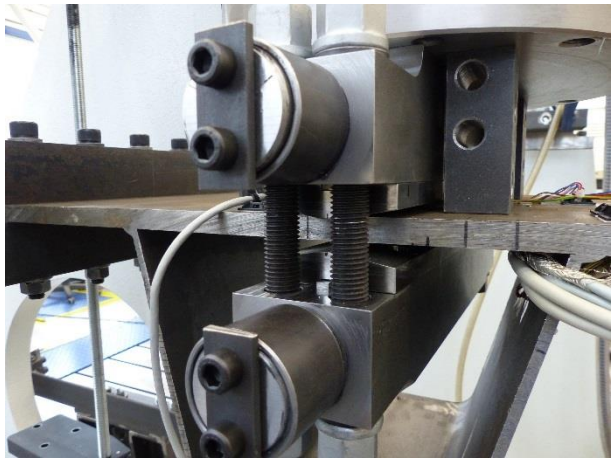

Fig. 2-9 Loading system of the test

2.3.2. Loads

Before applying dynamic loads on test specimens, quasi-static loadings were applied in order to stabilize the strain measurements in advance. Besides, it is beneficial to determining the strains and stresses more precisely. The forces were applied in three or four steps, and the target was achieved in the last step. A typical quasi-static loading with stress ratio *R* of zero was given in Fig. 2-10, in which the negative direction of force was to push the piston, and therefore added tensions at the rib-to-deck weld toe.

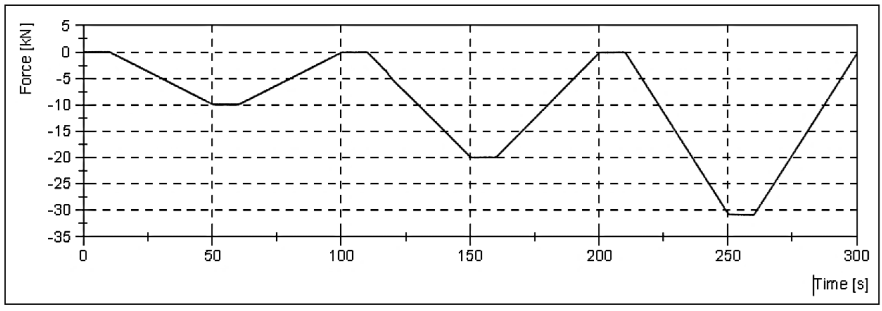

Fig. 2-10 An example of quasi-static loading (R=0)

Afterwards, dynamic loading was applied for both fatigue fracture and beach marks. The fatigue loading was using sinusoidal wave, as shown in Fig. 2-11. The frequencies of the loadings were 4 Hz due to the stability reason of the assembly. The only exception was part of the test on Specimen VIII at 6 Hz. The beach mark

loadings, as mentioned before, would have smaller amplitudes, but the normalized stress ratio between fatigue loading and beach mark loading, μ, was yet to be optimized. Different values of μ were used, ranging from 0.2 to 0.6. Most of them were set to be 0.4, as suggested by Schepens and Laseure (2015). However, the produced beach marks may still be difficult to distinguish by observing the fracture surface, if the same loading type, i.e. sinusoidal wave, was used for beach marks. Therefore, a quasi-triangular wave, as a more aggressive type, was applied for beach mark loadings, while the frequency was kept the same to the fatigue loading, 4 Hz, as shown in Fig. 2-12. When applying beach mark loading, extra cautions on the stability of specimens should be used as it brought more impact on them.

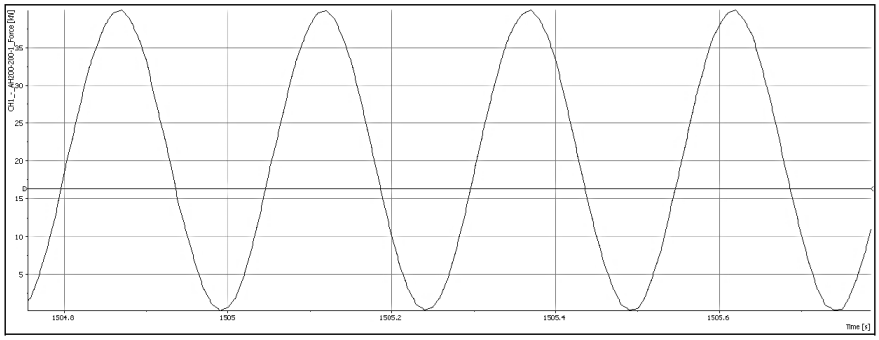

Fig. 2-11 An example of fatigue loading

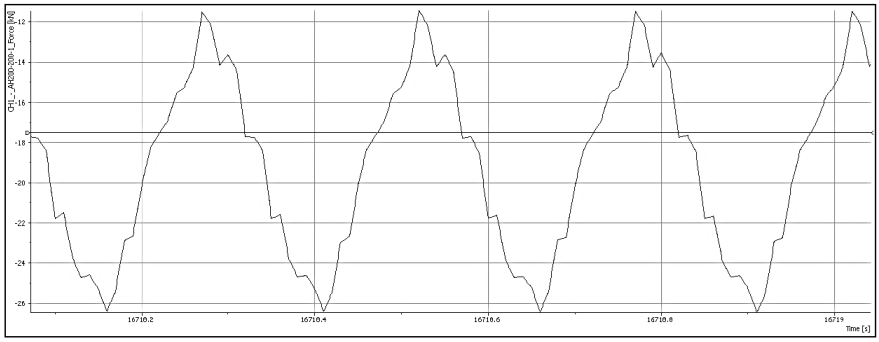

Fig. 2-12 An example of quasi-triangular beach mark loading

Eventually, eleven specimens in total were tested, among which nine were made of simultaneous welding sequence marked with Roman numbers, while the other two were made of separate welding sequence marked with Arabic numbers. Table 2-3 showed the summary of the applied loads on test specimens. It can be seen that most of the cases were carried out with stress ratio R equals 0 or -1. In

that case, the pistion will, at least once in a cycle, push the specimen downwards, and help the crack grow through the deck plate. The test was forced to end once the deformation of specimen exceeded the limit. The only exception was Specimen VIII with stress ratio of minus infinity, which means the piston will only pull the specimen upwards and the stresses around the weld was compression. The tests for Specimen VIII were stopped after more than 1.5 million cycles, as no sign of failure occured. From another aspect, it proved that the fatigue performance on the weld vicinities are way worse than that of deck plate, since no cracks were initiated from the top face till the test was stopped. The fatigue cycles for the weld toe failure on each test specimen were provided in Table 2-3. More details like the hot-spot stress and the corresponding S-N curves were provided in (Nagy, 2017).

Table 2-3 Summary of loading conditions and fatigue cycles on test specimens

Specimen No.	P_{max} *(kN)*	P_{min} *(kN)*	$P_{beachmark}$ *(kN)*	μ	R	N_{base} *(cycles)*	$N_{beachmarks}$ *(cycles)*
I	27	-27	-10.8	0.3	-1	156 535	119 220
II	40	-40	/	/	-1	62 844	/
III	40	-40	-24	0.2	-1	46 737	168 692
IV	0	-40	-24	0.4	0	147 425	19 500
VI	0	-27	-16.2	0.4	0	484 782	178 149
VII	0	-31	-18.6	0.4	0	272 852	337 525
VIII	40	0	24	0.6	-∞	> 1 527 492	640 000
IX	0	-35	-21	0.4	0	247 762	99 067
X	40	-40	-8	0.4	-1	40 809	24 402
9	30	-30	-18	0.2	-1	101 394	148 871
10	0	-31	-18.6	0.4	0	270 544	307 902

2.3.3. Test results and discussions

2.3.3.1. Crack locations

According to most of the previous studies carried out with small-scale specimens, crack initiation at the weld toe was mostly found (Kolstein, 2007). In contrast, other fatigue tests carried on full-scale specimens that consists of several longitudinal stiffeners and at least two crossbeams (Tsakopoulos and Fisher, 2005; Sim et al., 2009; Kainuma et al., 2016) observed fatigue crack from both weld toes and weld roots.

By this fatigue test, results show that the crack initiation at the weld toe was predominant in every specimen. The cracks propagated vertically towards the top face of deck plate, and longitudinally along the weld bead, as shown in Fig. 2-13. On the other hand, weld root crack was not observed at all, even though it is believed more possible to occur on the real bridges (Ya et al., 2011).

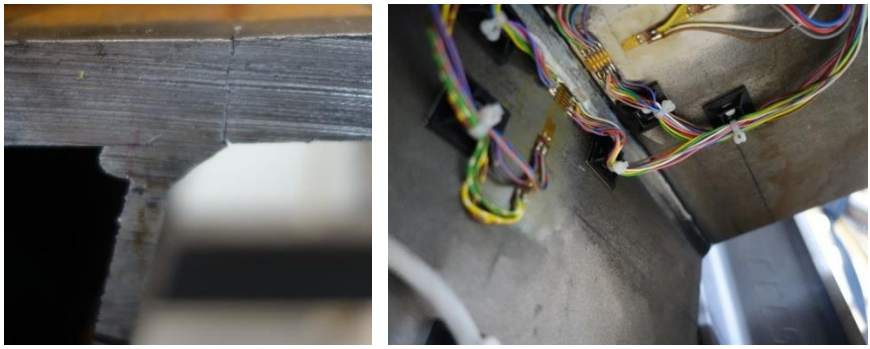

Fig. 2-13 Weld toe crack through the deck plate (Specimen 9)

In hindsight, it should be not so unexpected by comparing the structural difference between the specimens and actual OSDs. The lack of diaphragms on the specimens could be crucial, since they act locally as constraints of deck plate on the weld toe side rather than on the root side. If the diaphragms were simplified as the spring constraints, the sketches of local models at different longitudinal positions: a) near the diaphragm and b) at the mid-span between two diaphragms can be given in Fig. 2-14. With an intuitive knowledge on the possible deformations of both models, it can be inferred that these constraints would help to prevent the toe crack from initiation rather than the root crack. That explains the weld root cracks at the intersection of rib-to-deck and rib-to-diaphragm welded joints on actual OSDs, as described in Fig. 1-11 in Section 1.2.2. Overall, the specimens without diaphragms might not be as "orthotropic" as the actual OSDs, even if extra attentions were paid in the design phase to the stresses at weld toe and root. Hence, the test with the given boundary conditions and loadings was more or less similar to a three-point bending test on a stiffened beam. In that case, one of the most significant defect, namely the lack of penetration at the weld root, will not be too harmful as its orientation is parallel to the principal stress direction. On the other hand, the toe cracks observed in this study were still representative for the case of cracks at mid-span between two diaphragms. A typical example could be found in the experiment conducted by Sim et al. (2009), in which toe cracks were observed under loading at the mid-span between two diaphragms.

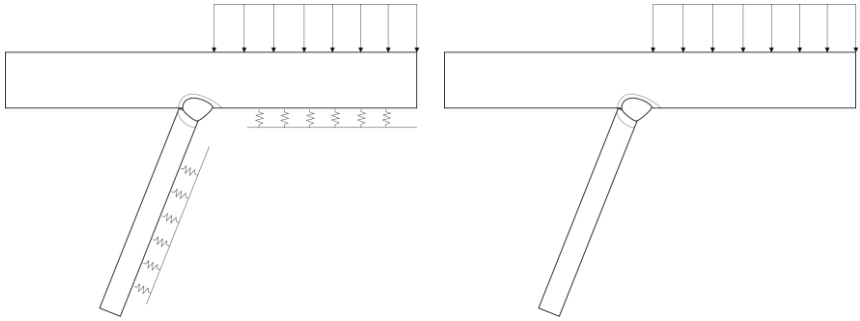

a) near the diaphragm b) at the mid-span between two diaphragms

Fig. 2-14 Sketches of simplified local models

Hence, if the study concerns the weld root crack on small-scale specimens, a different setup of fatigue test is required. Ya et al. (2011) proposed an experimental way which is similar to a cantilever with geometrical changes of cross-section, see Fig. 2-15a. Similarly, a test scheme based on this laboratory conditions could be proposed (Nagy et al., 2017), as shown in Fig. 2-15b. However, it has to be emphasized that both ways are still different from the realistic OSDs in terms of load type.

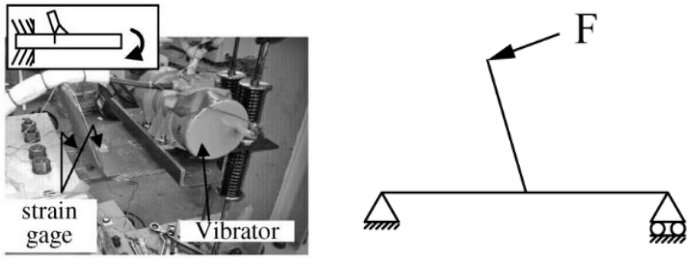

a) Ya et al., 2011 b) Nagy et al., 2017

Fig. 2-15 Scheme of root crack study for small-scale specimens

To summarize, as the weld toe crack was the main reason of fatigue failure on this test, it should be brought to the forefront in the subsequent fractographic and metallographic analyses, the numerical calculations and eventually, the realistic OSDs. The fatigue mechanisms achieved based on weld toe crack may benefit the analyses on weld root crack as well, but more experimental verification is still needed.

2.3.3.2. Beach marks

As can be seen in Table 2-3, ten of the specimens among eleven were designed to generate beach marks. By excluding one specimen that did not fracture in the test, in total nine specimens with beach marks were finally obtained. The beach marks were mainly produced by using the parameter μ with the value of 0.4. Nevertheless, it might produce wide beach marks when the stress ratio *R* varies. An instance of Specimen X was given in Fig. 2-16, in which the beach marks, or can be called more precisely as the "beach bands", were so wide that comparable to the fatigue fracture face. In addition, as Specimen X was the first specimen for the beach mark attempts, the relatively mild sinusoidal wave for beach mark cycles was adopted. Thus, the design of beach mark cycles should be investigated.

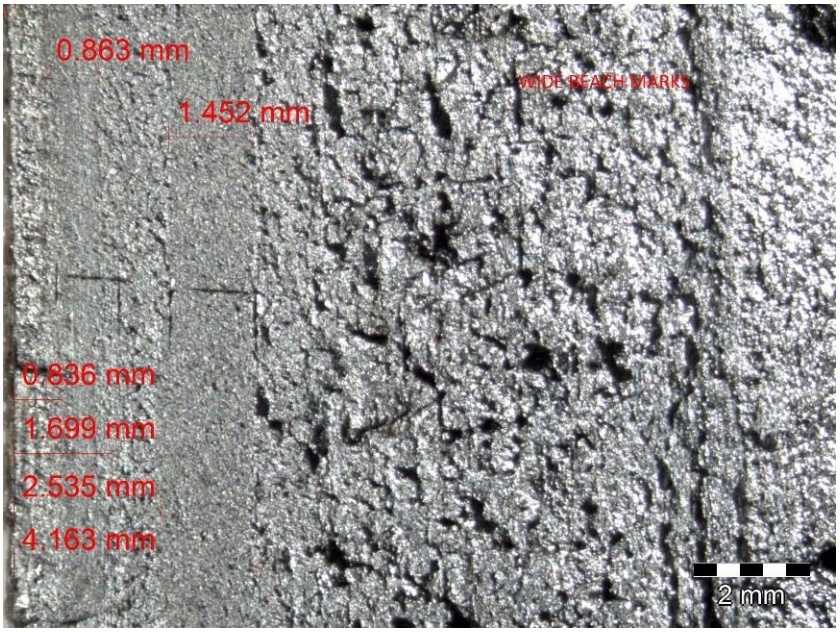

Fig. 2-16 Wide beach marks on Specimen X

In hindsight, it makes sense in terms of the stress range in the beach mark phase, $\Delta P_{beachmark}$. Firstly, the Equation (2-1) for parameter μ can be rearranged as follows,

$$\mu = \frac{P_{max} - P_{beachmark}}{P_{max} - P_{min}} = \frac{1}{1-R} - \frac{1}{1-R}\frac{P_{beachmark}}{P_{max}} = \frac{1 - R_{beachmark}}{1-R} \quad (2\text{-}2)$$

and then $\Delta P_{beachmark}$ can be given by,

$$\Delta P_{beachmark} = P_{max} - P_{beachmark} = P_{max}(1 - R_{beachmark}) = P_{max}\mu(1 - R) \quad (2\text{-}3)$$

It means that the parameter μ is not as normalized as expected, instead, it is dependent on both stress ratio R and beach mark stress ratio $R_{beachmark}$. Consequently, the stress range in the beach mark phase, $\Delta P_{beachmark}$, is a function of R and μ, and thus might be too large even with an "optimal" value of μ.

Afterwards, all specimens with R equals -1 were carried out with smaller value of μ, such as 0.2 or 0.3, lead to smaller stress ranges in the beach mark phase. It might result in undistinguishable beach marks, and hence the quasi-triangular wave, instead of the sinusoidal one, was adopted. As mentioned before, it took some tests to tune the setup. Eventually, the specimens with best quality beach marks were Specimen VII and Specimen 10, as the final two for the test, as shown in Fig. 2-17 and Fig. 2-18, respectively. As they were applied by same loading (31kN, $R=0$), the results would be comparable.

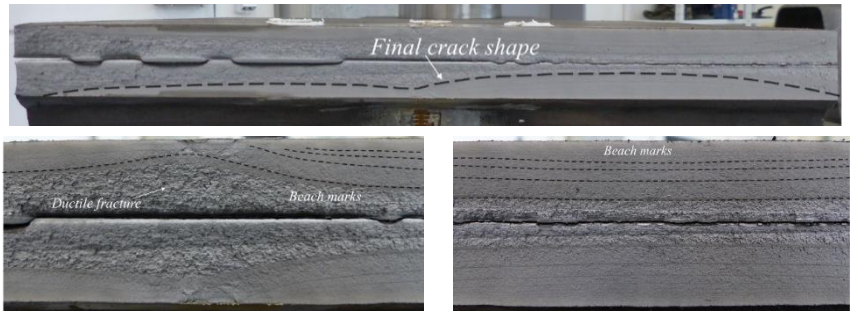

Fig. 2-17 Beach marks on Specimen VII

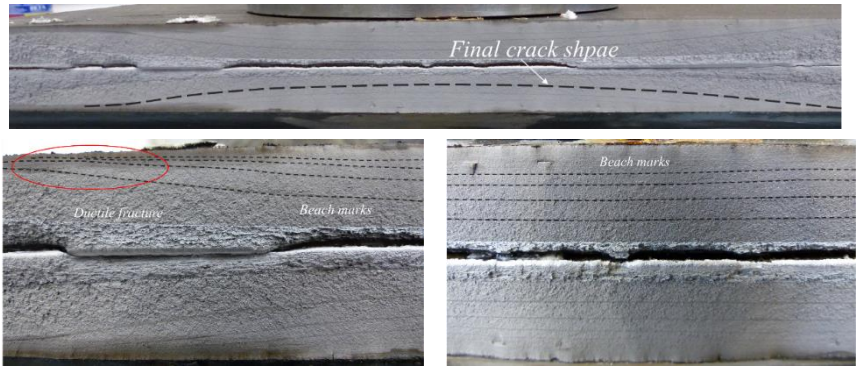

Fig. 2-18 Beach marks on Specimen 10

It is clear that in Specimen VII, there were two main cracks that were approximately in an elliptical shape, and merged in the middle. They were longitudinally originated around the quarter points of the whole length. However, the beach marks on Specimen 10 showed that there was only one main crack originated at the middle. By checking the beach marks on each specimen, it seems that the case of two main cracks were the majority. According to the results of strain gauges, the strain was not distributed uniformly along the longitudinal direction. The bending of the loading bar resulted in the slightly larger strains around the quarter positions (Nagy et al., 2017).

Another remarkable thing was the tail of beach marks, which was shown evidently by the one main crack cases like Specimen 10, as red-circled in Fig. 2-18. Basically the shape of the crack was semi-elliptical, but the tail of the beach marks turned out to be extended. This extension was due to the crack merge of the main crack and small secondary cracks. As the tests applied line loadings in full length, it is quite possbile to have initial cracks all along the longtudinal direction. The initial cracks near the tails seemed to form later and grow slower than the main one. Consequently, they merged with the main crack when it gets close enough, presented the tail we observed. The form of the initial cracks at the weld toe was addressed by the fractographic analyses in the next section.

Based on the beach marks of each specimen, a brief crack growth process could be drawn, as shown in Fig. 2-19. As the beach marks in Specimen X were too wide, they were measured by both edges, so that the crack growth curve was almost vertical in some sections. Besides, as the information about the initial crack was still unknown, the crack growth rate for the entire process could not be determined. This will be studied by the fractographic and metallographic analyses in the next section.

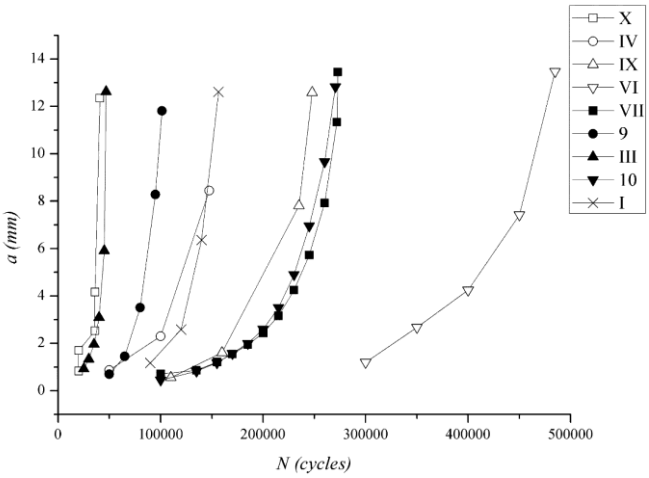

Fig. 2-19 Crack growth process on test specimens

2.4. Fractographic and metallographic analyses

2.4.1. Equipment and Procedures

Apart from the beach marks, additional information was also required for understanding the micro- and/or meso- scale behavior of the fatigue cracks. With regard to that, various equipment in the laboratory were applied for fractographic and metallographic analyses, including optical microscope Carl Zeiss Jena Neophot 32 (see Fig. 2-20 a)), stereomicroscope NIKON SMZ 800 (see Fig. 2-20 b)), scanning electron microscope (SEM) TESCAN VEGA 5130 SB with the energy dispersive spectroscopy (EDS) Bruker Quatanax 200 (see Fig. 2-20 c)), and hardness tester ZWICK ZHU 2.5/Z2.5 (see Fig. 2-20 d)).

The optical microscope and stereomicroscope were for low and medium magnified uses, such as checking beach marks, roughly evaluating fracture behaviors. As the optical microscope is able to magnify up to 1000x, part of the metallographic analyses could be conducted with it as well. The SEM with EDS were used to obtain highly magnified images, with the maximum ability of 8000x of magnification. It enabled us to perform phase and structural analyses on different microstructures and local heterogeneities that may affect the fatigue behavior. In addition, the EDS helped to conduct chemical analyses to identify the composition of impurities in the material. The hardness tester was used to obtain the hardness under influence of welding process.

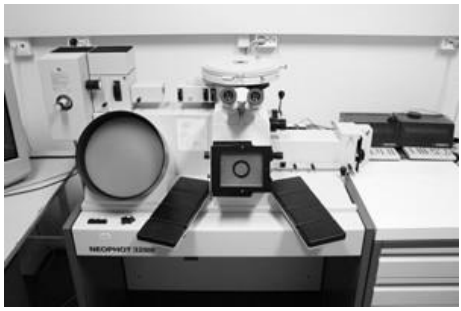

a) Carl Zeiss Jena Neophot 32

b) NIKON SMZ 800

c) Tescan Vega 5130SB & Bruker Quatanax 200

d) ZWICK ZHU 2.5/Z2.5

Fig. 2-20 Equipment used for analyzing the test specimens.

For the fractographic analysis, the fracture surfaces were firstly checked by optical microscope and stereomicroscope. The samples to be observed were cut out from the specimens, and prepared by ultrasonic cleaning to remove all possible exotic impurities. In that way, the beach marks and the zones that separate by them can determined, too. Afterwards, the SEM was applied to look into the microstructures in each zone to understand different fatigue behaviors. In additional, for the zones in which the fatigue striations are clear enough, the striation widths were measured. Ideally, the striation widths should be the direct indicators of the local crack growth rate. However, the uncertainties of the striations themselves, and the limited information obtained by fractographic images made it difficult to work in practice, which will be explained in the next section with more details.

For the metallographic analysis, it was carried out on the samples of uncracked part of welded joint in the first place, to achieve the overall knowledge on the microstructural characteristics of welded joints of OSDs. Furthermore, the samples of transverse sections of fracture were investigated as well, to get the microstructures of different sub-zones in heat-affected zone near the cracks, and to

acquire some obvious defects such as the lack-of-penetrations at the weld root. The samples for both were well polished via physical and chemical methods.

At last, the hardness test was conducted following the instructions from the metallographic results, which provide the hardness as an indicator of the mechanical behavior for various zones in welded joints.

2.4.2. Fractographic analyses

2.4.2.1. Crack initiation

The fractography of each specimen was studied based on the zones divided by beach marks. The crack initiation zone was numbered as Zone 0, then the zone till the first visible beach mark was Zone 1, and so on. Zone 0 was defined with respect to the different behavior that lead to a visible boundary, as shown in Fig. 2-21. The most important phenomenon in this zone, and also maybe for the entire crack growth life, was the primary intergranular decohesion, which was observed on fracture samples from all specimens, as shown in Fig. 2-22. A typical example on Specimen 10 was given by Fig. 2-22 c), in which the areas pointed by arrows are the place of decohesion, and can be regarded as the cause of crack initiation.

Undoubtedly, the actual cycle number spent before intergranular decohesion is not exactly zero. It should be related to the applied loading, too. But for a large-scale structure like OSD, it is believed that the crack initiation life is quite small (Kolstein, 2007) due to the inevitable weld defects. Consequently, the initial crack depth for each specimen was obtained by measuring the maximum depth of the intergranular decohesion. The results are shown in Table 2-4. Accordingly, the initial crack depth is mainly around 0.3 mm to 0.4 mm. Further information will be provided by metallographic analysis in the next section.

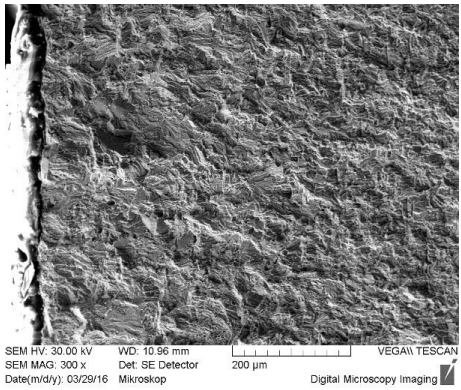

Fig. 2-21 Different fracture behavior (Specimen VI)

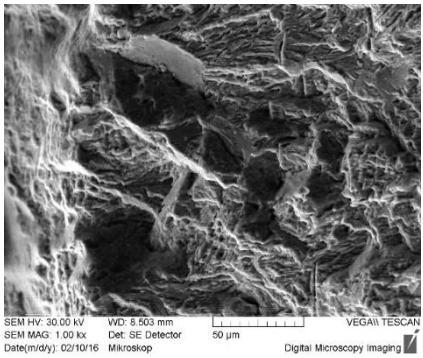

a) Specimen 9

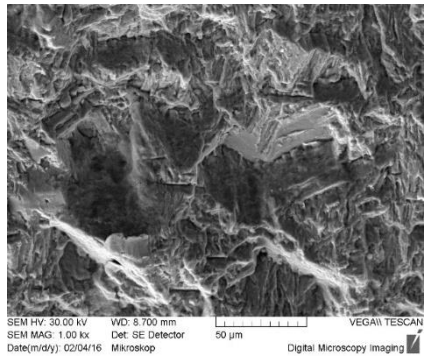

b) Specimen X

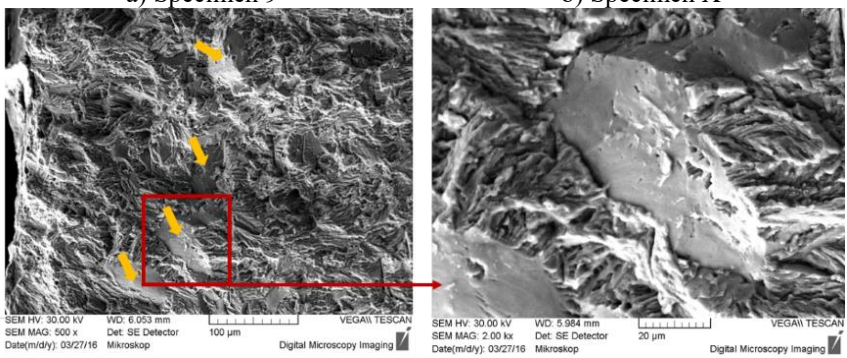

c) Specimen 10

Fig. 2-22 Intergranular decohesion on fracture surface

Table 2-4 Initial crack depth measured by fractography

Specimen	P_{max} (kN)	P_{min} (kN)	R	Initial crack depth (mm)
I	27	-27	-1	0.481
II	40	-40	-1	/
III	40	-40	-1	0.379
IV	0	-40	0	0.498
VI	0	-27	0	0.362
VII	0	-31	0	0.375
VIII	40	0	-∞	/
IX	0	-35	0	0.282
X	40	-40	-1	0.284
9	30	-30	-1	0.308
10	0	-31	0	0.288

2.4.2.2. Crack growth

In accordance with the zones after Zone 0, the stages of crack growth were studied. The major finding in this part was the secondary cracks on fracture surface. According to the comparison of Zone 1, 2, 3 and 4 in Fig. 2-23, it is clear that the

secondary cracks were increasing not only in numbers, but also in opening distances. In a mechanical point of view, this could be explained by the increasing bending load out of the plane due to the growth of main crack in the fatigue test. On the other hand, the microstructures observed in metallography might have some effects as well.

Apart from secondary cracks, some voids or inclusions were occasionally seen on the fracture surface. Two examples from Specimen VII were given in Fig. 2-24. It seemed that some voids could be induced by inclusions out of the observing plane that block the fusion in the welding process. They may help the secondary cracks to originate and affect the main crack growth. The composition of the inclusions were analyzed by EDS, as documented in Appendix A. Nevertheless, as the observation and analysis can be only conducted on one cross section, the spatial distribution of the voids/inclusions was not possible to obtain, and the out-of-plane dimension for the observed voids or inclusions could not be measured as well.

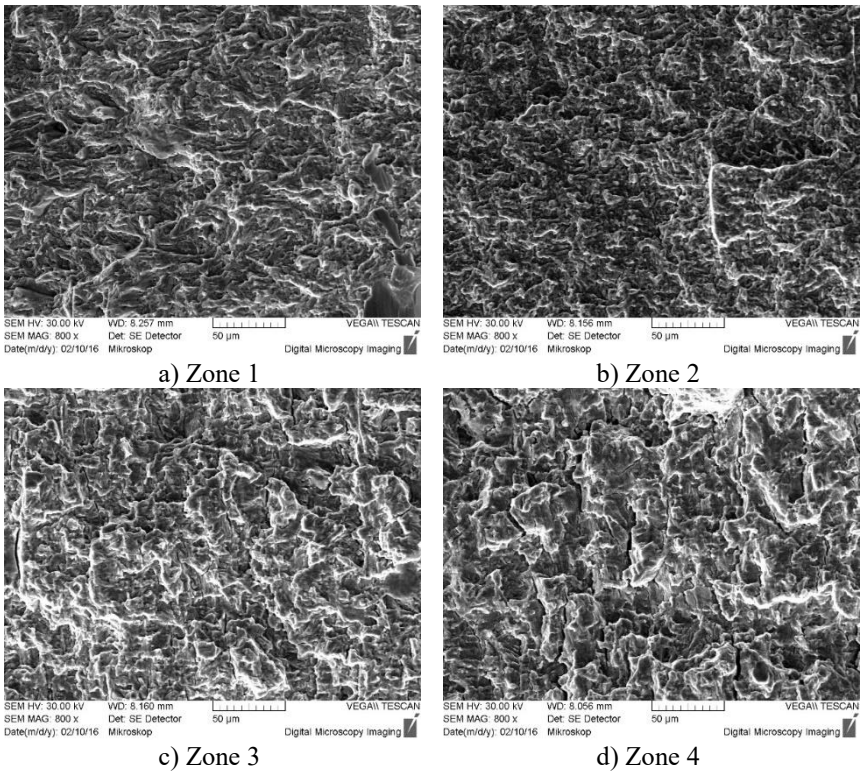

a) Zone 1 b) Zone 2

c) Zone 3 d) Zone 4

Fig. 2-23 The incremental secondary cracks with the main crack growth (Specimen 9)

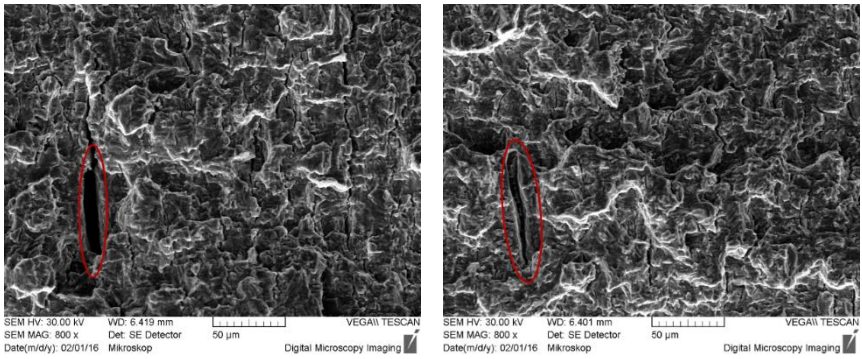

Fig. 2-24 Occasional voids/inclusions on the fracture surface (Specimen VII)

2.4.2.3. Fatigue striations

The fatigue striations were observed mainly in the stable growth stage of crack, i.e. in Zone 3, 4 and the subsequent ones. The striation widths were measured on these fractographic images. However, the results seemed not so optimal to be indicators of the crack growth rates, due to the difficulty in the measurements. It was inevitable even on the same image, as shown in Fig. 2-25. The reason could be quite complex: i) the two-dimensional image can only provide the projection of the striation width; ii) the direction of the fatigue crack growth can be diverse in such a small scale; iii) the microstructures may affect it; iv) the beach mark cycles, as variable amplitude fatigue cycles, may result in different crack growth rate in a small region. In addition, the measurement of striation width was limited to a tiny area compared to the size of a zone, hence not so representative for the whole zone. Therefore, the striation width measured on the image could a reference, but should not be given too much credit on.

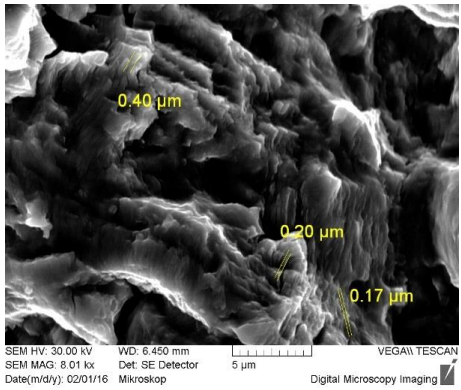

Fig. 2-25 The diversity in measuring the striation width (Specimen VII, Zone 5)

2.4.3. Metallographic analyses

2.4.3.1. Parental material

The parental material used in producing the specimens was steel S355, whose microstructure was observed by checking the uninfluenced site that was far away from weld region. As shown in Fig. 2-26, the microstructure was mainly ferrite and pearlite with lamellar heterogeneity in correspondence with the hot rolling direction. The precipitation of carbides in ferrite phase was also observed, but not significant in terms of fatigue behavior.

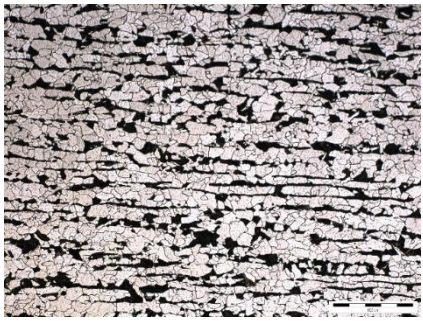

a) Optical microscopic view (mag. 250x)

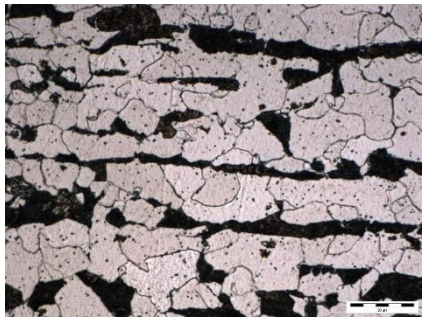

b) Optical microscopic view (mag. 1000x)

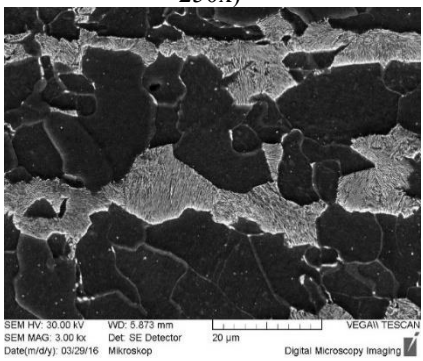

c) SEM view (mag. 3000x)

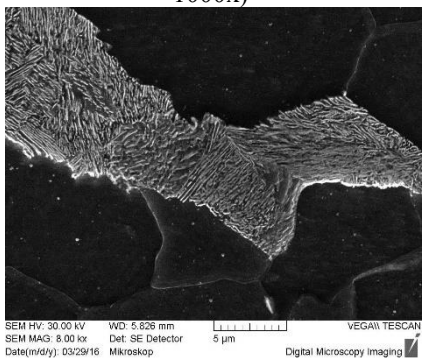

d) SEM view (mag. 8000x)

Fig. 2-26 Microstructures in parental material

2.4.3.2. Weld root

Large weld defects were found on weld root on various samples, including slags (see Fig. 2-27 a)), lack-of-penetration (see Fig. 2-27 b)) and overlapping (see Fig. 2-27 c)), while there was no defect in such a scale on weld toe. It can be seen that the lack-of-penetration often exists at the weld root. The exception was the excessive welds using extra high voltage in welding, which is clearly not a good solution for it introduces other deficiencies in another way.

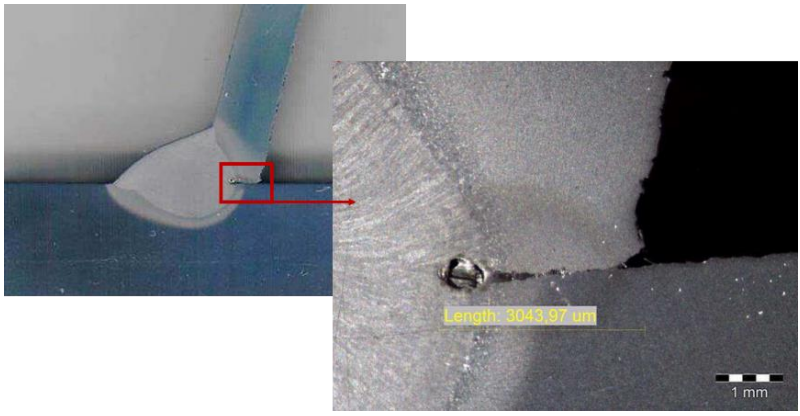

a) Slag and lack-of-penetration

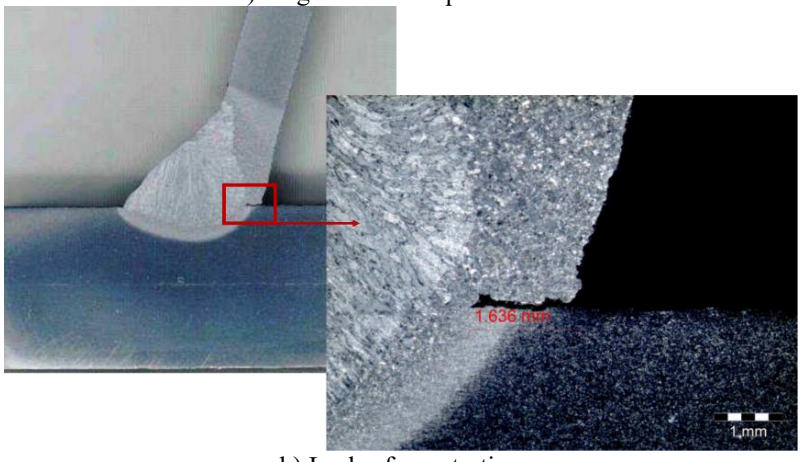

b) Lack-of-penetration

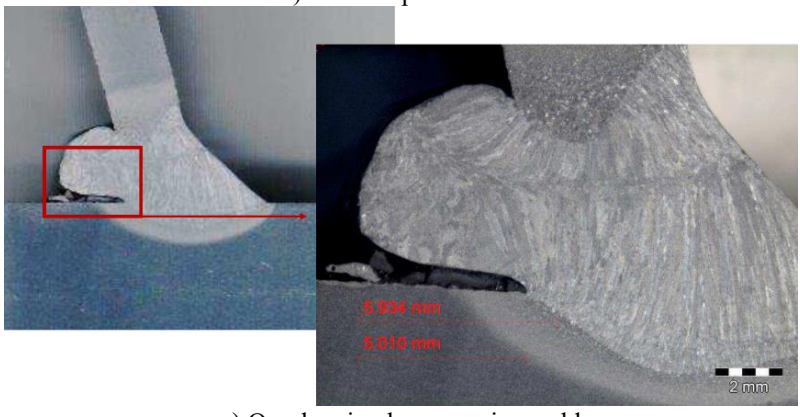

c) Overlapping by excessive weld

Fig. 2-27 Weld defects on weld root

The microstructures near the weld root were investigated. Fig. 2-28 presented the vicinity of a weld root, in which the dark part was a slag in connection with the lack-of-penetration. These defects changed the heat dissipation path and therefore, the microstructures. A coarse grained HAZ near the slag and a normalized zone with finer grains could be observed. Nevertheless, as the weld root crack was not the case for this test, it was not possible to draw a conclusion on the effect on fatigue fracture for the weld root defect and the microstructure nearby.

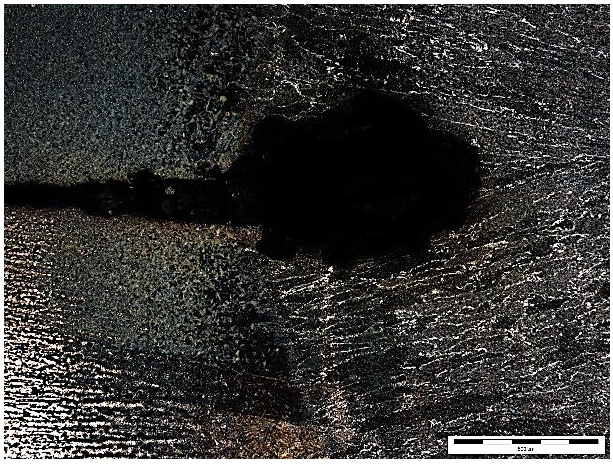

Fig. 2-28 The vicinity of weld root (mag. 64x)

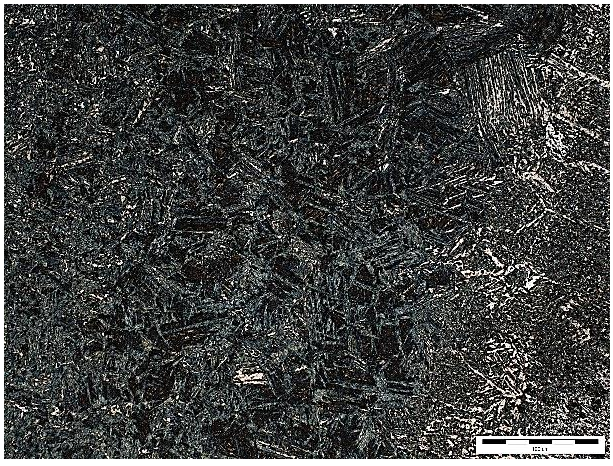

Fig. 2-29 The coarse grained HAZ near the slag (mag. 250x)

Fig. 2-30 The normalized zone near the parental material (mag. 250x)

2.4.3.3. Weld toe

Given that weld toe crack was the reason for fatigue failure on each specimen, the microstructures in the vicinities of weld toe might have higher values to explore than weld root defects for the effects on fatigue performance, despite in a relatively smaller scale.

As shown in Fig. 2-31, noticeable defects could not be found at the weld toe, even the micro-notches were hard to identify. When looked into the microstructure in the vicinity of HAZ, namely the most fragile area in the welded joints, different zones were addressed: I) the columnar in welding material (see Fig. 2-32); II) partially austenite zone (PAZ, see Fig. 2-33); III) fusion zone and IV) coarse grained HAZ (see Fig. 2-34).

For the columnar, the orientations of them were determined by the heat dissipation, and may lower the fatigue performance due to heterogeneity. However, as this zone is actually located in the part of welding material, which is still relatively tough for cracks to initiate, it should not be regarded as the key point. The crack was not supposed to initiate in PAZ too, as there were small and fine grains that may reinforce the fatigue resistance.

Fig. 2-31 The vicinity of weld toe (mag. 64x)

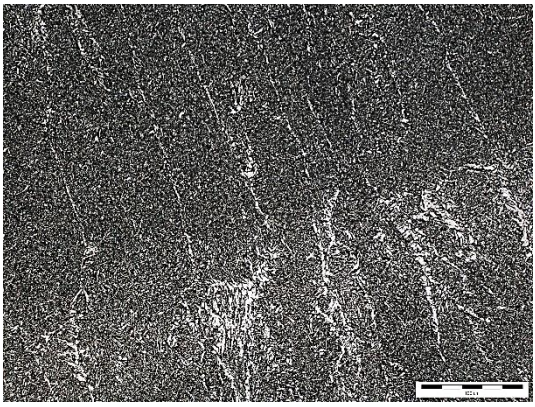

Fig. 2-32 Columnar in welding material (mag. 250x)

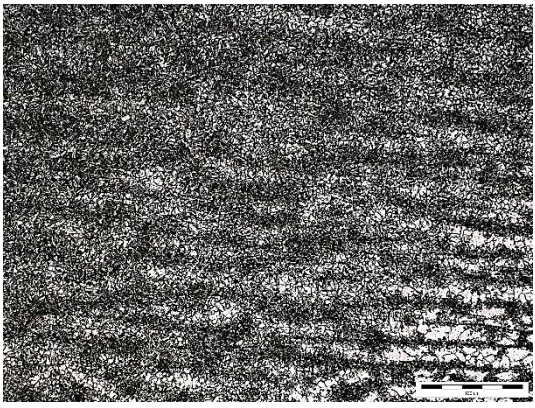

Fig. 2-33 Partially austenite zone (mag. 250x)

The vital zone among them was actually the coarse grained HAZ. It was located next to the fusion zone and was difficult to draw a boundary line in-between, which may explain why some previous studies tried to take the fusion zone as the critical part (Bhadeshia & Svensson, 1993, Fang et al., 2011). According to Fig. 2-34 b) and Fig. 2-34 c), their difference in the grain boundaries could be confirmed under magnification of 1000x. In coarse grained HAZ, the grain coarsening and the bainite/pearlite transformation occurs simultaneously due to the heat input. In a fatigue point of view, the latter phenomenon is actually beneficial since the bainite/pearlite is a kind of microstructure with higher fatigue strength. However, the grain expansion will lead to enlargement of grain boundaries, which is not preferred for the fatigue performance. A well magnified (1000x) metallographic image of coarse grained HAZ is given in Fig. 2-34 c), in which the orientation of the grain boundary was pretty obvious. In contrast, the microstructures in welding material is given in Fig. 2-35. It mainly consists of bainite and ferrite, and no clear grain boundaries can be drawn. As a consequence, the coarse grained HAZ tends to behave in a more heterogeneous way under cyclic loading.

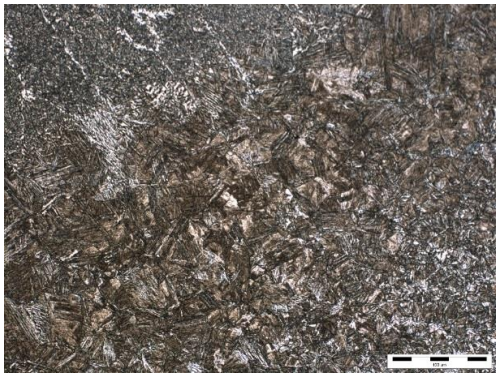

a) fusion zone and coarse grained HAZ (mag. 250x)

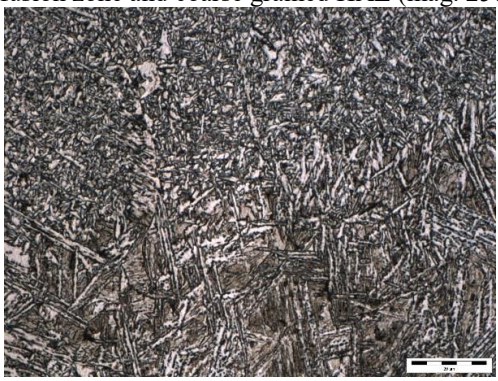

b) fusion zone (mag. 1000x)

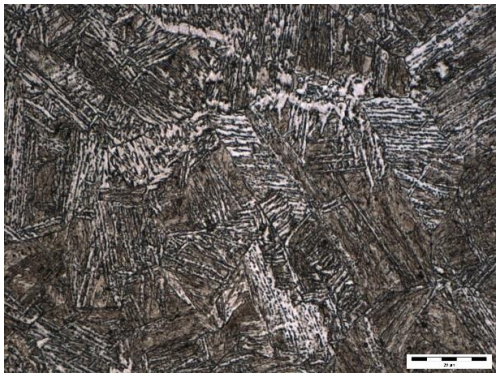

c) coarse grained HAZ (mag. 1000x)

Fig. 2-34 Microstructure of fusion zone and coarse grained HAZ

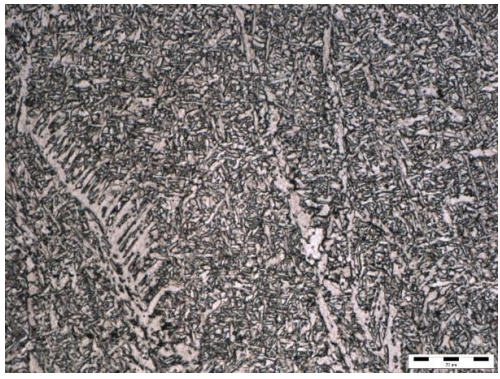

Fig. 2-35 Microstructure of welding material (mag. 1000x)

2.4.3.4. Cross section of fracture

Metallographic analyses were also carried out on the cross section of fractured sample cut out from Specimen IV, to search for the possible connections between fracture response and microstructures, as shown in Fig. 2-36. It can be seen that the ferrite and pearlite were oriented in a lamellar structure, and the interface appeared to be vulnerable to secondary cracks. Besides, the microstructural heterogeneity was observed due to the mixture of bainitic and acicular ferritic with different carbide precipitation.

When looking into the crack initiation part, the kink in the early stage (see bottom-right in Fig. 2-36) implied the effect of the grain boundaries on the fracture surface. In contrast, the intragranular fracture phenomenon in the normalized zone was given in Fig. 2-37. With respect to the aforementioned fractographic analyses, the conclusion can be drawn that the coarse grained HAZ was the major source of

initial crack, since the crack path did follow the intergranular decohesion in this zone. A similar fractographic analysis was available in (Schmidova and Hanus, 2011), providing another proof for that statement.

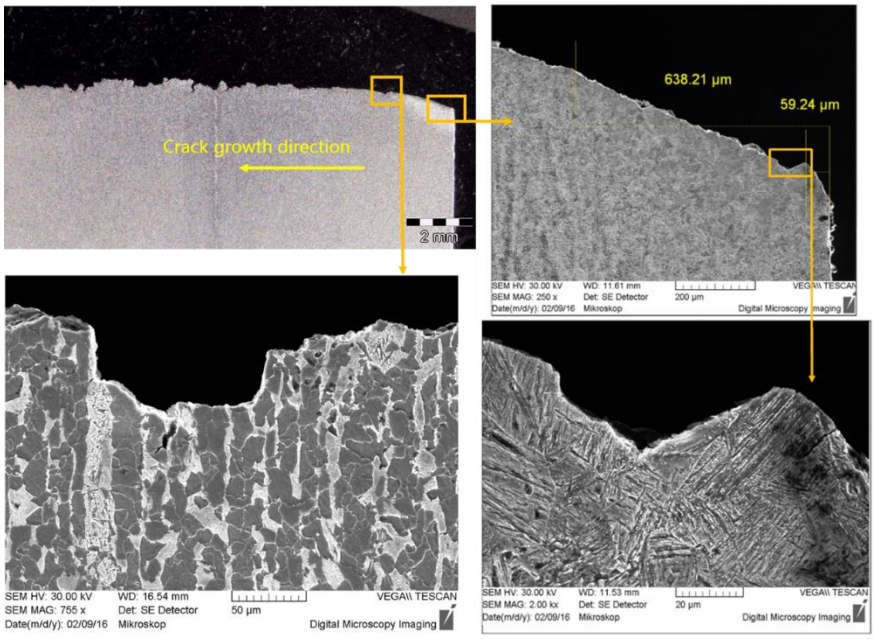

Fig. 2-36 Metallography on the cross section of the fractured sample

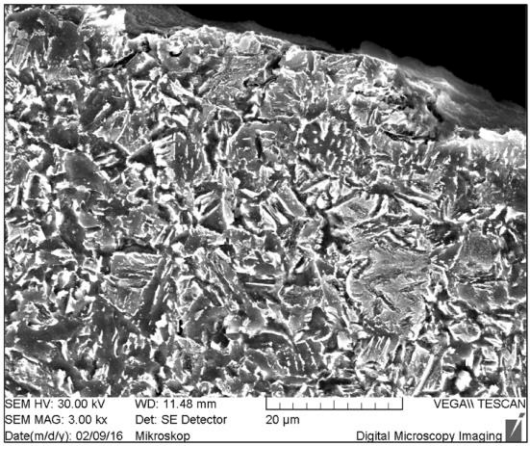

Fig. 2-37 The intra-granular fracture in the normalized zone (Specimen IV)

As different grain sizes are visible in metallography, the width of the coarse grained HAZ can be measured, and the initial crack depth can be obtained. It should be emphasized that the measurement on the metallography is not so accurate as it is dependent on the direction of the initial crack (see Fig. 2-38 a)). A more precise and comfortable way is to measure on the fractographic image, due to its easy access to determination of the main crack, as given in Table 2-4. A comparison in Specimen 10 is given by Fig. 2-38. As for the initial crack length, it is reasonable to consider a much larger scale than the depth, given that the existence of the coarse grained HAZ was universal along the longitudinal direction.

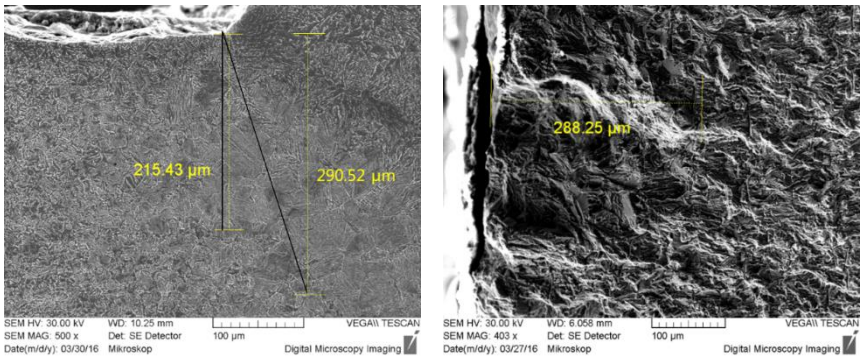

a) metallographic measure b) fractographic measure

Fig. 2-38 Initial crack depth measure based on coarse grained HAZ

2.4.4. Hardness test

As a macroscopic feasure that presented by the microstructures, hardness or hardness gradient can roughly express the influence of microstructural changes. Therefore, the hardness test could be helpful in estimating the different zones and their strength on the welded joint. In some studies, the hardness was used as a parameter to fatigue strength (Remes et al., 2012), although most of them were focused on low-cycle fatigue.

Two hardness tests were conducted. The first one was follwing a line perpendicular to the weld interface, as shown in Fig. 2-39. The measurements started at fusion zone, which is selected as the origin in Fig. 2-39, and the welding material, HAZ were all measured with same interval distance, 0.3mm. The other one measured the hardness on the possible crack path, i.e. started at the weld toe and went perpendicularly towards the top face of deck plate, as shown in Fig. 2-40. Three extra points were measured far away from the weld region in each hardness test, and the average of them was adopted as the reference hardness of the parental material.

The results from the hardness tests showed that the fusion zone is the hardest part, and the hardness gradient is quite high from the welding material to the fusion zone, and inside the HAZ. It is also revealed that the hardness of the materials outside HAZ are still higher than that of the parental material, even though little difference was observed on the physical appearance of microstructures.

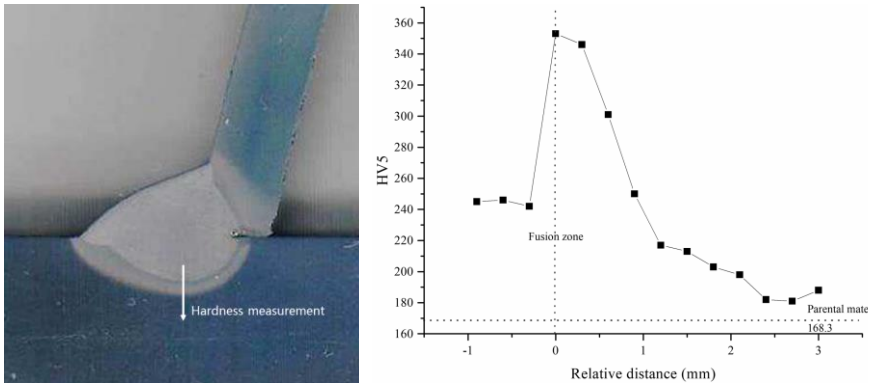

Fig. 2-39 The hardness test on the line perpendicular to the weld interface

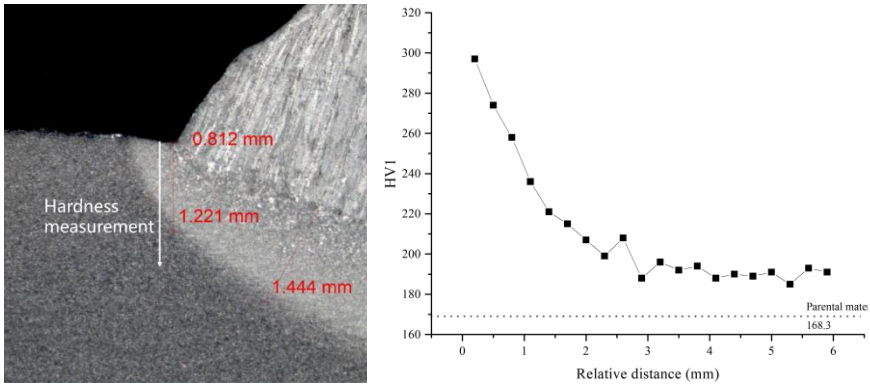

Fig. 2-40 The hardness test on the possible crack path

2.4.5. Preliminary analysis on crack growth rate

With the measured initial crack depth on fractographic images and the beach marks on all specimens, the full progress of crack growth rate could be determined. It is well-known that the crack growth rate is a function of the stress intensity factor (SIF), which cannot be obtained in the test. By assuming a semi-elliptical initial crack at the weld toe, an empirical equation could be applied to calculate the SIFs corresponding to every crack depth on beach mark, given as follows,

$$K = F\sigma_{nom}\sqrt{\pi a} \tag{2-4}$$

where σ_{nom} is the nominal stress, can be acquired by the strain gauge results; a is the crack depth; F is the shape factor. In the case of weld toe magnification, F is affected by all geometrical parameters such as the crack depth a, crack half length c, deck plate thickness T, weld toe flank angle θ, etc. An equation proposed by Bowness and Lee (2000) was adopted to calculate the shape factor, F, with non-dimensional geometrical parameters. Appendix B presents the detailed way of the calculation. As it is based on a numerical study on weld toe cracks on T-butt joints, the results obtained can only be regarded as an approximation to the test.

As a preliminary analysis, it should be noted that some parameters were hypothetic. The semi-axis length ratio between *a* and *c* was kept to be 0.05 for all crack depth, since the crack length was believed much larger than the depth as the previous analyses suggested. The weld toe flank angle was 37 degrees measured in the weld geometries in Fig. 2-27, although some variations can be seen. The ratio of attachment width to deck plate thickness was assumed to be 0.8. Consequently, the crack growth rate curve with respect to the SIFs could be drawn to verify the Paris law on this issue. To exclude the effect of the stress ratio, only the crack growth rate curves from cases with R equals zero were presented in Fig. 2-41, in a logarithmic coordinate system.

In accordance with Paris law, the entire progress of crack growth is generally described by three stages: I) threshold region; II) Paris region; III) stable tearing crack growth region (Schijve, 2001). By looking into the curves of the specimens in Fig. 2-41, two of them with same loading (Specimen VII and Specimen 10) made good agreements, while other curves showed similar behavior as well, but not as representative as less beach marks were achieved. It can be seen that in Stage I, the crack grwoth rate is of larger uncertainties and higher gradient than others. According to the aforementioned observations, the heterogeneities in microstructures could be the main reason for the uncertainties in Stage I, which is logical as the smaller initial cracks are more likely to be affected by microstructures. One interesting observation is that there exists a slight reduction inside Stage II, which makes a “pit” on the curve. Thus two sub-stages could be addressed, named as Stage II-a and Stage II-b hereinafter. The curve for Specimen VI presents another proof for it, even though the “pit” is not evident due to limited points.

In fact, a similar phenomenon was found by fatigue tests on aluminum alloys, as shown in Fig. 2-42, in which four stages, (named Stage 1, 2, 3, 4 to be distinguishable from this test) were determined (Bogdanov, 2014). When comparing these curves achieved by welded joints and pure materials, it can be

inferred that the curve intercept in Stage 2 may be altered in the case of welded joints, making it approximate to that of Paris region. It indicates that the weld defects induced by welding process may increase the Paris constant *C* for welded joints in this section.

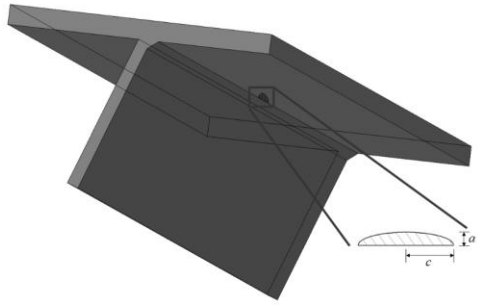

a) Hypothetic semi-elliptical crack

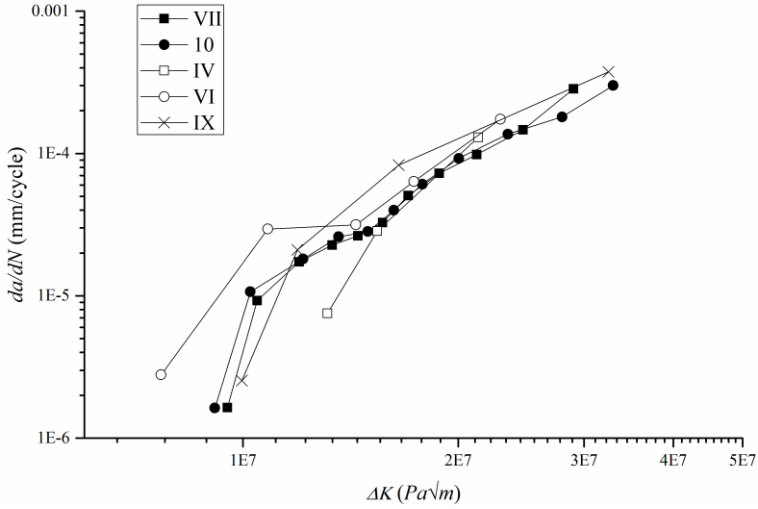

b) CGR curves for each specimen

Fig. 2-41 Preliminary graph for crack growth rate

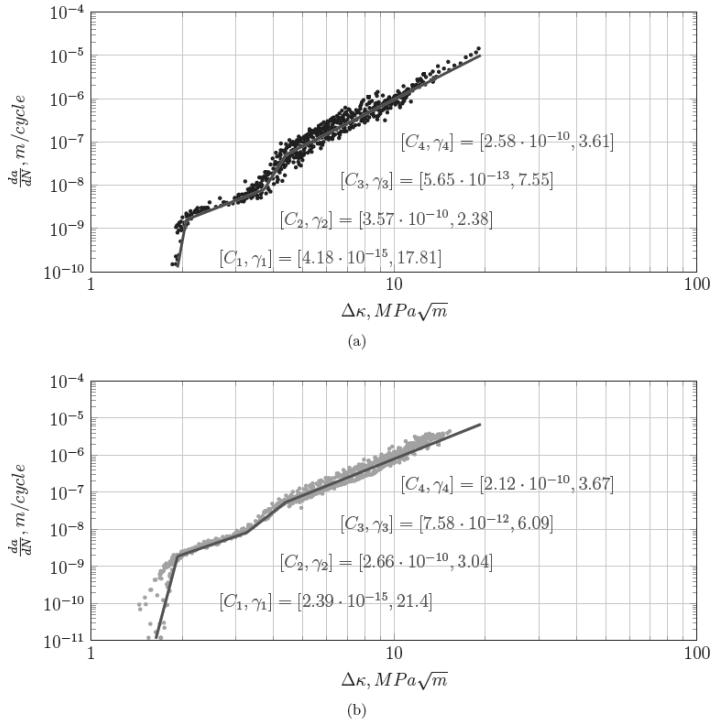

Fig. 2-42 Different stages of crack growth on a) Al 2024-T3 and b) Al 7075-T6 (Bogdanov, 2014)

To sum up, the preliminary analysis on CGR addressed the different stages of crack growth on welded joints of OSDs, even though the Stage III is not so obvious. One of the possible solutions to analyze it in the frame of Paris law, was to employ different Paris constant and exponent for each stage, as conducted by analyses on pure materials. According to the comparison of CGR curves of welded joints and pure materials, the weld defects may lead to larger Paris constant *C* in Stage II-a for welded joints. With respect to the uncertainties in it, a numerical tool with high effciency was required as it could be quite helpful for further investigation.

CHAPTER 3

CRACK GROWTH BASED ON EXTENDED FINITED ELEMENT METHOD

This chapter is based on

Wang, B., De Backer, H., and Chen, A. (2016). An XFEM based uncertainty study on crack growth in welded joints with defects. *Theoretical and Applied Fracture Mechanics*, *86, Part B*, 125-142.

3.1. Introduction

Based on the fatigue test results, it is obvious that the numerical simulation on fatigue crack on OSDs requires an effective and efficient way to conduct computations on massive cases with various weld geometries and random weld defects. Besides, the uncertainties in residual stress distribution may raise the same demand. Hence the classical FEM is not an option since it is more suitable for one specific and determined case and thus not efficient enough in both building and solving steps. In contrast, the extended finite element method (XFEM) is quite efficient since the geometry is independent to the mesh, which gives it a great advantage in generating and calculating a large number of models with different defects inside.

XFEM was firstly proposed by Belytschko et al. (1999, 2001). It originated from the idea of the Partition of Unity Method (PUM) that any function could be represented by the summation of a set of local functions. As long as the local functions are accurate to the real one, the combination of them should approximate the target function. By introducing this concept into FEM, the displacement field function could be partitioned into several functions in correspondence with the different local characteristics.

The computer implementation of XFEM was first proposed by Sukumar et al. (2003), and then Bordas et al. (2007) presented a general structure for XFEM code. Traditional FEM software, like ABAQUS, SAMCEF, MORFEO, DYNAFLOW, etc., started to introduce XFEM modules, though with some limitations. Works were also conducted on developing specified XFEM program, based on FEM software using the user defined sub-program like user elements subroutine (UEL) in ABAQUS (Giner et al., 2009, Shi et al., 2010), or based on general numerical computing language like MATLAB (Pais, 2011, Yu, 2014).

As XFEM is so powerful and practical on solving discontinuous problems, it is mainly applied in this study for two parts: i) the mesoscopic models built by an XFEM program coding with MATLAB; ii) the macroscopic models built in SAMCEF with its XFEM module. The XFEM program was developed based on the work by Pais (2011) and Yu (2014). According to the requirements on the issue of cracked weld joint of OSDs, this program was embedded one module for random defects, and one for parametric weld toe geometries. The general structure of this XFEM program is given in Fig. 3-1.

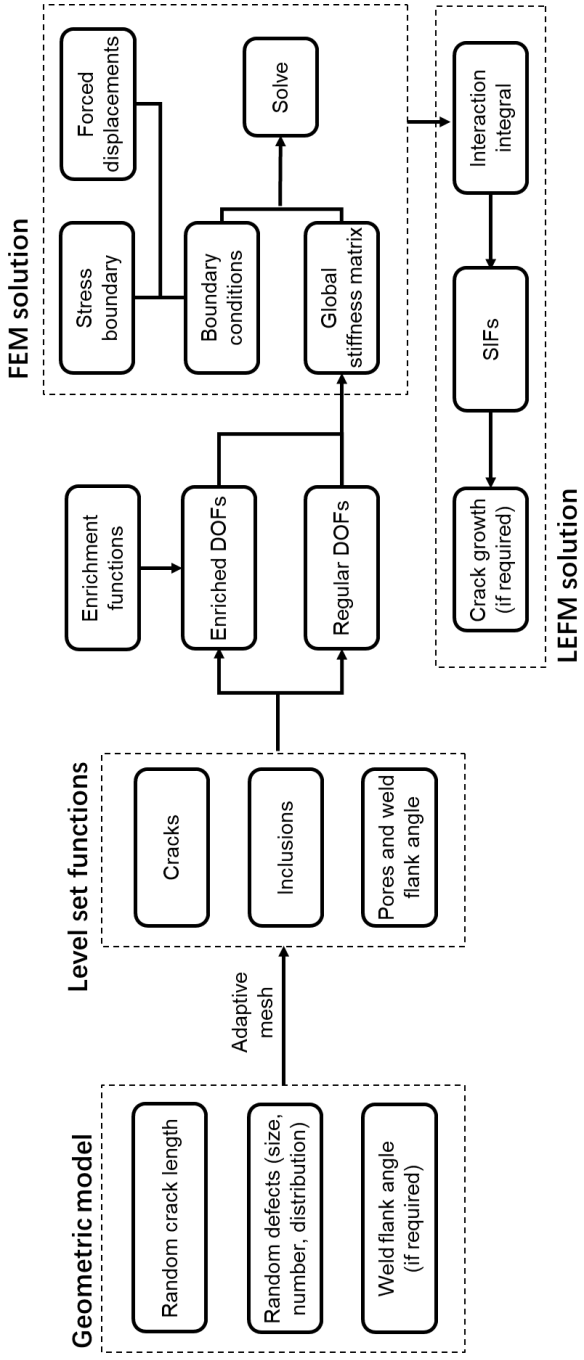

Fig. 3-1 General structure of the XFEM program

3.2. Level set method

To determine the enriched domain, Ω_d, the level set method is the common method (Pais, 2011, Yu, 2014). The level set method is a numerical way to describe the geometry of interface and trace its change, which has been applied in fluid dynamics (Chessa and Belytschko, 2003), image processing (Osher and Paragios, 2003) and structure optimization (Villanueva and Maute, 2014, Liu et al., 2016) etc.

The work conducted by Sukumar et al. (2001) might be the first attempt to represent the interfaces, and to develop the local enrichment for the interfaces using level set method. By introducing a continuous level set function, the structure interfaces can be determined. After the interface changed, it can be traced by solving the equations of level set functions. Therefore, it is only required to update the level set function values after the change of interfaces, which leads to a self-consistent way for crack propagation issues when combined with XFEM.

3.2.1. Level set function for crack

Crack is an open interface in terms of geometry, so two level set functions that are perpendicular to each other should be adopted, $\psi(x)$ and $\varphi(x)$, as shown in Fig. 3-2. It is clear that $\psi(x)=0$ and $\varphi(x)\leq 0$ represents the crack, while $\psi(x)=0$ and $\varphi(x)=0$ describes the crack tips.

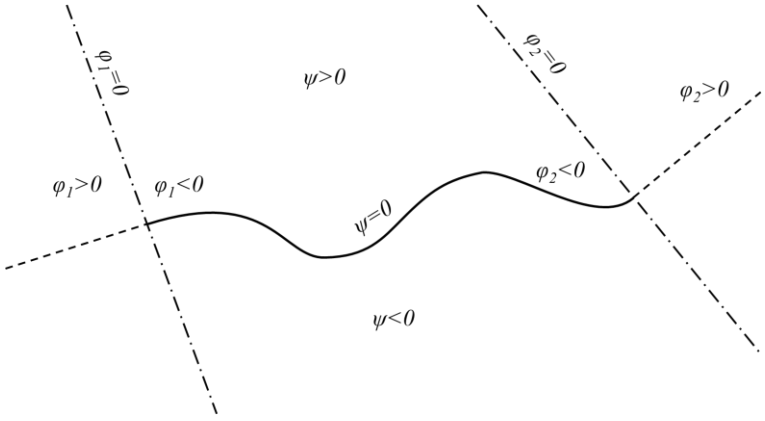

Fig. 3-2 Level set function for crack

3.2.2. Level set function for pores and inclusions

Pores and inclusions are regarded as the closed interface in the domain. For multiple closed interface in a circular shape in the domain, the level set function is put forward by Sukumar et al. (2001):

$$\varphi(\mathbf{X}, 0) = \min\left\{\left\|\boldsymbol{X} - \boldsymbol{X}_c^i\right\| - r_c^i\right\}_{i\ =\ 1,2,\ldots,n_c} \tag{3-1}$$

where n_c is the number of circular interfaces, $\boldsymbol{X}_c^i$ is the centre of the *i*th interface and r_c^i is the radius. Fig. 3-3a shows the level set function for the *i*th circular interface. The level set functions for closed interface with the shape of ellipse and polygon can be built in the similar way.

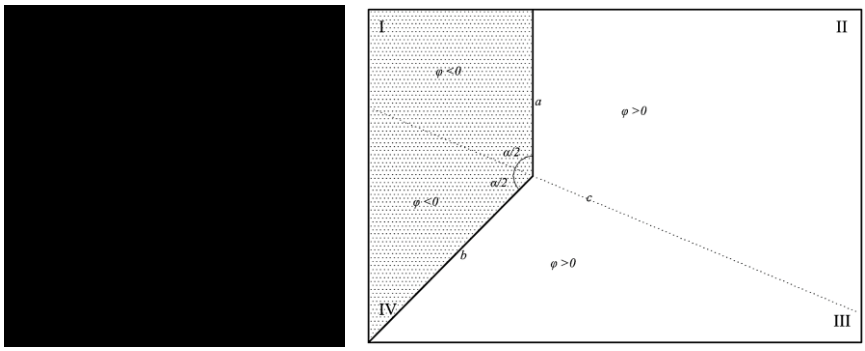

a) closed interfaces b) weld toe geometries

Fig. 3-3 level set functions

3.2.3. Level set function for weld geometry

When looking into the weld geometry, the crucial parameter is the flank angle in terms of the rib-to-deck weld toe of OSDs. It can be built by simply cutting the angle out, same as a polygonal void in the model. In that case, the level set function for a polygonal void given by Sukumar et al. (2001) could be a reference, which is defined as the projection distance between the point and the interface as follows,

$$\begin{cases} \varphi(\mathbf{X}, 0) = \|\boldsymbol{X} - \boldsymbol{X}_{min}\| sgn\big((\boldsymbol{X} - \boldsymbol{X}_{min}) \cdot \boldsymbol{n}_{min}\big), \\ sgn(\xi) = \begin{cases} 1 & if\ \ \xi \geq 0, \\ -1 & if\ \ \xi < 0, \end{cases} \\ \|\boldsymbol{X} - \boldsymbol{X}_{min}\| = min\|\boldsymbol{X} - \boldsymbol{X}_i\|, \end{cases} \tag{3-2}$$

where $\boldsymbol{X}_{min}$ is the orthogonal projection of $\boldsymbol{X}$ on the interface; $\boldsymbol{n}_{min}$ is the outward normal to the interface at $\boldsymbol{X}_{min}$.

To define the flank angle α, the definition could be simplified as there are only two segments that consist the interface. The level set function φ is given in Fig. 3-3

b). Line *c* is the bisector of flank angle α, which divides the model into an upper part and the lower one. Here the bisector is adopted due to the continuity requirement for the level set function. Line *a* and *b* divide the model into a shadow part and a regular one. The model is therefore separated into four regions: I, II, III, and IV. The level set function φ can then be defined by a sign function multiplied by the distance from the node to Line *a* or *b*.

$$\varphi = sign(x)d(x) \tag{3-3}$$

where

$$sign(x) = \begin{cases} 1, & Region\ II,\ III \\ -1, & Region\ I,\ IV \end{cases}$$

$$d(x) = \begin{cases} distance\ to\ Line\ a, & Region\ I,\ II \\ distance\ to\ Line\ b, & Region\ III,\ IV \end{cases}$$

It should be noted that the level set functions for all closed sections are using the same symbol φ, which is for the combination of various discontinuities, and the same enrichment function is to be applied, i.e.,

$$\varphi = \min(\varphi_i) \tag{3-4}$$

Therefore, the multiple pores together with the weld toe flank angle could be easily achieved with the same enrichment function as presented in next section. By properly setting the position and radius of the pore, it is possible to simulate the grinded or shot-peened weld toe geometry as well.

3.3. XFEM basics

3.3.1. Governing equation

The function of the displacement field $\boldsymbol{u}(x)$ is approximated by the following form:

$$\boldsymbol{u}(x) = \sum_{I\epsilon\Omega} N_I(x)(\boldsymbol{u}_I + \sum_{I\epsilon\Omega_d} \phi(x)\boldsymbol{a}_I \tag{3-5}$$

where $N_I(x)$ is the shape function in the traditional FEM, Ω & Ω_d are the entire domain and the enriched domain respectively, $\boldsymbol{u}_I$ & $\boldsymbol{a}_I$ are the traditional and enriched degrees of freedom (DOF), respectively, $\phi(x)$ is the enrichment function of Ω_d.

Different from regular FEM, the nodal displacement approximation in the above equation is not correct due to the enriched DOF. Therefore, the shifted enrichment function $\Upsilon_I^J(x)$ is put forward (Belytschko et al., 2001) to fix that:

$$\Upsilon_I^J(x) = \phi^J(x) - \phi_I^J(x) \tag{3-6}$$

where $\phi_I^J(x)$ is the value of the *J*th enrichment function at the *I*th node. In consequence, the shifted displacement field is given by,

$$\boldsymbol{u}(x) = \sum_I N_I(x)[\boldsymbol{u}_I + \sum_J \Upsilon_I^J(x)\boldsymbol{a}_I^J] \tag{3-7}$$

The basic form of governing equation in XFEM is the same as that in regular FEM, given in:

$$\boldsymbol{K\delta} = \boldsymbol{R} \tag{3-8}$$

where $\boldsymbol{K}$ is the global stiffness matrix; $\boldsymbol{\delta}$ are the nodal DOFs; $\boldsymbol{R}$ are the applied nodal forces. However, as XFEM uses enriched domain to compute the DOF, the global stiffness matrix $\boldsymbol{K}$ should considered as (Pais, 2011),

$$\boldsymbol{K} = \begin{bmatrix} \boldsymbol{K_{uu}} & \boldsymbol{K_{ua}} \\ \boldsymbol{K_{ua}^T} & \boldsymbol{K_{aa}} \end{bmatrix} \tag{3-9}$$

where $\boldsymbol{K_{uu}}$ is classical finite element stiffness matrix, $\boldsymbol{K_{aa}}$ is the enriched finite element stiffness matrix, and $\boldsymbol{K_{ua}}$ is a coupling matrix between the classical and enriched stiffness components. The elemental stiffness matrix $\boldsymbol{K_e}$ is given by:

$$\boldsymbol{K_e} = \int_\Omega \boldsymbol{B_\alpha^T C B_\beta} d\Omega \quad \alpha, \beta = u, a \tag{3-10}$$

where $\boldsymbol{B_u}$ is the strain matrix of regular FEM, calculated by regular shape function derivatives; $\boldsymbol{B_a}$ is that of enriched elements, calculated by enriched shape function derivatives; $\boldsymbol{C}$ is the constitutive matrix. In a two-dimensional domain, $\boldsymbol{B_u}$ and $\boldsymbol{B_a}$ can be given as:

$$\boldsymbol{B_u} = \begin{bmatrix} N_{I,x} & 0 \\ 0 & N_{I,y} \\ N_{I,y} & N_{I,x} \end{bmatrix} \tag{3-11}$$

$$\boldsymbol{B_a} = \begin{bmatrix} (N_I\Upsilon_I^J)_{,x} & 0 \\ 0 & (N_I\Upsilon_I^J)_{,y} \\ (N_I\Upsilon_I^J)_{,y} & (N_I\Upsilon_I^J)_{,x} \end{bmatrix} \tag{3-12}$$

where $N_{I,x}$ is the partial derivative of $N_I(x)$ with respect to *x*; $(N_I\Upsilon_I^J)_{,x}$ is the partial derivative of $N_I(x)\Upsilon_I^J(x)$ with respect to *x*.

In the same manner, the nodal DOFs $\boldsymbol{\delta}$ and the applied nodal forces $\boldsymbol{R}$ are given by:

$$\boldsymbol{\delta}^T = \{\boldsymbol{u} \quad \boldsymbol{a}\}^T \tag{3-13}$$

$$\boldsymbol{R}^T = \{\boldsymbol{R_u} \quad \boldsymbol{R_a}\}^T \tag{3-14}$$

where $\boldsymbol{u}$ and $\boldsymbol{a}$ are vectors of the regular and enriched DOFs, respectively; $\boldsymbol{R_u}$ and $\boldsymbol{R_a}$ are vectors of the applied forces and enriched force components.

3.3.2. Enrichment functions

In this research, enrichment functions were applied on the elements affected by cracks, weld geometries, circular inclusions and pores. Among them, the enrichment for cracks should be considered separately for the following two subcases: the elements fully penetrated by a crack and the elements with a crack-tip inside. According to previous theoretical studies on XFEM, the enrichment functions were listed as follows,

1. For the fully penetrated elements (Belytschko et al., 2001), the Heaviside enrichment function *H(x)* is applied,

$$H(x) = \begin{cases} 1, & above\ \ crack \\ -1, & below\ \ crack \end{cases} \tag{3-15}$$

2. For the elements with a crack-tip inside, the enrichment function takes the form of the following (Belytschko et al., 2001),

$$B_\alpha(x)_{,\alpha=1-4} = [\sqrt{r}\sin(\theta/2), \sqrt{r}\cos(\theta/2), \sqrt{r}\sin\theta\sin(\theta/2), \sqrt{r}\sin\theta\cos(\theta/2)] \tag{3-16}$$

   where r, θ are the coordinates based on the crack-tip polar coordinate system.

3. For the case of inclusions, the enrichment is addressed by Moës et al. (2003) as follows,

$$\psi(x) = \sum N_I(x)|\zeta_I| - |\sum N_I(x)\zeta_I| \tag{3-17}$$

   where ζ_I is the inclusion level set function.

4. For the case of pores, the enrichment strategy could be slightly different from inclusions, since it could be easily modeled by removing the calculation for the nodes inside the pores. Accordingly, the displacement field is given by Sukumar et al. (2001) as follows,

$$\boldsymbol{u}(x) = P(x)\sum N_I(x)\boldsymbol{u}_I, \quad where\ \ P(x) = \begin{cases} 1, outside\ \ pores \\ 0,\ inside\ \ pores \end{cases} \tag{3-18}$$

5. Similarly, the enrichment function for weld geometry could be applied in the same way as the pores:

$$\boldsymbol{u}(x) = P(x)\sum N_I(x)\boldsymbol{u}_I,\ where\ \ P(x) = \begin{cases} 1,\ Region\ \ II,\ \ III \\ 0,\ Region\ \ I,\ \ IV \end{cases} \tag{3-19}$$

3.3.3. Subdomains for numerical integration

Due to the discontinuities that XFEM deals with, the numerical integration in forming the element stiffness matrix by Equation (3-10) will be incorrect if the standard Gauss Integration is applied, as it requires smooth integrands. Thus, an approach was put forward by Moës et al. (1999) to solve it, by performing the integration in a set of triangular subdomains for the element with discontinuities inside. In that way, the error in results of XFEM, especially in the crucial areas near the discontinuities, is closely related to the scheme of forming and integrating subdomains.

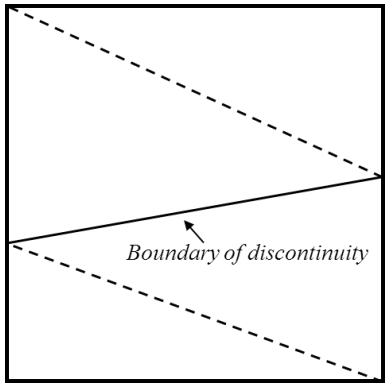

a) Element cut by boundary of discontinuity

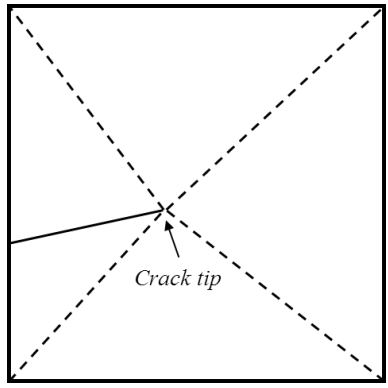

b) Element contains crack tip

Fig. 3-4 Subdomain for different types of elements

The division of the subdomains is shown in Fig. 3-4. For the elements cut by the boundary of interfaces, four Delaunay triangles were formed by the nodes, the intersections of interfaces and element boundaries. For the elements contains crack tip, five Delaunay triangles were constructed by the crack tip point, nodes and intersections. The number of Gauss points for integration in each triangular subdomain was 7 for the crack tip enrichment and 3 for others. While for the blended elements that contain enriched nodes, in total 6 × 6 Gaussian points were applied in the integration.

It should be remarked that the boundary of interfaces in Fig. 3-4 a) refers to not only the crack that go through the elements, but also the boundary of pores, inclusions, weld toe geometries. Since multiple interfaces in one element is not considered in this program, it may lead to incorrect results when fully-random

defects are generated in the model. To avoid that, it is forbidden in this program that the pores, inclusions are smaller than the mesh, or getting too close to the cracks. The XFEM solution for this kind of cases could refer to (Yu, 2014).

3.3.4. Calculation of stress intensity factor

The common way to calculate stress intensity factor (SIF) in XFEM is to use interaction integrals (Moës et al., 1999). For a two-dimensional problem, the J-integral of mixed-mode crack is given by,

$$J = \frac{K_I^2}{E^*} + \frac{K_{II}^2}{E^*} \tag{3-20}$$

$$E^* = \begin{cases} E & plane\ \ stress \\ \frac{E}{1-\nu^2} & plane\ \ strain \end{cases} \tag{3-21}$$

where E is the Young's modulus; ν is the poisson ratio. By assuming the current state as State 1, and an asymptotic field for Modes I or II as the auxiliary State 2, the J-integral is given by,

$$J^{(1,2)} = \int_\Gamma [\frac{1}{2}\left(\sigma_{ij}^{(1)} + \sigma_{ij}^{(2)}\right)\left(\varepsilon_{ij}^{(1)} + \varepsilon_{ij}^{(2)}\right)\delta_{1j} - \left(\sigma_{ij}^{(1)} + \sigma_{ij}^{(2)}\right)\left(u_{i,1}^{(1)} + u_{i,1}^{(2)}\right)]\boldsymbol{n_j} d\Gamma \tag{3-22}$$

where Γ is the contour around the crack tip, $\boldsymbol{n}$ is the normal vector of Γ. By rearranging terms, it can be rewritten as,

$$J^{(1,2)} = J^{(1)} + J^{(2)} + I^{(1,2)} \tag{3-23}$$

where $I^{(1,2)}$ is the interaction integral,

$$I^{(1,2)} = \frac{2}{E^*}(K_I^{(1)}K_I^{(2)} + K_{II}^{(1)}K_{II}^{(2)}) \tag{3-24}$$

Therefore, by setting the auxiliary State 2 to be pure Mode I ($K_I^{(2)} = 1$ and $K_{II}^{(2)} = 0$) or pure Mode II ($K_I^{(2)} = 0$ and $K_{II}^{(2)} = 1$), the SIF for State 1 can be given by,

$$K_I^{(1)} = \frac{I^{(1,Mode\ I)}E^*}{2} \tag{3-25}$$

$$K_{II}^{(1)} = \frac{I^{(1,Mode\ II)}E^*}{2} \tag{3-26}$$

The interaction integral in above equations could be solved by converting the contour integral to the surface integral,

$$I^{(1,2)} = \int_A [\sigma_{ij}^{(1)}u_{i,1}^{(2)} + \sigma_{ij}^{(2)}u_{i,1}^{(1)} - W^{(1,2)}\delta_{1j}]q_{,j} dA \tag{3-27}$$

where A is the circular integral domain whose center is at the crack tip with the radius of r_d; $W = \frac{1}{2}\sigma_{ij}\varepsilon_{ij}$, is the strain energy density; q is the weight function which equals one for nodes within the radius r_d, and zero for outer contour. The radius r_d was decided to equal three times the square root of element area, which will cover at least three elements around the crack tip, as previous studies did (Pais, 2011). This interaction integral domain could be enlarged to cover five elements, or set to be a square rather than a circular one as well, as Yu (2014) suggested.

3.4. Crack growth model

3.4.1. Linear-elastic fracture mechanics

The crack growth model in this XFEM program is theoretically based on fracture mechanics, or to be more precise, the linear-elastic fracture mechanics (LEFM). Compared to elastic-plastic fracture mechanics (EPFM), it is accurate enough in solving small-scale yielding cases, and quite practical when combined with XFEM.

In fracture mechanics, three types of crack opening modes were concluded, as shown in Fig. 3-5. According to the typical loads on rib-to-deck weld joints, the crack opening is believed to be a mix mode of Mode I and Mode II. In that case, the simplified two-dimensional model of crack tip field can be representative, and its polar coordinate system is defined, as shown in Fig. 3-6.

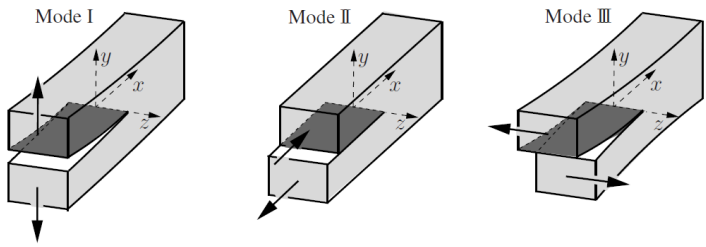

Fig. 3-5 Crack opening modes (Gross and Seelig, 2011)

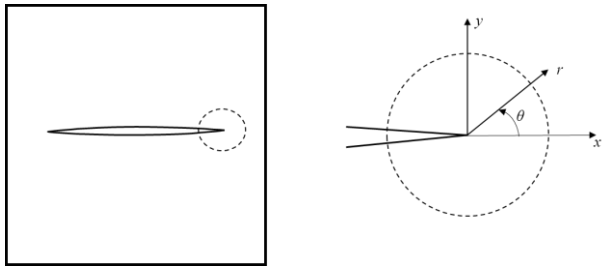

Fig. 3-6 Crack tip polar coordinate system

If the linear elastic part of the cracked body is dominating and the inelastic zone is so small that can be ignored, the crack tip field can be solved using LEFM, and the stress and deformation for Mode I crack can be given by,

$$\begin{Bmatrix}\sigma_x\\ \sigma_y\\ \tau_{xy}\end{Bmatrix} = \frac{K_I}{\sqrt{2\pi r}}\cos(\frac{\theta}{2})\begin{Bmatrix}1-\sin\left(\frac{\theta}{2}\right)\sin(\frac{3\theta}{2})\\ 1+\sin\left(\frac{\theta}{2}\right)\sin(\frac{3\theta}{2})\\ \sin\left(\frac{\theta}{2}\right)\cos(\frac{3\theta}{2})\end{Bmatrix} \tag{3-28}$$

$$\begin{Bmatrix}u\\ v\end{Bmatrix} = \frac{K_I}{2G}\sqrt{\frac{r}{2\pi}}(\kappa-\cos\theta)\begin{Bmatrix}\cos(\frac{\theta}{2})\\ \sin(\frac{3\theta}{2})\end{Bmatrix} \tag{3-29}$$

and that for Mode II crack is given by,

$$\begin{Bmatrix}\sigma_x\\ \sigma_y\\ \tau_{xy}\end{Bmatrix} = \frac{K_{II}}{\sqrt{2\pi r}}\begin{Bmatrix}-\sin(\frac{\theta}{2})[2+\cos\left(\frac{\theta}{2}\right)\cos\left(\frac{3\theta}{2}\right)]\\ \sin\left(\frac{\theta}{2}\right)\cos\left(\frac{\theta}{2}\right)\cos\left(\frac{3\theta}{2}\right)\\ \cos\left(\frac{\theta}{2}\right)[1-\sin\left(\frac{\theta}{2}\right)\sin(\frac{3\theta}{2})]\end{Bmatrix} \tag{3-30}$$

$$\begin{Bmatrix}u\\ v\end{Bmatrix} = \frac{K_{II}}{2G}\sqrt{\frac{r}{2\pi}}\begin{Bmatrix}\sin\left(\frac{\theta}{2}\right)(\kappa+2+\cos\theta)\\ \cos(\frac{\theta}{2})(\kappa-2+\cos\theta)\end{Bmatrix} \tag{3-31}$$

where

plane strain: $\kappa = 3-4\nu,\ \sigma_z = \nu(\sigma_x+\sigma_y)$

plane stress: $\kappa = (3-\nu)/(1+\nu),\ \sigma_z = 0$

According to the above equations, it is clear that the singular stress will appear when $r \to 0$, and the singular order is $r^{1/2}$. The solution for deformation is, therefore, in correspondence with the enrichment functions in Section 3.3.2. Thus, the aforementioned crack tip enrichment functions were based on LEFM, and the

necessity arises to verify if the linear-elastic assumption is available on the issue of cracked welded joint of OSDs. A criterion proposed by Irwin suggested that when the cracked body meets the small-scale yielding condition, i.e. the plastic area is much smaller than the SIF-dominated one, the result obtained by LEFM is accurate enough (Wang and Chen, 2009). By comparing the plastic area around crack tip with the crack length, the criterion for plane strain status is given by,

$$r_p/a \leq 0.1 \tag{3-32}$$

$$r_p = \frac{K^2}{6\pi\sigma_y^2} \tag{3-33}$$

where r_p is the plastic area around crack tip, a is the crack length. σ_y is the yield strength, K is the stress intensity factor.

Even though the accurate SIF for the fatigue crack on OSD is not yet obtained, an estimation can be provided in a conservative way. Take an instance of a crack on welded joint under applied remote stress of 100MPa, which is clearly larger than the stress ranges induced by heavy trucks on OSDs (Wang et al., 2016). The SIF is calculated according to Stress Intensity Factors Handbook (Murakami and Keer, 1993),

$$K_I = F\sigma\sqrt{\pi a} \tag{3-34}$$

where F is the shape factor; σ is the applied remote stress; W is the plate width, i.e. the thickness of the deck plate, 15 mm. In case of bending on a thick plate, F can be achieved by the handbook,

$$F = [1.122 - 1.40\left(\frac{a}{W}\right) + 7.33\left(\frac{a}{W}\right)^2 - 13.08\left(\frac{a}{W}\right)^3 + 14.0\left(\frac{a}{W}\right)^4] \tag{3-35}$$

or in case of the semi-elliptical crack at weld toe under bending, F can be obtained according to Bowness and Lee (2000) as in Section 2.4.5,

$$F = f_1\left(\frac{a}{T}, \frac{a}{c}\right) + f_2\left(\frac{a}{T}, \theta\right) + f_3\left(\frac{a}{T}, \theta, \frac{L}{T}\right) \tag{3-36}$$

The plastic area r_p with respect to different crack length a is shown in Fig. 3-7. It can be seen that until the crack grows to 10 mm in depth, the small-scale yielding condition is always met. Here the effect of residual stress on the plastic area was not taken into account. Even so, it is assumed that LEFM is suitable on this issue, since literatures showed the result will not be so different even when the elastoplastic behavior is considered (Pais, 2011).

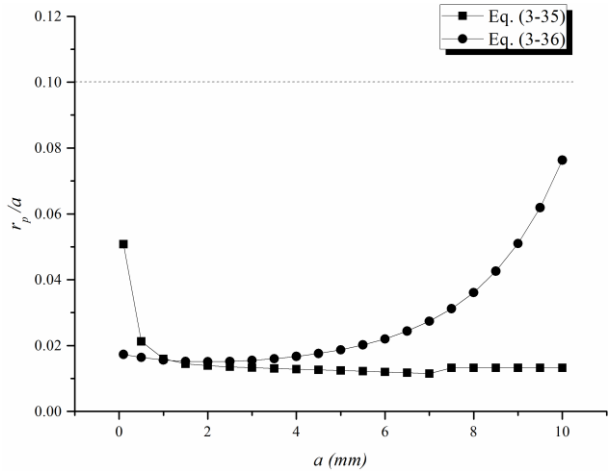

Fig. 3-7 Small-scale yielding verification

3.4.2. Crack growth rate

Paris law is the commonly-used model in calculation of fatigue crack growth rate, which indicates it is related to the stress intensity factor range. The classical Paris law is expressed in a form as,

$$\frac{da}{dN} = C(\Delta K)^m \tag{3-37}$$

where *da/dN* is the crack growth rate, i.e. the crack growth increment per cycle, *C* is the Paris constant, *m* is Paris exponent, *ΔK* is the stress intensity factor range.

Though the classical Paris law fits the experimental results quite well for Stage II cracks (in stable propagation phase, i.e. Paris region), it has some limitations as a semi-empirical law: i) unable to describe the early or short crack growth rate (near the threshold region) and unstable crack growth rate; ii) the constants *C* and *m* is regarded as material properties, while the evident factor stress ratio *R* is ignored; iii) the effects induced by crack tip plasticity, e.g. crack closure or overload retardation, cannot be considered. Consequently, several modified forms of Paris law were put forward, as has been reviewed in Section 1.2.4.2. However, given that the feasibility of these modified forms is yet to be proved on this issue, the way of calculating the crack growth in the following is to use the Paris law with material properties obtained in the fatigue test.

The realistic fatigue loading is another problem for calculating fatigue crack growth on rib-to-deck welded joints of OSDs with Paris law. For most of the actual projects like OSDs, the fatigue loading has variable amplitudes, while the constant

amplitude loading is adopted in fatigue tests such as in Chapter 2 and the subsequent fatigue category evaluation. As validated by these fatigue tests, the classical Paris law is more appropriate to be applied in the cases of constant amplitude loading. Though the modified Paris law provided the access to simulate the variable amplitude loading with respect to load interactions, the exact process of the fatigue crack growth is still difficult to obtain due to the computational feasibility problem caused by the high fatigue cycle number.

In order to analyze the variable amplitude loading induced fatigue, the damage-based prediction is commonly used. On condition that the influence of load interactions is negligible, the variable amplitude loading could be counted using the rainflow algorithm, and then the damage accumulation based on Miner's rule can be applied to predict the fatigue life, which is the commonly-used way in actual projects. For the fatigue crack growth model, the load sequence surely matters as it defines the plastic zone. Nevertheless, some studies imply that the SIF with consideration of plasticity caused by variable amplitude loading will have little difference (Elguedj et al., 2006, 2007).

3.4.3. Mixed-mode crack growth

To simulate the fatigue crack growth based on mode I and mode II SIFs, the crack growth direction and increment should be addressed. Different theories were available for both two- and three-dimensional problems. The important works on two-dimensions are the maximum circumferential stress criterion, minimum strain energy density criterion, maximum energy release rate criterion, and critical plane approach, etc. Among them, the maximum circumferential stress criterion is adopted in this study since it is practical on this issue and friendly to programming (Moës, 1999).

The maximum circumferential stress criterion is mainly focused on the kink angle of the crack, θ_c. It was proposed by Erdogan and Sih (1963), which suggests that the crack will grow to the direction perpendicular to maximum circumferential stress. As the crack tip stress field can be expressed in terms of SIFs, i.e. K_I and K_{II}, the kink angle can be given as follows,

$$\theta_c = 2\arctan\left[\frac{1}{4}\left(K_I/K_{II} \pm \sqrt{(K_I/K_{II})^2 + 8}\right)\right] \tag{3-38}$$

To achieve the fatigue crack growth increment for each cycle (or cycle block in a high cycle fatigue), the SIF should be given in a proper way. The early work on this issue is given by Tanaka (1974). By assuming there is no interaction between deformations induced by mode I and mode II loading, and the shear yield stress is one-half of the tension yield stress, an effective SIF, ΔK_{eff}, was put

forward. ΔK_{eff} is a function of K_I, K_{II} in two-dimensions, and could be extended to three-dimensions.

$$\Delta K_{eff} = \sqrt[4]{\Delta K_I^4 + 8\Delta K_{II}^4} \tag{3-39}$$

There are other studies based on different factors, such as the strain energy density, *J*-integral, etc., that concerned about mixed-mode crack growth, and were summarized by (Qian and Fatemi, 1996), providing options to future development of this program.

CHAPTER 4

XFEM BASED HOMOGENIZATION METHOD ON WELD DEFECTS

This chapter is based on

Wang, B., De Backer, H., and Chen, A. (2016). An XFEM based uncertainty study on crack growth in welded joints with defects. *Theoretical and Applied Fracture Mechanics*, *86, Part B*, 125-142.

4.1. Introduction

Weld defect could be a significant factor in fatigue behavior of welded joints. The typical weld defects in butt weld and fillet weld are given in Fig. 4-1 (Milella, 2012), which includes the undercuts, overlaps, lack of penetrations, lack of fusions, cracks, porosities and inclusions, etc. By checking the failure surfaces, Miki et al. (1993, 2001) presented the size of these defects on OSDs, and considered them as the main causes of fracture. Afterwards, as the developing of welding technologies and better quality control, the micro-flaws or rough surface conditions became more crucial nowadays. As a consequence, more attentions were paid to the effects of small defects to early-stage cracks.

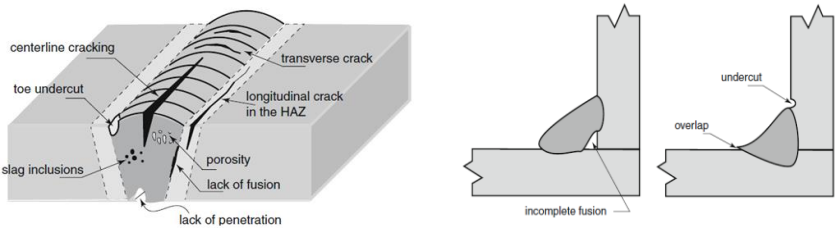

a) butt weld b) fillet weld

Fig. 4-1 Typical weld defects in a) butt weld and b) fillet weld (Milella, 2012)

As mentioned before, previous works on fatigue behavior affected by weld defects were mainly in the frame of continuum mechanics, focused on weld geometries, cracks or crack-like defects, and fictitious notch effects. That means more attention was paid to how the crack propagates due to the driving force provided by itself, while the effect of non-crack-like defects to crack propagation were overlooked. It is somewhat reasonable since the defects are so tiny as stated by Zerbst (2011) and as observed in the fractography analyses on fatigue test specimens in Chapter 2. However, by considering the scattered positions of them, appreciable influences on fatigue strength may occur, especially on large-scale structures due to the "size effect" called by Murakami (2002). In that case, reports about identifying and evaluating weld defects in OSDs are quite rare and needed.

To study these defects in welded joints of OSDs, homogenization is a preferred way due to multiscale concerns. As reports on the homogenization method were always based on the equivalent strain energy, they were proven to be more effective on the issue of the mechanical properties of materials (Hiriyur et al., 2011, Kumar et al., 2015) than for crack propagation. Therefore, a homogenization method for the non-crack-like defects in welded joints on a non-detectable scale was proposed in this chapter, to illustrate the effects on crack growth and fatigue performance.

4.2. Generation of RVEs

It was confirmed in Chapter 2 that there is initial crack caused by the coarse grained HAZ, which is regarded here as the start of main crack. If the frame of continuum mechanics and LEFM are to be applied, other defects could be considered as non-crack-like ones that affects the main crack propagation. In that way, the homogenization of these non-crack-like defects with XFEM will provide a simple solution to the concern of massive computation and of multiscale problem.

The inclusions and pores observed in the fatigue test were typical, according to which the characteristic size of them were figured in a range from several micrometers to tens of micrometers. With such small sizes, they are invisible to non-destructive test, and thus their locations are unable to determine. To consider their effects by continuum mechanics and LEFM, the possible way is to generate a large number of representative volume elements (RVEs) that contain weld defects with random sizes and locations, and solve them with programs that are capable of massive computation. Therefore, the XFEM and homogenization method are quite useful for this problem. As the initial crack was already addressed in Chapter 2, the target should be the non-crack-like defects. The inclusions and pores with circular shape were studied, whilst the possible secondary cracks, elliptical or polygonal inclusions and pores are not taken into account here for the sake of simplicity.

4.2.1. Random defects

The observed weld defects in the fatigue test on welded joints of OSDs were shown in Chapter 2 and Appendix A. According to the micro-chemical energy analyses, the main chemical composition is MnS combined with complex oxides. These inclusions also act as blocks to the fusion in welding process, and produce voids consequently, as illustrated in Fig. 2-24 in Chapter 2. In addition, the chemical reactions in the welding process may produce pores as well, even though it was not observed by limited fractography analyses in the fatigue test.

For the first step, the XFEM program was used to generate random distributed inclusions and pores in the model. The pseudo random number generator in MATLAB was employed here, and the numbers, sizes, and locations of inclusions and pores were basically assumed to follow uniform distribution to avoid bias, since no statistical data was available at present.

With respect to the principles of XFEM and level set function method, the following rules should be obeyed in generating random inclusions and pores: 1) the distance from the defect boundary to other boundaries, including the model boundaries, other defect boundaries and crack faces, should be large enough to

prevent two interfaces existing in one element; 2) the distance from the defect boundary to crack tip should be large enough to keep it out from the interaction integral domain, which will lead to incorrect result of SIFs. Given a predefined square element with side length of l, the first rule is met if the distance is larger than $\sqrt{2}l$, while the second one requires the distance larger than $(3+\sqrt{2})l$ if the interaction integral domain covers three elements.

The flowchart is given in Fig. 4-2. There is no difference in generating the geometries of inclusions and pores, as they were both assumed circular. The volume fractions of them are not involved in this flowchart, since they are proven to be not that critical in the given circumstance by the parametric analyses in Section 4.3.3. Anyway, it is quite easy in the program to be realized by changing the radii of the defects.

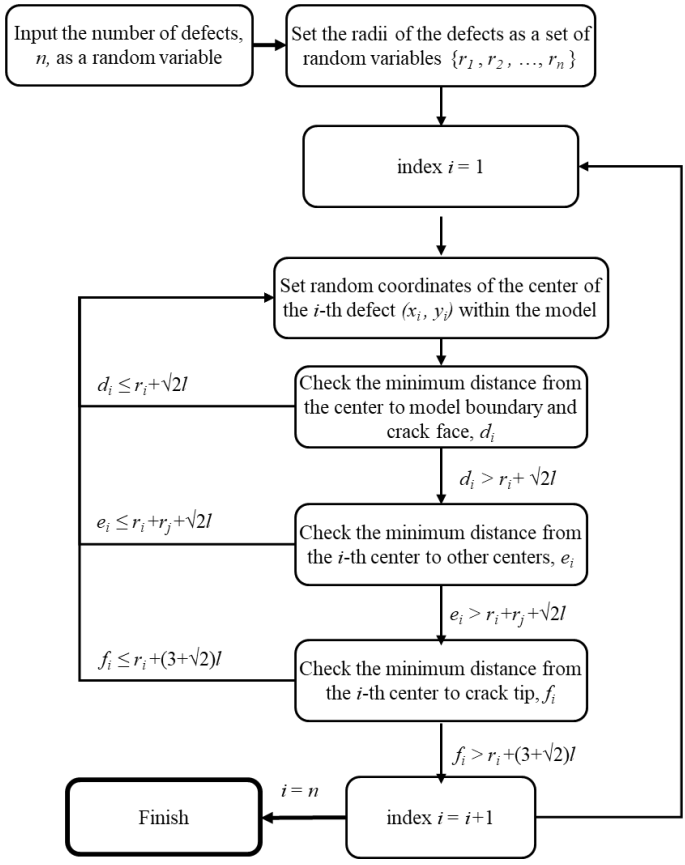

Fig. 4-2 The flowchart of generating random defects

4.2.2. RVEs for OSDs

As is well-known that the most possible site of defects is the HAZ in welded joints, the RVEs were extracted from HAZ of a rib-to-deck welded joint, as shown in Fig. 4-3. The RVEs were assumed to be in the plain strain status. The main crack was located on the edge. The instances of generated RVEs were shown in Fig. 4-4, with different numbers of inclusions n_I and pores n_P, but with the same volume fractions, i.e. $\lambda_I = \lambda_P = 0.05$. Hereinafter the subscript I refers to inclusions and P refers to pores. It should be noted that the realistic material in rib-to-deck welded joint is not a porous one, hence the RVEs with so many defects in Fig. 4-4 were just for demonstrating the capability of the program, while the sizes and numbers of defects were based on reasonable assumptions when conducting the calculation.

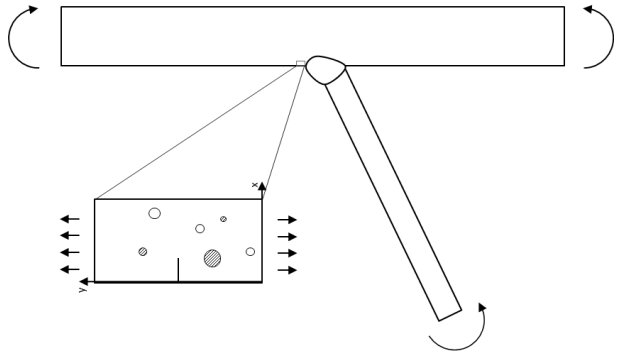

Fig. 4-3 RVE in the rib-to-deck welded joint of OSD

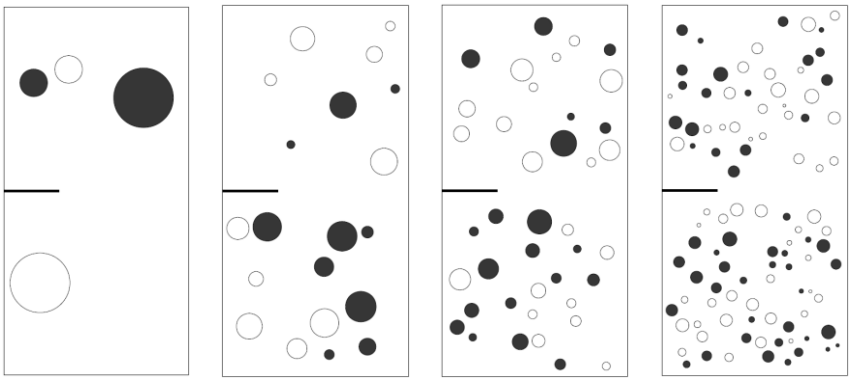

a) 2 inclusions & 2 pores | b) 10 inclusions & 10 pores | c) 20 inclusions & 20 pores | d) 50 inclusions & 50 pores

Fig. 4-4 Generated RVEs with randomly distributed inclusions & pores, $\lambda_I = \lambda_P = 0.05$

The mechanic properties of material matrix were the same as steel, while the inclusions were assumed to have a higher elastic modulus. The Paris constant C and Paris exponent m were assumed to be the ones provided by the IIW recommendation (Hobbacher, 2008). Usually the values of C and m are experiment-based, so these values may not be realistic, and tend to be conservative since they are design-oriented. However, the parametric analyses in Section 4.3.3 showed that the homogenization approach is independent to C and m, thus validated the feasibility of this approach. Another concern is the effect induced by the flank angle at the weld toe, given that the RVE was extracted from the HAZ close by. In fact, since the homogenization is mainly for the mesoscopic defects, it is not sensitive to macroscopic geometries. Again, a benchmark was provided as a proof in Section 4.3.3. Table 4-1 summarizes the material properties of the RVEs.

Table 4-1 Summary of material characteristics

Elastic modulus	Matrix E_M	2.16×10^{11} Pa
	Inclusions E_I	2.81×10^{11} Pa (1.3 times E_M)
Poisson's ratio	Matrix P_M	0.3
	Inclusions P_I	0.3
Paris constant C		1.65×10^{-11}
Paris exponent m		3

4.3. Homogenization method

4.3.1. Basics

In consideration of the differences in scale of civil engineering structures and welded defects, a method that fits multiscale problems seems necessary. Homogenization, as an important option among all the multiscale methods, was a simplified way for practical use in this research. With the help of XFEM, homogenization becomes quite efficient to study the mechanical performance and fatigue performance of heterogeneous materials. The previous studies on homogenization were always based on equivalent strain energy, which is proven to be an effective assumption if the study is focused on the mechanical performance of heterogeneous materials. However, on the issue of crack propagation, as Kumar et al. (2015) shown, the homogenization was limited to the areas with defects far away from the crack region, while the areas with defects near the crack were still heterogeneous in the model. The reason for this is that the relative location of defects and cracks plays a crucial role, which will be explained by parametric analyses afterwards.

In this research, a criterion of equivalent crack growth length was adopted. The main idea was to homogenize the heterogeneous RVE on the very first step, namely to obtain an equivalent crack growth length in the initial state by modifying material constant.

Firstly, by using the forward Euler method to Paris law, the fatigue crack growth is given by,

$$\Delta a = \Delta N[C(\Delta K)^m] \tag{4-1}$$

In a homogenized RVE, all the inclusions and pores will not exist, which makes ΔK related to the initial crack length and the boundary conditions only. Modifying the material constants is thus a possible way to produce equivalent effects on the crack growth rate (CGR) induced by pores and inclusions. Consequently, an objective function R, as given by Equation (4-2), was proposed to get the effective Paris Constant C_{eff} when R is minimized, and a homogenization coefficient a_c was put forward to normalize the effect, as given by Equation (4-3).

$$R = [C_0 \Delta N(\Delta K)^m]_{heter} - [C_{eff} \Delta N(\Delta K)^m]_{homo} \tag{4-2}$$

$$a_c = C_{eff}/C_0 \tag{4-3}$$

The flowchart of the homogenization process is given in Fig. 4-5.

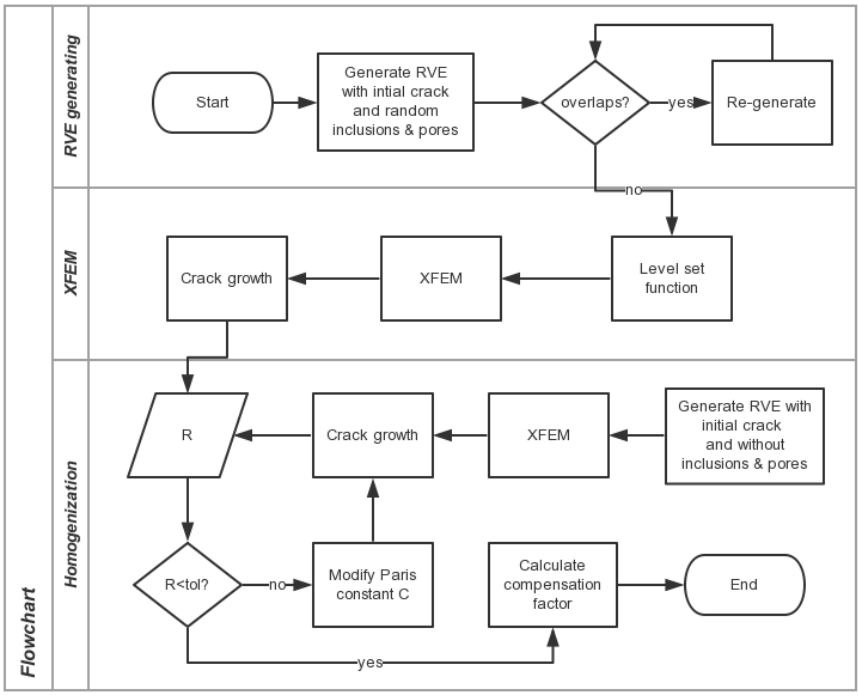

Fig. 4-5 Flowchart of the homogenization process

4.3.2. Numerical examples

Some numerical examples were given to demonstrate the feasibility of this approach, as shown in Table 4-2 and in Fig. 4-6 - Fig. 4-10. The size of the defects was different to keep the volume fractions around 0.05 for all examples. Besides, inclusions and pores were located not too close to the possible crack path, which is the central plane of the model, to avoid crack propagation into their interior. It is because in a two-dimensional model, the pore/inclusion at the crack tip will reduce the stress concentration and the crack may stop growing, whilst in reality, the entire crack front will not be affected by just one defect.

The crack growth was simulated using both the original XFEM model and the homogenized model. As a_c was obtained based on the initial state, the error between the two models becomes bigger as the crack grows, and its validity was checked in terms of crack length with respect to the first thousands of cycles. The results from Numerical Example 1 - 4 are quite favorable for the early stage of the crack growth, as shown in Table 4-2. However, the error could be relatively high in some cases, since the effects of the defect sizes and locations are quite significant. Numerical Example 5 in Fig. 4-10 gives a typical case that has an error of nearly

20 percent. According to Fig. 4-10 i), the XFEM model has an obvious deceleration of the crack growth when the cycle number is around 60000, while the homogenized model does not. The reason is that the pore and the inclusion, as circled in Fig. 4-10 c), would have different effects as the crack tip goes forward. The pore is getting to the rear of the crack tip and starts to behave oppositely from the initial state. While in the meantime, the inclusion is getting closer to the crack tip to help reducing the CGR as well. These two effects significantly slowed down the crack growth rate, thus leading to the inaccuracy in the homogenized model.

However, this kind of circumstances is not always troublesome since it requires the special relative location between the defects and the crack tip, and the defects to be big enough at that same instance. In most cases, the defects are insignificant by then, even though they are getting really close to the crack tip, because their size is not comparable to the size of the growing crack. For instance, the pore circled in Fig. 4-10 g) is extremely close to the crack tip, with its size (*0.131* mm in diameter) is fairly big, but the crack growth rate does not rise apparently, because the crack driving force is mainly dominated by the crack length at that moment.

It should therefore be stated that the homogenization approach is feasible for most cases, at least for the period that the crack grows slowly, which is quite important as the early stage for short crack growth is the dominant part of the total crack growth life. For the changing location between crack and defects, this method sometimes leads to inaccuracies in a homogenized model, but the influence is quite limited.

Table 4-2 Summary of numerical examples

No.	n_I	n_P	λ_I	λ_P	a_c	a in homogenized model (80000 cycles) (mm)	a in heterogenous model (80000 cycles) (mm)	diff.
1	5	5	0.0562	0.0473	1.0822	0.4238	0.4167	-1.67%
2	10	10	0.0466	0.0372	0.9596	0.3992	0.3925	-1.68%
3	50	50	0.0522	0.0520	1.1139	0.4341	0.4225	-2.67%
4	100	100	0.0562	0.0610	1.1530	0.4319	0.4329	0.24%
5	10	10	0.0521	0.0603	1.3405	0.4693	0.5621	19.78%

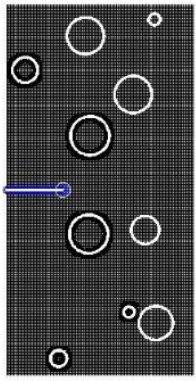

a) N=0, XFEM

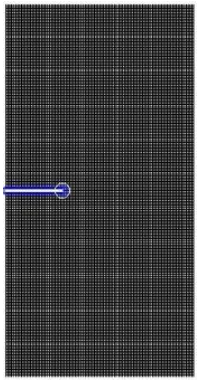

b) N=0, Homogenized

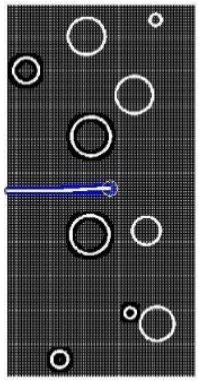

c) N=100000, XFEM

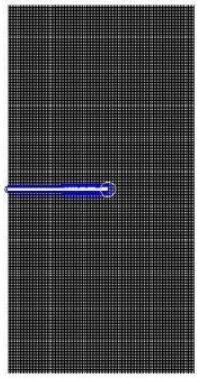

d) N=100000, Homogenized

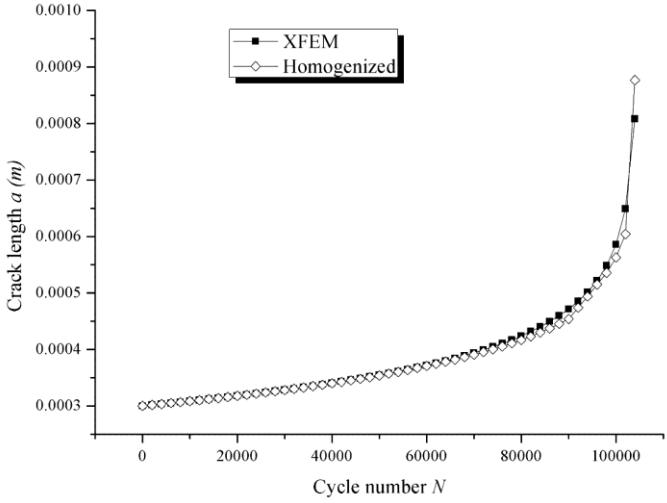

e) Comparison of results from XFEM & homogenized RVE

Fig. 4-6 Numerical Example 1

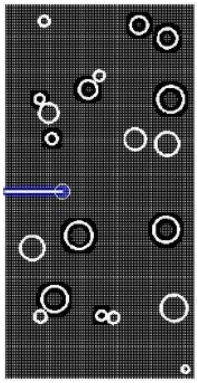

a) N=0, XFEM

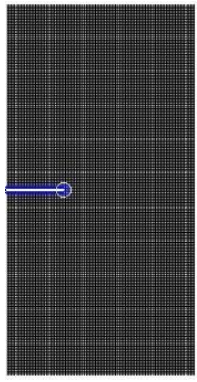

b) N=0, Homogenized

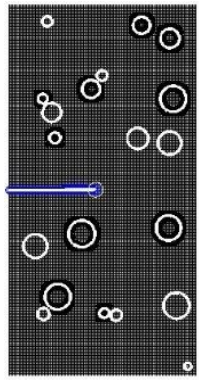

c) N=100000, XFEM

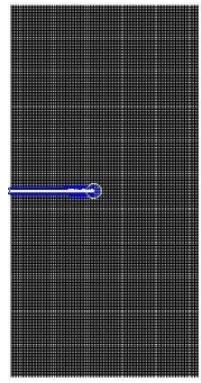

d) N=100000, Homogenized

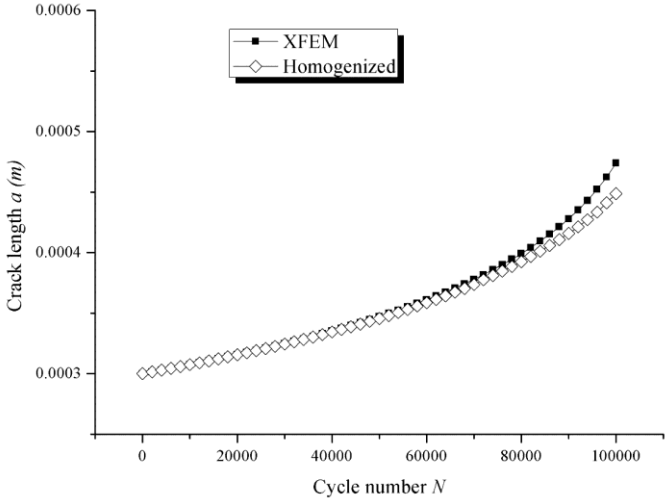

e) Comparison of results from XFEM & homogenized RVE

Fig. 4-7 Numerical Example 2

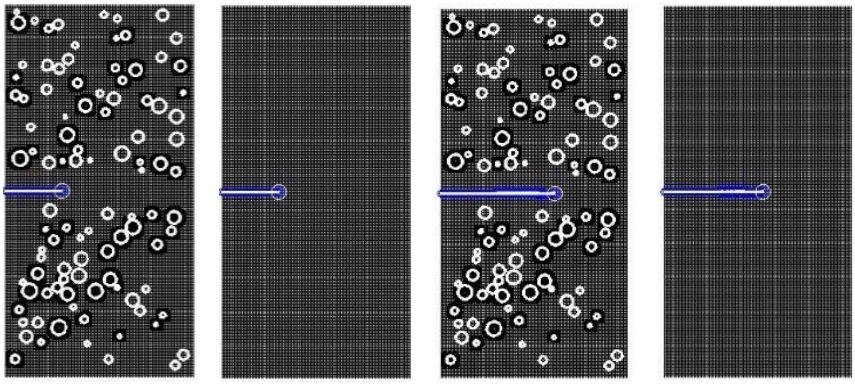

a) N=0, XFEM | b) N=0, Homogenized | c) N=100000, XFEM | d) N=100000, Homogenized

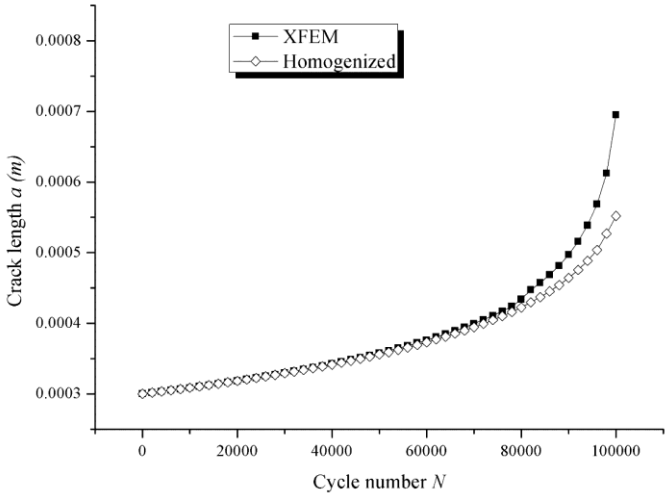

e) Comparison of results from XFEM & homogenized RVE

Fig. 4-8 Numerical Example 3

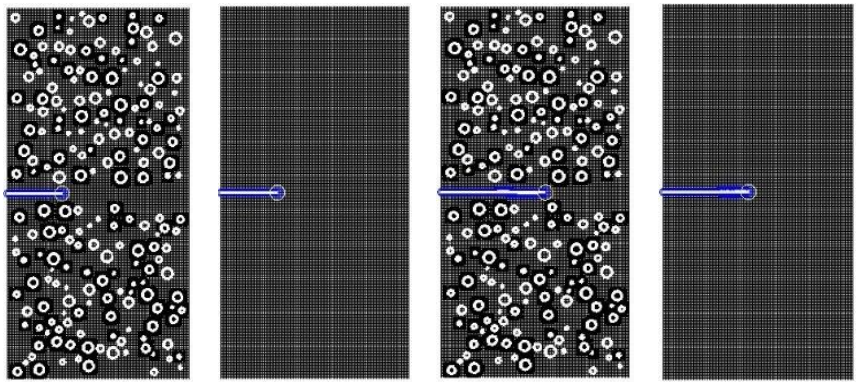

a) N=0, XFEM | b) N=0, Homogenized | c) N=100000, XFEM | d) N=100000, Homogenized

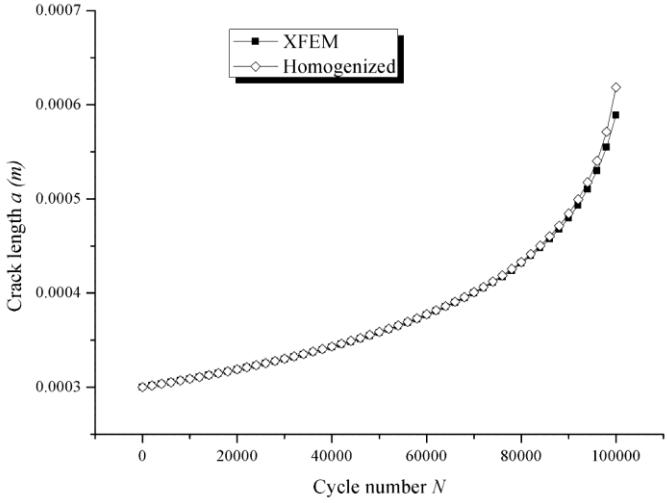

e) Comparison of results from XFEM & homogenized RVE

Fig. 4-9 Numerical Example 4

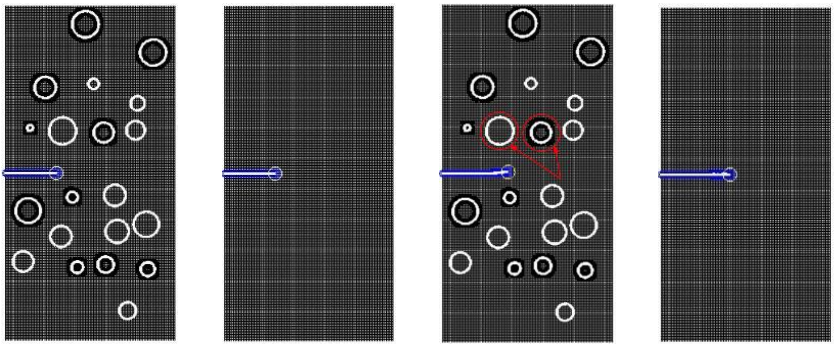

a) N=0, XFEM | b) N=0, Homogenized | c) N=60000, XFEM | d) N=60000, Homogenized

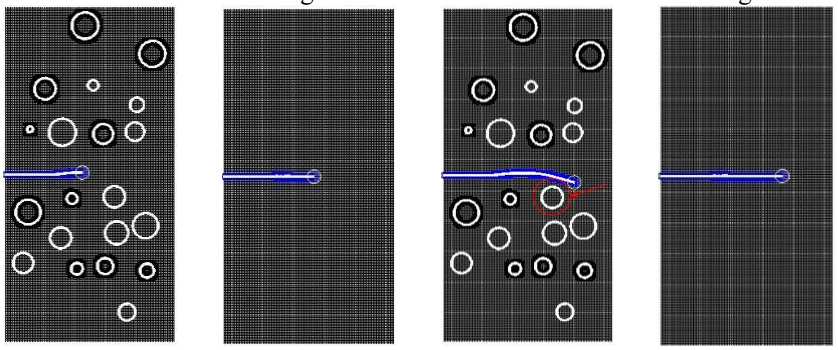

e) N=80000, XFEM | f) N=80000, Homogenized | g) N=92000, XFEM | h) N=84000, Homogenized

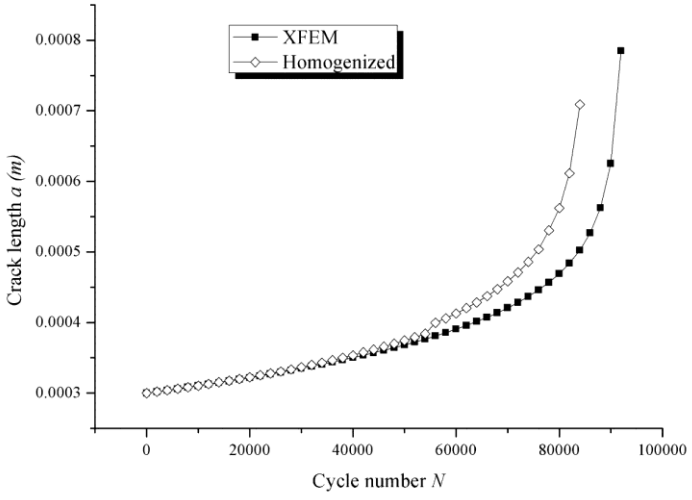

i) Comparison of results from XFEM & homogenized RVE

Fig. 4-10 Numerical Example 5

4.3.3. Parametric analyses

4.3.3.1. Volume fractions

As previous works on homogenization did, the parametric analysis was first carried out on the volume fractions of the defects (see Fig. 4-11 & Fig. 4-12). However, after homogenizing large numbers of RVEs, the coefficient of variance (CV) of a_c shows an unfavorable deviation from the mean value, especially for RVEs with a big volume fraction of pores. Anyway, the results provided a general understanding about the amount of cases required to be statistically stable. As for the parametric analysis, the attention should be switched to other parameters that cannot be covered by volume fractions.

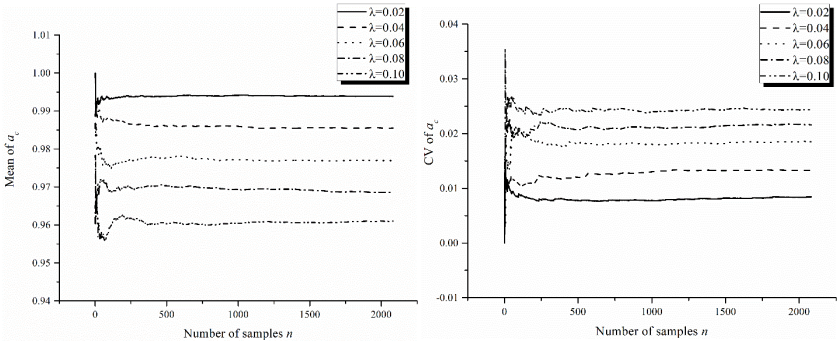

a) Mean of a_c b) CV of a_c

Fig. 4-11 The convergence of mean and CV of a_c with respect to volume fraction of inclusions λ_I

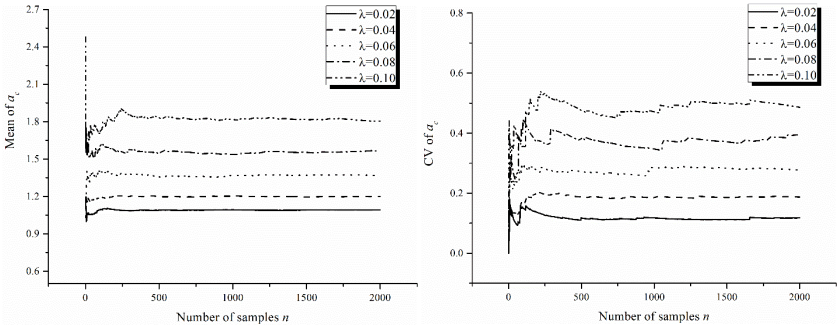

a) Mean of a_c b) CV of a_c

Fig. 4-12 The convergence of mean and CV of a_c with respect to volume fraction of pores λ_P

4.3.3.2. *Material properties and boundary conditions*

In the process of homogenization, there will be parameters that relate to defects, matrix material and boundary conditions, etc. As the coefficient a_c is supposed to demonstrate the influences of defects on the CGR, the key parameters should only be the defect-related ones. By changing parameters such as the elastic modulus of matrix E_M, the Paris constant C and the boundary tension σ, it is clear that they will have no influence on a_c, as shown in Fig. 4-13 - Fig. 4-15, where E_M and C are normalized by using the ratio of E_M to the elastic modulus of steel E_S and the ratio of C to C_0, respectively.

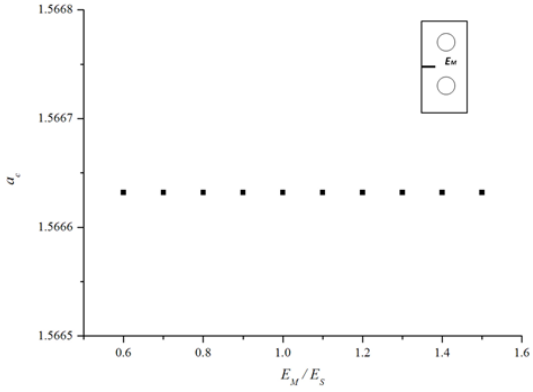

Fig. 4-13 Variation of homogenization coefficient a_c with normalized elastic modulus of matrix

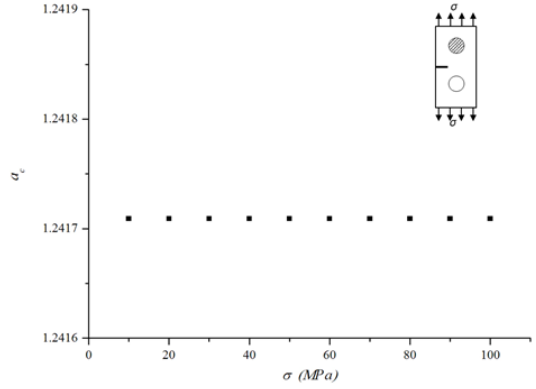

Fig. 4-14 Variation of homogenization coefficient a_c with tension σ

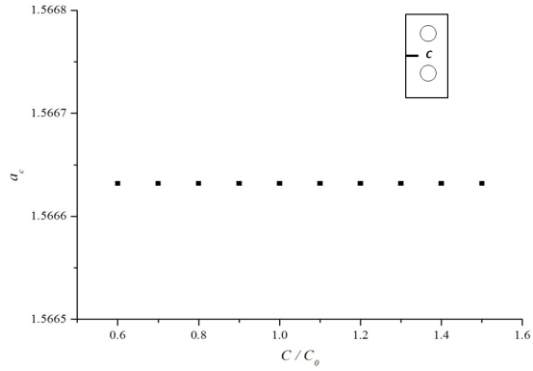

Fig. 4-15 Variation of homogenization coefficient a_c with normalized Paris constant

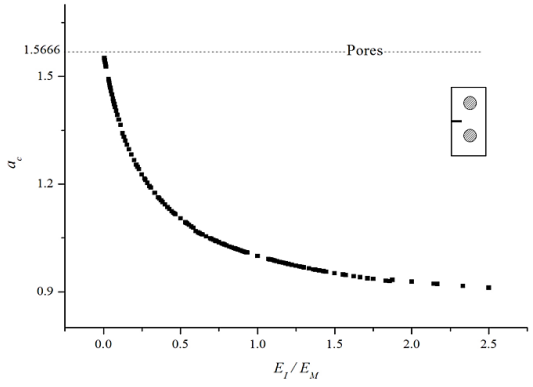

Fig. 4-16 Variation of homogenization coefficient a_c with normalized elastic modulus of inclusions

By changing the elastic moduli of the inclusions in the RVEs with two symmetrically distributed inclusions, the variations of a_c are presented in Fig. 4-16. By comparing the results with the ones with two symmetrically distributed pores in Fig. 4-15, it could be stated that the influence of inclusions will be equivalent to pores when $E_I << E_M$. The CGR will be smaller ($a_c < 1$) if $E_I > E_M$, and vice versa. However, the effects are also dependent on the locations in a quite significant way.

The effect of the number of pores was analyzed by generating RVEs with 2, 5, 10, 20, 50 and 100 pores inside. To avoid the influence of total size of the pores in the RVE, the volume fraction is fixed to 0.05 in each case. The effect of the number of inclusions was analyzed in the same way, too. Fig. 4-17 & Fig. 4-18 shows the results of 50 cases for each number of pores/inclusions, i.e. 300 cases in total. on

average, the rising number of pores will increase the CGR, while the inclusions will decrease it, though exceptions turn up occasionally due to the effect of some certain locations, as analyzed in numerical examples. The chance of an exception appearing, as well as the scatter of the results, is foreseeably smaller when the number of defects is larger, since the size of each defect is smaller and the location is more likely to be uniformly distributed.

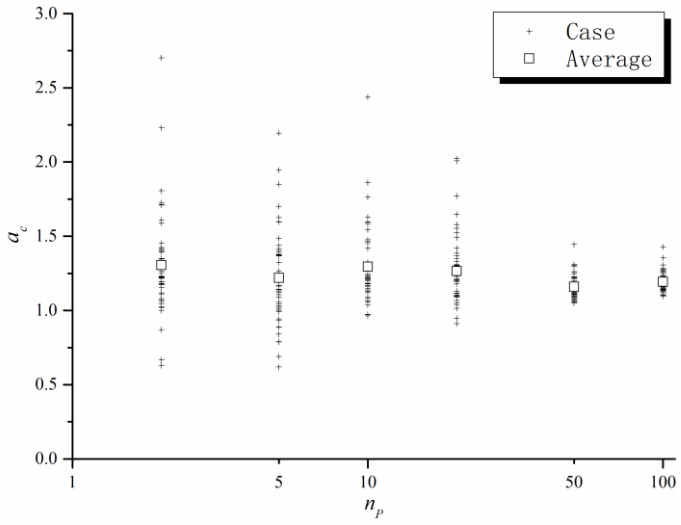

Fig. 4-17 Parametric analysis of a_c with respect to number of pores

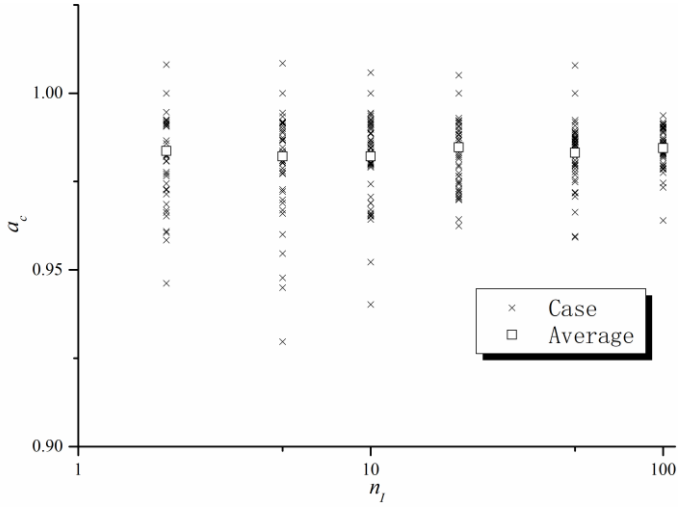

Fig. 4-18 Parametric analysis of a_c with respect to number of inclusions

The effect of sizes and locations on a_c was studied using RVEs including one defect with radii of 0.02, 0.05, 0.1 and 0.12mm. In consideration of the symmetry of the RVEs, inclusions/pores were set to only be located in the upper part of the RVEs. The surface plots of a_c are shown in Fig. 4-19 and Fig. 4-20, in which the crack tip coordinates are (0.3, 1). It is quite clear that the bigger the defects are, the more obvious influence they will produce. In some cases of really small defects, such as the inclusions with radii of 0.02mm, their effect even becomes negligible. Nevertheless, the interaction between size and location makes the effect on the CGR complicated. If the defects are located at the front of the crack tip, it is clear that the stiffer inclusions ($E_I > E_M$) will slow down the crack growth ($a_c < 1$), while the pores ($E_I << E_M$) will accelerate the crack growth ($a_c > 1$). However, the defects seem to have an opposite effect when they are located at the rear of the crack tip. In the cases of relatively bigger defects, such as the pores with radii of 0.12mm, the surface plots become quite steep, as shown in Fig. 4-19 d), which means these pores will have a completely different effect on CGR due to their location.

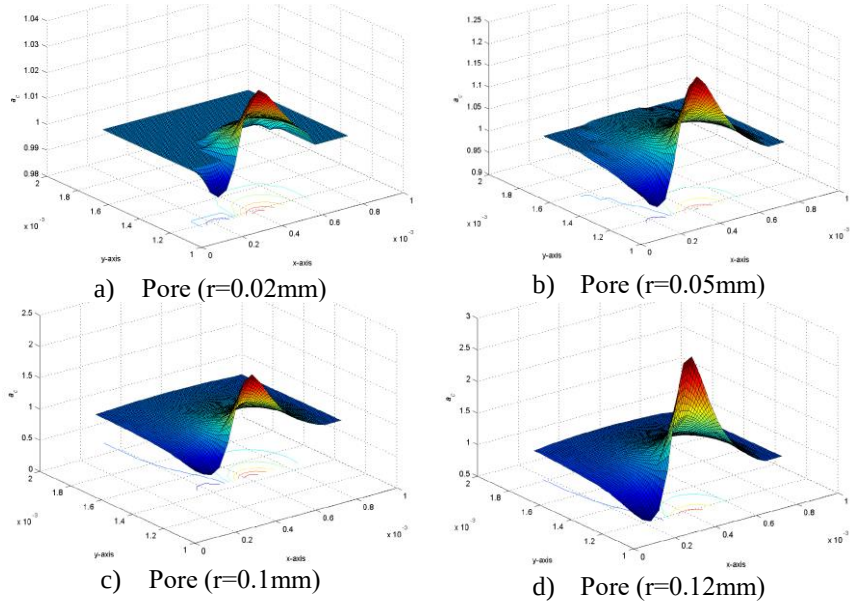

Fig. 4-19 Parametric analysis of a_c with respect to pore sizes and locations

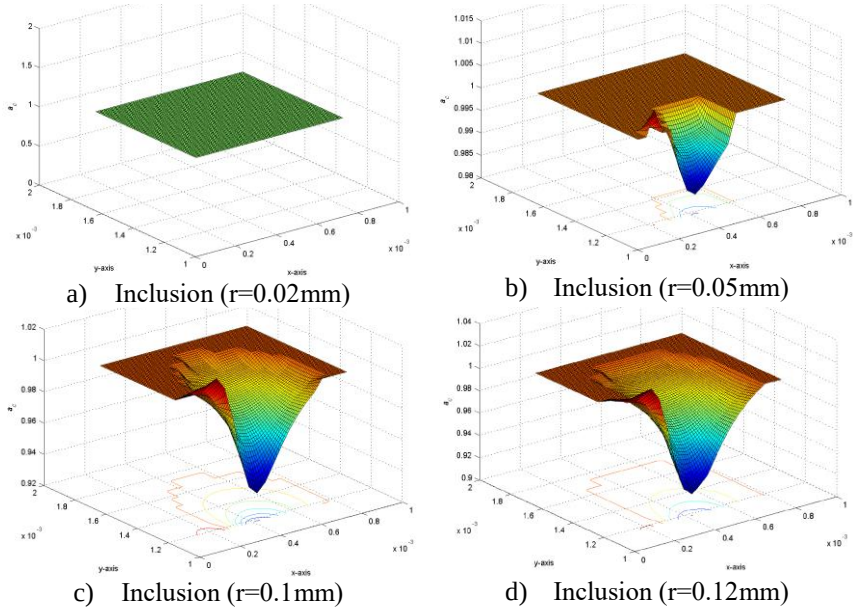

a) Inclusion (r=0.02mm) b) Inclusion (r=0.05mm)

c) Inclusion (r=0.1mm) d) Inclusion (r=0.12mm)

Fig. 4-20 Parametric analysis of a_c with respect to inclusion sizes and locations

4.3.3.3. Weld geometry

The effect induced by the weld geometry should be verified as well, since the stress concentration caused by it will affect crack growth length. A benchmark study is given in Fig. 4-21 to show that the homogenization factor a_c is independent of the flank angle. By applying a tensile stress of 100 MPa, the relative difference of a_c between a homogenized RVE with and without a flank angle is only 1.76%.

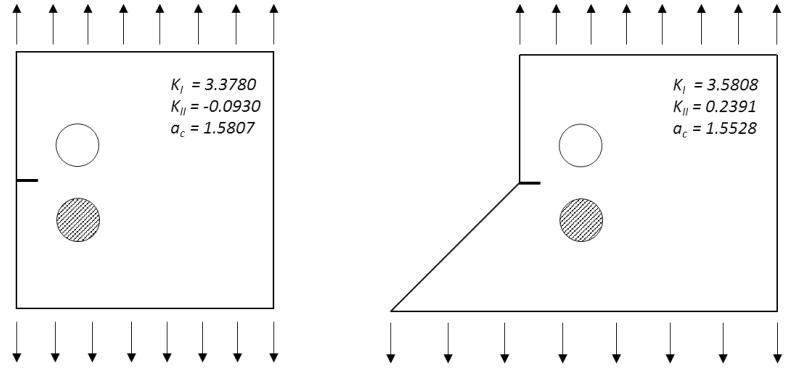

a) RVE without flank angle b) RVE with flank angle

Fig. 4-21 Comparison of a_c in RVEs with/without flank angle (unit: MPa√m)

According to all the parameters studied above, a_c is concluded as a function of defect-related parameters only, expressed as follows,

$$a_c = f(n, S, L, E) \tag{4-4}$$

where n is the number of defects; S is the size of defects; L refers to the location of defects; and E is the elastic modulus of inclusions.

4.4. Results and discussions

Due to insufficient knowledge on the weld defects of OSDs, the homogenization is based on the following hypotheses:

1) To consider the heterogeneity of the defects, a representative volume element (RVE) of rectangular shape (2mm × 1mm) was developed to describe the HAZ around the weld toe of OSDs. Pores and inclusions inside the selected area were simulated, while the possible defects out of this area were neglected. This may lead to a slight error as these defects will affect the crack only marginally.

2) The pores and inclusions were circular in shape with diameters ranging from 20μm to 90μm, according to the fatigue test and to Zerbst et al. (2012). The number of pores and/or inclusions in the model was limited to 10, as they were just occasionally observed in the fractography analyses of the test. To consider the randomness of their locations, sizes and numbers, the corresponding parameters were considered to be uniformly distributed random variables.

3) The initial crack was located at the fusion zone of the rib-to-deck weld toe, with a length of 0.1 to 0.3 mm, according to the fatigue test and some reports (Zhou, Shi, et al., 2016). As the initial crack has a size that is clearly larger than several times of grain sizes, it can be assumed to grow in a mechanical way that follows the Paris law.

According to the aforementioned hypotheses, RVEs were generated and homogenized. Results were given in Fig. 4-22, in which 2000 RVEs with randomly distributed pores and inclusions were homogenized for different value of a_0. The statistics of the results were also given in Table 4-3. Generally speaking, the average values of a_c are so small that give less than 4 percent difference to C_0, and it will reduce as the crack becomes larger.

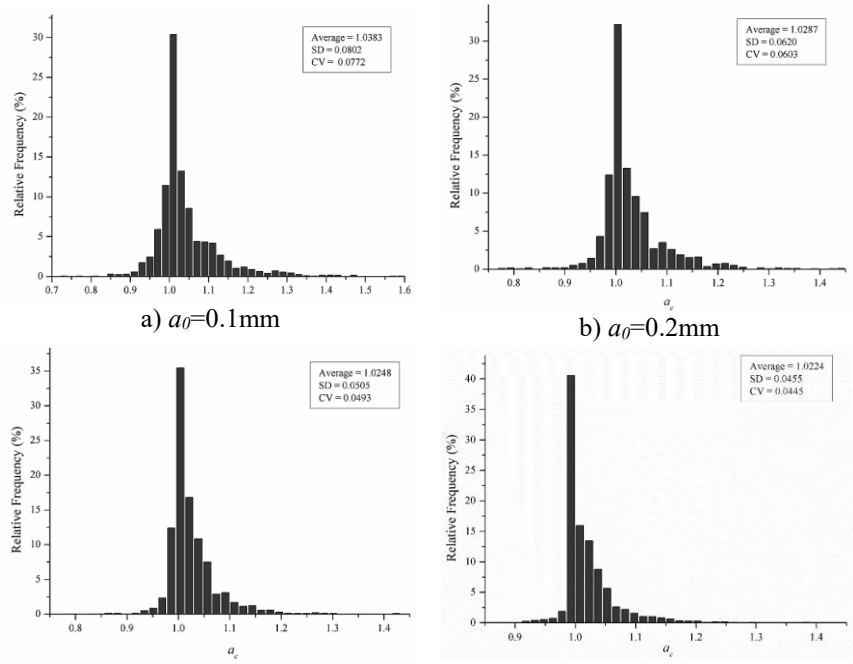

a) a_0=0.1mm b) a_0=0.2mm

c) a_0=0.3mm d) a_0=0.4mm

Fig. 4-22 Distribution of homogenization coefficient a_c for different a_0

Table 4-3 Statistics of a_c

a_0	a_c			
	Average	Maximum	SD	CV
0.1	1.0383	1.5834	0.0802	0.0772
0.2	1.0287	1.4370	0.0620	0.0603
0.3	1.0248	1.4395	0.0505	0.0493
0.4	1.0224	1.4363	0.0455	0.0445

Nevertheless, it cannot be addressed that these weld defects are negligible. With consideration of the weakest part, the standard deviation (SD) and the coefficient of variation (CV) for a_c will play a very important role for large structures like OSDs with a larger scatter bands of fatigue strength. The SD and CV for a_c is larger when a_0 is relatively small, implying better chance to affect the initial crack growth in an appreciable amount. On the other hand, SD and CV for a_c become smaller with larger crack length, and the average value also showed the same trend, implying a decrease of the effect of pores and inclusions. If we look into the different cases for a_0, the homogenization coefficient a_c in Fig. 4-22 d), i.e. the case for a_0 equals 0.4mm, are more centralized around the value of one, as a result of increasing dominance on crack-driving force by the crack itself.

Therefore, the conclusion can be drawn that the influence of the non-detectable weld defects could be ignored on condition that the initial crack is large enough. For the mesoscopic cracks in OSDs, the sizes and locations of the weld defects may affect the crack, especially in the early stage crack growth. In that case, the homogenization method can be applied if the analyses are in the frame of continuum mechanics and LEFM.

CHAPTER 5

MULTISCALE STUDY ON CRACK GROWTH IN WELDED JOINTS OF ORTHOTROPIC STEEL DECKS

5.1. Introduction

The multiscale method is one of the biggest problems on simulating fatigue crack growth on OSDs, as well as other large-scale engineering projects. Therefore, with respect to multiscale problems, two kinds of models, i.e. the concurrent model and the non-concurrent one, are adopted by researches when studying the fatigue behavior on actual projects with numerical ways (Li et al., 2009, Sumi and Inoue, 2011, Sun and Li, 2014, Sun et al., 2016). Generally speaking, the concurrent model may obtain results with higher accuracy. But on the issue of fatigue on large-scale engineering works, the concurrent model is quite difficult to put into practice, in case the geometrical changes caused by tiny fatigue cracks are to be taken into account in the model. Therefore, the non-concurrent model seems to be a better option as it neglected some coupling effects between the cracked part and the whole model.

This chapter is meant to achieve a multiscale method that can be verified by the fatigue test in Chapter 2, and then applied to study the fatigue crack growth on the welded joints of OSDs. According to the fractographic and metallographic analyses in Chapter 2, the initial crack is believed to form due to the fragile coarse grained HAZ, and the depth is about 0.2 to 0.5 mm. That scale is too tiny even compared with the test specimens, not to mention the actual OSDs. Hence, the non-concurrent model was selected, and the boundary conditions that are consistent to the loading in practice were of great concern.

5.2. Analyses on beach marks

In Chapter 2, the preliminary study according to the beach marks were given, with assumptions including the weld toe flank angle, the ratio of attachment width to deck plate thickness, and most importantly, the crack shape. In that way, the SIFs could be calculated using an empirical equation, and the crack growth rate (CGR) could be demonstrated. However, for the purpose of understanding the process of crack growth and eventually predicting the crack growth in practical OSDs, the beach marks, as the most important records on the fatigue crack growth history, are required to be investigated in detail for the first step. Given that as a prerequisite, the multiscale model can be established and validated afterwards.

5.2.1. Visual identification

Fig. 5-1 presents the fracture surfaces by images of the fractured deck plate folded on the specimens. Clearly, only a few beach marks can be observed on such a global view. Especially for the specimens applied with aggressive loadings, only the beach marks in the final stages are visible, due to the relatively rough crack faces compared with the ones induced by mild loadings. Even for the specimens with more beach marks, e.g. Specimen 10 and VII, the first few beach marks can only be identified from local views provided by microscopes. Therefore, it is only possible to measure the depth of the small beach marks, as shown in Fig. 5-2, whilst the length is unknown.

Based on the observation with naked eyes and microscopes, the following remarks can be given with respect to the crack shape in different stages.

1) The early-stage beach marks are sometimes discontinuous, because of the randomness of the microstructures near the weld toe, and the tails at the longitudinal end of the beach marks due to crack merging, as elaborated in Chapter 2.

2) It is difficult to determine the actual shape of early-stage beach marks. As the initial cracks were caused by the intergranular decohesion in the coarse grained HAZ, the depths of them could be uniformly distributed if an ideal line loading is applied along the longitudinal direction. However, it is not the case for the actual loading in the test or in the reality. Thus, the initial crack is not in a full-length of the specimen, instead, the shape is more of a long and shallow semi-ellipse, which is reasonable according to the formation of the initial cracks and some previous studies (Ya et al., 2011).

3) As for the beach marks that are able to analyze in a global view, to determine the actual shapes are still quite complicated. The beach marks for different stages are always so long that their tails at the longitudinal end are hardly making differences. The phenomenon that two cracks initiated at the quarter points merging in the middle, e.g. Specimen VII, VI, and IX, is also significant. In that case, the interaction between cracks will affect the appearance of beach marks.

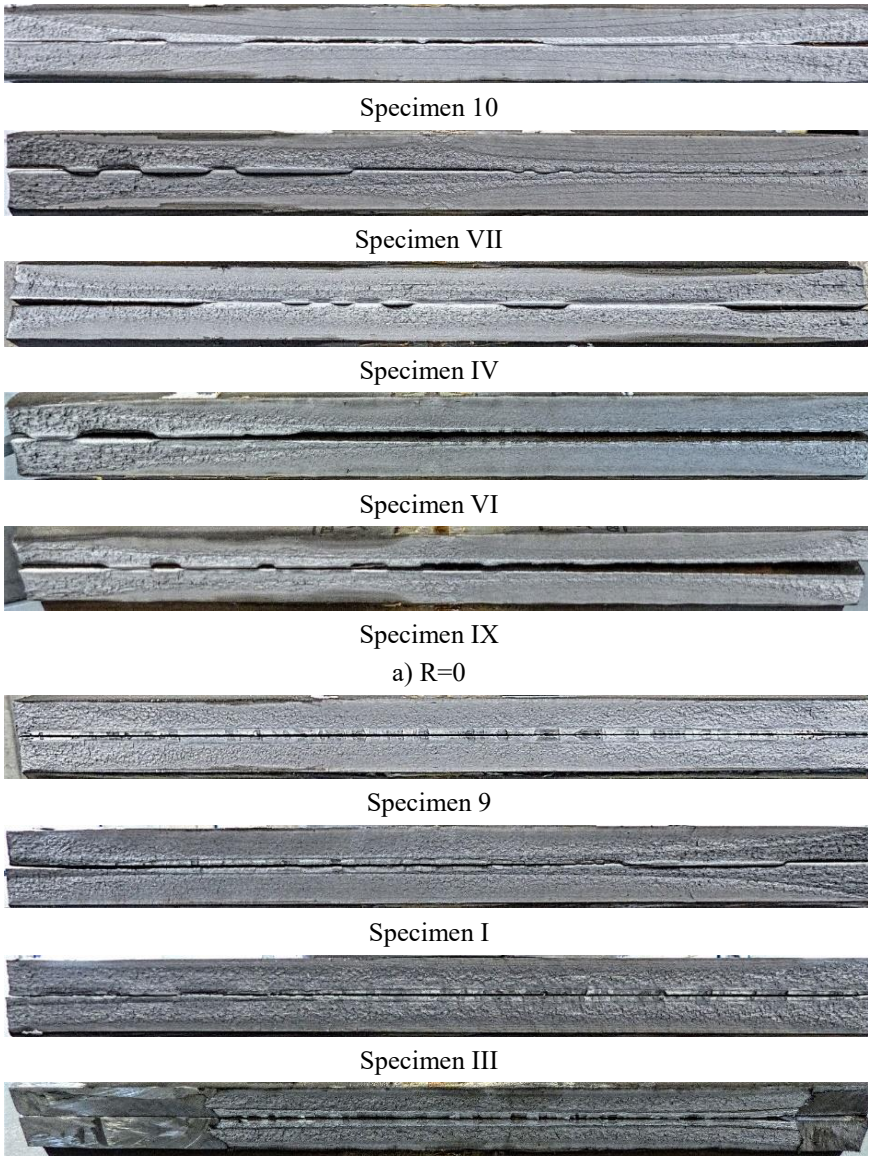

Fig. 5-1 Fracture surfaces and beach marks on test specimens

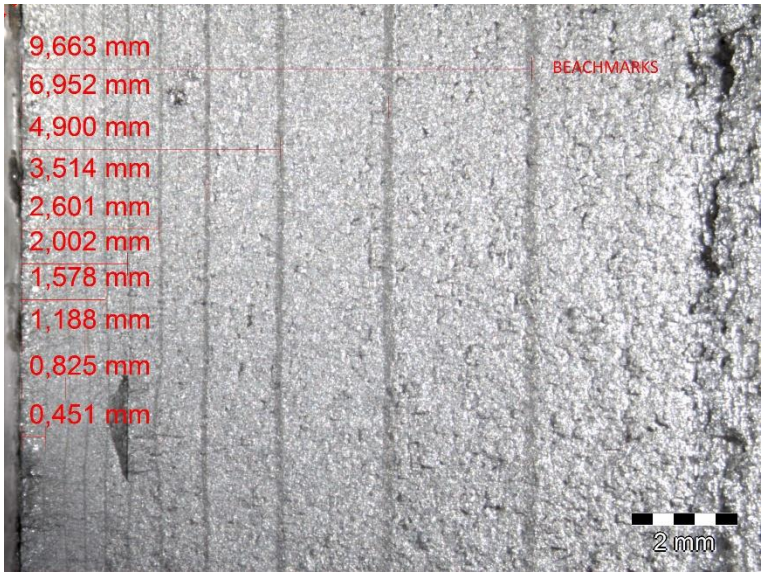

Fig. 5-2 Beach mark measurement by microscope (Specimen 10)

By the above analyses on the shape of beach marks, four steps should be addressed on the process of the crack propagation.

1) A number of tiny cracks initiated because of the intergranular decohesion in coarse grained HAZ.

2) All cracks grown vertically and longitudinally, and merged with each other, which made the crack growth rate in longitudinal direction higher than expected.

3) The main crack formed, whose deepest point was dependent on both the loading and previous processes by the tiny cracks.

4) The main crack grown vertically by the driving force from the SIFs, and longitudinally due to both the SIF driving force and more importantly, the consecutive crack merging.

Specimen 10 could provide a good example to draw an ideal shape of cracks, because of the number of beach marks and more importantly, the clearance for crack shape identification on this specimen. When compared with Specimen VII, it has the crack with more approximately semi-elliptical shape, even though not so accurate while the crack is still small. Based on the analyses above and the beach marks, the ideal shape of the crack face in the fatigue test is demonstrated in Fig. 5-3. It is assumed semi-elliptical, but with apparently extended tails by comparing

to the beach marks obtained by other studies with local loading (Liu, 2010, Kainuma et al., 2016), implying the obvious increment of crack growth rate on the longitudinal direction when applying a line loading. When putting into practical uses for OSDs, it could be regarded as a more approximate shape to the realistic one, as the fatigue cycles are resulted by moving wheels.

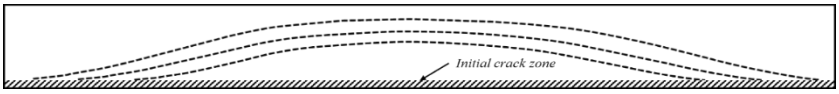

Fig. 5-3 Ideal shape of the crack with consideration of merging of initial cracks

5.2.2. Determination of crack dimensions

Due to the aforementioned problems in determining the actual shapes of beach marks, namely the crack faces, a simplification is applied to give the equivalent main cracks based on the principles given by the IIW recommendations (Hobbacher, 2008). For the first step, the lengths of large beach marks are roughly measured by simply cut the initial crack zone to the edge with slopes same as the visible ends. This will lead to negligible errors on condition that the length is large enough. If two main cracks can be distinguished clearly, the length is determined to be the summary of both lengths. The depths are the measured maximum value. As a result, the equivalent semi-elliptical crack face can be obtained. Fig. 5-4 demonstrates the way by giving Specimen VII as an example. Although the parts in rectangles cannot be recognized clearly, the length is determined with extending the beach marks to the edge. The depth is determined by choosing the maximum one from all sub-cracks, i.e. the maximum value of a_1 and a_2.

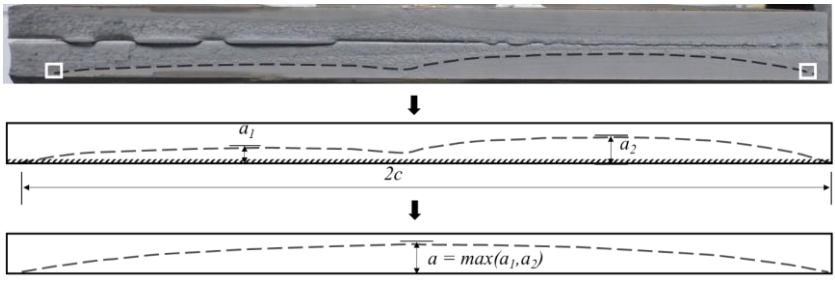

Fig. 5-4 The equivalent semi-elliptical crack on Specimen VII

As for the small cracks indicated by first few beach marks, it is not proper to take the same way of dealing with the large ones, since the initial crack zone could introduce noticeable errors when measuring the length. To get over it, a damage-based method is put forward to fit the lengths with measurable data.

Assuming that only one semi-elliptical crack existed in the specimen, the applied fatigue cycle, N_{app}, will introduce damages, D, by enlarging the area of it, i.e.

$$N_{app} \propto D \propto Area \tag{5-1}$$

As mentioned before, the crack propagation in the depth direction is dominant by SIFs, and thus the fracture mechanics is introduced,

$$\frac{da}{dN} = C\Delta K^m = \ C[F\Delta\sigma\sqrt{\pi a}]^m \tag{5-2}$$

hence,

$$N_{app} = \int dN \ = \int \frac{da}{C[F\Delta\sigma\sqrt{\pi a}]^m} \propto Area \tag{5-3}$$

It builds the relationship between the measurable depth and the area of the crack, although a full-analytical expression is not available due to the unknown and complicated shape factor, F. Based on that, a hypothesis, even not so precisely, can be put forward that the crack area changes with the crack depth in accordance with the power law,

$$Area = p_1 a^{p_2} \tag{5-4}$$

With all the large beach marks whose length and depth are measured, the data was fitted by the curve fitting toolbox in MATLAB, to get the value of coefficients p_1 and p_2, as shown in Fig. 5-5. By introducing the area formula for semi-ellipse to Equation (5-4), the length of the small beach marks can then be achieved by extrapolation.

$$Area = \pi ac/2 = 180.1a^{1.163} \tag{5-5}$$

It is worth to mention that the fitting excludes all specimens under load ratio of -1. It is partly because the first few beach marks were barely seen even in microscope. But more importantly, because of the aggressive fatigue load, the distinguishable ones always reached the longitudinal end of specimen. Therefore, the shape should not be considered as semi-elliptical anymore, and the behavior is believed to be different as well. In the same manner, the validation of the multiscale study in next sections is carried out with respect to the specimens under load ratio of zero only.

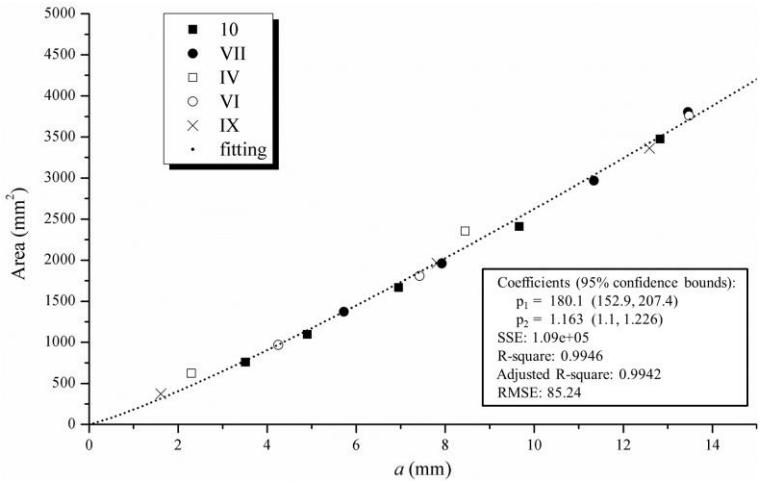

Fig. 5-5 The curve fitting on the crack area varies with the depth

5.3. Numerical model of fatigue test

5.3.1. Macroscopic model

With respect to the fatigue test setup, a macroscopic model was firstly built in SAMCEF, as shown in Fig. 5-6 a). The element type used was solid element, and the total number of elements was 419 380. For modelling the boundary conditions precisely, the contact functions were defined between the specimen, the supports and the loading bar. However, the model was not possible to compute even using XFEM, since the complex contact functions of the model make the computation too heavy to conduct.

Therefore, another model was built with the simplified boundary conditions, as shown in Fig. 5-6 b), and a coarser mesh was used to reduce the total element number to 144 966. The supportive system was modeled as in Fig. 2-4a), which means the bolted support on the left was set to be fixed deformation on all directions on a facet, and the simple support on the right was a fixation on the longitudinal and vertical directions on a line. The load was defined according to the results from the previous model rather than simply applied a line loading. The reason was that the load distribution on the specimen was not uniform due to the deformation of the loading bar. Also, it was not even on a same transverse location of the top and bottom face of the deck plate, due to the deformation of the specimen itself. The applied load on the simplified model is given in Fig. 5-7. By applying this loading, the sensitivity check on the simplified model was conducted, where

the maximum displacement was slightly reduced by less than 1% (from 5.04 mm to 4.99 mm).

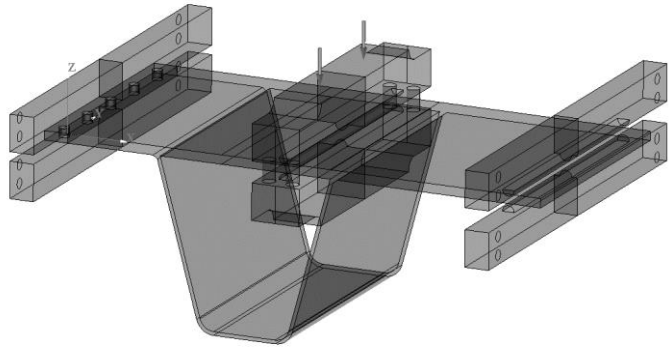

a) Model according to the test setup

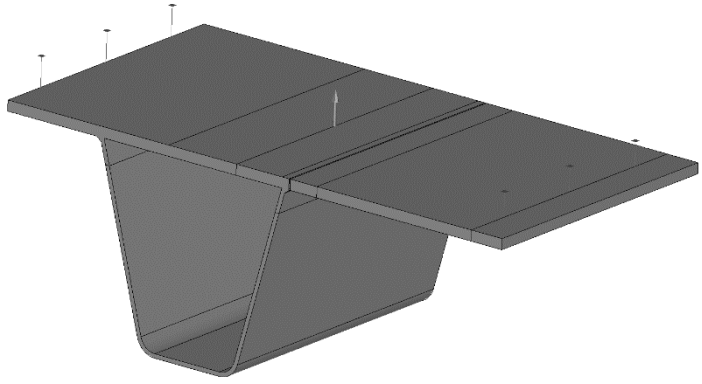

b) Simplified model

Fig. 5-6 Macroscopic model in SAMCEF

With the XFEM module in SAMCEF, a user-defined XFEM domain that contains a crack can be defined in the model, and the mesh around the crack will be refined in an adaptive way to generate elements that are fine enough to calculate the SIFs along the crack front. Ideally, it is possible to verify the test based on all beach marks achieved in this way. Nevertheless, even with the simplified model, the computations were still too heavy to conduct for small cracks in early stages. The main reason could be attributed to the shape of initial cracks, which is shallow but long, thus requires an enormous number of elements in the XFEM domain. Fig. 5-8 presents the refined mesh of the XFEM domain for a semi-elliptical crack with

depth of 2mm and length of 128.4 mm, according to one beach mark on Specimen 10. It can be seen that the element shape is converted into tetrahedra for adaptive refinement first, and the region around the crack, especially the crack front, is refined. For an initial crack that is less than 0.3 mm in depth and more than 90 mm in length, which is in correspondence with another beach mark of Specimen 10, the density of the elements would be too high to achieve. Since the XFEM has already provided the advantage by allowing the crack body to intersect the elements, the refinement of mesh is only determined in accordance with the requirement of stress field around the crack front. Even with this benefit, the macroscopic model was only feasible for the beach marks whose depths were larger than 1.5mm. It therefore implies the necessity to build a multiscale way on this issue, especially aiming at the early-stage cracks.

Attempts were given to solve the cases of early-stage cracks in different ways. Among them, the empirical equation by Bowness and Lee (2000) adopted in the preliminary analyses was not the best option. That is because one of the crucial factors, i.e. the nominal stress, is defined based on the assigned bending moments in the equation, which is not the case for our fatigue test. Also from a perspective for the practical use in the next step, the nominal stress is difficult to determine for the actual projects, too. Eventually, two alternative ways with respect to multiscale concerns were considered: i) a sub-model based way; ii) a non-concurrent model based way.

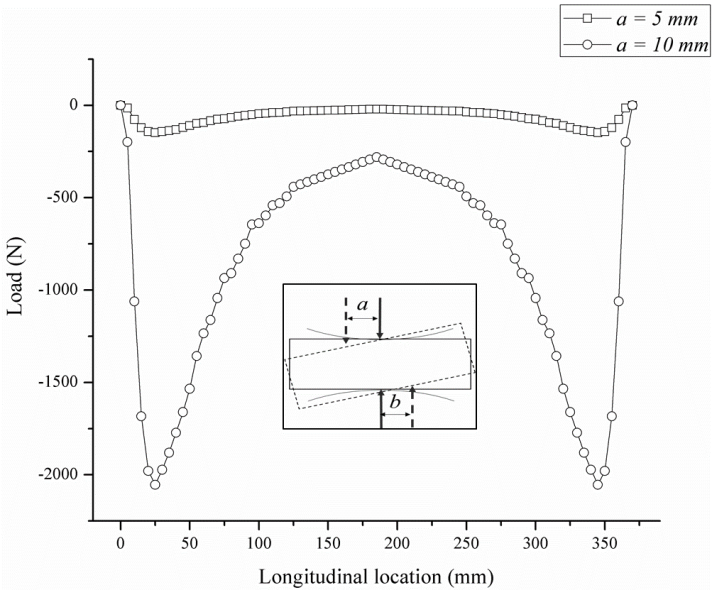

a) On top face

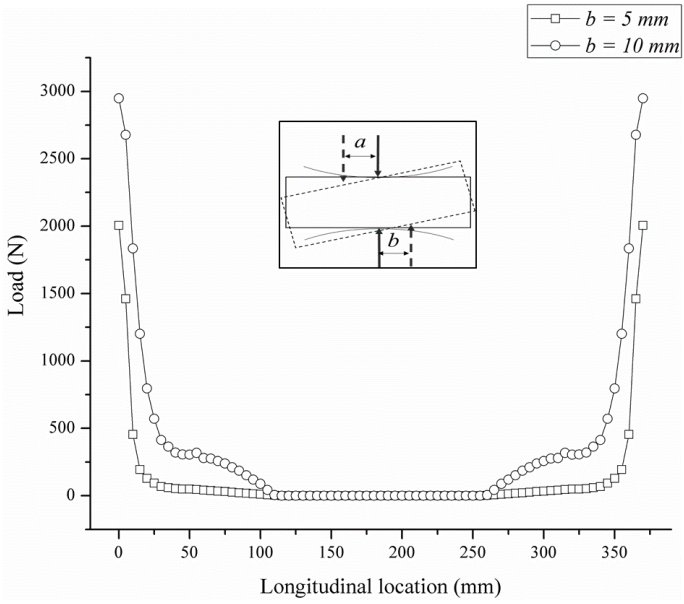

b) On bottom face

Fig. 5-7 Load distribution on deck plate

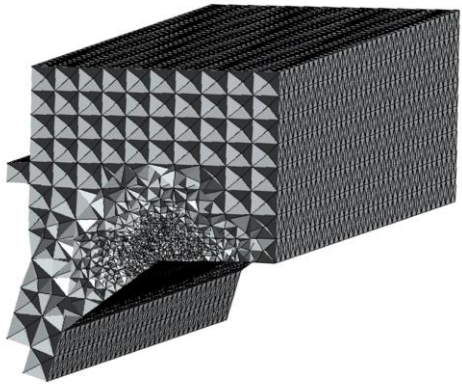

Fig. 5-8 The mesh refinement around a crack of 2mm depth in the XFEM domain

5.3.2. A sub-model based multiscale method

To study the early-stage cracks, a sub-model based multiscale method was adopted in the first place. By introducing the displacement extracted from the macroscopic model to a sub-model, the feasibility of the calculation can be improved when compared to a completely-refined model.

For the first step, the macroscopic model was modified by cutting out the boundaries of sub-model to make sure that there were nodes on them, as shown in Fig. 5-9 a). The sub-model could be built with the XFEM program afterwards, in correspondence with this small cracked region in the macroscopic model. The sub-model was built in two-dimensions for the sake of efficiency, and more importantly due to the unaffordable fine mesh required in three-dimensions, as was already checked by the macroscopic model. With respect to the requirements of beach marks to be calculated by the sub-model, the dimension of it was set to be 2 mm × 2mm (the extra length in x-direction due to the flank angle is not included). Since the sub-model did not contain random defects, the adaptive mesh presented in Fig. 4-2 was not employed. Instead, a fine mesh with the element size of 10 μm was used, lead to at least 40,000 elements in the sub-model.

The boundary conditions of the sub-model, namely the forced displacements, were realized in the same way as classical FEM does, by multiplying big numbers on diagonal elements when forming the global stiffness matrix. It should be remarked that in a sub-model, the results are significantly dependent on these boundary conditions, which means the displacement obtained by the macroscopic model have to be as precise as possible. Thus, the macroscopic model should include cracks same as the sub-model.

Afterwards, the displacements on the section for the deepest point of the crack front were applied on the sub-model. As shown in Fig. 5-9 b), the boundaries of sub-model are presented by the bold lines, and the displacements of all nodes on them are interpolated according to the that of nodes on the macroscopic model, i.e. the blue-dotted ones on Fig. 5-9 b). As a two-dimensional model, the sub-model is assumed to be in plain strain status to provide an approach that considers the out-of-plane length for the crack.

To verify this method, cases with different crack depth, a, and length, c, were calculated. For instance, the crack noted as *a0.3c3* refers to a crack with 0.3 mm depth and 3 mm length. Firstly, four cases, i.e. *a0.3c3, a0.3c5, a1c10, a1c20*, were compared. The stress field around the crack tip for case of *a0.3c3* is given in Fig. 5-10 as an instance. The obtained SIFs are given in Table 5-1, in which the results obtained by sub-model are always much larger than that by SAMCEF model. The reason is that the forced displacements on boundaries for the sub-model were linked to those on the section of deepest crack front in the macroscopic model. As the plain strain status was assumed on the sub-model, the displacements were actually exaggerated and lead to larger results. If the results from cases of same depth but different length are compared, i.e. *a0.3c3* against *a0.3c5*, and *a1c10*

against *a1c20*, the difference is minor, which implies that the difference could be negligible when the crack is long enough.

Afterwards, for some beach marks that are able to compute by both macroscopic model in SAMCEF and by the sub-model, the accuracy of this method was checked. Hereinafter, the beach marks are noted by both specimen number and beach mark number. For example, S10BM4 refers to the 4th beach mark identified on Specimen 10. Results from three beach marks are compared, i.e. S10BM4, SVIIBM4, SIXBM2, as shown in Table 5-1. It can be seen that the differences are always around 5%, which are small but still noticeable.

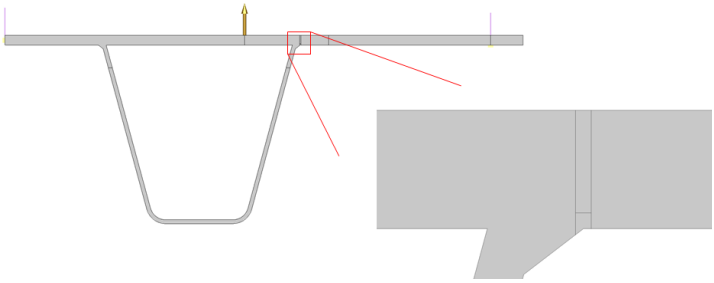

a) The cutout on the macroscopic model

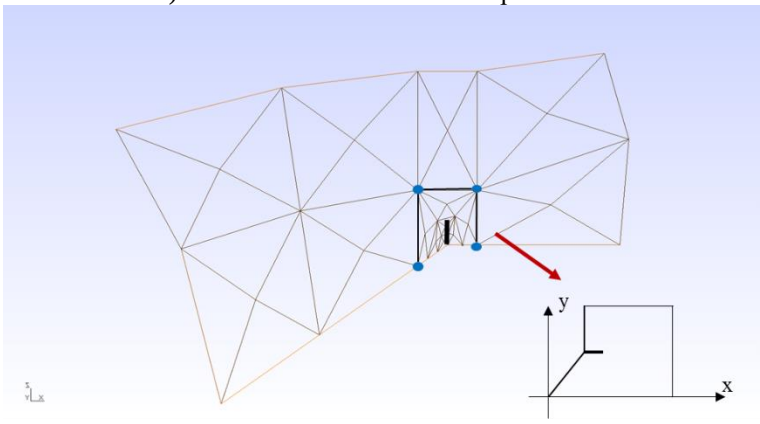

b) The boundary nodes of sub-model

Fig. 5-9 The Sub-model based multiscale method

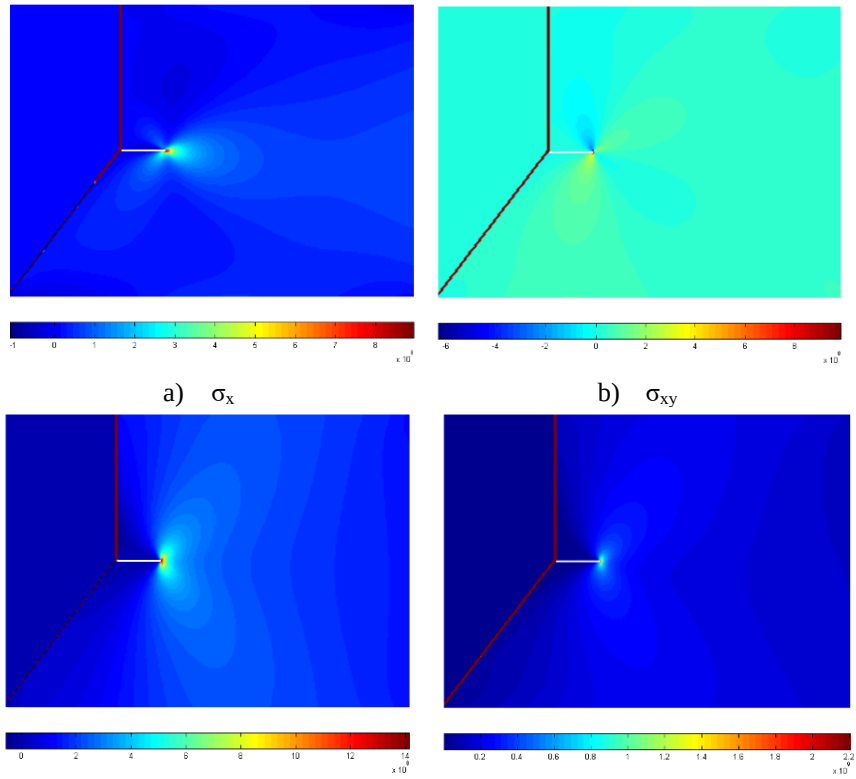

a) σ_x b) σ_{xy}

c) σ_y d) Von Mises Stress

Fig. 5-10 Stress field on a weld toe (corresponding to the bold part in Fig. 5-9)

Table 5-1 Verification of results obtained by sub-model

Crack	Crack dimensions		K (MPa·√m)		diff.
	a (mm)	*c* (mm)	sub-model	SAMCEF	
a0.3c3	0.3	3	10.03	8.6	16.66%
a0.3c5	0.3	5	10.28	8.87	15.89%
a1c10	1	10	13.46	11.73	14.75%
a1c20	1	20	13.84	12.15	13.87%
S10BM4	1.578	123.510	15.15	14.31	5.90%
SVIIBM4	1.551	123.158	14.87	14.15	5.12%
SIXBM2	1.611	147.500	17.05	16.26	4.89%

To summarize, this sub-model based multiscale method could give a solution to the cases for early-stage cracks. But after all, the sub-model is kind of a refined model that zooms in to the macroscopic one, and thus not an independent model.

By any means, the results are largely dependent on the coarse macroscopic model. As it is in two-dimensions, the sub-model will eventually need to choose one section to link to the three-dimensional one, and this essential difference could lead to inevitable errors. Furthermore, the efficiency of this method is not preferred due to the lack of program interface between SAMCEF model and the MATLAB based sub-model.

5.3.3. A non-concurrent multiscale method

Given that the sub-model was not so ideal on this issue, a non-concurrent multiscale method was put forward, with a similar concept as the classical way of calculating SIFs using nominal stresses. The basic idea was to build a non-concurrent model that is independent to the macroscopic one. It is the preferred way in terms of feasibility, efficiency and accuracy, since the macroscopic model failed to deal with the early-stage cracks, and the dependent sub-model lead to some errors.

Firstly, a two-dimensional model with an initial crack was built using the XFEM program, with respect to the full thickness of the deck plate and the weld toe flank angle. It was referred as the XFEM model hereinafter, as given by Fig. 5-11. The boundary conditions in the XFEM model were full fixation of the left edge and application of the bending/membrane stresses on the right edge. In most of the cases, the membrane stresses were so small that can be ignored (Wang et al., 2017), and only the bending stresses were applied to the XFEM model.

The SIFs for crack lengths of 0.1 - 0.5 mm were calculated using the XFEM model, with a bending stress of 100 MPa, as shown in Fig. 5-12. The SIF range for mixed mode crack can be obtained by Equation (3-39) (Tanaka, 1974). Nevertheless, K_{II} is often much smaller than K_I in this case, as shown in Fig. 5-12, and the biquadrate in Equation (3-39) even made it negligible. Hence, the SIF range generally varies with K_I only.

Two benchmarks are presented to validate this XFEM model by comparing the Mode-I SIFs, as shown in Fig. 5-13. To be comparable with the SIFs obtained by stress intensity factor handbook (Murakami and Keer, 1993) and Newman-Raju Equation (Newman and Raju, 1981), XFEM model is built without considering the flank angle, as shown in Fig. 5-13 a). Since Newman-Raju Equation was proposed to calculate the Mode-I SIFs for a semi-elliptical crack, the SIFs presented here were at the deepest point of a crack with aspect ratio of 0.01, which makes it quite close to the plain strain status in other cases. It can be seen that the adopted boundary conditions agreed with the existing studies that using nominal stress, as long as the boundary is far away from the crack. In case that the flank angle is

considered, the distance between the crack and boundaries, *w/2*, should be further verified, since the flank angle itself will lead to stress concentration. Therefore, a set of XFEM models with the flank angle equals 40 degrees and various values of *w/2* were built to calculate and compare the SIFs, as shown in Fig. 5-13 b). Due to the stress concentration, the bending stresses for each XFEM model were determined accordingly. The SIFs obtained by *w/2* larger than 5mm are quite close, indicating the small error using this non-concurrent multiscale method.

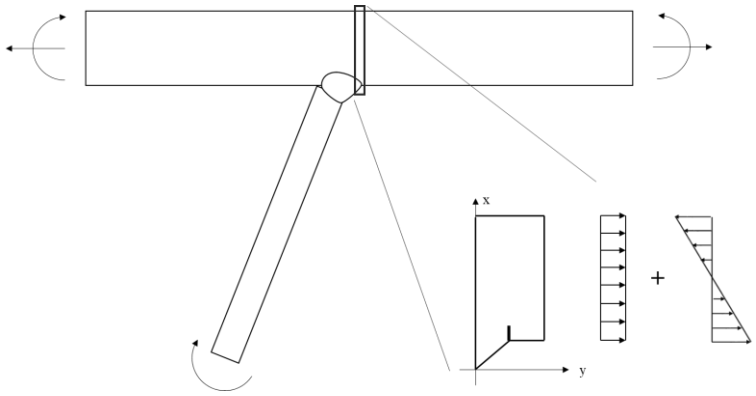

Fig. 5-11 The scheme of XFEM model

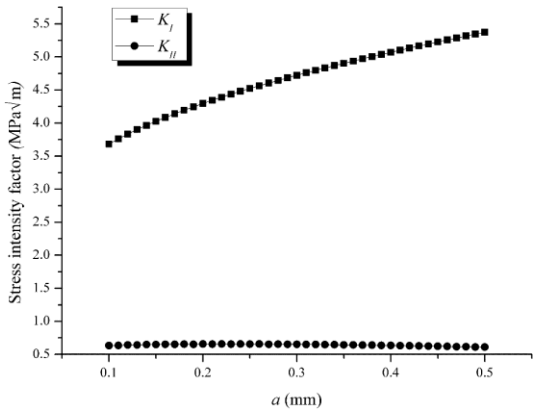

Fig. 5-12 Stress intensity factors under bending stress of 100 MPa

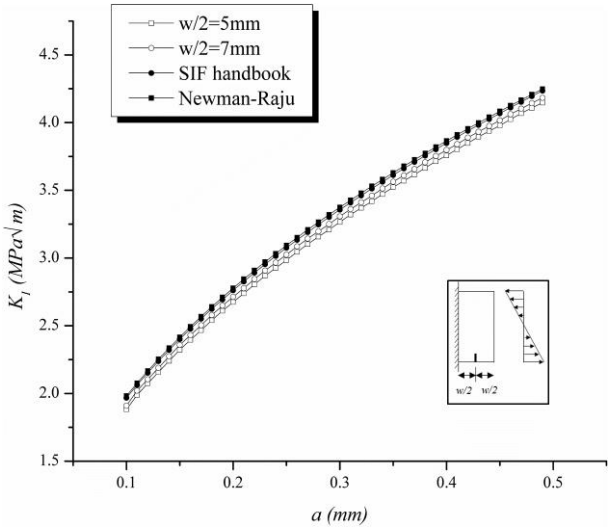

a) without flank angle

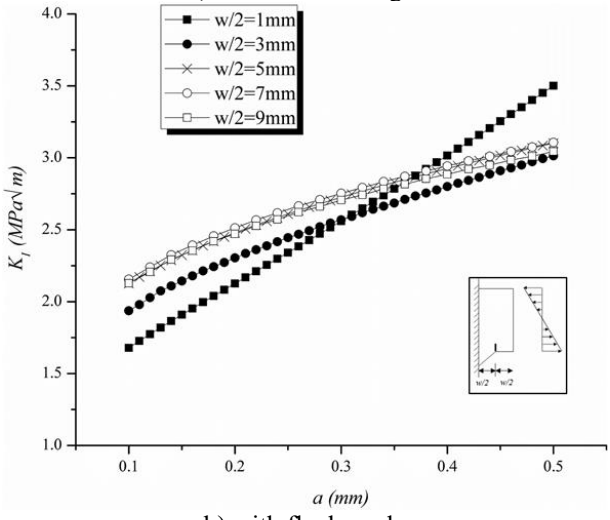

b) with flank angle

Fig. 5-13 Validation of XFEM model

Afterwards, this XFEM model was used to calculate the SIFs for beach marks of early-stage cracks. As the boundary conditions are of great importance in a non-concurrent multiscale method, the model is valid on condition that the crack is small enough so that the bending stress ranges keep almost the same value. Hence the bending stress ranges to be applied should be determined properly. For instance, the strains measured in the fatigue test of Specimen 10 at different positions are shown in Fig. 5-14, in which the smaller strain ranges can be easily distinguished

as beach mark cycles. Therefore, the strain ranges in different stages can be compared. A simple and concise way was to compare the average value of the strain ranges before the *i*-th beach mark, $\Delta\varepsilon_i$, as defined in Fig. 5-14 a). Table 5-2 provides the strain ranges at different gauges till the 4th beach mark, which refers to the crack in a depth of 1.578 mm. It can be observed that the reduction of the strain range is only 2.75% for Strain Gauge BD7 (*w/2* = 11 mm) and 3.82% for Strain Gauge BD6 (*w/2* = 9 mm), which are almost negligible. Given that the crack depth to be calculated by XFEM model was even smaller, the half width of XFEM model, *w/2*, was set to be 8 mm. Hence, the size of it is 16 × 15mm (the extra length due to the flank angle is not included). As it was much larger than the sub-model, the element size of 20 μm was adopted for the sake of computing efficiency, leading to at least 600,000 elements in the XFEM model.

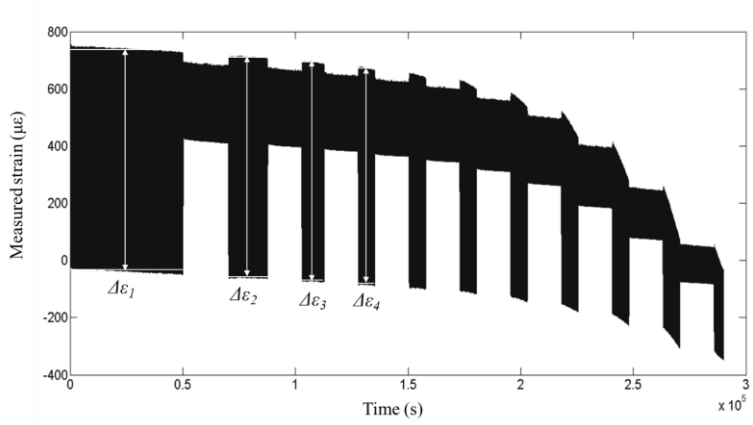

a) Strain gauge BD7 (*w/2* = 11 mm)

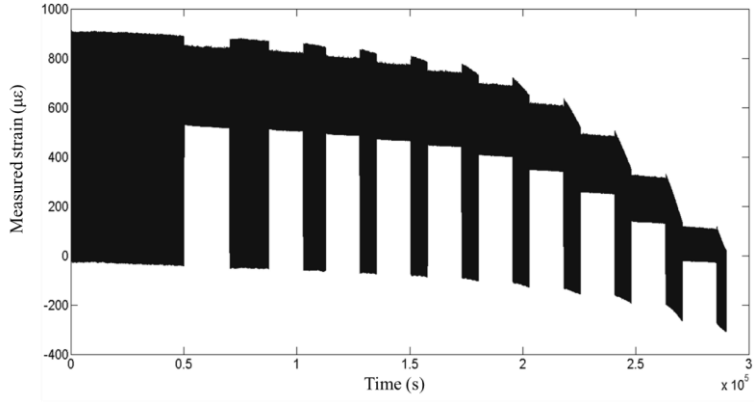

b) Strain gauge BD6 (*w/2* = 9 mm)

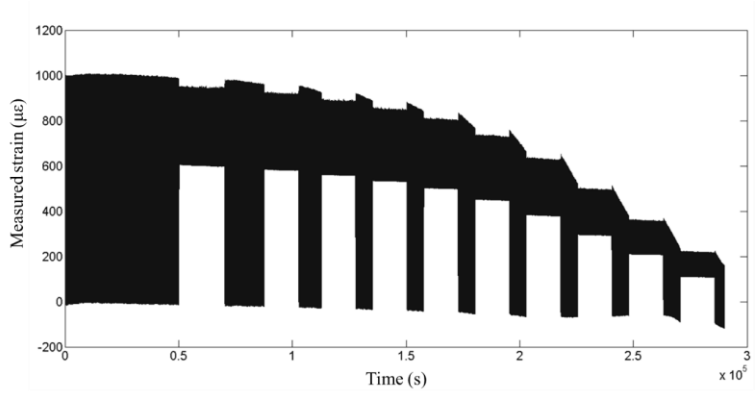

c) Strain gauge BD5 (*w/2* = 7 mm)

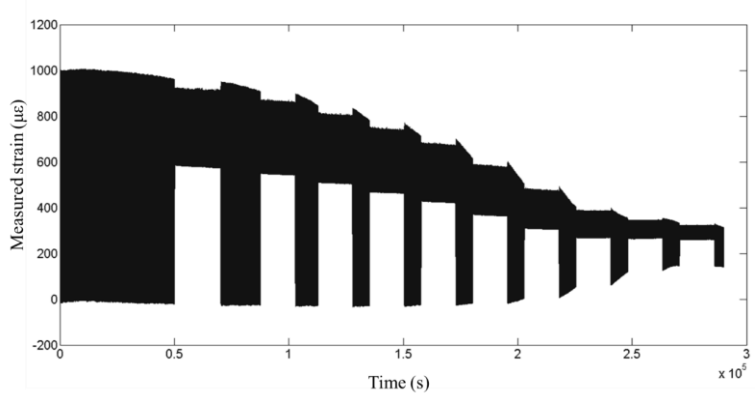

d) Strain gauge BD4 (*w/2* = 5 mm)

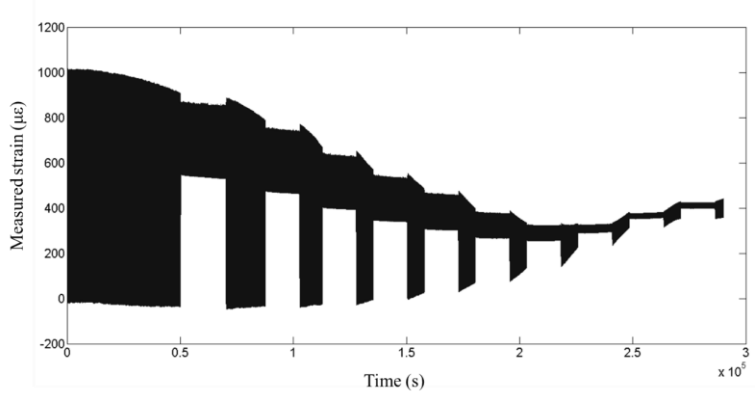

e) Strain gauge BD3 (*w/2* = 3 mm)

Fig. 5-14 Time history of strain measured for Specimen 10

Table 5-2 The reductions of strain range at different strain gauges

Strain gauge	*w/2* (mm)	$\Delta\varepsilon_1$ (με)	$\Delta\varepsilon_2$ (με)	$\Delta\varepsilon_3$ (με)	$\Delta\varepsilon_4$ (με)	$(\Delta\varepsilon_4-\Delta\varepsilon_1)/\Delta\varepsilon_1$
BD3	3	981.134	861.631	738.358	610.268	-37.80%
BD4	5	979.824	934.435	881.065	817.893	-16.53%
BD5	7	984.391	966.775	943.271	913.578	-7.19%
BD6	9	910.794	903.099	891.315	876.024	-3.82%
BD7	11	757.798	753.430	746.284	736.927	-2.75%

In the same manner as the sub-model does, the results of the early-stage beach marks obtained were compared with those calculated by macroscopic model. Again, results of three beach marks, i.e. S10BM4, SVIIBM4, SIXBM2, are presented in Table 5-3. Clearly, the differences are always minus which means it obtained smaller results than that from SAMCEF model. It should be attributed to the boundary conditions that extracted from un-cracked model, which may underestimate the stress concentration. It is also the reason that this method is not applicable on cracks with large sizes. However, the better agreement with the SAMCEF model was achieved when compared to the sub-model way, implying that it is more suitable on this issue. Furthermore, its efficiency is largely increased as being non-concurrent and independent to the macroscopic model. Eventually, the SAMCEF model combined with the non-concurrent multiscale method was applied to calculate the SIFs for all beach marks in the test, as wells as in the practical application when the traffic flow was taken into account in Chapter 6.

Table 5-3 Verification of results obtained by XFEM-model

Beach mark	Crack dimensions		K (MPa·√m)		diff.
	a (mm)	*c* (mm)	XFEM-model	SAMCEF	
S10BM4	1.578	123.510	13.81	14.31	-3.52%
SVIIBM4	1.551	123.158	13.74	14.15	-2.90%
SIXBM2	1.611	147.500	15.70	16.26	-3.46%

5.4. Crack growth in the fatigue test

5.4.1. Analyses based on beach marks

With the macroscopic model and the non-concurrent XFEM model, the SIFs during the fatigue test were calculated with respect to the beach marks, as summarized in Table 5-4. A few remarks should be addressed to obtain these results:

1) The initial crack depth was measured according to the observation of the

intergranular decohesion on coarse grained HAZ, as indicated in Chapter 2. These measured "initial" cracks were marked as beach mark No. 0 hereinafter. The actual cycles spent before is believed fairly small but cannot be confirmed with the test. Also, the depth was not uniform according to the fractographic analyses, and the biggest value was selected to represent the crack tip. Therefore, these values may not be realistic, and are noted by gray blocks in Table 5-4.

2) The lengths of beach marks that are able to measure on the fractures of specimen were noted in bolded numbers. As mentioned before, they were just roughly measurement, and the precision is only 0.5 mm. These values are used in the curve fitting in Fig. 5-5, and the rest lengths are calculated by Equation (5-5).

3) All the beach marks were attempted to calculate with SAMCEF model first, and only the failed ones are then applied with the non-concurrent method. The boundary conditions for these cases were provided by the macroscopic model without cracks embedded. Therefore, only the cases calculated by XFEM models were noted with applied stress ranges in Table 5-4.

4) The SIF ranges were calculated for the entire semi-elliptical edge, namely the crack front, in SAMCEF model, while the ones presented in Table 5-4 are those at the crack tip, i.e. the deepest point on the crack front. Nevertheless, it is not necessarily the position where the maximum value of SIF occurs. Due to the limited size of the specimens, the maximum value could shift from the crack tip to sideways as the crack grows larger. Hence in some cases, the SIF of larger crack even reduced, e.g. S10BM10 compared to S10BM11, SVIIBM11 compared to SVIIBM12, and SVIBM4 compared to SVIBM5.

Accordingly, the shape factor, F, can be obtained if the $\Delta\sigma$ in Table 5-4 is selected as the reference stress,

$$F = \Delta K/(\Delta\sigma\sqrt{\pi a}) \tag{5-6}$$

The results are shown in Fig. 5-15, in which the shape factors for all beach marks, and extra points for cracks smaller than 0.3 mm are presented as well. The results from the empirical formula by Bowness and Lee (2005) are provided as a contrast. However, due to the different definition of the reference stress, the value of F can be different. It is certain that both curves could be shifted vertically to get a better match, but no validation can be found based on the fatigue test. Therefore,

only the trend of both curves can be compared, which turns to be matching with each other when the crack depths are smaller than 8 mm. Afterwards, the aforementioned effect due to the limited size of specimen will affect it significantly. In the end of the fatigue life, the *F* may even go lower than 1, which means the maximum SIFs are completely shifted along with the main direction of the crack growth.

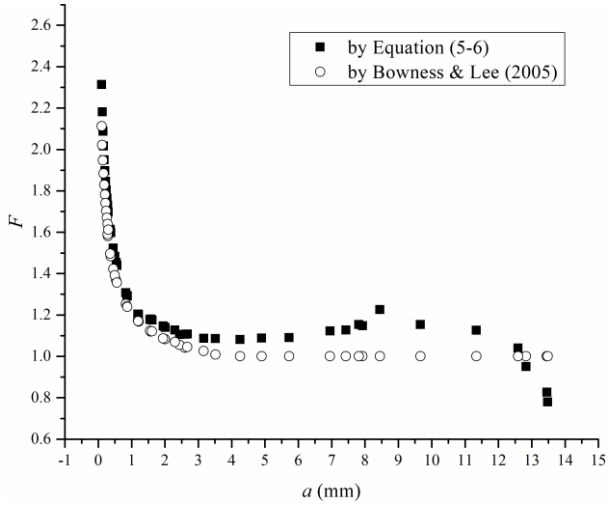

Fig. 5-15 The shape factor *F*

It should be noted that the crack growth rate can only be achieved by the distance between two beach marks and the cycles, and thus is an average value for one period. Therefore, the SIF for each beach mark cannot be used directly when drawing crack growth rate curve, instead, a representative SIF range for one period is required. As the Paris law indicated, the CGR changes with SIF range in power law, and therefore a linearity can be expected when taking the logarithm of them,

$$log_{10}(\frac{\Delta a}{\Delta N})_i = log_{10}C + mlog_{10}\overline{\Delta K}_i \tag{5-7}$$

where *i* refers to the period before the *i*-th beach mark, $\overline{\Delta K}_i$ is the representative SIF range for this period. Being a linearity, it is easy to get $\overline{\Delta K}_i$ as follows,

$$log_{10}\overline{\Delta K}_i = (log_{10}\Delta K_{i-1} + log_{10}\Delta K_i)/2 \tag{5-8}$$

where ΔK_i is the SIF range for the *i*-th beach mark. The results are shown in Table 5-5.

Table 5-4 Summary of calculation on specimens with R=0

Specimen	Beach mark	N	a (mm)	c (mm)	a/c	Δσ (MPa)	ΔK (MPa·√m)
10	0	0	0.288	93.613	0.003	172.21	8.89
	1	100000	0.451	100.699	0.004	172.21	9.87
	2	135000	0.825	111.116	0.007	172.21	11.46
	3	155000	1.188	117.920	0.010	172.21	12.67
	4	170000	1.578	123.505	0.013	\	14.31
	5	185000	2.002	128.390	0.016	\	15.57
	6	200000	2.601	133.987	0.019	\	17.23
	7	215000	3.514	**137.500**	0.026	\	19.65
	8	230000	4.900	**142.500**	0.034	\	23.24
	9	245000	6.952	**152.500**	0.046	\	28.57
	10	260000	9.663	**159.000**	0.061	\	34.60
	11	270544	12.827	**172.500**	0.074	\	32.85
VII	0	0	0.375	97.724	0.004	172.21	9.45
	1	100000	0.539	103.678	0.005	172.21	10.30
	2	135000	0.863	111.944	0.008	172.21	11.60
	3	155000	1.210	118.273	0.010	172.21	12.74
	4	170000	1.551	123.158	0.013	\	14.15
	5	185000	1.947	127.808	0.015	\	15.44
	6	200000	2.436	132.567	0.018	\	16.66
	7	215000	3.162	138.324	0.023	\	18.66
	8	230000	4.251	145.159	0.029	\	21.51
	9	245000	5.725	**152.500**	0.038	\	25.20
	10	260000	7.925	**157.500**	0.050	\	31.18
	11	272000	11.341	**166.500**	0.068	\	36.61
	12	272852	13.453	**180.000**	0.075	\	29.26
IV	0	0	0.498	102.331	0.005	222.21	13.04
	1	50000	0.874	112.166	0.008	222.21	15.03
	2	100000	2.299	**172.500**	0.013	\	21.29
	3	147425	8.447	**177.500**	0.048	\	44.37
VI	0	0	0.362	97.173	0.004	149.99	8.17
	1	300000	1.199	118.098	0.010	149.99	11.07
	2	350000	2.673	134.584	0.020	\	15.23
	3	400000	4.251	**145.000**	0.029	\	18.74
	4	450000	7.425	**155.000**	0.048	\	25.83
	5	484782	13.480	**177.500**	0.076	\	24.05
IX	0	0	0.282	93.259	0.003	194.43	9.99
	1	110000	0.561	104.346	0.005	194.43	11.75
	2	160000	1.611	**147.500**	0.011	\	16.26
	3	235000	7.815	**160.000**	0.049	\	35.15
	4	247762	12.591	**170.000**	0.074	\	40.20

Table 5-5 Summary of the representative SIF ranges and the corresponding CGRs

Specimen	i	$\Delta a/\Delta N$ (m/cycle)	$\overline{\Delta K}$ (MPa·√m)	Specimen	i	$\Delta a/\Delta N$ (m/cycle)	$\overline{\Delta K}$ (MPa·√m)
10	1	1.628E-09	9.37	VII	1	1.641E-09	9.87
	2	1.069E-08	10.64		2	9.261E-09	10.93
	3	1.815E-08	12.05		3	1.732E-08	12.16
	4	2.600E-08	13.23		4	2.273E-08	13.23
	5	2.827E-08	14.66		5	2.640E-08	14.56
	6	3.993E-08	16.38		6	3.263E-08	16.04
	7	6.087E-08	18.40		7	4.840E-08	17.63
	8	9.240E-08	21.37		8	7.260E-08	20.04
	9	1.368E-07	25.77		9	9.826E-08	23.28
	10	1.807E-07	31.44		10	1.467E-07	28.03
	11	3.001E-07	33.71		11	2.846E-07	33.78
IV	1	7.525E-09	14.00		12	2.479E-06	32.73
	2	2.850E-08	17.89	VI	1	2.789E-09	9.51
	3	1.296E-07	30.74		2	2.948E-08	12.98
IX	1	2.540E-09	10.83		3	3.156E-08	16.89
	2	2.100E-08	13.58		4	6.348E-08	22.00
	3	8.272E-08	25.73		5	1.741E-07	24.92
	4	3.742E-07	41.18				

Consequently, the relationship between crack growth rate, *da/dN*, and the SIF range, ΔK, can be drawn for specimens with load ratio of zero in logarithm coordinates, as show in Fig. 5-16. Comparing with the preliminary analyses in Chapter 2, the graph seems to be more converged, especially in the early-stage. It can be seen that the results for Specimen 10 and VII are in good agreement, as they were carried out by the same load history. Additionally, results from these two specimens can be regarded as the references to further analysis and to compare with others, as they contains the most points among all curves. By contrast, results for Specimen IV are showing clearly lower CGR than others. It should be attributed to the fitting for crack shape, where Specimen IV has only two measurable points and thus the least weight in the fitting. As shown in Fig. 5-5, points for Specimen IV also seem slightly further away from the fitting curve than other points do.

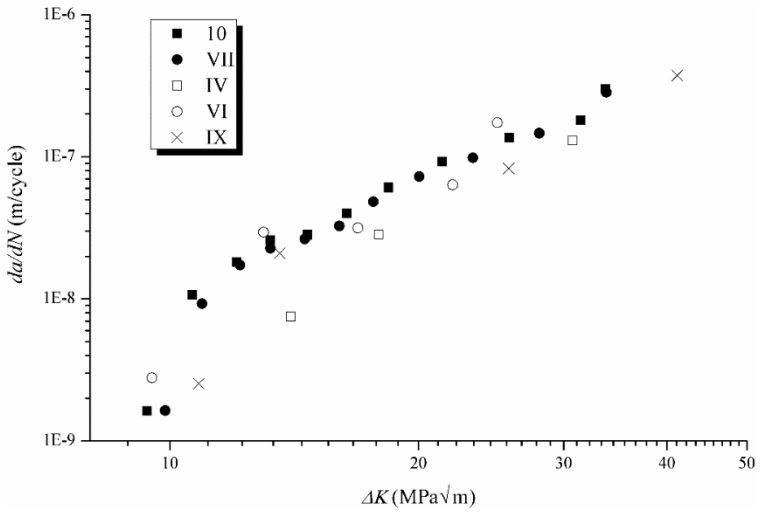

Fig. 5-16 Crack growth rate for specimens with R=0

The different stages of crack growth for welded joints of OSDs can be distinguished by CGR curves as well. Due to limited points on other specimens, analyses are conducted on Specimen 10 and VII only, whose CGR curves contained most points, as shown in Fig. 5-17. Again, the slight reduction in Stage II was observed, leading to the "pit" on curves for both specimens, which can be evidently identified with the help of the linear fit curve provided in Fig. 5-17. Another proof of this phenomenon could be found on the CGRs for Specimen VI in Fig. 5-16, even though the points are not sufficient to reveal the entire process. The stages of crack growth can then be elaborated as follows.

Stage I: the initial crack stage, in which the crack growth rate is low but increases sharply. In this stage, microscopic and mesoscopic heterogeneities will affect the crack growth, and lead to bigger uncertainties than other stages. According to the beach marks on Specimen 10 and VII, this stage lasts till the crack goes to the depth about 0.5 mm.

Stage II-a: the transition stage, in which the increment of CGR, i.e. the slope of the curve, slows down gradually. In the meantime, the uncertainty induced by the microscopic and mesoscopic heterogeneities gets smaller, since two curves are getting closer to each other. In general, the CGRs of pure materials in this stage should be lower than that in the next one, while for welded joints the microstructures in HAZ may lead to higher CGRs. In the end of this stage, as the crack (around 2-mm-depth) is getting further away from the HAZ, the reduction of CGR can be identified on the curve instead of a smooth transition to the next one.

Stage II-b: the stable crack propagation stage. It is the stage that the points of Specimen 10 and VII match with each other perfectly. Therefore, the classical Paris law can be expected to be applied, and the material constants in Paris law can be estimated.

Stage III: the unstable crack propagation stage.

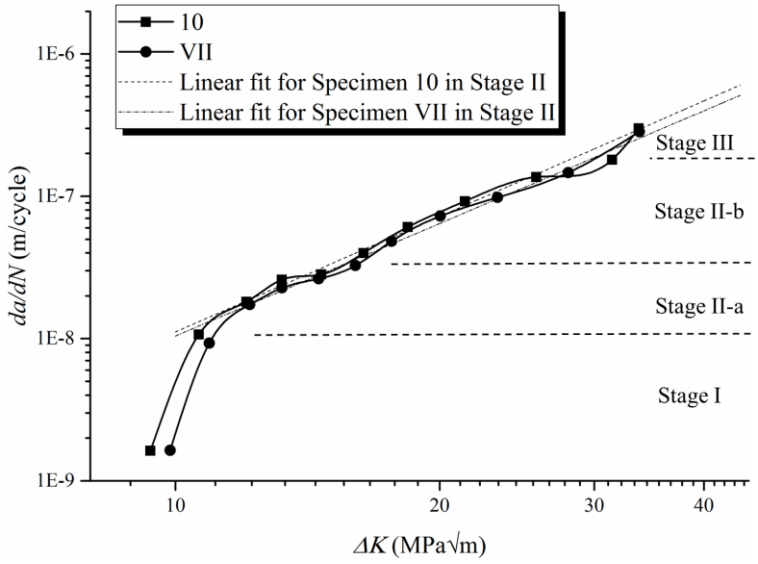

Fig. 5-17 Typical CGR curves and different stages

5.4.2. Material constants estimation

As suggested before, in Stage II-b the crack-tip is away from the HAZ and thus can be assured that crack propagates stably following Paris law during this period. The material constants in Paris law can be estimated by the results, and applied on the prediction of actual welded joints of OSDs. However, it is not hard to notice that the rest points, except the clearly different Stage I, can actually be interpreted by Paris law as well. In that case, the CGRs for other specimens can be used to estimate the material constants, although some errors can be introduced due to the different stages. Hence, two different datasets, i.e. Dataset 1 and Dataset 2, were adopted in the fitting to estimate the material constants. The former one referred to the points in Stage II-b for Specimen 10 & VII, while the latter referred to the points for all specimens by ignoring Stage I. Additionally, as recommended by most of the literature, such as the IIW recommendation (Hobbacher, 2008), BS 7910 (BSI, 2013), the value of Pairs exponent, m, was set to three with some confidence. To be comparable, fittings were carried out based on m equals three or the fitted value.

Hence, four groups of fittings, named as Fit 1, 2, 3 and 4, are given in Table 5-6. Based on Equation (5-7), the curve fitting toolbox in MATLAB was applied to obtain the fitted values of the material constants, as well as the parameters illustrating the goodness of the fitting. The results are shown in Table 5-6 and Fig. 5-18. According to the results, it can be seen that the fittings with Dataset 2 (Fit 3 & 4) are quite close to those with Dataset 1 (Fit 1 & 2), even though the latter ones have better fitting parameters, such as the sum of squared errors (SSE), R-square, and root mean square errors (RMSE). As a result, Fit 3 and 4 provides the material constants that are applicable to most parts of the crack growth process with acceptable errors in fatigue life estimation. It would be quite favored by the actual projects for the sake of simplicity. When comparing the results without fixing m (Fit 2 & 4) to those with fixed m (Fit 1 & 3), the former ones, as can be expected, showed slightly better fitting qualities. Besides, as the curves of Fit 2 and 4 give the higher value of da/dN when ΔK is small, the estimations are more conservative for the critical part of fatigue life, namely the early-stage crack propagation.

Table 5-6 Summary of the fittings of material constants

		Fit 1	Fit 2	Fit 3	Fit 4
Fitting with		Dataset 1*	Dataset 1*	Dataset 2*	Dataset 2*
Coefficients	C	8.511×10^{-12}	1.905×10^{-11}	7.943×10^{-12}	2.570×10^{-11}
	95% confidence bounds	(7.943×10^{-12}, 9.120×10^{-12})	(7.762×10^{-12}, 4.786×10^{-11})	(7.079×10^{-12}, 8.710×10^{-12})	(1.259×10^{-11}, 5.129×10^{-11})
	m	3 (fixed)	2.726	3 (fixed)	2.603
	95% confidence bounds	\	(2.419, 3.033)	\	(2.369, 2.837)
Goodness of fit	SSE	0.0225	0.0155	0.3849	0.2657
	R-square	0.9683	0.9782	0.9287	0.9508
	Adjusted R-square	0.9683	0.9758	0.9287	0.9489
	RMSE	0.0475	0.0415	0.1172	0.0992

* Dataset 1 refers to the points in Stage II-b for Specimen 10 & VII, and Dataset 2 refers to the points excluding Stage I for all specimens

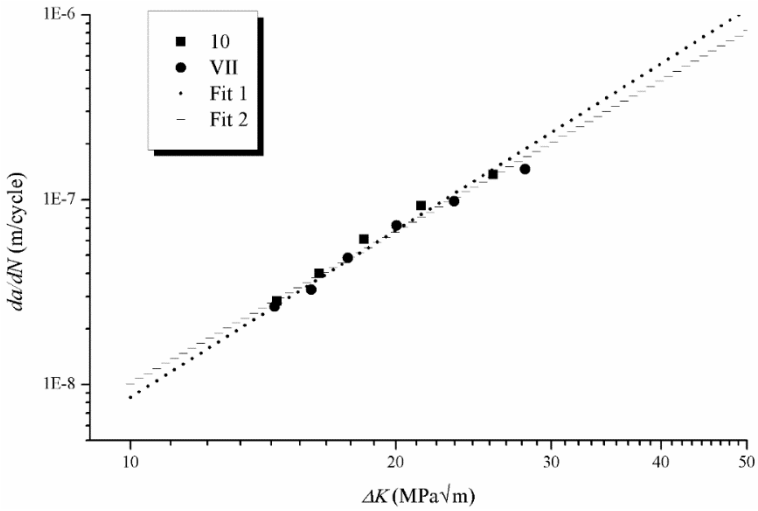

a) for Dataset 1

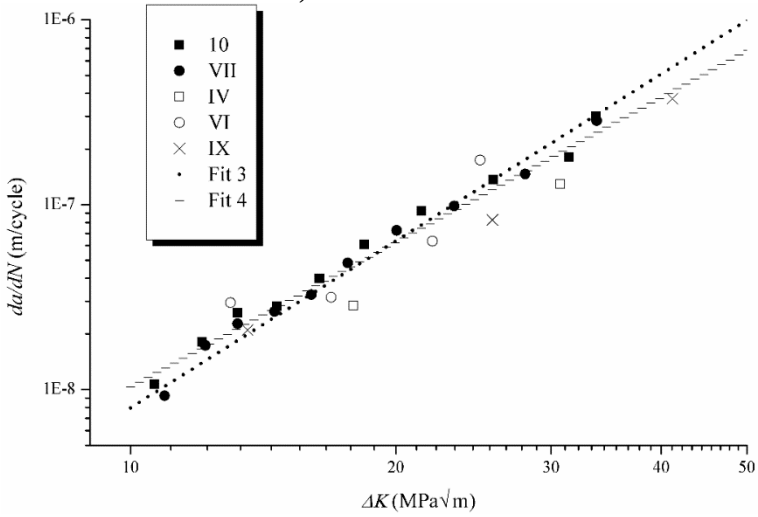

b) for Dataset 2

Fig. 5-18 Curve fitting to estimate the material constants

By estimating these material constants, it is possible to predict the fatigue life of welded joints of the actual OSDs. But prior to that, it is worth to give more discussions on the CGR curves in Fig. 5-17, to get better understanding on the entire process and the advantages/disadvantages of the method applied in this study.

5.5. Discussions

5.5.1. Crack growth simulation

Provided by the above study based on the beach marks, it is curious that if the crack growth can be simulated step by step based on the Paris law. It means to predict the crack path in a quasi-static way with a given initial crack, which is also the method adopted by other studies (Pais, 2011; Kumar et al., 2014; Nagy et al., 2016). In this study, the macroscopic model built in SAMCEF gives the access to conduct this simulation.

Firstly, a semi-elliptical crack with a depth similar to the measured initial crack was embedded in the SAMCEF model. With consideration of the limitation of the computation ability, the crack was 0.2 mm in depth and 6 mm in semi-length, and the length for each crack growth step was fixed to be 0.2 mm. The loading was identical to the one applied on Specimen 10 and VII. In each step of computation, the SIFs on all nodes on the crack front were calculated. The node with the maximum SIF will grow 0.2 mm forward, while the crack growth length for other nodes will be determined according to their SIFs. As the length of each crack growth step being fixed, the crack growth path was not dependent on the material constants in Paris law, which will only affect the crack growth rate.

Fig. 5-19 a) presents the crack front for 45 steps in the crack growth simulation. The coordinates are the same as in Fig. 5-6, where the X-axis is the transverse direction, Y-axis is the longitudinal direction and Z-axis is the vertical direction. The results show that the ratio of the semi-axis length of the crack is changing during the growth, and the crack growth length in depth is generally larger than that in longitudinal direction. After 45 steps, the crack grows to a depth of about 5.5 mm. However, the shape of the crack front cannot meet any beach mark on the specimens. The main reason is, as mentioned before, the crack will grow longitudinally not only because of the SIFs, but also by merging with other cracks. On the other hand, due to the differences in crack shapes, the SIFs cannot be calculated in a correct way as well. Fig. 5-19 b) presents the comparsion of SIFs at the crack tip, namely the deepest point, obtained by the crack growth simulation , with the same applied loadings as on Specimen 10 and VII. It indicates that the difference is small for the first few steps, but increases significantly afterwards. In the case of crack growth simulation, the SIFs even reduce slightly after several steps. That being said, the maximum value of SIF is not at the crack tip any more at that moment.

Another example was then carried out to show the case of a long crack. The crack was 2 mm in depth and 128.4 mm in length, which was in fact the crack growth based on the beach mark S10BM5. The length for each crack growth step was fixed to be 1.5 mm. The loading was identical to the one applied on Specimen 10 and VII.

Fig. 5-20 a) presents the crack front for 13 steps in the crack growth simulation. If the tail part of each crack front was cropped out, the crack front shapes are quite similar to the beach marks given in Fig. 5-3. So it is a clearer example to show the different crack growth between the vertical direction and the longitudinal one, and the same conclusion can be addressed. Fig. 5-20 b) presents the comparsion of SIFs at the crack tip obtained by the crack growth simulation and by the beach marks on Specimen 10 and VII. It shows that the differences are smaller than that in the previous case, since the initial crack is long enough. However, the problem is not solved as long as the longitudinal crack growth is not simulated correctly, and thus the differences still persists and becomes larger after a few steps.

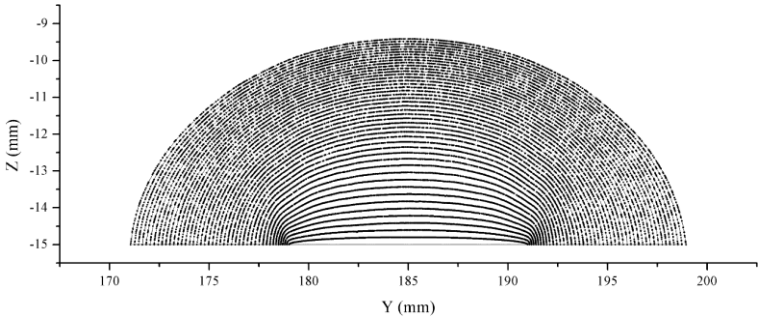

a) Crack front

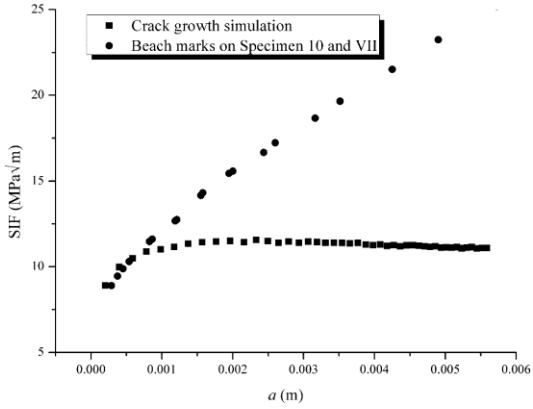

b) Stress intensity factors at the deepest point

Fig. 5-19 Crack growth simulation of an initial crack with 0.2 mm in depth

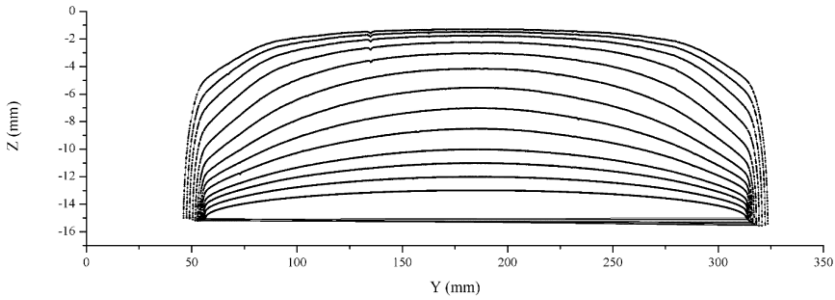

a) Crack front

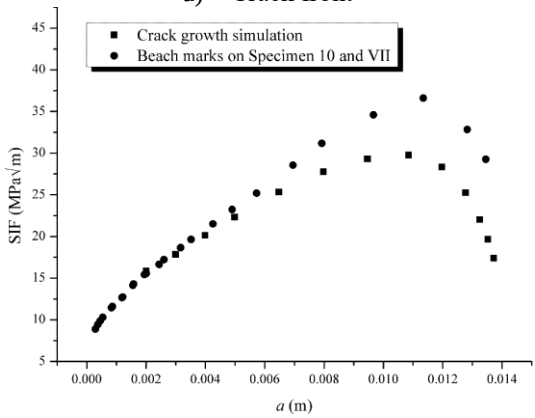

b) Stress intensity factors at the deepest point

Fig. 5-20 Crack growth simulation of an initial crack with 2 mm in depth

To sum up, the simulation on crack growth are not so applicable, since the driving force of the crack growing longitudinally is also dependent on the consecutive crack merging. On condition that the initial cracks along the HAZ of welded joints are not properly determined, the results from the crack growth simulation cannot be accurate enough. In that case, the best option for now is still to analyze the crack growth process based on the beach marks, or based on the fitted equation for crack shapes, e.g. Equation (5-5).

5.5.2. Early-stage cracks

In the early stages, the cracks have different CGRs from Paris law, as well as the larger randomness in CGR, e.g. Stage I in Fig. 5-16. By looking into the beach marks and the cycles presented in Table 5-4, the process of early-stage crack growth is surely of great importance, since the largest part of fatigue life is consumed in this period.

One similar concept in literatures is the short crack, which is difficult to give a widely-accepted definition to distinguish from long cracks. Bogdanov (2014)

suggests that the physically short crack for metals is between 0.05mm and 0.5mm, which is very close to the Stage I crack in our fatigue test. Whilst on the issue of fatigue of OSDs, Chen (2010) implied the size of short cracks is generally in the range between 0.1mm and 1mm. The discussion provided here is mainly concerned about the different CGR and the randomness in Stage I in Fig. 5-16, and thus the size is generally in the range between 0.1 mm and 0.5 mm. With the limited test data, it has to be noted that these values are determined without intensions to draw a conclusion.

On the different behavior of crack growth in Stage I, one popular way is by introducing the threshold value of SIF, which lead to the modified form of Paris law as follows,

$$\frac{da}{dN} = C(\Delta K - \Delta K_{th})^m \tag{5-9}$$

where ΔK_{th} is the threshold value of SIF. However, it seems not a best choice in this study, since the introduction of ΔK_{th} can only shift the CGR curves horizontally in a logarithm coordinate system. The values for other constants, i.e. *C* and *m*, will change therewith, but still incapable of taking the Stage I into account.

Therefore, more attentions should be paid to the substantial feature for it, i.e. the microstructure in HAZ. The effect of microstructures is believed to connect with the hardness, which are measured as elaborated in Section 2.4.4 of Chapter 2. According to Remes et al. (2012), the Coffin-Manson formula can be applied to investigate the short crack growth with respect to hardness. In the first place, the Vickers hardness obtained by the test can be converted to the Brinell hardness,

$$\mathrm{HB} = 0.9801 \cdot \mathrm{HV}^{0.9941} \tag{5-10}$$

where HB is the Brinell hardness; HV is the Vickers hardness. And the fatigue strength coefficient, σ_f', and the fatigue ductility coefficient, ε_f', can be estimated by,

$$\sigma_f' = 4.25\mathrm{HB} + 225 \tag{5-11}$$

$$\varepsilon_f' = \frac{1}{E}(0.32\mathrm{HB}^2 - 487\mathrm{HB} + 191000) \tag{5-12}$$

Accroding to Noroozi et al. (2005) and Bogdanov (2014), the damage calculated by Coffin-Manson formula can be expressed in the same way as CGR in Paris law, and the Paris constant *C* and the exponent *m* for Stage I cracks are given by,

$$C = 2\rho^*\left(\frac{\Psi_1^2}{4\pi\rho^*\sigma_f'^2}\right)^{-\frac{1}{2b}} \tag{5-13}$$

$$m = -1/b \tag{5-14}$$

where ρ^* is the elementary material block size; Ψ_1 is the averaging constant corresponding to the 1st elementary block; b is the fatigue strength exponent.

With respect to the crack path, the hardness test results at fusion zone (FZ) and the sites that are 0.3 mm and 0.6 mm away from the FZ are adopted to estimate the Paris constant C and the exponent m for Stage I cracks. The results of the estimation are given in Table 5-7.

Table 5-7 Estimation of material constants for Stage I

HV test site	Specimen 10			Specimen VII		
	Fusion zone (FZ)	FZ+0.3mm	FZ+0.6mm	Fusion zone (FZ)	FZ+0.3mm	FZ+0.6mm
E	2.1×10^5	2.1×10^5	2.1×10^5	2.1×10^5	2.1×10^5	2.1×10^5
ν	0.3	0.3	0.3	0.3	0.3	0.3
HV	297	274	258	353	346	301
HB	281.47	259.80	244.72	334.21	327.62	285.24
σ'_f	1421	1329	1265	1645	1617	1437
b (Remes, et al., 2012)	-0.09	-0.09	-0.09	-0.09	-0.09	-0.09
ε'_f	0.3775	0.4099	0.4333	0.3047	0.3133	0.3720
Ψ_1 (Noroozi et al., 2005)	1.633	1.633	1.633	1.633	1.633	1.633
ρ^* (Bogdanov, 2014)	4E-5	4E-5	4E-5	4E-5	4E-5	4E-5
C	2.181×10^{-19}	4.592×10^{-19}	7.953×10^{-19}	4.286×10^{-20}	5.187×10^{-20}	1.926×10^{-19}
m	11.111	11.111	11.111	11.111	11.111	11.111

It indicates that the Paris constant C for Specimen 10 is always bigger than that for Specimen VII, resulting in higher CGRs for Specimen 10. It agrees with the observation in the test. However, as some parameters used are borrowed from other studies, these results are not comparable to the measured ones. Furthermore, because of the limited points in Stage I obtained in the test, it is not possible to fit these parameters as well. Therefore, the only conclusion can be drawn here is that the hardness in a small region of HAZ will affect the CGR, and the CGR will be lower when the hardness is greater. It could be the main source of the randomness of CGR in Stage I.

5.5.3. Influence of weld defects

Apart from the different material behavior induced by the microstructures in the HAZ, the weld defects may introduce extra randomness on CGR, especially when the crack is still small, e.g. in Stage I. The homogenization method enables to consider the influence of weld defects, and the results are presented in Fig. 4-22 in Chapter 4. It is worth to emphasize that the results were achieved when Paris component, *m*, equals three, while in Stage I the value can be so different. In that case, if the homogenization method is applied, the homogenization coefficient, a_c, will be changed. According to Equation (4-2) and Equation (4-3), the updated a_c for Stage I can be obtained with the modified *m.*

$$a_c = C_{eff}/C_0 = (\Delta K_{heter}/\Delta K_{homo})^m \tag{5-15}$$

Based on the results in Fig. 4-22 in Chapter 4, the modified values of a_c for Stage I cracks are given in Fig. 5-21, using Paris exponent equals 11.111 provided in Table 5-7.

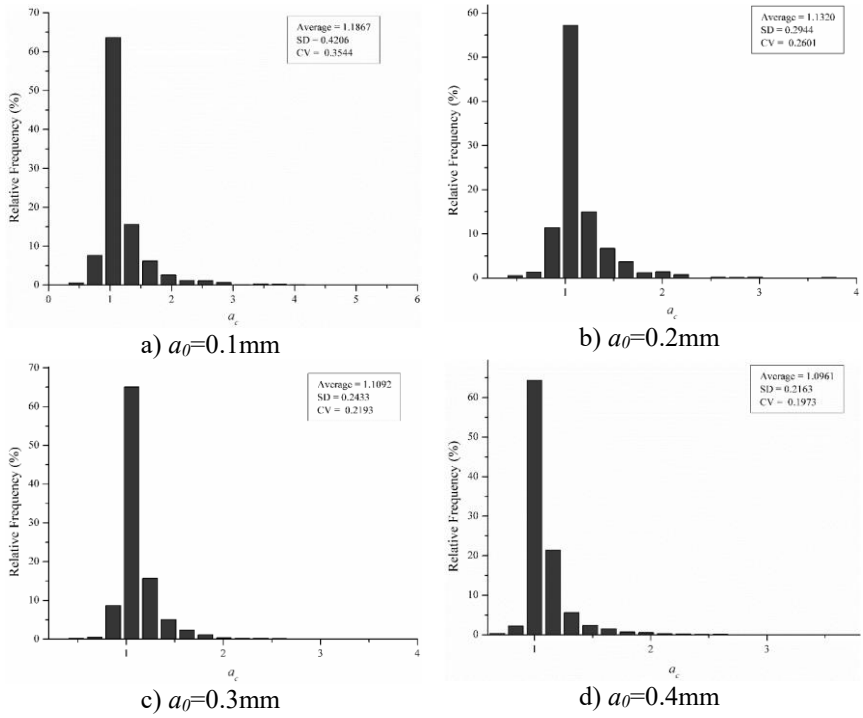

a) a_0=0.1mm b) a_0=0.2mm

c) a_0=0.3mm d) a_0=0.4mm

Fig. 5-21 The homogenization coefficient a_c for Stage I cracks

The results show much greater influence compared to the previous ones with *m* equals three, and thus will lead to larger randomness of CGR in Stage I. To

illustrate the effect, the Paris constant C at 0.3 mm away from the fusion zone in Table 5-7 is taken as an example. And the homogenization coefficient a_c with 95% confidence is applied to show the possible region of CGR in terms of C_{eff}. The results are given in Fig. 5-22. By comparing the original curves and the ones modified by a_c, it is clearly that the two curves are getting close, implying that the randomness is reducing when the SIFs get bigger. On the other hand, the greater difference between two curves with different C_0 implies that the uncertainties induced by the microstructures are still larger than that induced by the weld defects. By any means, the actual dimensions, as well as the spatial distribution of the weld defects, are not yet determined. Therefore, the above discussion is based on the same hypotheses as in Chapter 4, and should be further investigated in the future.

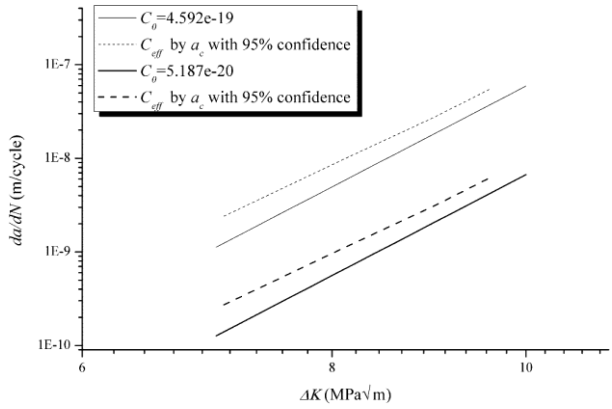

Fig. 5-22 The CGR for Stage I cracks affected by weld defects

CHAPTER 6

APPLICATION ON ORTHOTROPIC STEEL DECKS UNDER RANDOM TRAFFIC FLOW

This chapter is based on:

Wang, B., De Backer, H., and Chen, A. (2016). An XFEM based uncertainty study on crack growth in welded joints with defects. *Theoretical and Applied Fracture Mechanics*, *86, Part B*, 125-142.

Wang, B., Zhou, X.Y, De Backer, H., Chen, A, and Schmidt F. (2017). Macro crack initiation life for orthotropic steel decks considering weld heterogeneity and random traffic loading. *Structure and Infrastructure Engineering. (Accepted)*

6.1. Introduction

Previous chapters provided the analyses on fatigue crack behavior on rib-to-deck welded joints of OSDs through experimental and numerical studies on small-scale specimens. It should be remarked that the loadings on the specimens are designed and thus determinate, whilst for the actual projects, it will have to introduce the realistic traffic flow to achieve better prediction on the fatigue lives of OSDs.

This chapter gives three examples of application of the multiscale method built in Chapter 5 on actual OSDs, with consideration of the realistic traffic loadings based on measurements or standards. The first example is based on a traffic flow measured in a short term in Europe; the second is based on the traffic loadings recommended by Eurocode; and the third one is based on a long-term traffic flow measurement in China. These case studies demonstrated the feasibility of the established method, and the results showed the evident difference of the traffic loadings from various areas.

6.2. Methodology

As stated in Chapter 5, the behavior of early-stage cracks showed larger uncertainties and randomness, whilst the behavior for the rest is more stable. In that case, the study is conducted with respect to two parts, i) the fatigue life for early-stage crack till it can be detected for the first time, which is called macro-crack initiation life (MCIL) hereinafter; ii) the rest fatigue life, which is called macro-crack growth life (MCGL) hereinafter. In the first part, the variation of Paris constant C induced by the heterogeneity is considered, thus makes a probabilistic method necessary. In contrast, the second part should be carried out in a deterministic context, so that it will be easier to combine with the inspections and maintenance works of bridge. Due to the less scattered CGRs in this stage, the error in the deterministic study will be fairly small, especially compared to the early stage where most of the uncertainties exist.

It should be stated at first that, due to insufficient knowledge on the weld defects of OSDs, the study was based on the following hypotheses:

1) To consider the heterogeneity of the defects, the homogenization was adopted in the same way as addressed in Section 4.4. It means that the pores and inclusions were in circular shape with diameters ranging from 20 μm to 90 μm, the number of them was limited to 10, and the parameters concerning their locations, sizes and numbers were all

considered to be uniformly distributed random variables..

2) The initial crack was located at the coarse grained HAZ near the rib-to-deck weld toe, with a depth ranging from 0.1 to 0.4 mm. It was determined according to the observations in the fatigue test. Similar values can be found in some reports related to material defects, e.g. Atzori et al. (2005), and some studies on railway bridges, e.g. Zhou et al. (2016). The crack will grow in a mechanical way that follows the Paris law. Given that the initial crack direction is difficult to determine, it is conservative to assume the shortest crack path that through the deck plate thickness perpendicularly.

3) The end point of calculating MCIL was determined when the cracks grow to a detectable size, a_d. Although a_d was considered as a random variable due to the variety of NDT in previous works (Cremona and Lukic, 1998), it was set to 0.5 mm in this study, with respect not only to the possible detectable precision of NDT, but also to the conservative requirements for practical use on OSDs, as other studies (Wang et al., 2011, Bogdanov, 2014) applied. Furthermore, the value of 0.5 mm was also close to the crack depth corresponding to beach mark S10BM1 and SVIIBM1, near the transition point between Stage I and Stage II-a.

4) The material constants in Stage I are not able to be obtained with confidence. As the CGR in Stage I is always, no matter how scattered it is, lower than that in other stages, it is conservative to use the fitted material constants in Table 5-6 for the whole crack growth process. With consideration of both the applicability and accuracy, the material constants given by Fit 4 were adopted. However, the degree of conservation was yet to be checked for each case study.

5) The residual stress induced by welding process was believed quite large in the study, which could be the case in most scenarios according to (Roy et al., 2003, Barsoum and Barsoum, 2009). It means the SIF ranges can be obtained purely from the stress history, without excluding the zero-value SIFs due to the compressive stresses. Besides, it was also a conservative way to investigate the fatigue life.

To calculate the MCIL, the local XFEM model was firstly built with respect to the weld toe flank angles. It was in two-dimensions and assumed to be in plane-strain status, as shown in Fig. 5-11. This provides great efficiency in the homogenization of the weld defects and the calculation of the SIFs, but might exaggerate the out-of-plane length of cracks. In contrast, a three-dimensional

model is more realistic, but not efficient enough or even next to impossible if the random weld defects are to be considered. Fortunately, the slender shape of early-stage cracks will prevent the conservative margin from being too large. In addition, the IIW recommendations (Hobbacher, 2008) also suggests that the two-dimensional simplification will lead to slightly conservative results. The accuracy is, therefore, acceptable when solving the early-stage crack issues with this local XFEM model. Afterwards, the macroscopic model was built to provide the boundary conditions for the local one. It should be noted that as the crack was not embedded in the macroscopic model, as the its size is small enough that the result from the macroscopic model could be used, in a similar way, as the classical way to obtain SIFs by nominal stresses.

As for the realistic traffic loading, the random traffic flow based on the weigh-in-motion (WIM) system is optimal, since it provides the accurate characteristics about the traffic, including the statistic axel numbers, axel weights, the transverse wheel positions, etc. In case there is no available information about the traffic on the certain OSD, the traffic load history could be provided by standards or codes. Then, the stress effects of the wheel load for the cracked area can be obtained by rainflow counting algorithm.

After obtained the SIF ranges induced by traffic flow, the damage was calculated and accumulated with respect to the crack depth. The damage is the reciprocal of the integral of dN, and the total damage, D, is the sum of damage induced by all cycles, as given by,

$$D = \sum_k \left[\frac{c_k}{\int dN_k}\right] = \sum_k \left[c_k / \int_{a_0}^{a_d} \frac{da}{C(\Delta K_k)^m}\right] \tag{6-1}$$

where k represents the k-th cycle; c_k is the cycle count. Hence, the MCIL can be obtained from

$$N_d = L_d / D \tag{6-2}$$

where L_d is the data length of the wheel loads in days, in correspondence to all cycles counted when calculating D; N_d is the fatigue life in days. Hence, instead of evaluating damage based on classical nominal stresses, the crack growth under effects of weld defects is into account when calculating MCIL, by introducing the homogenization method to calculating damage via Paris constant C. In this way, the load sequence for variable amplitude fatigue is not taken into account, as it will not result in noticeable differences in terms of long-term fatigue life calculation (Pais, 2011; Nagy, 2017).

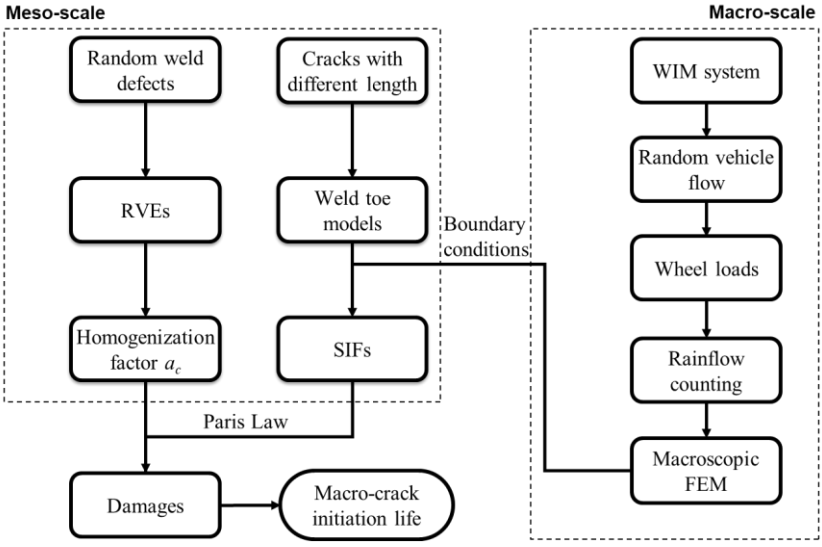

Fig. 6-1 The flowchart for estimating macro-crack initiation life

To calculate the MCGL, the Equation (6-1) and (6-2) can be applied with the initial crack depth, a_0, being a constant of 0.5 mm, and the randomness of the Paris constant, C, can be ignored as well. Hence, it will lead to a deterministic result. The end point of the MCGL is selected to be half thickness of the deck plate, since it is when the visual detection can surely address the cracks as the paint film damaged will provide a clear sign at that moment (Ryan et al., 2006). On the other hand, this end point is determined with respect to the test results in literatures, which suggest the crack may stop growing then (Kainuma et al., 2016). It can be attributed to that the crack tip is beyond the possible range that affected by the welding process. Then the SIF range becomes much smaller as residual stress is faded, which means the aforementioned Hypothesis (5) is not valid anymore. Nevertheless, it cannot be justified due to the difficulty in measuring the residual stress in the direction of deck plate thickness, and the study on residual stress is also not in the scope of this thesis. Anyway, all the initial/end point and the hypotheses proposed here are given with compromises from different aspects, and thus are open for discussion.

6.3. A case study based on the traffic flow in Europe

A case study was carried out based on the numerical model of the orthotropic steel deck of Millau Viaduct, which is a well-known multi-span cable-stayed bridge in the south of France. The view of this bridge and the design of the cross-section is shown in Fig. 6-2.

a) general view

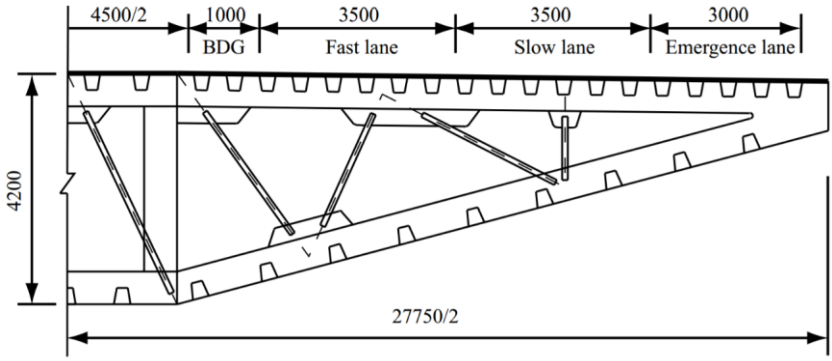

b) cross-section (unit: mm)

Fig. 6-2 The orthotropic steel deck of Millau Viaduct (Zhou et al., 2015)

6.3.1. Traffic flow

In this study, a set of measured traffic data from the A9 motorway in France is used. The traffic data was collected by Zhou et al. (2015) using a piezoceramic weigh-in-motion (WIM) system installed in one direction of the bidirectional 6-lane motorway near Saint-Jean-de-Vedas (SJDV) in southeast France. As it is only about 100 km away from the site that Millau Viaduct located, the characteristics of traffic flow are believed quite representative.

The WIM system provided not only the axle weights and distances of vehicles traveling in the slow and fast lanes, but also the vehicle transverse dimensions and the transverse in-lane positions, which means a more precise position of the vehicle rather than a distribution by lanes. This is realized by an extra diagonal sensor strip, which is different from the conventional two parallel sensor strips often used in ordinary WIM systems. A detailed description of this type of WIM system can be found in (Jacob et al., 2013). In fact, the distribution of the transverse in-lane position of vehicles is site-specific. In other words, it depends significantly on the profile of the lane cross section (Zhou et al., 2015), and maybe the customs of local drivers and the road surface conditions, too. To evaluate the fatigue performance or fatigue life of critical joints of existing structures, it is therefore preferred to use measured distributions of transverse in-lane positions, instead of models recommended in standards or codes.

The WIM system recorded the traffic data from January 2010 to May 2010, and a total of 581,011 trucks representing traffic flow for 86 days were selected from the original data by excluding records that are unreasonable, or in the weekends and system inactivity. Obviously, in order to obtain a reasonable evaluation and prediction of the performance of an existing bridge structure, measured traffic data over a sufficiently long period is recommended, e.g. one year as suggested by Sivakumar et al. (2011). This kind of long-term data, however, is not always available due to various facts, such as limited storage for the huge amounts of data in continuous recording, the available budget for conducting long-term measurements, etc. Prediction or evaluation of the performance of bridge or its components with short-term measurements is thus quite common in practice, by using variance reduction techniques that are able to fully exploit the potential of short-term data. A common method to analyze the traffic load effect is to use microscopic traffic simulation to generate long-term traffic loads or load effects (Chen and Wu, 2011; O'Connor and O'Brien, 2005; Enright and O'Brien, 2013).

Based on the principle of generating traffic flow with the same features, a Monte-Carlo simulation program was designed in (Zhou, 2013; Zhou et al., 2016b). By employing the measured traffic data for 86 working days, the traffic data for 900 working days were generated to calculate the fatigue life. More details can be found in (Wang et al., 2017). Fig. 6-3 showed a typical transverse stress history on the bottom face of deck plate at 8 mm away from the weld toe. And as there are always large amount of zero values when no vehicles are running over, the X-axis in Fig. 6-3 is the reduced time by eliminating the zero-value sections in the traffic flow simulation.

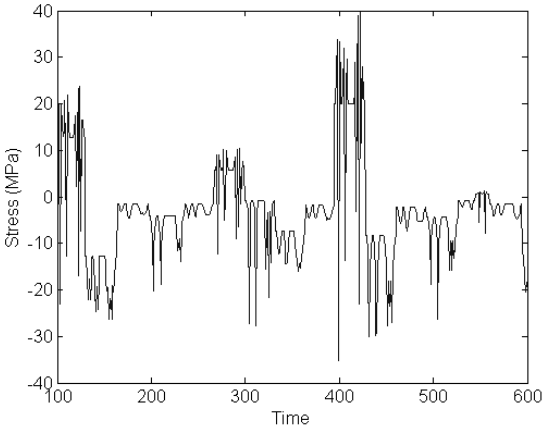

Fig. 6-3 Typical time history of stress

6.3.2. Numerical models

As widely accepted that the fatigue damage of welded joints of OSDs is mainly due to local effects, the numerical model was built as a partial structure instead of the whole bridge structure. It focused on a deck segment under the slow lane, as it is more fatigue-prone due to heavy trucks. The thickness of the deck plate was 14 mm, and that of the trapezoidal stiffener was 6 mm. Due to the lack of design specification and on-site measurements, the actual weld toe flank angle, α, was not available. By assuming that the weld will form equal flank angle at toe on deck plate and on the stiffener, the flank angle was set to be 40 degrees, as shown in Fig. 6-4.

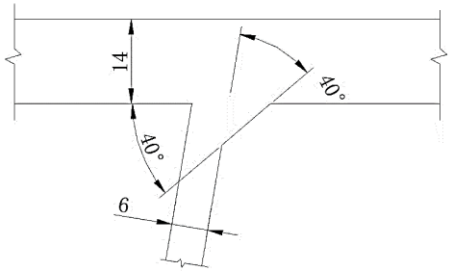

Fig. 6-4 The detailed geometry at the welded joint

The FEM model of this bridge was established in ANSYS 13.0. A coarse model was built in the first place, which consists of five trapezoidal stiffeners and two diaphragms. Boundary conditions were applied by fixing the longitudinal

translation but allowing the rotation around the y-axis for the two diaphragms, and restraining the vertical deformation on the lateral boundary. This model consisted of Shell 63 elements, which is a linear-elastic shell element defined in ANSYS, in a total number of 52156. However, it will not achieve the precise geometry of the welded joints as a shell model, not to mention the relatively coarse mesh will lead to insufficient accuracy for the XFEM model in the next step. In that case, a sub-model of the weld vicinity (see Fig. 6-5) was built by Solid 185 elements, which is an eight-node solid element defined in ANSYS, and the element number was 181000.

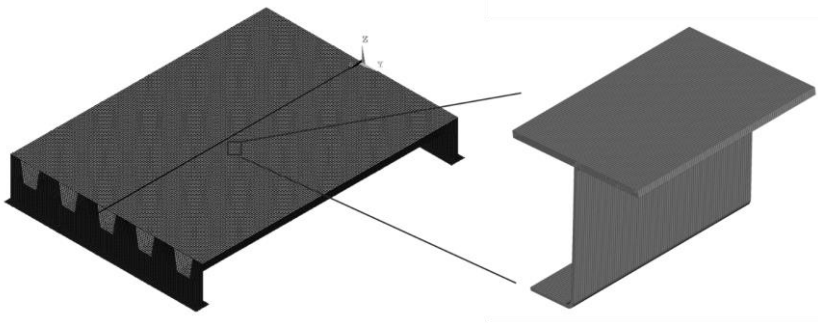

Fig. 6-5 Coarse model and sub-model of the Millau Viaduct

The material properties were the same as steel, i.e. the elastic modulus of 2.1×10^{11} Pa, the Poison's ratio of 0.3, and the density of 7850 kg/m^3. By applying a moving wheel load of 45 kN on an area of 0.45 m by 0.4 m, which was used to represent the landing area of one tire, along the FEM model in both longitudinal and transverse directions, influence surfaces for various responses can be obtained. Fig. 6-6 illustrates the influence surfaces of bending and membrane stresses at the location of 8 mm to the weld. Accordingly, the bending stresses were always much higher than the membrane stresses, despite of the different wheel locations.

Afterwards, a two-dimensional XFEM model with an initial crack was built in the same way as illustrated in Fig. 5-11 in Chapter 5, whose dimensions were determined according to the geometry of the bridge. Then the SIFs can be calculated accordingly, as given in the next section.

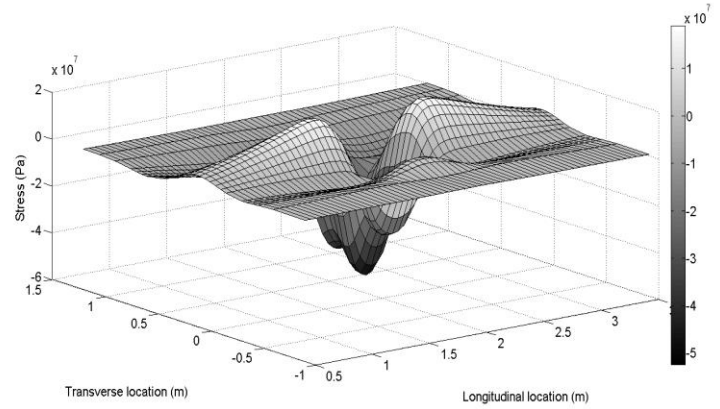

a) Bending stresses

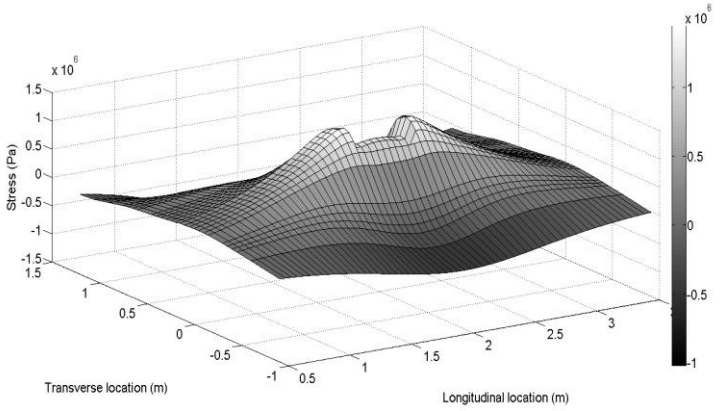

b) Membrane stresses

Fig. 6-6 The influence surfaces of the transverse stress at 8 mm to the welded joint

6.3.3. Stress intensity factors

The SIFs for crack depths of 0.1 - 0.5 mm, namely in the range of MCIL, were calculated using the XFEM model. Fig. 6-7 presents the results by applying a bending stress of 100 MPa, which is almost the same as Fig. 5-12. Again, the results show that the Mode-I SIFs are much larger than the Mode-II SIFs, and thus are the dominant part in crack growth. It should be noted that the similarity of the results presented by Fig. 5-12 and Fig. 6-7 implies that the differences induced by deck plate thickness are tiny and ignorable when cracks are in such a small size. The empirical way provides another support to that statement as it suggests the shape factor is a function of the non-dimensional parameter *a/t*. However, it will not

devalue the design of thick deck plate, as it mainly benefits the fatigue resistance by reducing the stresses at key positions.

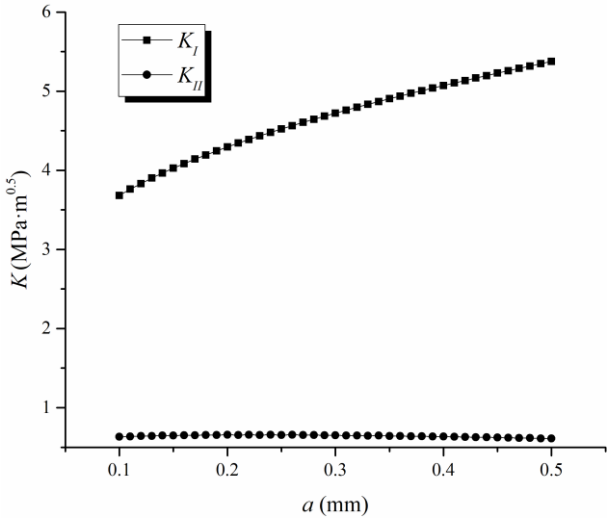

Fig. 6-7 Stress intensity factors obtained by XFEM model

As discussed in Chapter 5, however, the SIFs given by the local XFEM model are limited to small scale cracks due to the plane strain assumption in two-dimensions. Whilst for large cracks, the actual shape of the crack in three-dimensions, i.e. the length and depth of the semi-elliptical crack, is important, which invalidates the solution by the local XFEM model.

Assuming that the shape is always following Equation (5-5), it is possible to obtain the SIFs according to the shape factors that are dependent on the geometries the welded joints. In that case, the curve for shape factors given in Fig. 5-15 could help to obtain the SIFs with respect to different thicknesses of deck plate and flank angles by data fitting. By removing the points corresponding to crack depths larger than half thickness of the deck plate, the curve was best fitted by the following equation in terms of a non-dimensional variable, *a/t*,

$$F(a/t) = \ p_1 * \exp(-p_2 * a/t) + p_3 \tag{6-3}$$

where a is the crack depth; t is the thickness of the deck plate; p_1, p_2, p_3 are the fitted coefficients. Among them, p_3 is the asymptotic value that the curve approaches, meaning that the effect of geometry will become stable when the crack itself is large enough. In the classical way of calculating shape factor, for example Newman-Raju Equation and Bowness-Lee Equation, the shape factor always

following an asymptotic value of one. Similarly, by fitting the results from the fatigue test, the value of p_3 can be considered a constant afterwards. The other two coefficients, p_1 and p_2, can always be fitted with the SIFs of early-stage cracks achieved by XFEM model for various geometries. Table 6-1 and Fig. 6-8 illustrate the fitting results of the coefficients and the curve of shape factor. It can be seen that the difference between shape factors given by test specimens and those given by Millau Viaduct is fairly small.

Table 6-1 Summary of the fitting for Equation (6-3)

		Test specimens	Millau Viaduct (MV)
Geometrical parameters	t (mm)	15	14
	α (°)	37	40
Coefficients	p_1	1.157	1.260
	p_2	32.75	36.96
	p_3	1.109	1.109
Goodness of fit	SSE	1.245E-02	1.759E-03
	R-square	0.9952	0.9961
	Adjusted R-square	0.9949	0.9959
	RMSE	0.0194	0.0078

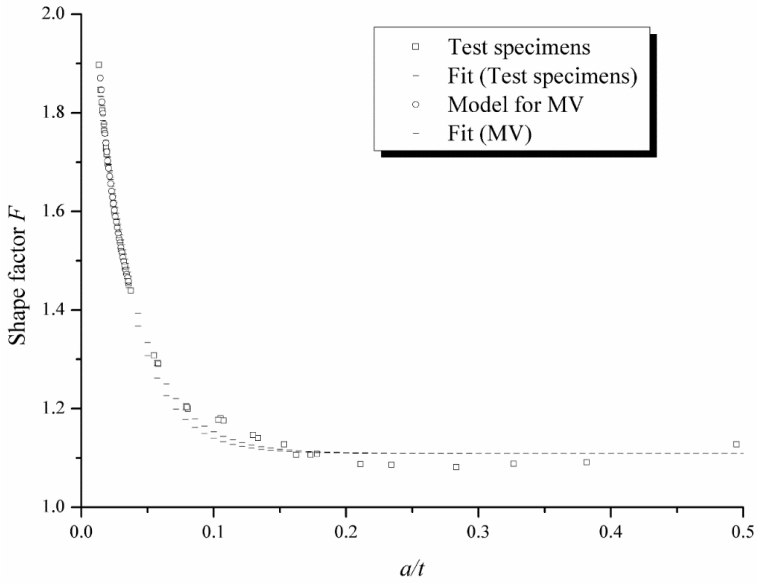

Fig. 6-8 Shape factors for Millau Viaduct calculated by data fitting

With the obtained shape factors and stress ranges induced by realistic wheel loads, it is possible to calculate the damage with respect to SIFs using Equation (6-1). The ΔK_k for different crack depth required for Equation (6-1) is computed by

$$\Delta K_k = \Delta K_0 \Delta\sigma_k / \Delta\sigma_0 \tag{6-4}$$

where $\Delta\sigma_k$ is the stress range for the k-th cycle; ΔK_0 is the SIFs calculated for a standard case; $\Delta\sigma_0$ is the stress range applied in the standard case, i.e. 100 MPa.

Another concern is about the SIF threshold value, ΔK_{th}. According to the IIW recommendations (Hobbacher, 2008), a threshold value of $\Delta K_{th} \leq$ 2.0MPa$\sqrt{m}$ was recommended when a surface crack depth is less than 1 mm. Also note that the value is not a deterministic one due to the uncertainties in the early-stages of crack growth. Eventually, the ΔK_k whose value is lower than 2.0 MPa$\sqrt{m}$ was excluded when calculating damages in this study, i.e. ΔK_{th} = 2.0 MPa$\sqrt{m}$.

6.3.4. Calculation of fatigue life

According to the aforementioned hypotheses, five different cases of initial crack depths, which include four deterministic cases with an initial crack depth of 0.1, 0.2, 0.3, and 0.4 mm and one case with a random initial crack depth in a uniform distribution between 0.2 mm and 0.4 mm, were considered. 2000 RVEs were generated for each case, and thus in total 10000 cases were calculated.

For each initial crack depth case, a histogram of MCIL was obtained, showing the distribution of days that the cracks in RVEs reaches the detectable length. In addition, the histogram was converted to the cumulative probability curve. For the cases with determined initial crack depth, the results are shown in Fig. 6-9. Statistics of MCIL, in terms of mean value, standard deviation and coefficient of variation, are summarized in Table 6-2. Accordingly, it can be seen that the cumulative probability curve always presents a rapid increase phase. As a result, the MCILs corresponding to 50%, 90%, 95% and 99% are sharing similar results. It means that the MCIL significantly depends on the initial crack depth, indicating the better predictability once the initial crack depth is acquired.

In practice, however, the initial crack depth is usually unknown or random. A case study with a random initial crack depth would be helpful to understand such a realistic situation. In the present study, the initial crack depth was considered to have a uniform distribution, varying from 0.2 mm to 0.4 mm as suggested by the observation on test specimens. Given that no knowledge is available about the initial cracks on the Millau Viaduct, it is reasonable to choose a uniform distribution to avoid bias. Results for the histogram of the MCIL and the corresponding cumulative probabilities are shown in Fig. 6-10. Accordingly, the

MCILs are much more scattered than those achieved by determined initial crack depths, as larger standard deviations and coefficients of variance are obtained, leading to a big difference in MCILs for cumulative probabilities of 50%, 90%, 95% and 99%, as shown in Table 6-2. For a conservative approach in engineering projects, the cumulative probability of 50%, which is corresponding to the safety factor of 2, could be an advisable indicator, suggesting that MCIL is about 2082 working days.

As the results are also largely affected by the material constants in Paris law (Wang et al., 2016), another group of results obtained by the Paris constant C_0 and exponent m according to IIW recommendations (Hobbacher, 2008) was calculated as a contrast. Again, five cases of initial crack depth were considered to generate histograms of MCIL and corresponding cumulative distribution curves, as shown in Fig. 6-11 and Fig. 6-12. The Statistics of MCIL, in terms of mean value, standard deviation and coefficient of variation, are summarized in Table 6-3.

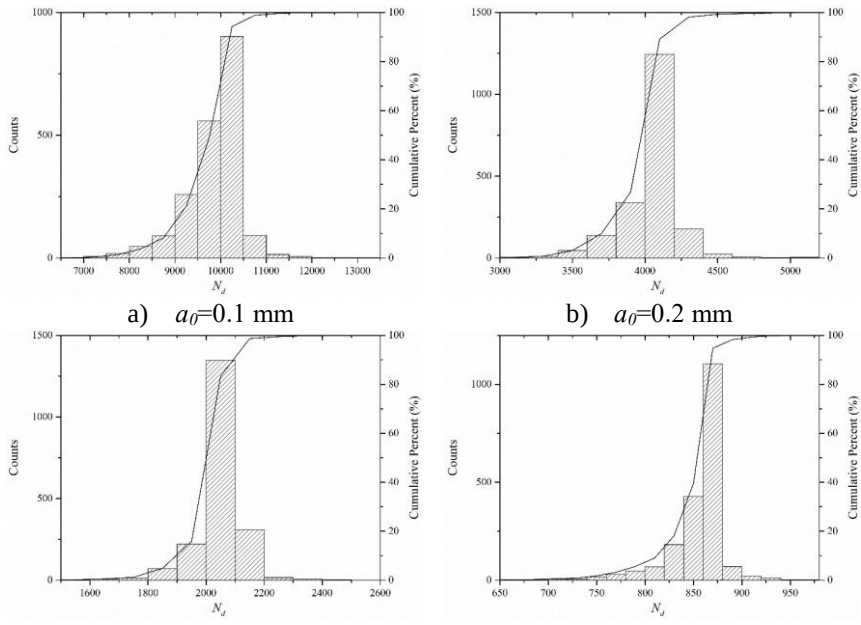

a) a_0=0.1 mm b) a_0=0.2 mm

c) a_0=0.3 mm d) a_0=0.4 mm

Fig. 6-9 Distribution of macro crack initiation life N_d for determined a_0, with C_0=2.571×10^{-11}, m=2.603, according to the fatigue test

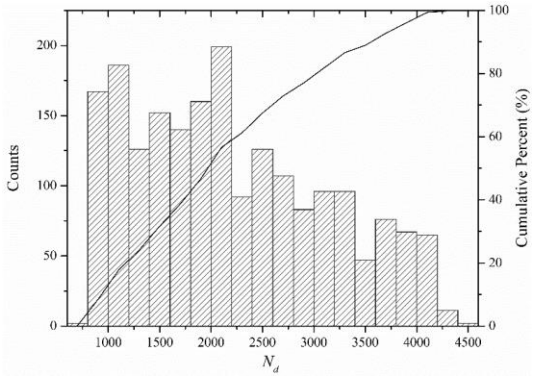

Fig. 6-10 Distribution of macro crack initiation life N_d for random a_0, with C_0=2.571×10^{-11}, m=2.603, according to the fatigue test

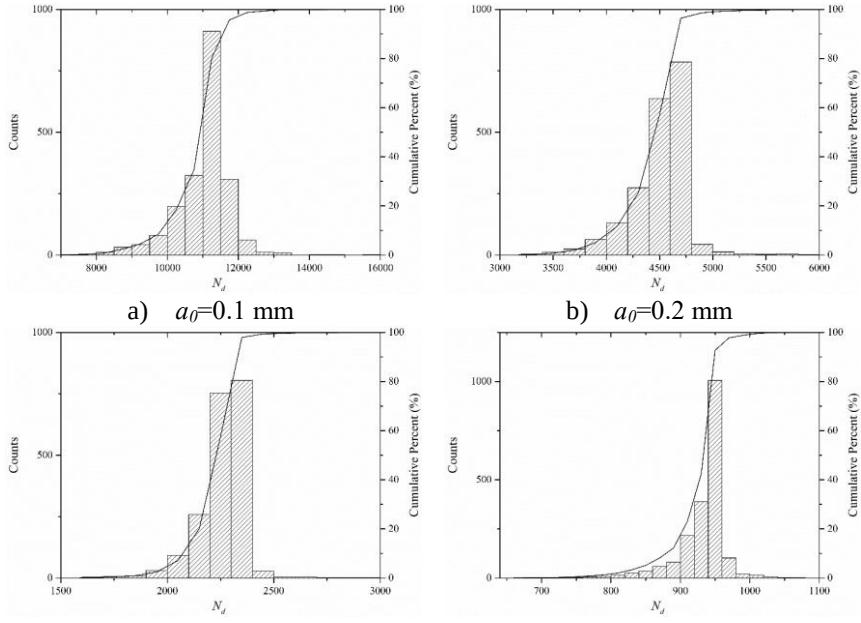

a) a_0=0.1 mm b) a_0=0.2 mm

c) a_0=0.3 mm d) a_0=0.4 mm

Fig. 6-11 Distribution of macro crack initiation life N_d for determined a_0, with C_0=1.65×10^{-11}, m=3, according to (Hobbacher, 2008)

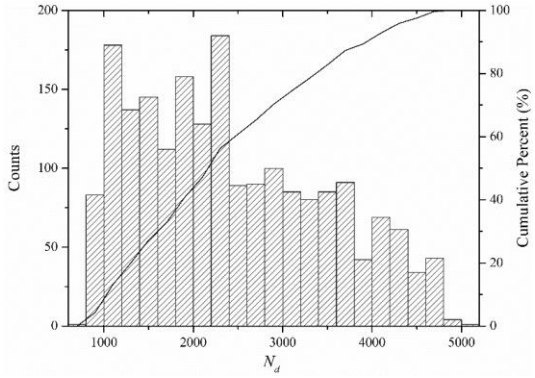

Fig. 6-12 Distribution of macro crack initiation life N_d for random a_0, with C_0=1.65×10^{-11}, m=3, according to (Hobbacher, 2008)

Table 6-2 Statistics of MCIL obtained by material constants from the fatigue test

a_0 (mm)	MCIL (days)						
	Mean value	Standard deviation	CV	Cumulative probability			
				50%	90%	95%	99%
0.1	9851	596	0.0605	10011	10352	10531	11093
0.2	4059	199	0.0490	4112	4208	4275	4511
0.3	2056	81	0.0393	2077	2116	2132	2222
0.4	856	30	0.0349	866	876	880	912
0.2~0.4	2206	936	0.4243	2082	3618	3893	4184

Table 6-3 Statistics of MCIL obtained by material constants from IIW Recommendation (Hobbacher, 2008)

a_0 (mm)	MCIL (days)						
	Mean value	Standard deviation	CV	Cumulative probability			
				50%	90%	95%	99%
0.1	11052	767	0.0694	11256	11698	11932	12670
0.2	4488	253	0.0563	4555	4678	4763	5068
0.3	2254	102	0.0451	2280	2330	2350	2465
0.4	933	37	0.0400	945	958	964	1004
0.2~0.4	2425	1040	0.4287	2283	4004	4315	4647

By comparing the MCILs obtained by the material constants from IIW Recommendation and that from the fatigue test, it can be addressed that they are pretty close. The MCIL corresponding to cumulative probability of 50% is 2283 working days.

For the final step, the MCGL was calculated with an initial crack depth of 0.5 mm in a deterministic way, in which the variation of material constants is not taken into account. Similarly, two groups of material constants, i.e. one from the Fit 4 in Table 5-6 and the other from the IIW Recommendation, were adopted, denoted as "Test" and "IIW", respectively. The results from both groups of material constants were also in good agreement with each other, indicating an MCGL around 7000 working days, as given in Fig. 6-13. By combining the MCGLs with the 95 percent confidence interval for the MCILs, the whole fatigue life for initial crack depth ranging from 0.2 mm to 0.4 mm can be obtained as well, as shown in Fig. 6-14.

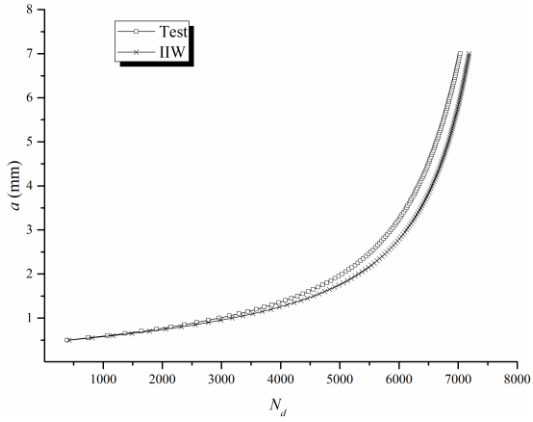

Fig. 6-13 Macro-crack growth life from 0.5 mm to 7 mm

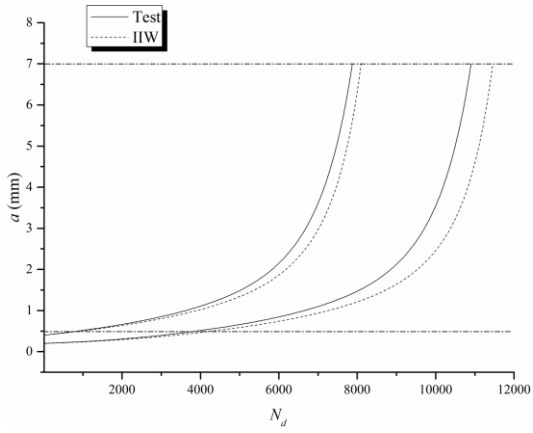

Fig. 6-14 Fatigue life for initial crack depth ranging from 0.2 mm to 0.4 mm

The results indicate that the MCGL is the main part of whole fatigue life, while the MCIL takes a small part that accounts one third in maximum. It is not fully consistent with the fatigue test results, which could be attributed to that the same material constants C & m were applied in the calculation. In that way, the calculated CGR is higher in Stage I when compared to the fatigue test results. As the stress range spectrum caused by traffic flow in this region seems quite moderate, there should be many cycles assigned to Stage I, and the damage induced by these cycles will be significantly overestimated in this calculation. Anyway, even in a conservative scenario that assuming an initial crack depth of 0.4 mm, the Millau Viaduct will not suffer from fatigue problem in at least 8000 working days, i.e. 32 years. Therefore, the fatigue life of Millau Viaduct could be much larger in the reality, and will not be the major concern in the maintenance.

6.4. A case study based on Eurocode

Another case study is carried out on the KW5 Bridge in Antwerp, Belgium, which is a tied arch bridge crossing the Albert Canal. The view of this bridge is shown in Fig. 6-15 a), together with the photograph of its orthotropic steel deck in Fig. 6-15 b), showing the design of the crossbeam, trapezoidal longitudinal stiffeners and cut-outs. Given the shape of cut-outs, it is not hard to recognize that KW5 bridge will act as a railway bridge. However, as the on-site test data obtained by heavy trucks were available for it, this case study was conducted to show the calculation based on the typical measured data combined with the traffic flow given by the Fatigue Load Model 4 in Eurocode (NBN, 2004).

a) general view b) orthotropic steel deck

Fig. 6-15 KW5 Bridge over the Albert Channel, Belgium (photo from De Backer et al., 2008)

6.4.1. On-site test

The on-site test for measuring the traffic loading effects was conducted before the ballast was paved on the bridge, by using high precision strain gauges (De Backer et al., 2007). The strain gauges were installed in the vicinity of the welded joints, as shown in Fig. 6-16. By driving the test trucks that weight about 44 tons over the bridge, the strains were measured, as illustrated in Fig. 6-17. Due to the importance of local effects in fatigue life estimation, the transverse in-lane position was taken as a parameter in the test. In correspondence with the Eurocode 1 (NBN, 2004), five different transverse in-lane positions were considered, and the distribution is following a discrete normal distribution. When calculating the damages, it was assumed that the tire located right above the central line of trapezoidal stiffener for conservative concerns.

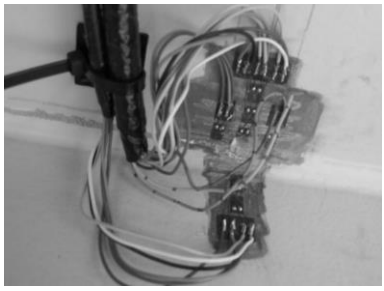

Fig. 6-16 Strain gauges at the weld toe (De Backer et al., 2007)

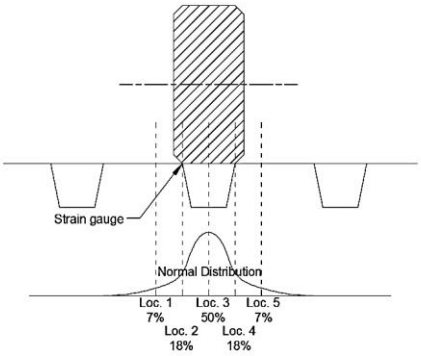

Fig. 6-17 Test scheme and the assumed possibility of transverse locations

6.4.2. Stress intensity factors

As the design of the OSD of the KW5 Bridge is basically the same as the test specimen, i.e. 15-mm-thick deck plate and 6-mm-thick stiffeners, the shape factors are assumed to be the identical as well. Therefore, the Equation (6-3) with the coefficients given in Table 6-1 can be applied to calculate the shape factors. In that case, the stress ranges for calculating SIFs should be sufficiently distinct from the crack site, and the strain gauge that is 11 mm away from the weld toe was selected in this study.

The test data for each transverse position were shown in Fig. 6-18 ~ Fig. 6-22, in which the effects of the five axles of the truck could be clearly distinguished. These strains were measured at the bottom side of the deck plate only, as the data at the top side are always not available due to the pavement cover. Nevertheless, according to the influence surface in Fig. 6-6, it can be inferred that the measured strains can be regarded as the direct indicators of bending stresses. Afterwards, the rain-flow counting algorithm was applied to obtain the effective load cycles for each location, as shown in Table 6-4, with the stress amplitudes under 5MPa

excluded. With these bending stress ranges, the damage with respect to the crack depth could be obtained.

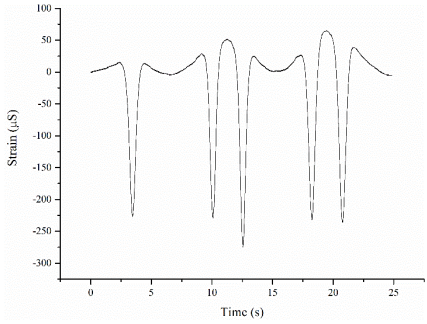

Fig. 6-18 Measured strain on Location 1

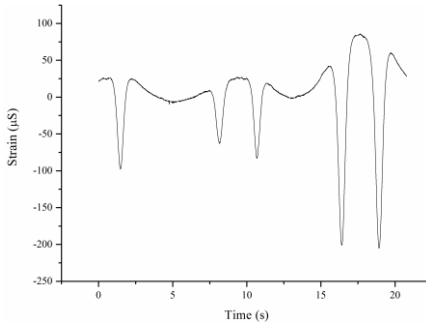

Fig. 6-19 Measured strain on Location 2

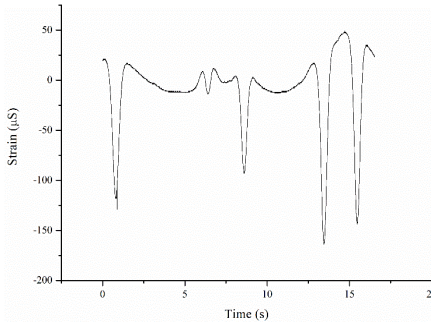

Fig. 6-20 Measured strain on Location 3

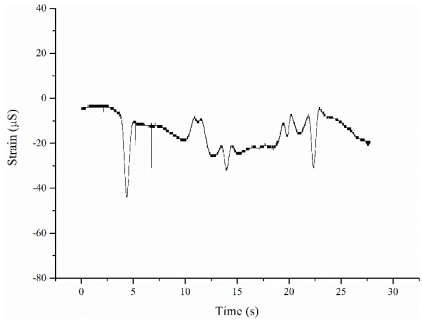

Fig. 6-21 Measured strain on Location 4

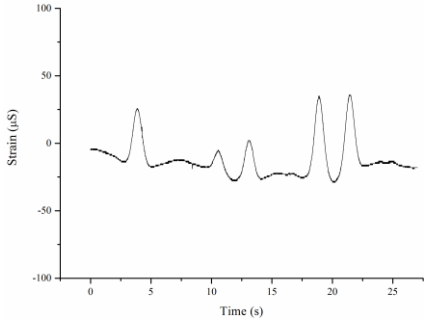

Fig. 6-22 Measured strain on Location 5

Table 6-4 Rain-flow counting for test data

Loc.	Possibility	Rain-flow Counting								
1	0.07	Stress Amplitude (MPa)	25.52	26.88	27.09	29.51	27.20	34.34	35.70	31.61
		Mean stress (MPa)	-22.16	-20.79	-21.00	-18.59	-21.53	-23.42	-22.05	-17.96
		Cycle Count (-)	0.50	0.50	0.50	0.50	1.00	0.50	0.50	0.50
2	0.18	Stress Amplitude (MPa)	9.24	13.02	11.55	14.70	25.52	30.14	30.56	27.83
		Mean stress (MPa)	-3.99	-7.56	-5.88	-5.88	-16.70	-12.08	-12.50	-15.23
		Cycle Count (-)	1.00	0.50	1.00	0.50	0.50	0.50	0.50	0.50
3	0.5	Stress Amplitude (MPa)	11.55	15.33	19.43	22.37	20.27	18.80		
		Mean stress (MPa)	-7.98	-11.76	-15.02	-12.08	-9.98	-11.45		
		Cycle Count (-)	1.00	1.00	0.50	0.50	0.50	0.50		
4	0.18	Stress Amplitude (MPa)	\							
		Mean stress (MPa)	\							
		Cycle Count (-)	\							
5	0.07	Stress Amplitude (MPa)	5.67	6.62	6.72	6.83	5.78			
		Mean stress (MPa)	-0.21	0.74	0.63	0.74	1.79			
		Cycle Count (-)	0.50	0.50	0.50	0.50	0.50			

6.4.3. Calculation of fatigue life

In the same way as the previous case study, five different cases of initial crack depths were considered, i.e. four cases with determined initial crack depth of 0.1, 0.2, 0.3, and 0.4 mm and one case with a random initial crack depth in a uniform distribution between 0.2 mm and 0.4 mm.

As the on-site test data using the test truck can only specify one certain type and one certain weight, further information on the realistic traffic flow was required. Here the composition of various types of lorries is adopted as suggested by Fatigue Load Model 4 in Eurocode 1 (NBN, 2004). Accordingly, the number of heavy vehicles is 2 million lorries per year and per slow lane, assuming that the KW5 bridge is a highway bridge with high flow rates of lorries. And the percentages and weights of different types of lorries were provided. Hence, the damage can be obtained by,

$$D_y = \sum_l T_y P_l w_l D_t \tag{6-5}$$

$$N_y = 1/D_y \tag{6-6}$$

where T_y refers to the total volume of lorries per year and per slow lane, i.e. 2 million; P_l is the percentage of different types of lorries; D_t is the damage induced by the test truck; w_l is the weight ratio of the lorries in Fatigue Load Model 4 and the test truck, that is 44 tons.

Fig. 6-23 & Fig. 6-24 gives the MCIL counted by year, which seems extremely small. The statistics of results are given in Table 6-5. For instance, if the initial crack depth is 0.3 mm, which is quite close to the measurement in the fatigue test, for example Specimen 10, VII, VI and IX, the results showed a large probability that a macro-crack will initiate in only 0.19 years, i.e. less than 3 months. Again, another group of Paris constant and exponent according to IIW recommendations (Hobbacher, 2008) was adopted to check if the short fatigue life is resulted by the effects of material-related constants. The results are shown in Fig. 6-25, Fig. 6-26, and Table 6-6. Unsurprisingly, the results are quite similar to the ones achieved according to the fatigue test, same as the previous case study on Millau Viaduct.

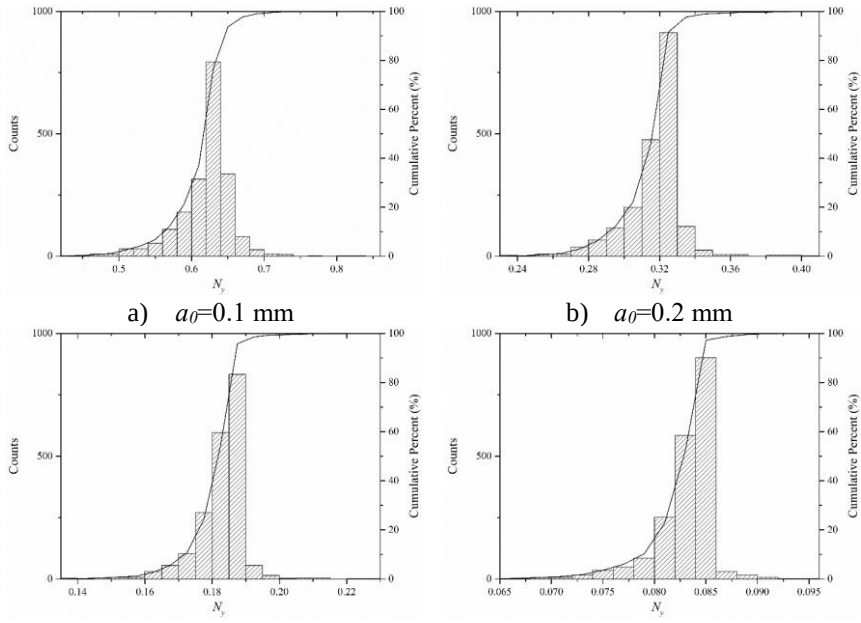

Fig. 6-23 Distribution of macro crack initiation life N_y for determined a_0, with C_0=2.571×10^{-11}, m=2.603, according to the fatigue test

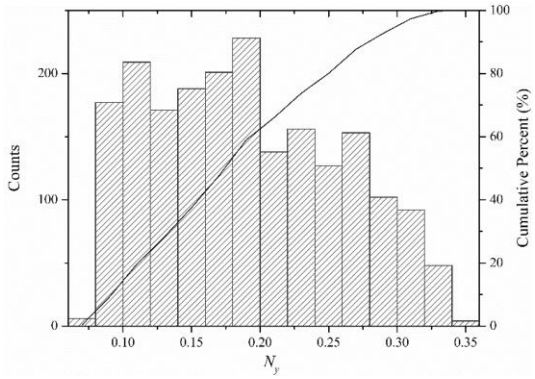

Fig. 6-24 Distribution of macro crack initiation life N_y for random a_0, with C_0=2.571×10^{-11}, m=2.603, according to the fatigue test

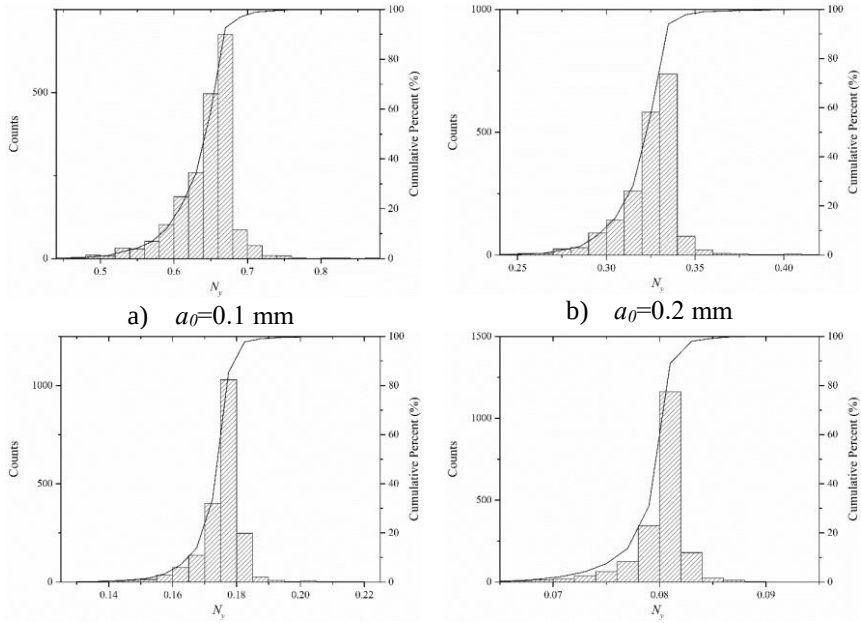

a) a_0=0.1 mm b) a_0=0.2 mm

c) a_0=0.3 mm d) a_0=0.4 mm

Fig. 6-25 Distribution of macro crack initiation life N_y for determined a_0, with C_0=1.65×10^{-11}, m=3, according to (Hobbacher, 2008)

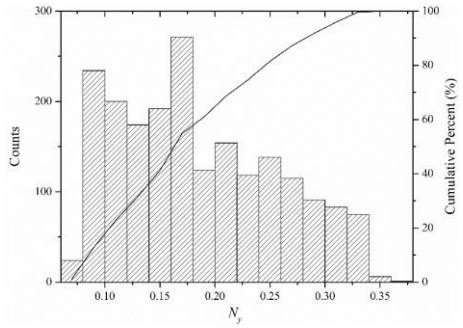

Fig. 6-26 Distribution of macro crack initiation life N_y for random a_0, with C_0=1.65×10^{-11}, m=3, according to (Hobbacher, 2008)

Table 6-5 Statistics of MCIL obtained by material constants from the fatigue test

a_0 (mm)	MCIL (years)						
	Mean value	Standard deviation	CV	Cumulative probability			
				50%	90%	95%	99%
0.1	0.6430	0.0389	0.0605	0.6535	0.6757	0.6874	0.7241
0.2	0.3240	0.0159	0.0490	0.3282	0.3359	0.3412	0.3601
0.3	0.1756	0.0069	0.0393	0.1774	0.1807	0.1821	0.1898
0.4	0.0802	0.0028	0.0349	0.0811	0.0821	0.0825	0.0855
0.2~0.4	0.1861	0.0713	0.3834	0.1776	0.2942	0.3137	0.3340

Table 6-6 Statistics of MCIL obtained by material constants from IIW Recommendation (Hobbacher, 2008)

a_0 (mm)	MCIL (years)						
	Mean value	Standard deviation	CV	Cumulative probability			
				50%	90%	95%	99%
0.1	0.6825	0.0474	0.0694	0.6951	0.7224	0.7368	0.7824
0.2	0.3327	0.0187	0.0563	0.3376	0.3468	0.3531	0.3757
0.3	0.1782	0.0080	0.0451	0.1803	0.1842	0.1858	0.1949
0.4	0.0804	0.0032	0.0400	0.0815	0.0826	0.0831	0.0865
0.2~0.4	0.1894	0.0739	0.3901	0.1804	0.3020	0.3228	0.3445

Afterwards, the MCGL for the crack growth from 0.5 mm to 7.5 mm, i.e. the half thickness of deck plate, is presented in Fig. 6-27. The whole fatigue lives according to the MCGLs and the 95 percent confidence interval for the MCILs are presented in Fig. 6-28, in which the initial crack depth is ranging from 0.2 mm to 0.4 mm.

Both results obtained by the Paris constant C and Paris exponent m from fatigue test and IIW Recommendation seemed far away from the reality, as the total fatigue life is as short as 1.5 years. Besides, the MCILs only account for a proportion of about one fifth in maximum, which is evidently smaller than the case study on Millau Viaduct. One possible reason is that the current method is inappropriate to use consistent material constants for the whole fatigue life, which will lead to larger CGR of Stage I cracks.

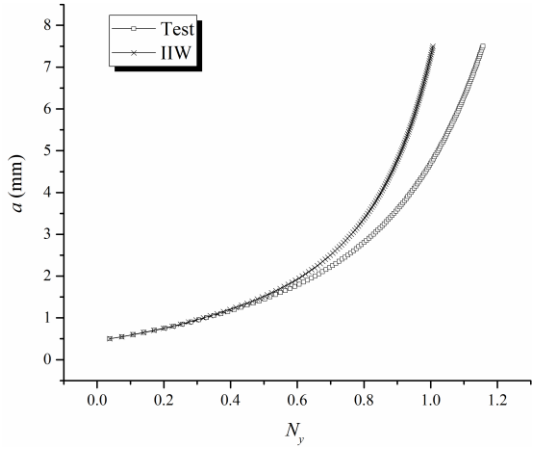

Fig. 6-27 Macro-crack growth life from 0.5 mm to 7.5 mm

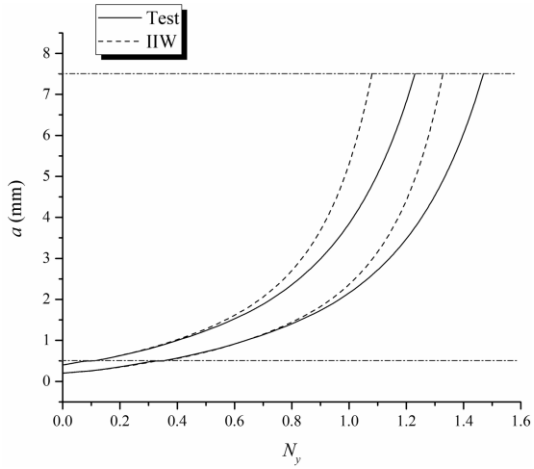

Fig. 6-28 Fatigue life for initial crack depth ranging from 0.2 mm to 0.4 mm

With respect to the early stage crack growth rate, the two-stage Paris law recommended by BS 7910 (BSI, 2013) will lead to a better solution, as shown in Fig. 6-29. It is proved to be more precise by literature such as Mehmanparast et al., (2017). In that case, the material constants for Stage I and the transition point between stages are quite critical. Several groups of material constants are compared in Table 6-7.

Firstly, it can be found that the material constants in Stage II from the standards and the fatigue test, i.e. Paris constant C_2 and Paris exponent m_2, are close to each other. The results achieved above also proved that they are in good agreement as well. On the other hand, the material constants in Stage I, i.e. C_1 and m_1, are so different, especially for C_1 whose values are always in various magnitude order, which is even true for different stress ratio R. Unfortunately, the fatigue test could not provide these material constants in Stage I as a contrast, since the production and identification of beach marks in this stage is next to impossible.

Secondly, the variation of transition point value should be regarded as well. As shown in Fig. 6-29 b), it is simply the x-coordinate of the intersection point. Due to the big differences in C_1 and m_1, the intersection point can be quite different, which makes it another critical factor as it specifies the stage and the subsequent material constant to be used.

Consequently, the method of calculating the fatigue life is conducted according to the two-stage model in BS 7910, where the material constants in Stage I for welded joints are recommended to be the group of "Mean + 2SD" for $R \geqslant 0.5$, i.e. $C_1=9.38\times10^{-13}$, $m_1=5.10$, $C_2=2.70\times10^{-11}$, $m_2=2.88$. It is not exactly the real case, as the strain histories in Fig. 6-18 ~ Fig. 6-22 are always negative, leading to applied stress ratios smaller than 0.5. Obviously, it is a choice with understandable concern of conservation. This, in another way, implies that the residual stress is believed large enough for welded joints in BS 7910, which exactly agrees with the Hypothesis (5) as mentioned before.

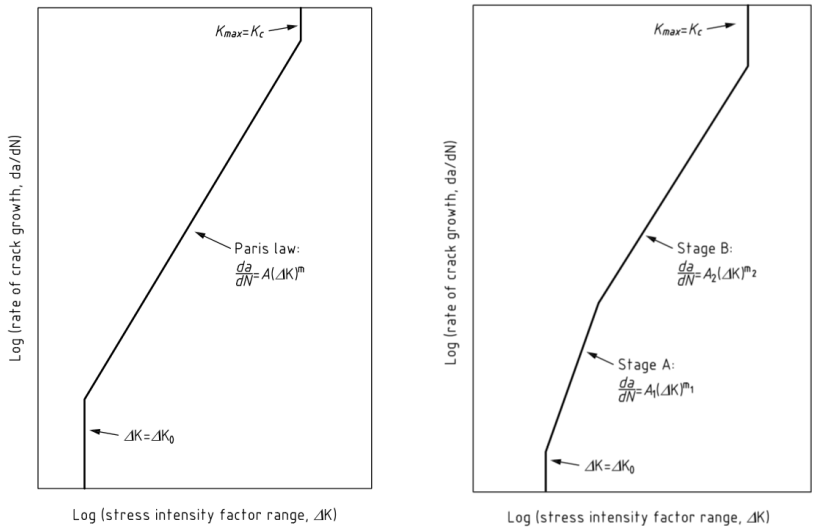

a) Simple Paris law crack growth relationship

b) Two-stage crack growth relationship

Fig. 6-29 Comparison of a) simple Paris law and b) two-stage crack growth relationship (BS 7910)

Table 6-7 Comparison of material constants for different stages (*da/dN* in m/cycle and ΔK in MPa √ m)

			BS 7910 (R<0.5)	BS 7910 (R≥0.5)	IIW	Fatigue test fitting
Stage I	Mean	C_1	2.10×10^{-17}	2.14×10^{-13}	\	\
		m_1	8.16	5.10	\	\
	Mean+2SD	C_1	7.59×10^{-17}	9.38×10^{-13}	\	\
		m_1	8.16	5.10	\	\
Stage II	Mean	C_2	8.32×10^{-12}	1.22×10^{-11}	\	\
		m_2	2.88	2.88	\	\
	Mean+2SD	C_2	1.41×10^{-12}	2.70×10^{-11}	1.65×10^{-11}	2.57×10^{-11}
		m_2	2.88	2.88	3.00	2.60
Transition point			9.96	4.50	\	\
ΔK_{th}			2	2	2	2

In the same manner, the results for determined and random initial crack depth are shown in Fig. 6-30 and Fig. 6-31, respectively. The results of MCIL becomes larger than the previous ones. If the mean value is simply taken as an indicator, the MCIL in Table 6-8 is around 1.5 - 1.8 times of that given in Table 6-5 and Table

6-6. The biggest difference, i.e. 1.8 times, is given when comparing the results from a_0 equals 0.1 mm, since the shorter crack depth makes more cycles being in Stage I due to the low SIF values.

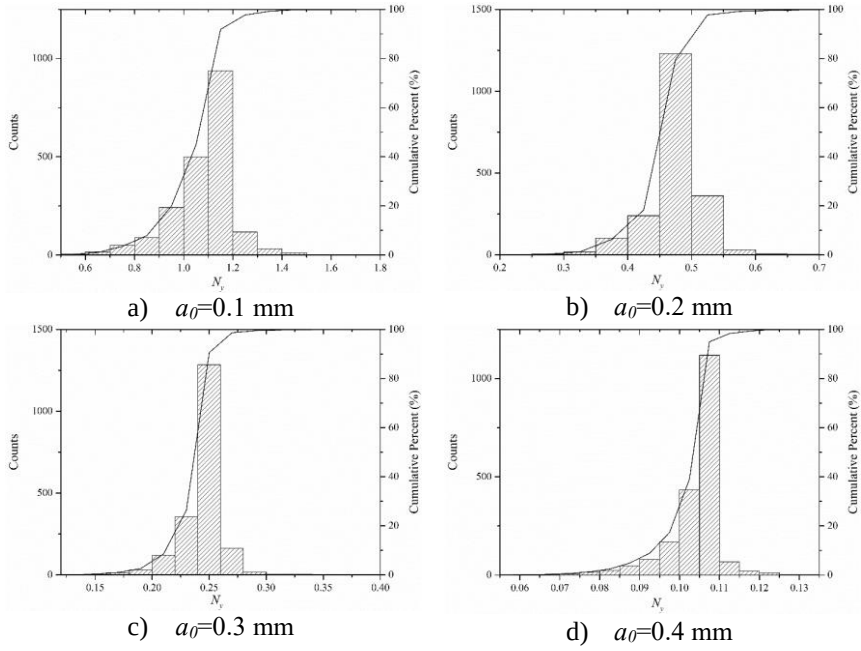

a) a_0=0.1 mm b) a_0=0.2 mm

c) a_0=0.3 mm d) a_0=0.4 mm

Fig. 6-30 Distribution of macro crack initiation life N_y for determined a_0, according to BS 7910 (BSI, 2013)

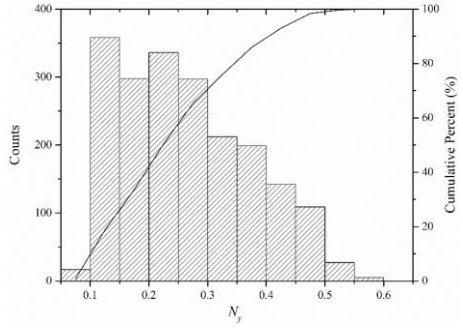

Fig. 6-31 Distribution of macro crack initiation life N_y for random a_0, according to BS 7910 (BSI, 2013)

Table 6-8 Statistics of MCIL obtained by material constants from BS 7910 (BSI, 2013)

a_0 (mm)	MCIL (years)						
	Mean value	Standard deviation	CV	Cumulative probability			
				50%	90%	95%	99%
0.1	1.2644	0.1452	0.1149	1.3006	1.3887	1.4362	1.5904
0.2	0.5569	0.0525	0.0943	0.5700	0.5964	0.6150	0.6834
0.3	0.2865	0.0215	0.0749	0.2919	0.3027	0.3072	0.3331
0.4	0.1212	0.0080	0.0658	0.1238	0.1267	0.1280	0.1372
0.2~0.4	0.3070	0.1288	0.4194	0.2902	0.5019	0.5449	0.5922

Afterwards, the MCGLs are given in Fig. 6-32, and the whole fatigue lives with respect to initial crack depth of 0.2 ~ 0.4 mm are presented in Fig. 6-33. The results obtained by BS 7910 are similar to the previous ones. The shortest MCGL is given by IIW recommendation, and the longest one is provided by the fatigue test. The one obtained by BS 7910 is in between. Nevertheless, they all lead to a result that the MCGL is around 1 year, which is still unrealistic. It means the introduction of Stage I material constants does not matter that much in calculating MCGL in this case. While speaking of material constants in Stage II, it should be noted that the values in BS 7910 are even higher than that from the fatigue test and IIW recommendation.

To sum up, the calculation of fatigue life is certainly improved by applying the two-stage model. Especially for the part of MCIL, the results seem better to a certain degree. However, the MCGL is not really affected by it. Eventually, the whole fatigue life is still not even close to the reality though. With respect to that, more discussion is provided in the next section.

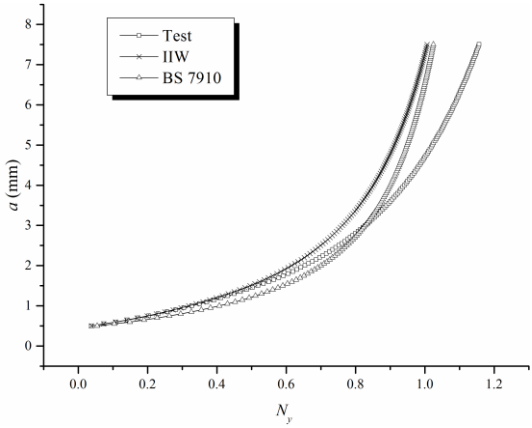

Fig. 6-32 Macro-crack growth life from 0.5 mm to 7.5 mm according to BS 7910

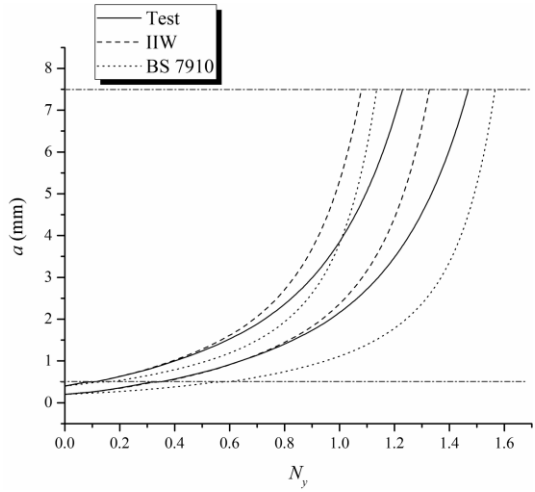

Fig. 6-33 Fatigue life for initial crack depth ranging from 0.2 mm to 0.4 mm, according to BS 7910

6.4.4. Discussions

Obviously, attention should be paid to the fact that the fatigue lives calculated by various ways are all far away from the actual case. As the results are affected by the material constants, weld defects, crack sizes, and applied loads etc., the reason could be complicated.

Firstly, the material constants could be important as their values in Stage I are so different even in magnitude order. It has been discussed in Chapter 5, that the UniGrow model enables to estimate the material constants for early-stage cracks, in which there are parameters that are difficult to determine though. Anyway, when looking back to the values in Table 5-7, the big uncertainty on this issue can be addressed, as the material constants are also quite different from the standards. The huge difference in material constants may lead to fatigue lives vary even in magnitude orders.

Secondly, due to the big differences in material constants, the weld defects such as the pores and inclusions may affect the fatigue life in a rather trivial way. Chapter 4 achieved the homogenization factor a_c to take the weld defects into account. However, the maximum value of a_c is less than 1.6 in Table 4-3. Even in the extreme case, the Paris exponent m of 11.11 given in Table 5-7 is considered, the maximum value of a_c only reached 4.42, which is still not comparable to the difference of Paris constant C in magnitude order. It is surely that the effect of weld defects can be larger if they are assumed to have bigger size and numbers. However, the material in the welded joint is not really in a porous structure, thus it should not

be the actual case. Certainly, discussion is open as a comprehensive knowledge about the microstructures is not available yet.

Another significant reason is that the effect of the pavement on this bridge was not considered. Since the KW5 bridge is actually a railway bridge, there was no pavement or ballast on it during the test by heavy trucks. As a consequence, the stress concentration could be much more severe, and the measured strain histories were larger than that on an actual bridge with OSD, resulting in the underestimation of the fatigue life.

Apart from the above, one concern should be raised that the traffic flow is all based on heavy lorries according to Eurocode 1. Therefore, no credit is given to the small vehicles, which are the biggest component of the traffic flow with their weights are always lighter than 3 tons. Hence, when heavy lorries are considered only, the majority of cycles will not lead to SIFs that are in Stage I. It explains the reason that only limited improvements were achieved by employing two-stage model in BS 7910. To better illustrate the effect of low CGRs in Stage I, one more case study is carried out in the next section, with the realistic traffic flow measured by WIM system.

6.5. A case study based on the traffic flow in China

Using the numerical way same as in the case study of Millau Viaduct, another case study was carried out on Runyang Yangtze River Bridge, China. Since the bridge is located in the east part of China, which is the region that has one of the largest traffic volumes per year, the fatigue life is the most concerned problems for it. Thus, the traffic flow was measured on this bridge for one year, providing a realistic input for this study.

Runyang Yangtze River Bridge is a large-span bridge consisting of a suspension bridge in the southern branch and a cable-stayed bridge in the northern one. The case study is conducted for the suspension bridge, abbreviated as RYRB hereinafter, whose main span is 1490-meter-long and used to be the largest in China and third largest in the world. The general view is shown in Fig. 6-34 a). The structural type of main girder is steel box girder with orthotropic steel deck. The design of the cross-section is given in Fig. 6-34 b). The thickness of deck plate is 14 mm, and that of the trapezoidal stiffener is 6 mm, i.e. the same as the Millau Viaduct. The only difference is the lower soffit width of stiffener of RYRB is 169.3 mm, while that of Millau Viaduct is 200 mm.

a) general view

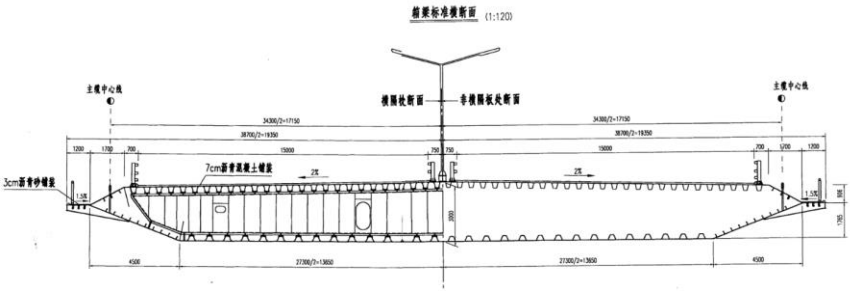

b) cross-section (unit: mm)

Fig. 6-34 The Runyang Yangtze River Bridge in Jiangsu, China

6.5.1. Traffic flow

Different from the first case study using Monte-Carlo simulation based on short-term data, the traffic flow is measured for a long period on this bridge with a WIM system. It was installed in both directions, i.e. all 6 lanes of the bridge, and consisted of two parallel piezoceramic sensors and one induction coil on each lane. Additionally, the temperature sensor was also included for the calibration of the temperature strains. Unlike the WIM system on SJDV in the case study of Millau Viaduct, this one was designed without the diagonal piezoceramic sensor and thus was not able to measure the exact transverse in-lane position of vehicles.

The final output of this WIM system can provide data about the type, speed, total length, wheel bases, number of axles, axle weights for each vehicle, as well as the lane it runs over and the temperature at that moment. The technical specifications of the WIM system are listed in Table 6-9. One thing worth to mention is the difficulty in determining the single or double tire for each axle, which may affect the stress range history due to the different landing area. None of the measured data could be an accurate indicator. To evaluate it, more discussions will be provided with respect to the influence surface in the next section.

Since the RYRB has been put into service for more than 11 years, the total traffic volume per year can be quite stable at present. Therefore, when predicting the fatigue life in the future, the calculation can be based on the traffic data for a recent year, which is the year of 2016 in this case. Due to the system maintenance, the traffic data for the period from June 15 to June 19, and from November 18 to December 4 are not available, which gives the data for 345 days in total. However, if the history of the fatigue life is to be traced, this measured traffic flow may be larger than the actual case in term of total volume, and the fatigue life will be underestimated.

Table 6-9 The technical specifications of the WIM system on RYRB

Total weight error	< 10%	Accuracy for vehicle classification	
Maximum axle weight	> 30t per axle		
Measured traffic flow accuracy	> 98%	Car	95%
Vehicle speed	25 ~ 180 kph	Light lorry	95%
Vehicle speed error	< 1.5%	Medium lorry	98%
Wheel base error	< 2%	Heavy lorry	99%
Total length error	< 7%	Coach	95%
Temperature	-30 ~ 65°C	Articulated vehicle	99%

The result of the traffic flow in the year of 2016 is given by months as shown in Fig. 6-35. Generally speaking, the traffic flow keeps consistent on each month. There is a slight decrease in January and increase in October, which are both due to the festival events. Whilst the sudden decrease on June, November, December are clearly because of the less data obtained as mentioned before. Fig. 6-36 presents the vehicle number distribution on different lanes. The lanes are numbered from west to east, which means Lane 1, 2, 3 are the lanes towards the south with Lane 1 being the slow lane; Lane 4, 5, 6 are to the north with Lane 6 being the slow lane. As the transverse influence line for rib-to-deck welded joint is quite short, the fatigue damage can be evaluated by separate lanes. The vehicle number distribution implies that the largest part of vehicles is on fast lanes, i.e. Lane 3 and 4, and that on slow lanes, i.e. Lane 1 and 6, is the least.

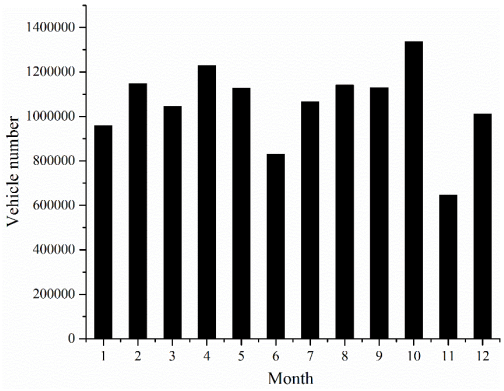

Fig. 6-35 The vehicle number on RYRB measured by WIM system in the year of 2016

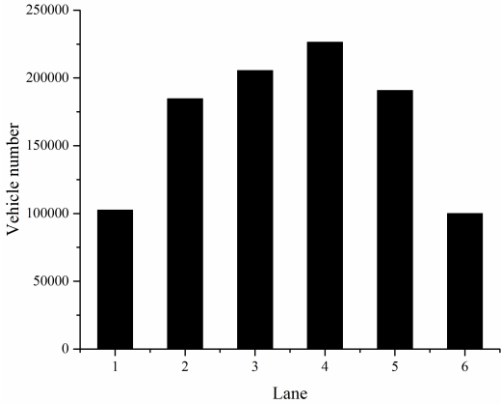

Fig. 6-36 The vehicle number distribution on different lanes on RYRB

However, the number of vehicles with more than three axles, namely the lorries, is a factor with greater importance than the total vehicle number on this issue. Fig. 6-37 demonstrates the number of vehicles for this part. Obviously, the number of lorries on the fast lanes is nearly negligible. From another perspective, the accumulative weight on different lanes also indicates that the fast lanes are of least importance in terms of fatigue, as shown in Fig. 6-38. Besides, this figure shows the total weight of traffic flow to the south is smaller than that to the north, as the data of Lane 1, 2, 3 are always lower than the corresponding lanes, i.e. Lane 4, 5, 6, respectively.

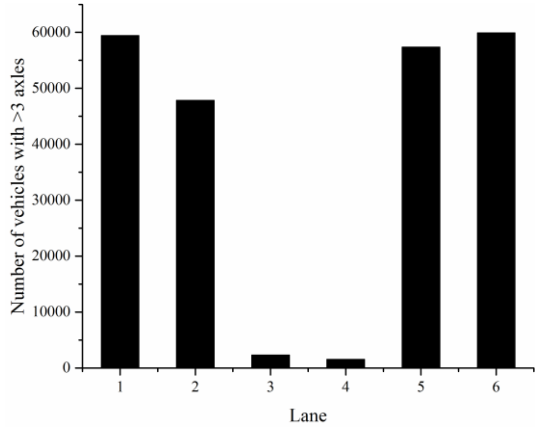

Fig. 6-37 The number of vehicles with more than 3 axles on RYRB

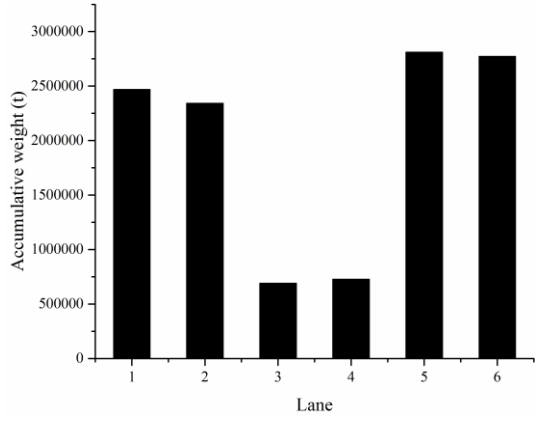

Fig. 6-38 The accumulative total weight on each lane of RYRB

Therefore, the conclusion can be drawn that the slow lane is more fatigue-prone than the fast one, due to the larger number of heavy vehicles and

accumulative total weights. According to the data from WIM system on RYRB, more attentions should be paid to the rib-to-deck welded joints on Lane 5 and 6.

6.5.2. Stress range history

To calculate the fatigue life of rib-to-deck welded joint of RYRB, the history of applied stress ranges was required for the first step. The macroscopic FEM model and the local XFEM model were built in the same way as the case study on Millau Viaduct. In fact, the design of the fatigue-prone details on these two bridges were very similar for the same 14-mm-thick deck plate and 6-mm-thick stiffeners. Consequently, the influence surfaces were basically the same. In that case, details of the numerical models are not provided here to avoid unnecessary repetitions. The study can be carried out based on same preconditions addressed before, including:

1) The bending stresses are the main part of load on the welded joint, and the membrane stresses can be ignored;

2) The semi-width of XFEM model can be selected to be 8 mm, by which the SIFs obtained are the same as in the Millau Viaduct;

3) The SIFs for the large cracks can be calculated with the shape factor given by Equation (6-3).

To obtain the stress range history, the influence surface was firstly achieved by the FEM model. As the transverse in-lane position was not available, the same condition as the case study for KW5 Bridge was applied. It means the transverse in-lane position follows discrete normal distribution on 5 locations as given in Fig. 6-17, and the tire will be positioned right above the central line of trapezoidal stiffener (Loc. 3) when the vehicle is running at the middle of lane. For the sake of simplicity in dealing with data of such a long period, it is assumed that each axle will cause one stress range cycle, whose value is determined by the static influence surface with a dynamic amplification factor. In case a road surface with good roughness is applied, the value of 1.2 is given by Eurocode (NBN, 2004).

The stress range was also affected by the landing area of the tires, which was related to the single or double tire(s) on each axle. The landing area of the single tire was 0.3 m × 0.2 m, and that of the double one is 0.6 m × 0.2 m. With respect to the loading dispersal through the 70-mm-thick bituminous concrete pavement, the loading area on the numerical model is 0.44 m × 0.34 m for single tire and 0.74 m × 0.34 m for double tires. Compared to the single tire, the double tire will reduce the stress concentration due to the enlargement of loading area. On the other hand, it also shows greater possibility to affect the stress and to induce more fatigue

cycles, due to the short influence line of OSDs. The effects in these two ways are opposite, or in another word, compensatory to each other. The stress ranges induced by single and double tire(s) were obtained by applying the same axle weight of 10 tons, as shown in Fig. 6-39. The difference on stress ranges were not so evident. More data regarding the tire types on each vehicle were preferred to get better accuracy in calculating the fatigue lives though.

Eventually, the calculation was carried out under the assumption that the single tire was used on the first two axles, and the double tire on all extra axles. It is rational to regard the first two axles using single tires as light-weighted car is the most frequent vehicle type on the bridge. While for the extra axles, the vehicle type should be the lorry or articulated vehicle, for which the double tires should be the dominate tire type.

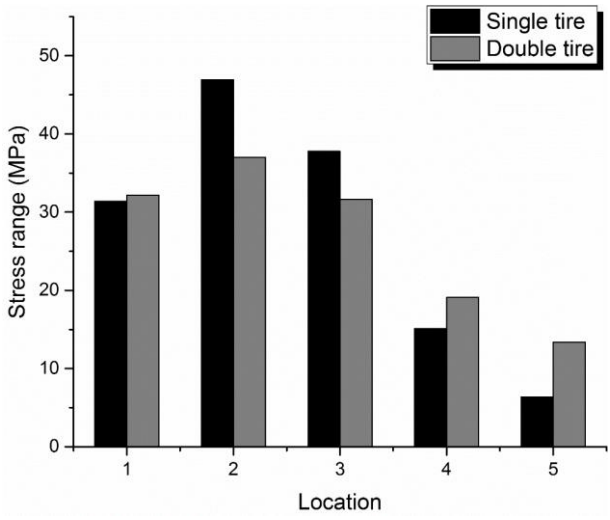

Fig. 6-39 Comparison of the stress ranges induce by single and double tire with the axle weight of 10 tons

6.5.3. Calculation of fatigue life

Since the stress range histories were generated in each lane, the fatigue life was firstly evaluated in a deterministic way without consideration of randomness induced by initial crack size and weld defects. If a 0.3-mm-deep initial crack was embedded, the fatigue life for different lanes were obtained using the two-stage model from BS 7910, as shown in Fig. 6-40. As can be expected, the fast lane had obviously longer fatigue life than other lanes, and the slow lanes were slightly more fatigue-prone than the middle lanes. It means the slow lane is the controlling case

in terms of fatigue damage on OSDs. Accordingly, the following studies were all based on the traffic flow on Lane 6, as it has the shortest fatigue life among all lanes.

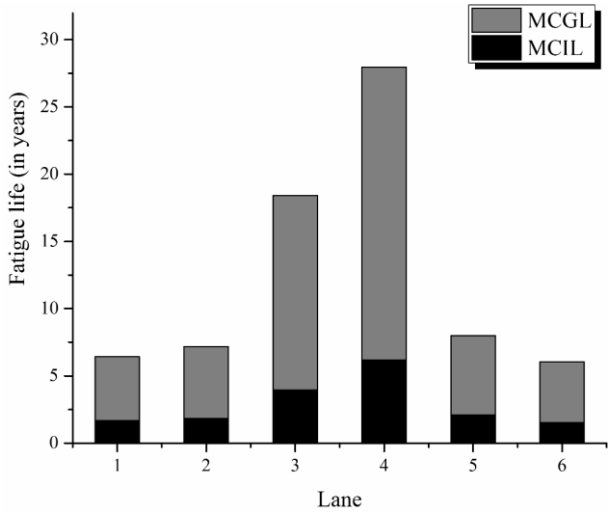

Fig. 6-40 The fatigue lives for different lanes by assuming a_0=*0.3* mm

The results of MCIL for RYRB were calculated with respect to initial crack size and weld defects, using three groups of material constants. The distributions of MCIL with respect to the material constants fitted by the fatigue test are given in Fig. 6-41 and Fig. 6-42. And those results according to IIW recommendation are shown in Fig. 6-43 and Fig. 6-44. When looking into the statistic characteristics of these two groups of results, respectively in Table 6-10 and Table 6-11, it seems the MCIL for RYRB is both around 0.8 years if the initial crack is 0.3-mm-deep. In the case of random initial crack depth, the macro-crack may be initiated in 1.4 years by 50 percent chances.

However, if the two-stage model in BS 7910 was applied, the results would be larger with a decent amount, as shown in Fig. 6-45, Fig. 6-46 and Table 6-12. For instance, the MCIL for RYRB is around 1.4 years if the initial crack is 0.3-mm-deep. When the random initial crack depth is considered, the macro-crack may be initiated in 2.6 years by 50 percent chances, and nearly 5 years by 95 percent chances. It is hard to say the value is precise, but it meets the experience on the fatigue problems on OSDs with big traffic volume, and thus could be advisable for the inspection and maintenance work.

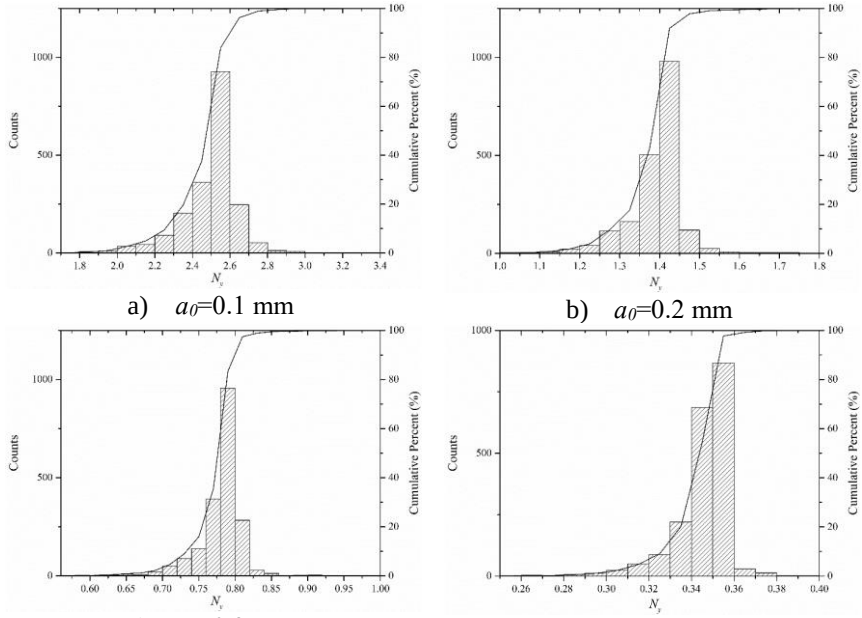

Fig. 6-41 Distribution of macro crack initiation life N_y for determined a_0, with C_0=2.70×10^{-11}, m=2.603, according to the fatigue test

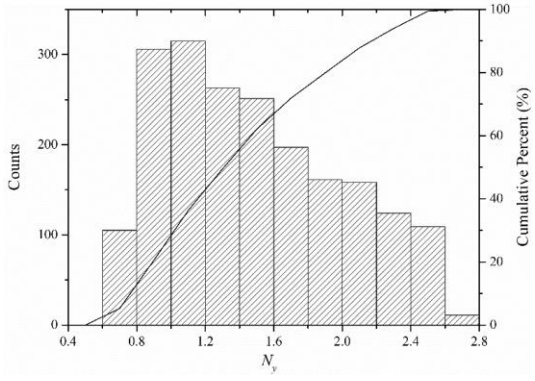

Fig. 6-42 Distribution of macro crack initiation life N_y for random a_0, with C_0=2.70×10^{-11}, m=2.603, according to the fatigue test

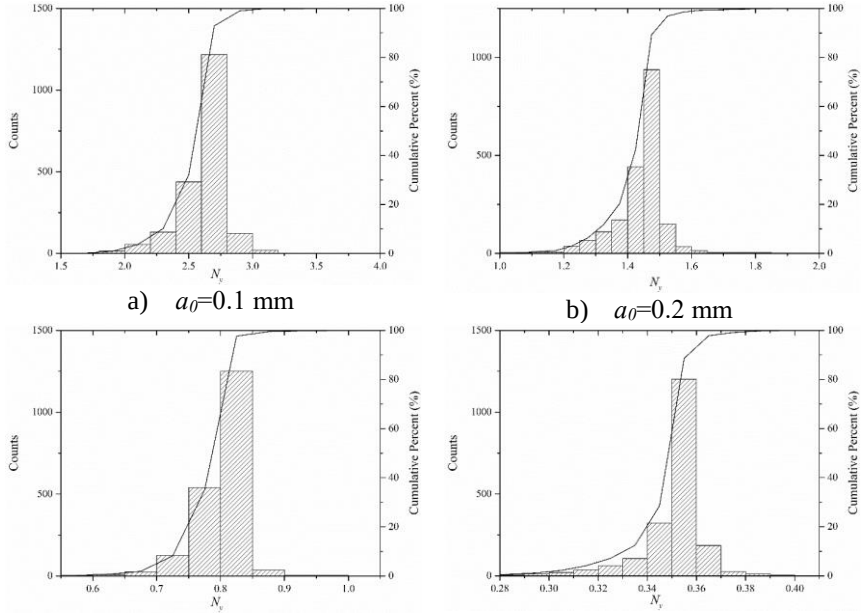

a) a_0=0.1 mm b) a_0=0.2 mm

c) a_0=0.3 mm d) a_0=0.4 mm

Fig. 6-43 Distribution of macro crack initiation life N_y for determined a_0, with C_0=1.65×10^{-11}, m=3, according to (Hobbacher, 2008)

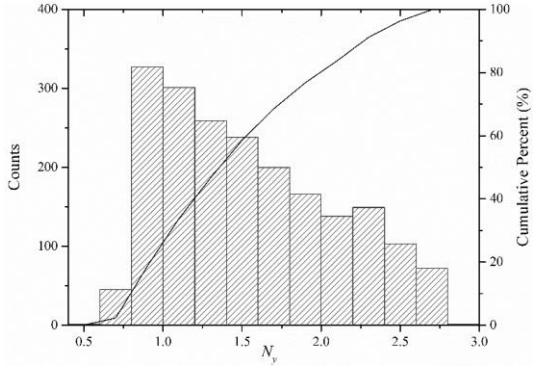

Fig. 6-44 Distribution of macro crack initiation life N_y for random a_0, with C_0=1.65×10^{-11}, m=3, according to (Hobbacher, 2008)

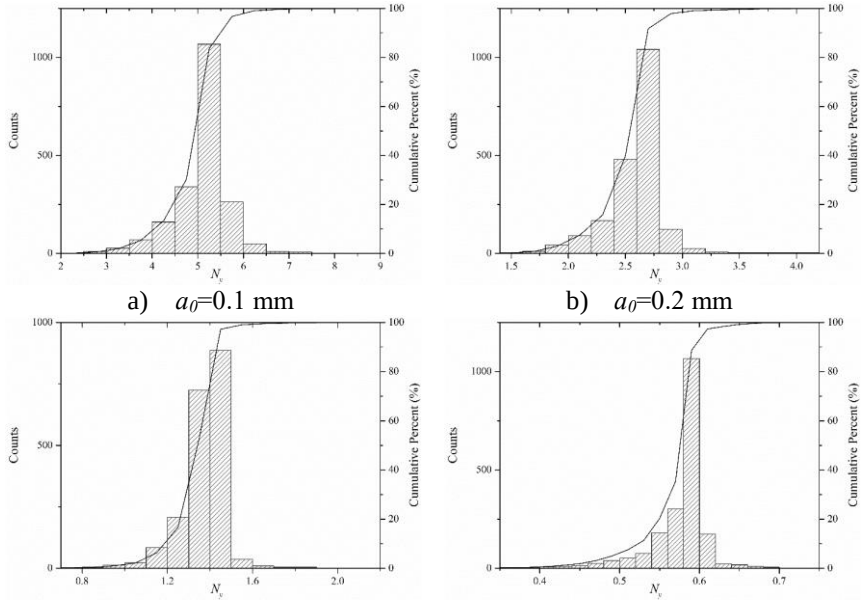

a) a_0=0.1 mm b) a_0=0.2 mm

c) a_0=0.3 mm d) a_0=0.4 mm

Fig. 6-45 Distribution of macro crack initiation life N_y for determined a_0, with two-stage model in BS7910 (BSI, 2013)

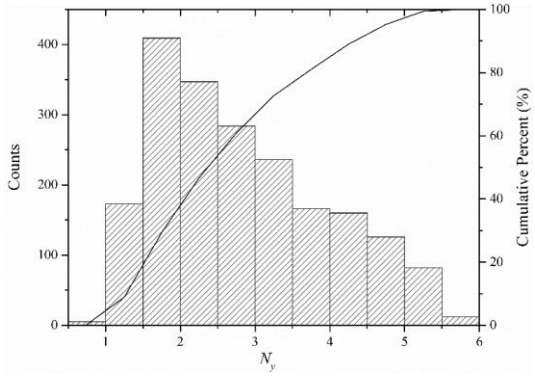

Fig. 6-46 Distribution of macro crack initiation life N_y for random a_0, with two-stage model in BS7910 (BSI, 2013)

Table 6-10 Statistics of MCIL obtained by material constants fitted with fatigue test

a_0 (mm)	MCIL (years)						
	Mean value	Standard deviation	CV	Cumulative probability			
				50%	90%	95%	99%
0.1	2.5011	0.1514	0.0605	2.5418	2.6284	2.6738	2.8167
0.2	1.3918	0.0682	0.0490	1.4100	1.4430	1.4658	1.5468
0.3	0.7812	0.0307	0.0393	0.7892	0.8040	0.8101	0.8443
0.4	0.3455	0.0121	0.0349	0.3494	0.3535	0.3554	0.3682
0.2~0.4	1.4900	0.5109	0.3429	1.4130	2.2524	2.4035	2.5729

Table 6-11 Statistics of MCIL obtained by material constants from IIW Recommendation (Hobbacher, 2008)

a_0 (mm)	MCIL (years)						
	Mean value	Standard deviation	CV	Cumulative probability			
				50%	90%	95%	99%
0.1	2.6412	0.1821	0.0694	2.6726	2.7777	2.8331	3.0083
0.2	1.4414	0.0811	0.0563	1.4628	1.5024	1.5298	1.6276
0.3	0.8018	0.0361	0.0451	0.8111	0.8286	0.8359	0.8768
0.4	0.3520	0.0141	0.0400	0.3566	0.3615	0.3636	0.3788
0.2~0.4	1.5478	0.5429	0.3507	1.4554	2.3638	2.5272	2.7102

Table 6-12 Statistics of MCIL obtained by material constants from BS 7910 (BSI, 2013)

a_0 (mm)	MCIL (years)						
	Mean value	Standard deviation	CV	Cumulative probability			
				50%	90%	95%	99%
0.1	5.1192	0.5880	0.1149	5.2657	5.6225	5.8146	6.4391
0.2	2.5927	0.2445	0.0943	2.6537	2.7768	2.8634	3.1818
0.3	1.3694	0.1026	0.0749	1.3949	1.4465	1.4681	1.5921
0.4	0.5782	0.0381	0.0658	0.5904	0.6043	0.6104	0.6544
0.2~0.4	2.8411	1.1335	0.3990	2.6046	4.5619	4.9709	5.4130

In terms of MCGL, the difference between three different models was not so obvious. According to the results shown in Fig. 6-47, the MCGLs are always in a range from 4 to 4.5 years. One noticeable change compared to Fig. 6-32 for KW5 Bridge is that the results from BS 7910 is obviously larger than those from the test. The reason is, when big amounts of light vehicles, such as cars and light lorries, are taken into account, the CGRs in Stage I are more influential as more cycles will

be in that stage. Therefore, the total damage will be smaller than that caused by the traffic loadings in Eurocode, which consists of heavy lorries weight more than 20 tons only.

The whole fatigue life of RYRB is then provided in Fig. 6-48, by combining the 95 percent confidence interval for the MCILs and deterministic MCGLs. It indicates that the crack will go through the deck plate and reach the half thickness in a period ranging from 4.3 to 7.2 years. The value is surely in the same magnitude order as the actual project presents. However, this is only a result given in a conservative context, and is hard to be determined accurately, as there are a bunch of parameters that will have effects. More discussions on the results were given in the next section.

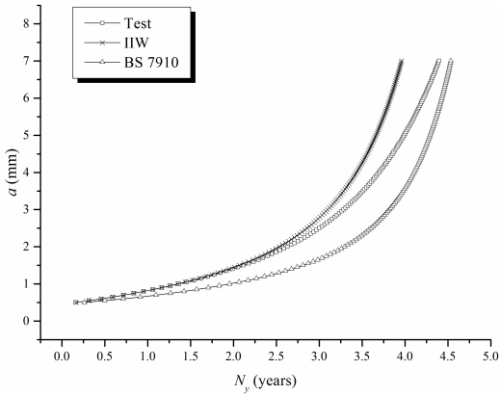

Fig. 6-47 Macro-crack growth life from 0.5 mm to 7 mm

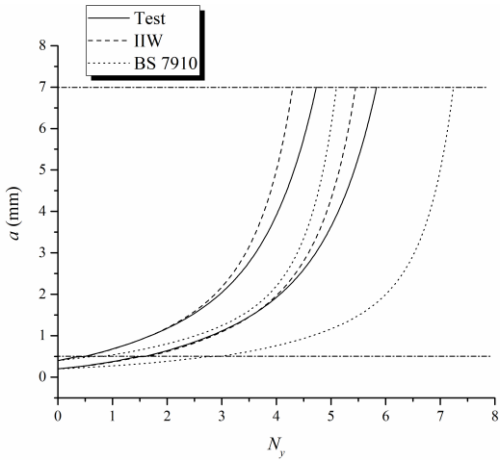

Fig. 6-48 Fatigue life for initial crack depth ranging from 0.2 mm to 0.4 mm

6.5.4. Discussions

The parameters, such as the unknown weld defects, the residual stresses, are certainly important for the results, as discussed before. Apart from that, this case study was carried out conservatively in other aspects, and the possible sources of error should be analyzed.

Firstly, only the load dispersal effect of the pavement was taken into account in the calculation, and the effect on reducing the stresses of weld joints was neglected. Literatures show a reduction up to 20 to 30 percent of stresses (De Backer et al., 2008), depending on the type of it. However, this effect is severely affected by the temperatures and thus hard to quantify.

Secondly, the traffic flow was measured for the year of 2016, which means the traffic volume has already increased to a certain level. Therefore, the stress range history was in fact overestimated when applying to the initial crack. However, as the WIM system was not installed on RYRB for the early years, no data was available to evaluate the error.

Thirdly, the applied transverse in-lane position was from the Eurocode, which follows normal distribution and could be unrealistic. The measured transverse in-lane positions by the WIM system of Millau Viaduct implied that a Gumbel distribution will be more proper (Wang et al., 2017). Nevertheless, it was also dependent on the lane layout and the driving custom in the local region, thus the suggestion on the Eurocode was applied.

Additionally, the results were related to material constants in both Stage I and II. The material constants in Stage I are quite sensitive factors to the results, since it not only determines the CGR but also affects the transition point that defines the stages. Therefore, the material constants are extremely significant when the realistic traffic load, which consists of big amounts of light vehicles, is considered. However, their values provided in various sources are surely far away from consistent. On the other hand, the material constants in Stage II are pretty similar, and thus is more reliable.

In summary, regarding the various parameters, the precise fatigue life calculation for OSD requires a thorough knowledge concerning multiple areas. However, the limit on the experimental or measuring method makes it difficult, especially for the Stage I crack growth rate, residual stresses and weld defects.

CHAPTER 7

CONCLUSIONS AND FUTURE RESEARCHES

7.1. Conclusions

On the issue of the common fatigue problems on orthotropic steel decks (OSDs), the traditional studies are proven to be not reliable, as the fatigue tests fail to achieve consistent results, and the numerical investigations are not always on the safe side according to the experiences on actual projects. It could be attributed to the fact that the parameters in multiple scales are not taken into account, especially the ones related to the early-stage fatigue cracks. This study is carried out with respect to multiscale concerns, to propose an efficient and simple method that is applicable on the actual projects.

In **Chapter 1**, a general introduction on the issue of fatigue problems on orthotropic steel decks was provided. The literature related to the fatigue design, and fatigue-prone details on OSDs were reviewed first, leading the subject to that related to the weld fatigue under structural loadings, which is a multiscale problem essentially. Accordingly, a few objectives were put forward for this study.

For the first step, a fatigue test on small scale specimens was conducted, as elaborated in **Chapter 2**. The test results suggested that the fatigue crack always occurs at the rib-to-deck weld toe, and caused final fracture of the specimens. In order to understand the behavior in the whole process of fatigue crack growth, the applied loadings were designed to generate beach marks during the test, and the fractographic and metallographic analyses were carried out after the specimen fails. A preliminary analysis implied that the heterogeneities of microstructures and weld defects will affect the crack growth rates (CGRs) in early stages. Therefore, with respect to the uncertainties in such a meso-scale, a tool with great efficiency for massive computation was to be developed.

Chapter 3 introduced the brief idea of extended finite element method (XFEM), which was perfect in dealing with the discontinuity problems. As the geometries were independent to meshes, the XFEM apparently owns the advantage of being free for re-mesh, which was quite beneficial when random weld defects were to be evaluated by solving a big number of representative volume elements (RVEs). Therefore, an XFEM program was developed using MATLAB, with which the random defects can be taken into account. Additionally, to be feasible on the RVEs extracted from rib-to-deck welded joints, a specific level-set function was established regarding the weld geometries, namely the weld toe flank angles.

Based on the XFEM program, **Chapter 4** proposed a homogenization method on weld defects, with a criteria of equivalent crack growth length. Numerical examples and parametric analysis were conducted for validation. However, there

lacked knowledge on the sizes, numbers and spatial distributions of weld defects, due to the limitation of detection or identification technologies, even though they can be occasionally observed by scanning electron microscope (SEM). Therefore, the homogenization can only be conducted under several assumptions about the weld defects.

In **Chapter 5**, multiscale methods were built in a numerical way with respect to the fatigue test. The identification of the beach marks, namely the crack shapes and dimensions, was given in the first place. Accordingly, a relation between the crack face area and the crack depth was proposed to avoid the problem in calculation because of the longitudinal initial crack merging. Then two multiscale methods were established and compared, and the crack growth behaviors in correspondence with the stress intensity factors were analyzed. As a result, different stages in crack growth can be addressed, among which the Stage I and II are of main concern on this issue. The achieved material constants in Stage II seemed to agree with the ones provided in the standards, but those for Stage I is not clear enough, as the fatigue test cannot provide sufficient information on the CGRs in this stage.

Chapter 6 further introduced all the methods and knowledges above into the application on three actual projects, including the Millau Viaduct in southeast France, the KW5 Bridge on Albert Canal, Belgium, and the Runyang Yangtze River Bridge, China. In summary of the results, the traffic flow on the bridge will affect the fatigue lives significantly. Apart from that, the material constants of the fatigue-prone details are of great importance as well, thus three groups of them are applied in the calculation, including: *a*) fitted by the test results given in Chapter 5; *b*) from the IIW recommendation; *c*) from the British standard BS 7910, abbreviated as Group *a*, *b*, and *c* hereinafter, respectively. Among them, the Group *c* was using a two-stage model that pays more attentions to the low CGR in Stage I, and thus will achieve better results.

In the study on Millau Viaduct, the traffic flow was provided using Monte-Carlo simulation based on a short-term data from WIM system. The WIM system was designed with an extra diagonal piezoceramic sensor, thus the precise transverse in-lane position of tires were measured. With the numerical method provided in Chapter 5, the fatigue lives were calculated with material constants of Group *a* & *b*. The results were in good agreement with each other, showing the fatigue life of more than 32 years even in a conservative scenario. It can be concluded that the fatigue problem is not a major concern for Millau Viaduct, due to the relatively small traffic volume in that region.

As for the study on KW5 Bridge, the traffic flow and transverse in-lane positions were hypothetic according to Eurocode 1 (NBN, 2004). The fatigue cycles were calculated based on the on-site test results of strains. However, the fatigue lives were extremely low when calculated by material constants of Group *a* & *b*. With respect to the low CGR in Stage I, the material constants of Group *c* were then introduced. The results were improved to a certain degree, but still far from acceptable, which could be attributed to the large and design-oriented traffic volume consists of lorries only.

In that case, the study on Runyang Yangtze River Bridge was carried out, with a long-term traffic flow data measured by WIM system for one year. When using the results corresponding to a cumulative probability of 50 % as an indicator, the MCILs obtained by material constants of Group *a* & *b* were less than 1.5 years, which were still quite small. In contrast, that value obtained by two-stage model of Group *c* was 2.6 years. The fatigue life till crack reaching half thickness of the deck plate was in a range from 5 to 7.2 years, which was in the same order of magnitude as the actual project presents, even provided in a conservative context. The result can be advisable on the time to conduct visual inspections and further retrofitting works.

7.2. The outcome regarding the objectives

To further emphasize the outcome of this study, the following key points are elaborated in correspondence with the problems and objectives brought up in Chapter 1.

1) **A process-oriented fatigue test on specimens of OSD was designed and conducted.** During the test, beach marks were produced by applying cyclic loads with different ranges and types, according to which the crack sizes and crack growth rates in different stages can be addressed. After the fatigue failure of each specimen, the fractography and metallography in the region of interest were analyzed. The results pointed out that the coarse grained HAZ is vulnerable to cyclic loads, as the intergranular crack occurs primarily there, and thus can be regarded as the initial crack.

2) **An XFEM program was developed in order to numerically investigate the randomness in crack sizes, weld defects of mesoscopic models, and a homogenization method with a criteria of equivalent crack growth length was put forward to make it feasible in multiscale problems.** To validate the homogenization method, some numerical examples are provided, showing that the error is tiny due to the relatively small crack growth rate of early-stage cracks. The parametric analysis of the homogenization method presented the main factors of the weld

defects on crack growth problems. It can be inferred that the large standard deviation of the effects from non-detectable weld defects could be important, since the weakest part is always critical for macroscopic structures.

3) **Two types of multiscale methods were established to link the macroscopic model and the mesoscopic one.** The homogenization method gives the access to consider weld defects in multiscale problems. However, the crack itself, especially being a long and shallow one in the early-stage, is difficult to consider due to the computation ability issue. Thus, two types of multiscale methods, i.e. a sub-model based one and a non-concurrent one, were established and applied to calculate the stress intensity factors of the cracks in the test, and to reproduce the crack growth process of the test. Both of them were built with a combination of the XFEM program developed in Chapter 3 and the software SAMCEF with an XFEM module embedded. The comparison of them confirmed that the non-concurrent multiscale method is of good accuracy, and most importantly, has great efficiency in calculating the stress intensity factors, as it uses a mesoscopic model fully independent to the macroscopic one.

4) **Three case studies on actual projects were carried out, obtaining the fatigue life of OSDs under realistic or standards-specified traffic loads.** The fatigue life was calculated in two parts, i.e. the calculation of macro crack initiation life (MCIL), and macro crack growth life (MCGL). The former one was given in a probabilistic way for the sake of the randomness induced by the initial crack depth and other weld defects. Whilst the latter one was provided in a deterministic way as the uncertain influence factors were of less scatter then. The results show that the traffic flow on the Millau Viaduct is much lighter or easier than that on the Runyang Yangtze River Bridge. Hence, the fatigue problem will not be a concern for Millau Viaduct in decades, while in contrast, the Runyang Yangtze River Bridge may suffer from it in less than ten years. In addition, according to the short and unrealistic fatigue life obtained for KW5 Bridge, the traffic load recommended by Eurocode is not proper when using fracture mechanics to evaluate the fatigue performance.

7.3. Future researches

This dissertation provides proposals to study the fatigue problems on OSDs in a multiscale context. With parameters obtained by the fatigue test, the fatigue lives of projects under various random traffic loadings are calculated, and validated by comparing with the ones with standards or specifications. On the other hand, some hypotheses are addressed as preconditions in building and conducting the method, and the obtained results should be used with caution, as discussed in the previous chapters. To better understand the fatigue behavior and predict the fatigue life with higher accuracy, future works are required for the following aspects.

7.3.1. Residual stress acquisition

The residual stress is often taken as a major reason of the fatigue failure, and the reduction of it is proven quite beneficial to the fatigue performance of structures. However, as the residual stress itself will not produce a stress range, it mainly affects the mean stress of fatigue cycles, or in another classical way on fatigue studies, the stress ratio. A similar concept of effective stress ratio was proposed by (Barsoum & Barsoum, 2009) to consider the weld residual stress. In case the fracture mechanics is applied on this issue, the residual stress could affect the SIF range, as the compressive stresses will lead to zero-value SIFs instead of negative ones. Hence, the fatigue life of welded joint is surely getting shorter if the tensile residual stress, as the mean stress, is larger than the stress induced by compressive applied loads. Another possible solution is to use an effective stress intensity factor range as a combination of the maximum value and the applied value. It will, of course, result in a different set of material properties compared to classical Paris law. By any means, the comprehensive knowledge on residual stresses is required. Various problems may appear in the residual stress acquisition by experimental or numerical ways, especially on the spatial distribution. Afterwards, it is possible to investigate and understand the effect of residual stress on fatigue performance profoundly.

7.3.2. Fatigue behavior in Stage I

The discussions in previous chapters, especially the ones in Chapter 5 and 6, indicated the importance of a clear view of fatigue behavior in Stage I. The homogenization method shows that the weld defects may only take a small part of the reasons that causes the scattered CGRs in Stage I. However, the realistic sizes, shapes, and spatial distributions of them are waiting to be determined, which is still a job with considerable difficulties. On the other hand, the heterogeneous materials in the welded joints could be a more important factor waiting to be explored. Literatures have proposed different models to calculate the crack growth on that issue (Remes et al., 2012, Mikheevskiy et al., 2015), and basically a relevance can be addressed between the microscopic hardness and the material properties concerning fatigue performance. The problem is that not all parameters in these models are measurable, or even next to impossible to determine for macroscopic structural projects, not to mention that none of these models showed universal applicability. Therefore, future works should be focused on this part, to propose a model that is feasible for welded joints of OSDs.

7.3.3. Retrofitting work on cracked components of OSDs

The end point in this study is set to be the moment crack reaches half thickness of deck plate, as it is when the visual inspection can easily address fatigue crack due to the damage of paint films. Additionally, as the crack tip is already far away from the HAZ, it can be inferred that the effect of residual stress could be a lot less than that in the initial state, even though the actual distribution may not be clearly known. Under that circumstance, the cracked area can be retrofitted and renovated to keep other types of damages from being introduced, such as corrosion and rust. If that is not the case, the crack may grow through the deck plate in a much lower CGR or even stop growing by itself. Hence, one of the future researches is the retrofitting job to prevent further damages for cracks, including the evaluation of the necessity to retrofit as well.

7.3.4. Other types of cracks on OSDs

Even though the fatigue crack at weld toe caused the failure on all specimens in the fatigue test and in other reported tests on small-scale specimens, it is not the most observed type of crack on actual OSDs. Comparatively, fatigue cracks on the rib-to-diaphragm welded joints are more common. Most of the cracks, including the rib-to-deck weld toe crack, belong to the detectable and fixable category, and are not so harmful to the whole OSD. The only exception is the rib-to-deck weld root crack, which is dangerous because of the apparent difficulty in inspections. After it goes through the weld bead or, in the worst case, the deck plate, the fatigue damage could have caused severe reduction of serviceability. The maintenance cost can be quite high then. Therefore, future research on predicting the rib-to-deck weld root crack should be conducted, to provide practical recommendations on dealing with this type of crack. For that purpose, the experimental study is certainly preferred, on large-scale specimens, or on well-designed small-scale specimens with diaphragms as analyzed in Chapter 2.

7.3.5. Novel fatigue design methods for OSDs

After all, the studies on fatigue mechanisms and all influence factors should be put into practice, and thus gives two requirements to the design methods for OSDs to fulfill: i) in a probabilistic context and ii) with solutions to multiscale problems. The former one provides the capability to consider the mesoscopic or even microscopic characteristics, as they are inevitably with uncertainties, whilst the latter one ensures the feasibility on the macroscopic structures. Based on the widely-applied methods nowadays, the design theory for reliability is a suitable option. In the meantime, a direct probabilistic design theory may provide an alternative way. From another perspective, a design method with respect to the cost

during the whole life-cycle is also valuable on this issue, due to the considerable amount of it compared to the construction cost. It is quite true for structures like OSDs specifically, since the fatigue crack is not really devastating to the structural safety itself, but requires frequent inspections and retrofits for the sake of serviceability.

APPENDIX A

With the micro-chemical energy analyses using the energy dispersive spectroscopy (EDS) device of the laboratory, Bruker Quatanax 200, the chemical composition of inclusions can be achieved. Two inclusions found by both fractographic and metallographic analysis, noted as Inclusion I and Inclusion II respectively, were given as an instance here.

Fig. A-1 presents an analysis on Inclusion I by fractograhpy, which seems like a void or a secondary crack on the image. According to the results, the chemical composition of it is MnS, indicating that there is an entity of it, and lead to a void on the fracture face consequently. In contrast, Fig. A-2 gives a clearer instance by analyzing Inclusion II on metallogrphy. Simiarly with the previous one, the inclusion is also mainly MnS, while there could be other complex oxides combined as well.

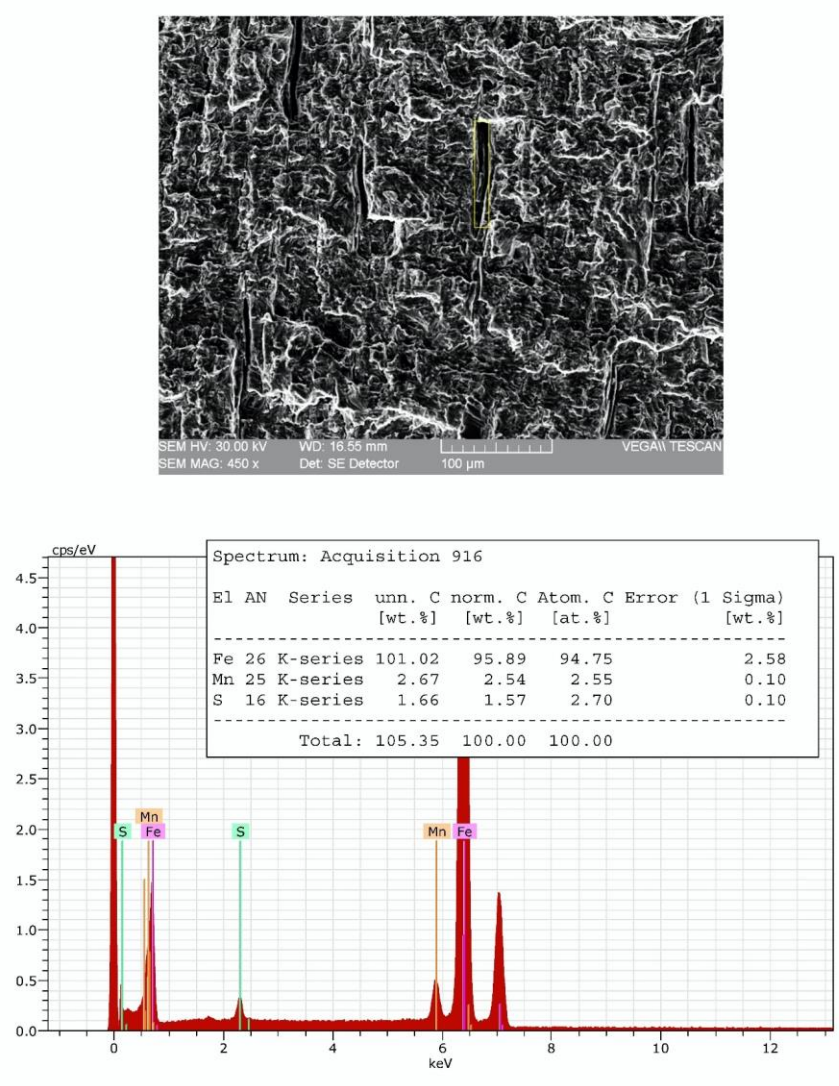

Fig. A-1 The micro-chemical energy analyses on Inclusion I

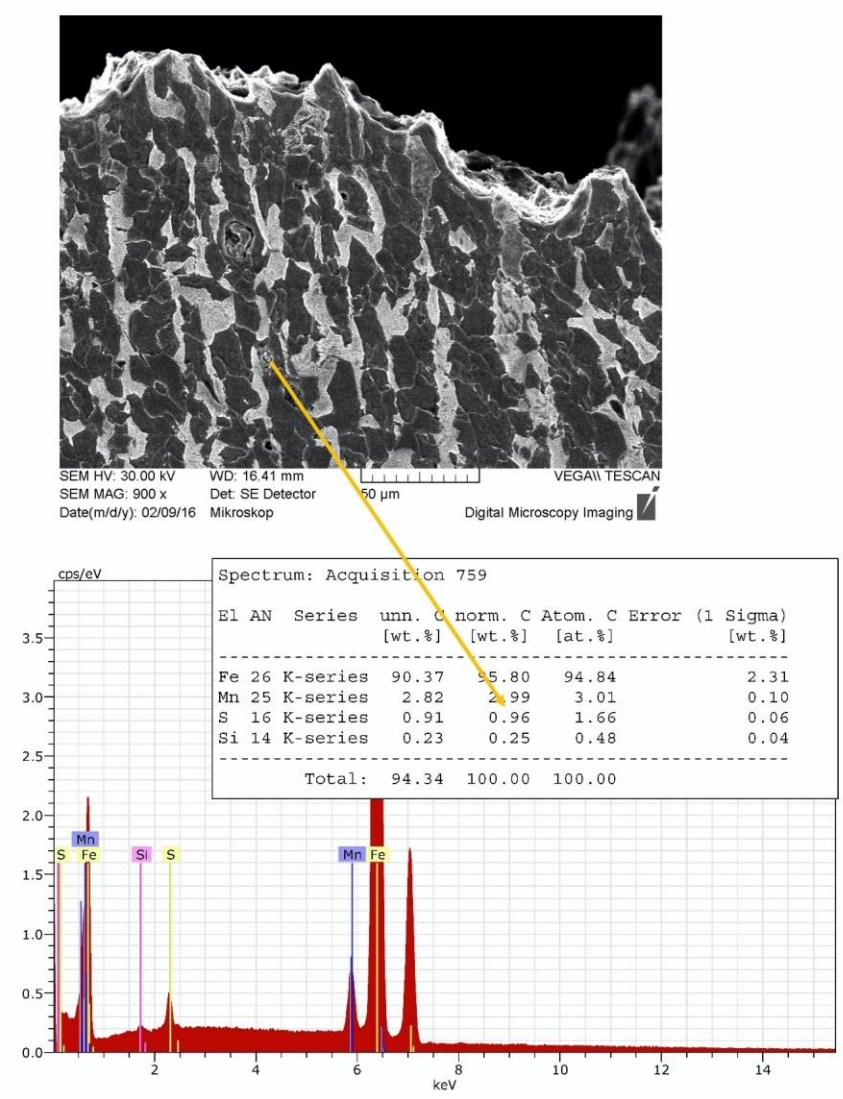

Fig. A-2 The micro-chemical energy analyses on Inclusion II

APPENDIX B

To analyze the crack growth rate for the test specimens, a method of calculating the SIFs is necessary under the frame of fracture mechanics. A widely-accepted way is to calculate it based on Equation (2-4), in which the shape factor *F* is related to complex geometrical parameters. On the issue of a semi-elliptical cracks on T-butt joint, Bowness and Lee (2000) conducted a parametric study on the effect of geometry to SIFs, stated that the crack depth *a*, the crack half length, *c*, the deck plate thickness, *T*, the weld toe flank angle, θ, and the attachment (including the stiffener and the weld) width on deck plate, *L*, are the main factors, as shown in Fig. B-1.

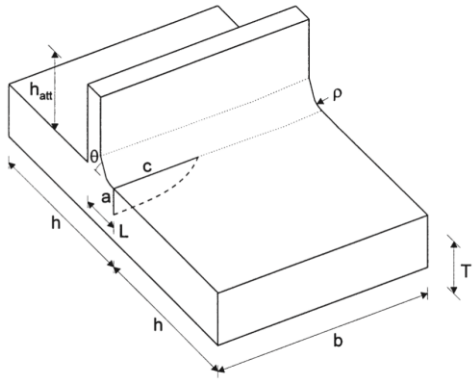

Fig. B-1 Geometrical parameters that affect the SIF of weld toe crack (Bowness and Lee, 2000)

Accordingly, the empirical equation they put forward to calculate *F* was adopted in the preliminary study on the test, as given by

$$F = f_1\left(\frac{a}{T}, \frac{a}{c}\right) + f_2\left(\frac{a}{T}, \theta\right) + f_3\left(\frac{a}{T}, \theta, \frac{L}{T}\right) \quad \text{(B-1)}$$

where f_1, f_2, f_3 are the fitted equations, whose form will differ for the different point on crack front and for the different loading types. For the case of deepest point on crack front under bending loading, f_1, f_2, f_3 are given by,

$$f_1\left(\frac{a}{T}, \frac{a}{c}\right) = 0.065916\left(\frac{a}{T}\right)^{A_1+[A_2(\frac{a}{T})]^{A_3}} + 0.52086\exp\left[\left(\frac{a}{T}\right)^{-0.10364}\right] + A_4 \quad \text{(B-2)}$$

where

$$A_1 = -0.014992\left(\frac{a}{c}\right)^2 - 0.021401\left(\frac{a}{c}\right) - 0.23851$$

$$A_2 = 0.61775\left(\frac{a}{c}\right)^{-1.0278}$$

$$A_3 = 0.00013242\left(\frac{a}{c}\right) - 1.4744$$

$$A_4 = -0.28783\left(\frac{a}{c}\right)^3 + 0.58706\left(\frac{a}{c}\right)^2 - 0.37198\left(\frac{a}{c}\right) - 0.89887$$

$$f_2\left(\frac{a}{T},\theta\right) = A_5(1-\frac{a}{T})^{A_6} + A_7(\frac{a}{T})^{A_8} \quad \text{(B-3)}$$

where

$$A_5 = 0.11052(\theta)^2 - 0.19007(\theta) + 0.059156$$

$$A_6 = -15.124(\theta)^2 + 15.459(\theta) - 0.0036148$$

$$A_7 = -0.047620(\theta)^2 + 0.16780(\theta) - 0.081012$$

$$A_8 = -17.195\left(\frac{a}{T}\right)^2 + 12.468\left(\frac{a}{T}\right) - 0.51662$$

$$f_3\left(\frac{a}{T},\theta,\frac{L}{T}\right) = A_9\left(\frac{a}{T}\right)^{A_{10}\theta^2+A_{11}\theta+A_{12}} + A_{13}\left(\frac{a}{T}\right)^{A_{14}} + A_{15}\left(\frac{a}{T}\right)^2 + A_{16}\left(\frac{a}{T}\right) + A_{17} \quad \text{(B-4)}$$

where

$$A_9 = 0.75722(\theta)^2 - 1.8264(\theta) + 1.2008$$

$$A_{10} = -0.013885\left(\frac{L}{T}\right)^3 - 0.014872\left(\frac{L}{T}\right)^2 + 0.55052\left(\frac{L}{T}\right) - 0.072404$$

$$A_{11} = -0.065232\left(\frac{L}{T}\right)^3 + 0.54052\left(\frac{L}{T}\right)^2 - 1.8188\left(\frac{L}{T}\right) - 0.0022170$$

$$A_{12} = -0.034436\left(\frac{L}{T}\right)^2 + 0.28669\left(\frac{L}{T}\right) + 0.36546$$

$$A_{13} = -0.61998(\theta)^2 + 1.4489(\theta) - 0.90380$$

$$A_{14} = 0.43912(\theta)^2 - 1.3345(\theta) + 0.57647$$

$$A_{15} = -0.35848\left(\frac{L}{T}\right)^2 + 1.3975\left(\frac{L}{T}\right) - 1.7535$$

$$A_{16} = 0.31288\left(\frac{L}{T}\right)^2 - 1.3599\left(\frac{L}{T}\right) + 1.6611$$

$$A_{17} = -0.0014701\left(\frac{L}{T}\right)^2 - 0.0025074\left(\frac{L}{T}\right) - 0.0089846$$

As for other cases like crack ends (longitudinal tip of crack) and/or under membrane loading, similar equations were provided, which are not listed here since they are not the main concern in this study.

BIBLIOGRAPHY

AASHTO (American Association of State Highway and Transportation of Officials). (2012). *LRFD Bridge Design Specifications*. Washington D.C.

Abbas, S., Alizada, A., & Fries, T.-P. (2010). Model-independent approaches for the xfem in fracture mechanics. *Int J Numer Methods Eng, 1*, 0-10.

ASTM International. (2013). *ASTM E837-13a: Standard Test Method for Determining Residual Stresses by the Hole-Drilling Strain-Gage Method.* ASTM International, West Conshohocken, U.S.

ASTM International. (2015). *ASTM E647-15e1: Standard Test Method for Measurement of Fatigue Crack Growth Rates.* ASTM international, West Conshohocken, U.S.

Atzori, B., Lazzarin, P., & Meneghetti, G. (2008). Fatigue strength assessment of welded joints: From the integration of paris' law to a synthesis based on the notch stress intensity factors of the uncracked geometries. *Engineering Fracture Mechanics, 75*(3), 364-378.

Atzori, B., Meneghetti, G., & Susmel, L. (2005). Material fatigue properties for assessing mechanical components weakened by notches and defects. *Fatigue & Fracture of Engineering Materials & Structures, 28*(1-2), 83-97. doi: 10.1111/j.1460-2695.2004.00862.x

Aygül, M., Al-Emrani, M., & Urushadze, S. (2012). Modelling and fatigue life assessment of orthotropic bridge deck details using fem. *International Journal of Fatigue, 40*, 129-142. doi: http://dx.doi.org/10.1016/j.ijfatigue.2011.12.015

Aygül, M., Bokesjö, M., Heshmati, M., & Al-Emrani, M. (2013). A comparative study of different fatigue failure assessments of welded bridge details. *International Journal of Fatigue, 49*, 62-72. doi: http://dx.doi.org/10.1016/j.ijfatigue.2012.12.010

Baby, S., Balasubramanian, T., & Pardikar, R. J. (2003). Ultrasonic sizing of embedded vertical cracks in ferritic steel welds. *Theoretical and Applied Fracture Mechanics, 40*(2), 145-151. doi: http://dx.doi.org/10.1016/S0167-8442(03)00042-9

Barati, E., & Azimi, M. (2016). Use of j-integral for prediction of critical fracture load in plates with u-notches under mixed mode loading. *Theoretical*

and Applied Fracture Mechanics, 82, 51-58. doi: http://dx.doi.org/10.1016/j.tafmec.2015.12.006

Barsoum, Z., & Barsoum, I. (2009). Residual stress effects on fatigue life of welded structures using lefm. *Engineering Failure Analysis, 16*(1), 449-467. doi: http://dx.doi.org/10.1016/j.engfailanal.2008.06.017

Basan, R., Rubeša, D., Franulović, M., & Križan, B. (2010). A novel approach to the estimation of strain life fatigue parameters. *Procedia Engineering, 2*(1), 417-426. doi: http://dx.doi.org/10.1016/j.proeng.2010.03.046

Beghini, M., Bertini, L., & Fontanari, V. (1997). Fatigue life evaluation by weight functions for orthotropic bridge decks. *Theoretical and Applied Fracture Mechanics*, 28(1), 41-50.

Beghini, M., Bertini, L., & Vitale, E. (1994). Fatigue crack growth in residual stress fields: Experimental results and modelling. *Fatigue & Fracture of Engineering Materials & Structures*, 17(12), 1433-1444.

Belytschko, T., & Black, T. (1999). Elastic crack growth in finite elements with minimal remeshing. *International Journal for Numerical Methods in Engineering, 45*(5), 601-620.

Belytschko, T., Moës, N., Usui, S., & Parimi, C. (2001). Arbitrary discontinuities in finite elements. *International Journal for Numerical Methods in Engineering, 50*(4), 993-1013.

Beretta, S., & Previtali, B. (2009). Estimate of maximum pore size in keyhole laser welding of carbon steel. *Science and Technology of Welding & Joining, 14*(2), 106-116.

Berto, F., & Lazzarin, P. (2009). A review of the volume-based strain energy density approach applied to v-notches and welded structures. *Theoretical and Applied Fracture Mechanics, 52*(3), 183-194. doi: http://dx.doi.org/10.1016/j.tafmec.2009.10.001

Berto, F., & Lazzarin, P. (2010). Fictitious notch rounding approach of pointed v-notch under in-plane shear. *Theoretical and Applied Fracture Mechanics, 53*(2), 127-135. doi: http://dx.doi.org/10.1016/j.tafmec.2010.03.003

Berto, F., Lazzarin, P., & Radaj, D. (2008). Fictitious notch rounding concept applied to sharp v-notches: Evaluation of the microstructural support factor for different failure hypotheses. Part i: Basic stress equations. *Engineering Fracture Mechanics, 75*(10), 3060-3072. doi: http://dx.doi.org/10.1016/j.engfracmech.2007.12.011

Berto, F., Lazzarin, P., & Radaj, D. (2009). Fictitious notch rounding concept applied to sharp v-notches: Evaluation of the microstructural support factor for different failure hypotheses: Part ii: Microstructural support analysis. *Engineering Fracture Mechanics, 76*(9), 1151-1175. doi: http://dx.doi.org/10.1016/j.engfracmech.2008.01.015

Bhadeshia, H., & Svensson, L. (1993). Modelling the evolution of microstructure in steel weld metal. *Mathematical Modeling of Weld Phenomena, 1*, 109-182.

Bogdanov, S. (2014). *Fatigue life prediction based on the advanced fatigue crack growth model and the monte-carlo simulation method.* (Doctor), University of Waterloo

Bordas, S., Nguyen, P. V., Dunant, C., Guidoum, A., & Nguyen-Dang, H. (2007). An extended finite element library. *International Journal for Numerical Methods in Engineering, 71*(6), 703-732. doi: 10.1002/nme.1966

Bowness, D., & Lee, M. M. K. (2000). Prediction of weld toe magnification factors for semi-elliptical cracks in t–butt joints. *International Journal of Fatigue, 22*(5), 369-387. doi: http://dx.doi.org/10.1016/S0142-1123(00)00012-8

BSI (British Standards Institution). (2000). BS 5400 *Steel, Concrete and Composite Bridges.* London.

BSI (British Standards Institution). (2013). BS 7910 *Guide to methods for assessing the acceptability of flaws in metallic structures.* London.

Chan, H.-t. T., Ko, J. M., & Li, Z.-X. (2000). *Fatigue analysis for steel bridge deck sections under blocked cycles of traffic loading*.

Chan, K. S. (2010). Roles of microstructure in fatigue crack initiation. *International Journal of Fatigue, 32*(9), 1428-1447. doi: http://dx.doi.org/10.1016/j.ijfatigue.2009.10.005

Chen, C.Y. (2002). *Fatigue and fracture (in Chinese)*. Huazhong University of Science and Technology Press, Wuhan, China.

Chen, S. R. & Wu, J. (2011). Modeling stochastic live load for long-span bridge based on microscopic traffic flow simulation. Computer & Structures, 89 (9–10), 813–824

Chen, Y. (2013). *Study of fatigue performance for detail welding structure of steel bridge decks under vehicle loading (in Chinese).* (Doctor), Chang'an University, Xi'an, China.

Chen, Z. (2010). *Fatigue and reliability analyses of multiload suspension bridges with washms.* (Doctor), The Hong Kong Polytechnic University.

Cheng, X., Fisher, J. W., Prask, H. J., Gnäupel-Herold, T., Yen, B. T., & Roy, S. (2003). Residual stress modification by post-weld treatment and its beneficial effect on fatigue strength of welded structures. *International Journal of Fatigue, 25*(9), 1259-1269.

Chessa, J., & Belytschko, T. (2003). An enriched finite element method and level sets for axisymmetric two-phase flow with surface tension. *International Journal for Numerical Methods in Engineering, 58*(13), 2041-2064. doi: 10.1002/nme.946

Crémona, C., & Lukić, M. (1998). Probability-based assessment and maintenance of welded joints damaged by fatigue. *Nuclear Engineering and Design, 182*(3), 253-266. doi: http://dx.doi.org/10.1016/S0029-5493(97)00295-1

De Backer, H., Amelie Outtier, and Philippe Van Bogaert. (2008a). Alternatives for bridge surfacings with orthotropic plated deck: A fatigue point of view. *Foundations of Civil and Environmental Engineering, 11*(2008).

De Backer, H., Outtier, A., & Van Bogaert, P. (2007). High precision strain gauge measurements in areas of high stress concentrations of orthotropic plated bridge decks. *Insight-Non-Destructive Testing and Condition Monitoring, 49*(7), 384-389.

De Backer, H., Outtier, A., & Van Bogaert, P. (2008b). Analytical calculation of internal forces in orthotropic plated bridge decks based on the slope-deflection method. *Journal of Constructional Steel Research, 64*(12), 1530-1539. doi: http://dx.doi.org/10.1016/j.jcsr.2008.01.009

El Haddad, M. H., Topper, T. H., & Smith, K. N. (1979). Prediction of non propagating cracks. *Engineering Fracture Mechanics, 11*(3), 573-584. doi: http://dx.doi.org/10.1016/0013-7944(79)90081-X

Elber, W. (1971). The significance of fatigue crack closure *Damage tolerance in aircraft structures*: ASTM International.

Elguedj, T., Gravouil, A., & Combescure, A. (2006). Appropriate extended functions for x-fem simulation of plastic fracture mechanics. *Computer methods in applied mechanics and engineering, 195*(7–8), 501-515. doi: http://dx.doi.org/10.1016/j.cma.2005.02.007

Elguedj, T., Gravouil, A., & Combescure, A. (2007). A mixed augmented lagrangian-extended finite element method for modelling elastic–plastic fatigue crack growth with unilateral contact. *International Journal for*

Numerical Methods in Engineering, 71(13), 1569-1597. doi: 10.1002/nme.2002

Enright, B., & O'Brien, E. J. (2013). Monte carlo simulation of extreme traffic loading on short and medium span bridges. *Structure and Infrastructure Engineering, 9*(12), 1267-1282. doi: 10.1080/15732479.2012.688753

Erdogan, F., & Sih, G. C. (1963). On the crack extension in plates under plane loading and transverse shear. *Journal of Basic Engineering, 85*(4), 519-525. doi: 10.1115/1.3656897

Fang, D., Liu, Y., Chen, Y., & Wang, Q. (2011). Super long life fatigue performances of welded joints of Q345 bridge steel *(in Chinese)*. *Transactions of the China Welding Institution,* 32(08), 77-80.

Feng, Y.C. (2009). *Fatigue behavior research of orthotropic steel bridge deck(in Chinese).* (Master), Chang'an University, Xi'an, China.

Fisher, J.W. (1989). *The fatigue and fracture of steel bridge (in Chinese)*: China Railway Press, Beijing, China.

Fisher, J. W. (1970). *Effect of weldments on the fatigue strength of steel beams*: Highway Research Board, National Research Council.

Fisher, J. W., Fisher, T. A., & Kostem, C. N. (1979). Displacement induced fatigue cracks. *Engineering Structures, 1*(5), 252-257. doi: http://dx.doi.org/10.1016/0141-0296(79)90006-3

Fricke, W., von Lilienfeld-Toal, A., & Paetzold, H. (2012). Fatigue strength investigations of welded details of stiffened plate structures in steel ships. *International Journal of Fatigue, 34*(1), 17-26. doi: http://dx.doi.org/10.1016/j.ijfatigue.2011.01.021

Gabauer, W. (2000). The determination of uncertainties of ramberg-osgood parameters (from a tensile test).

Giner, E., Sukumar, N., Tarancón, J. E., & Fuenmayor, F. J. (2009). An abaqus implementation of the extended finite element method. *Engineering Fracture Mechanics, 76*(3), 347-368. doi: http://dx.doi.org/10.1016/j.engfracmech.2008.10.015

Grbovic, A., & Rasuo, B. (2012). Fem based fatigue crack growth predictions for spar of light aircraft under variable amplitude loading. *Engineering Failure Analysis, 26*, 50-64. doi: http://dx.doi.org/10.1016/j.engfailanal.2012.07.003

Gross, D., & Seelig, T. (2011). *Fracture mechanics: With an introduction to micromechanics*: Springer Science & Business Media.

Guo, L. (2005). *Structual-state-assessment-oriented finite element modeling of long span bridge and its applications (in Chinese).* (Doctor), Southeast University, Nanjing, China.

Guo, T., Liu, Z. X., & Zhu, J. S. (2015). Fatigue reliability assessment of orthotropic steel bridge decks based on probabilistic multi-scale finite element analysis. *Advanced Steel Construction, 11*(3), 334-346.

Gurney, T. R. (1979). *Fatigue of welded structures*: CUP Archive.

Gurney, T. R. (1991). *The fatigue strength of transverse fillet welded joints: A study of the influence of joint geometry*: Elsevier.

He, D. D., Li, Z. X., Sheng, H. Q., & Chen, C. (2013). Multi-scale experimental study on fatigue damage behaviour and its effect on structural nonlinear response. *Fatigue & Fracture of Engineering Materials & Structures, 36*(2), 102-114. doi: 10.1111/j.1460-2695.2012.01703.x

Hertelé, S., Gubeljak, N., & De Waele, W. (2014). Advanced characterization of heterogeneous arc welds using micro tensile tests and a two-stage strain hardening ('ugent') model. *International Journal of Pressure Vessels and Piping, 119*, 87-94.

Hertelé, S., O'Dowd, N., Van Minnebruggen, K., Verstraete, M., & De Waele, W. (2014). Fracture mechanics analysis of heterogeneous welds: Validation of a weld homogenisation approach. *Procedia Materials Science, 3*, 1322-1329.

Hiriyur, B., Waisman, H., & Deodatis, G. (2011). Uncertainty quantification in homogenization of heterogeneous microstructures modeled by xfem. *International Journal for Numerical Methods in Engineering, 88*(3), 257-278.

Hobbacher, A. (2008). IIW recommendations for fatigue design of welded joints and components, doc. IIW-1823. *WRC Bulletin, 520*.

Huang, X., Torgeir, M., & Cui, W. (2008). An engineering model of fatigue crack growth under variable amplitude loading. *International Journal of Fatigue, 30*(1), 2-10. doi: http://dx.doi.org/10.1016/j.ijfatigue.2007.03.004

Jacob, B., Bouteldja, M., & Stanczyk, D. (2013). Installation and experimentation of ms-wim systems with three strip sensor technologies - early results

International conference on heavy vehicles hvparis 2008 (pp. 163-174): John Wiley & Sons, Inc.

Ji, B., Chen, D.-h., Ma, L., Jiang, Z.-s., Shi, G.-g., Lv, L., Xu, H.-j., & Zhang, X. (2012). Research on stress spectrum of steel decks in suspension bridge considering measured traffic flow. *Journal of Performance of Constructed Facilities, 26*(1), 65-75. doi: doi:10.1061/(ASCE)CF.1943-5509.0000249

Jones, R., Peng, D., Singh Raman, R. K., Huang, P., Tamboli, D., & Matthews, N. (2015). On the growth of fatigue cracks from material and manufacturing discontinuities under variable amplitude loading. *JOM, 67*(6), 1385-1391. doi: 10.1007/s11837-015-1437-1

Judt, P. O., & Ricoeur, A. (2015). Crack growth simulation of multiple cracks systems applying remote contour interaction integrals. *Theoretical and Applied Fracture Mechanics, 75*, 78-88. doi: http://dx.doi.org/10.1016/j.tafmec.2014.11.001

Kainuma, S., Jeong, Y.-S., Yang, M., & Inokuchi, S. (2016a). Welding residual stress in roots between deck plate and u-rib in orthotropic steel decks. *Measurement, 92*, 475-482.

Kainuma, S., Yang, M., Jeong, Y.-S., Inokuchi, S., Kawabata, A., & Uchida, D. (2016b). Experiment on fatigue behavior of rib-to-deck weld root in orthotropic steel decks. *Journal of Constructional Steel Research, 119*, 113-122. doi: http://dx.doi.org/10.1016/j.jcsr.2015.11.014

Kolstein, M. H. (2007). *Fatigue classification of welded joints in orthotropic steel bridge decks*: TU Delft, Delft University of Technology.

Kumar, S., Singh, I. V., & Mishra, B. K. (2014). A multigrid coupled (fe-efg) approach to simulate fatigue crack growth in heterogeneous materials. *Theoretical and Applied Fracture Mechanics, 72*, 121-135. doi: http://dx.doi.org/10.1016/j.tafmec.2014.03.005

Kumar, S., Singh, I. V., & Mishra, B. K. (2015). A homogenized xfem approach to simulate fatigue crack growth problems. *Computers & Structures, 150*, 1-22.

Lassen, T., & Recho, N. (2013). *Fatigue life analyses of welded structures: Flaws*: John Wiley & Sons.

Lassen, T., & Sørensen, J. D. (2002). A probabilistic damage tolerance concept for welded joints part 2: A supplement to the rule based s–n approach. *Marine Structures, 15*(6), 615-626. doi: http://dx.doi.org/10.1016/S0951-8339(02)00021-7

Lassen, T., & Sørensen, J. D. (2002). A probabilistic damage tolerance concept for welded joints. Part 1: Data base and stochastic modelling. *Marine Structures, 15*(6), 599-613. doi: http://dx.doi.org/10.1016/S0951-8339(02)00020-5

Lautrou, N., Thevenet, D., & Cognard, J. Y. (2009). Fatigue crack initiation life estimation in a steel welded joint by the use of a two-scale damage model. *Fatigue & Fracture of Engineering Materials & Structures, 32*(5), 403-417. doi: 10.1111/j.1460-2695.2009.01344.x

Lazzarin, P., Berto, F., & Zappalorto, M. (2010). Rapid calculations of notch stress intensity factors based on averaged strain energy density from coarse meshes: Theoretical bases and applications. *International Journal of Fatigue, 32*(10), 1559-1567.

Lee, H., Kim, K., & Kim, C. (2000). Fracture resistance of a steel weld joint under fatigue loading. *Engineering Fracture Mechanics, 66*(4), 403-419.

Lee, Y.-L. (2005). *Fatigue testing and analysis: Theory and practice* (Vol. 13): Butterworth-Heinemann.

Leitner, M., Gerstbrein, S., Ottersböck, M. J., & Stoschka, M. (2015). Fatigue strength of hfmi-treated high-strength steel joints under constant and variable amplitude block loading. *Procedia Engineering, 101*(0), 251-258. doi: http://dx.doi.org/10.1016/j.proeng.2015.02.036

Li, Z. X., Chan, T. H. T., & Ko, J. M. (2001). Fatigue damage model for bridge under traffic loading: Application made to tsing ma bridge. *Theoretical and Applied Fracture Mechanics, 35*(1), 81-91. doi: http://dx.doi.org/10.1016/S0167-8442(00)00051-3

Li, Z. X., Chan, T. H. T., Yu, Y., & Sun, Z. H. (2009). Concurrent multi-scale modeling of civil infrastructures for analyses on structural deterioration—part i: Modeling methodology and strategy. *Finite Elements in Analysis and Design, 45*(11), 782-794. doi: http://dx.doi.org/10.1016/j.finel.2009.06.013

Li, Z., Guo, L., & Xu, Y. (2005). Measurement and analysis on fatigue damage of bridge welded components *(in Chinese). Journal of Southeast University (Natural Science Edition),* 35(03), 415-420.

Lindgren, L.-E. (2001a). Finite element modeling and simulation of welding part 1: Increased complexity. *Journal of Thermal Stresses, 24*(2), 141-192. doi: 10.1080/01495730150500442

Lindgren, L.-E. (2001b). Finite element modeling and simulation of welding. Part 2: Improved material modeling. *Journal of Thermal Stresses, 24*(3), 195-231. doi: 10.1080/014957301300006380

Lindgren, L.-E. (2001c). Finite element modeling and simulation of welding. Part 3: Efficiency and integration. *Journal of Thermal Stresses, 24*(4), 305-334. doi: 10.1080/01495730151078117

Liu, P., Luo, Y., & Kang, Z. (2016). Multi-material topology optimization considering interface behavior via xfem and level set method. *Computer methods in applied mechanics and engineering, 308*, 113-133. doi: http://dx.doi.org/10.1016/j.cma.2016.05.016

Liu, Y.P. (2010). *Study on fatigue crack growth behavior in welded steel plates used for bridges (in Chinese).* (Doctor), Huazhong University of Science and Technology, Wuhan, China.

Maddox, S. J. (1974). *The fatigue behaviour of trapezoidal stiffener to deck plate welds in orthotropic bridge decks*: Bridge Design Division, Structures Department, Transport and Road Research Laboratory.

Maddox, S. J. (1991). *Fatigue strength of welded structures*: Abington Pub.

Madenci, E., & Oterkus, E. (2014). *Peridynamic theory and its applications*: Springer.

Mahadevan, S., & Ni, K. (2003). Damage tolerance reliability analysis of automotive spot-welded joints. *Reliability Engineering & System Safety, 81*(1), 9-21. doi: http://dx.doi.org/10.1016/S0951-8320(03)00057-7

Maljaars, J., van Dooren, F., & Kolstein, H. (2012). Fatigue assessment for deck plates in orthotropic bridge decks. *Steel Construction, 5*(2), 93-100. doi: 10.1002/stco.201210011

Matsuishi, M., & Endo, T. (1968). Fatigue of metals subjected to varying stress. *Japan Society of Mechanical Engineers, Fukuoka, Japan*, 37-40.

Mehmanparast, A., Brennan, F., & Tavares, I. (2017). Fatigue crack growth rates for offshore wind monopile weldments in air and seawater: Slic inter-laboratory test results. *Materials & Design, 114*, 494-504. doi: http://dx.doi.org/10.1016/j.matdes.2016.10.070

Mikheevskiy, S., Bogdanov, S., & Glinka, G. (2011). Statistical analysis of fatigue crack growth based on the unigrow model *Icaf 2011 structural integrity: Influence of efficiency and green imperatives* (pp. 415-425): Springer.

Mikheevskiy, S., Bogdanov, S., & Glinka, G. (2015). Analysis of fatigue crack growth under spectrum loading – the unigrow fatigue crack growth model. *Theoretical and Applied Fracture Mechanics, 79*, 25-33. doi: http://dx.doi.org/10.1016/j.tafmec.2015.06.010

Mikheevskiy, S., & Glinka, G. (2009). Elastic–plastic fatigue crack growth analysis under variable amplitude loading spectra. *International Journal of Fatigue, 31*(11), 1828-1836.

Miki, C., Fahimuddin, F., & Anami, K. (2001). Fatigue performance of butt-welded joints containing various embedded defects. *Doboku Gakkai Ronbunshu, 2001*(668), 29-41. doi: 10.2208/jscej.2001.668_29

Miki, C., Tateishi, K., Fan, H.-d., & Tanaka, M. (1993). Fatigue strengths of fillet-welded joints containing root discontinuities. *International Journal of Fatigue, 15*(2), 133-140. doi: http://dx.doi.org/10.1016/0142-1123(93)90007-D

Milella, P. P. (2012). *Fatigue and corrosion in metals*: Springer Science & Business Media.

Miller, K. J. (1993). The two thresholds of fatigue behaviour. *Fatigue & Fracture of Engineering Materials & Structures, 16*(9), 931-939.

Moës, N., Cloirec, M., Cartraud, P., & Remacle, J. F. (2003). A computational approach to handle complex microstructure geometries. *Computer methods in applied mechanics and engineering, 192*(28), 3163-3177.

Moës, N., Dolbow, J., & Belytschko, T. (1999). A finite element method for crack growth without remeshing. *International Journal for Numerical Methods in Engineering, 46*(1), 131-150.

Moreno, B., Martin, A., Lopez-Crespo, P., Zapatero, J., & Dominguez, J. (2015). On the use of nasgro software to estimate fatigue crack growth under variable amplitude loading in aluminium alloy 2024-t351. *Procedia Engineering, 101*, 302-311. doi: http://dx.doi.org/10.1016/j.proeng.2015.02.037

Murakami, Y. (2002). *Metal fatigue: Effects of small defects and nonmetallic inclusions*: Elsevier.

Murakami, Y., & Keer, L. M. (1993). Stress intensity factors handbook, vol. 3. *Journal of Applied Mechanics, 60*, 1063.

Nagy W. (2017). *Fatigue Assessment of Orthotropic Steel Decks Based on Fracture Mechanics*. (Doctor), Ghent University, Ghent, Belgium.

Nagy W., Wang B., Culek B., Van Bogaert P., & De Backer, H. (2017). Experimental fatigue assessment of the stiffener-to-deck plate connection in orthotropic steel decks. *International Journal of Steel Structures (submitted)*

Nagy, W., Schotte, K., Van Bogaert, P., & De Backer, H. (2016). Fatigue strength application of fracture mechanics to orthotropic steel decks. *Advances in Structural Engineering, 19*(11), 1696-1709

Nagy, W., Van Bogaert, P., & De Backer, H. (2015a). *Determining residual stresses in welded connections of orthotropic steel bridge decks with a hole-drilling technique.* Paper presented at the ISEC-08 Implementing Innovative Ideas in Structural Engineering and Project Management.

Nagy, W., Van Bogaert, P., & De Backer, H. (2015b). Lefm based fatigue design for welded connections in orthotropic steel bridge decks. *Procedia Engineering, 133*, 758-769.

NBN (European Committee for Standardization). (2004). EN 1991-2, Eurocode 1: Actions on structures - part 2: Traffic loads on bridges. Brussels, Belgium.

Newman, J. C., & Raju, I. S. (1981). An empirical stress-intensity factor equation for the surface crack. *Engineering Fracture Mechanics, 15*(1), 185-192. doi: http://dx.doi.org/10.1016/0013-7944(81)90116-8

Noroozi, A. H., Glinka, G., & Lambert, S. (2005). A two parameter driving force for fatigue crack growth analysis. *International Journal of Fatigue, 27*(10–12), 1277-1296. doi: http://dx.doi.org/10.1016/j.ijfatigue.2005.07.002

Noroozi, A. H., Glinka, G., & Lambert, S. (2007). A study of the stress ratio effects on fatigue crack growth using the unified two-parameter fatigue crack growth driving force. *International Journal of Fatigue, 29*(9–11), 1616-1633. doi: http://dx.doi.org/10.1016/j.ijfatigue.2006.12.008

Noroozi, A. H., Glinka, G., & Lambert, S. (2008). Prediction of fatigue crack growth under constant amplitude loading and a single overload based on elasto-plastic crack tip stresses and strains. *Engineering Fracture Mechanics, 75*(2), 188-206. doi: http://dx.doi.org/10.1016/j.engfracmech.2007.03.024

Nunn, D. E., & Cuninghame, J. R. (1974). *Stresses under wheel loading on steel orthotropic decks with trapezoidal stiffeners*: Bridge Design Division, Structures Department, Transport and Road Research Laboratory.

Nykänen, T., Li, X., Björk, T., & Marquis, G. (2005). A parametric fracture mechanics study of welded joints with toe cracks and lack of penetration. *Engineering Fracture Mechanics, 72*(10), 1580-1609. doi: http://dx.doi.org/10.1016/j.engfracmech.2004.11.004

O'Connor, A. & O'Brien, E. J. (2005). Traffic load modelling and factors influencing the accuracy of predicted extremes, Canadian Journal of Civil Engineering, 32 (1), 270–278.

Okura, I., Takigawa, H., & Fukumoto, Y. (1989). Structural parameters governing fatigue cracking in highway bridges. *Doboku Gakkai Ronbunshu, 1989*(410), 253-256. doi: 10.2208/jscej.1989.410_253

Omura, T., Koyama, M., Hamano, Y., Tsuzaki, K., & Noguchi, H. (2017). Generalized evaluation method for determining transition crack length for microstructurally small to microstructurally large fatigue crack growth: Experimental definition, facilitation, and validation. *International Journal of Fatigue, 95*, 38-44. doi: http://dx.doi.org/10.1016/j.ijfatigue.2016.10.010

Osher, S., & Paragios, N. (2003). *Geometric level set methods in imaging,vision,and graphics*: Springer-Verlag New York, Inc.

Pais, M. J. (2011). *Variable amplitude fatigue analysis using surrogate models and exact xfem reanalysis*. (Doctor), University of Florida, Florida, U.S.

Paris, P., & Erdogan, F. (1963). A critical analysis of crack propagation laws. *Journal of Basic Engineering, 85*(4), 528-533. doi: 10.1115/1.3656900

Park, W., & Miki, C. (2008). Fatigue assessment of large-size welded joints based on the effective notch stress approach. *International Journal of Fatigue, 30*(9), 1556-1568. doi: http://dx.doi.org/10.1016/j.ijfatigue.2007.11.012

Polák, J. (2003). Cyclic deformation, crack initiation, and low-cycle fatigue. *Comprehensive structural integrity, 4*, 1-39.

Pommier, S., Lopez-Crespo, P., & Decreuse, P. Y. (2009). A multi-scale approach to condense the cyclic elastic-plastic behaviour of the crack tip region into an extended constitutive model. *Fatigue & Fracture of Engineering Materials & Structures, 32*(11), 899-915. doi: 10.1111/j.1460-2695.2009.01392.x

Prabel, B., Combescure, A., Gravouil, A., & Marie, S. (2007). Level set x-fem non-matching meshes: Application to dynamic crack propagation in elastic–plastic media. *International Journal for Numerical Methods in Engineering, 69*(8), 1553-1569.

Pugno, N., Ciavarella, M., Cornetti, P., & Carpinteri, A. (2006). A generalized paris' law for fatigue crack growth. *Journal of the Mechanics and Physics of Solids, 54*(7), 1333-1349. doi: http://dx.doi.org/10.1016/j.jmps.2006.01.007

Qian, J., & Fatemi, A. (1996). Mixed mode fatigue crack growth: A literature survey. *Engineering Fracture Mechanics, 55*(6), 969-990. doi: http://dx.doi.org/10.1016/S0013-7944(96)00071-9

Qian, Z., & Abruzzese, D. (2009). Fatigue failure of welded connections at orthotropic bridges. *Frattura ed Integrità Strutturale*(9), 105.

Radaj, D. (1996). Review of fatigue strength assessment of nonwelded and welded structures based on local parameters. *International Journal of Fatigue, 18*(3), 153-170. doi: http://dx.doi.org/10.1016/0142-1123(95)00117-4

Radaj, D. (1997). Fatigue notch factor of gaps in welded joints reconsidered. *Engineering Fracture Mechanics, 57*(4), 405-407.

Radaj, D. (2003). *Welding residual stresses and distortion: Calculation and measurement*: Elsevier Science & Technology.

Radaj, D., Berto, F., & Lazzarin, P. (2009). Local fatigue strength parameters for welded joints based on strain energy density with inclusion of small-size notches. *Engineering Fracture Mechanics, 76*(8), 1109-1130. doi: http://dx.doi.org/10.1016/j.engfracmech.2009.01.009

Radaj, D., Sonsino, C. M., & Fricke, W. (2009). Recent developments in local concepts of fatigue assessment of welded joints. *International Journal of Fatigue, 31*(1), 2-11. doi: http://dx.doi.org/10.1016/j.ijfatigue.2008.05.019

Ramazani, A., Li, Y., Mukherjee, K., Prahl, U., Bleck, W., Abdurakhmanov, A., Schleser, M., & Reisgen, U. (2013). Microstructure evolution simulation in hot rolled dp600 steel during gas metal arc welding. *Computational Materials Science, 68*, 107-116.

Remes, H. (2008). Strain-based approach to fatigue strength assessment of laser-welded joints.

Remes, H. (2013). Strain-based approach to fatigue crack initiation and propagation in welded steel joints with arbitrary notch shape. *International Journal of Fatigue, 52*(0), 114-123. doi: http://dx.doi.org/10.1016/j.ijfatigue.2013.03.006

Remes, H., Varsta, P., & Romanoff, J. (2012). Continuum approach to fatigue crack initiation and propagation in welded steel joints. *International Journal of Fatigue, 40*(0), 16-26. doi: http://dx.doi.org/10.1016/j.ijfatigue.2012.01.007

Roy, S., Fisher, J. W., & Yen, B. T. (2003). Fatigue resistance of welded details enhanced by ultrasonic impact treatment (uit). *International Journal of Fatigue, 25*(9), 1239-1247.

Ryan, T. W., Hartle, R., Mann, J. E., & Danovich, L. (2006). Bridge inspector's reference manual. *Report No. FHWA NHI*, 03-001.

Saiprasertkit, K., Hanji, T., & Miki, C. (2012). Fatigue strength assessment of load-carrying cruciform joints with material mismatching in low- and high-cycle fatigue regions based on the effective notch concept. *International Journal of Fatigue, 40*, 120-128. doi: http://dx.doi.org/10.1016/j.ijfatigue.2011.12.016

Schepens, I., & Laseure, N. (2015). *Fatigue of offshore structures subjected to variable amplitude loading.* (Master), Ghent University, Ghent, Belgium.

Schijve, J. (1981). Some formulas for the crack opening stress level. *Engineering Fracture Mechanics, 14*(3), 461-465.

Schijve, J. (2001). *Fatigue of structures and materials*: Springer.

Schijve, J. (2012). Fatigue predictions of welded joints and the effective notch stress concept. *International Journal of Fatigue, 45*, 31-38. doi: http://dx.doi.org/10.1016/j.ijfatigue.2012.06.016

Schmidova, E., & Hanus, P. (2011). Effect of welding on the fracture behaviour of the ferritic corrosion-resistant steel. *Materials Engineering*.

Shi, J., Chopp, D., Lua, J., Sukumar, N., & Belytschko, T. (2010). Abaqus implementation of extended finite element method using a level set representation for three-dimensional fatigue crack growth and life predictions. *Engineering Fracture Mechanics, 77*(14), 2840-2863. doi: http://dx.doi.org/10.1016/j.engfracmech.2010.06.009

Sih, G. C., & Madenci, E. (1985). Prediction of failure in weldments — part ii: Joint with initial notch and crack. *Theoretical and Applied Fracture Mechanics, 3*(1), 31-40. doi: http://dx.doi.org/10.1016/0167-8442(85)90051-5

Silling, S. A., & Askari, E. (2005). A meshfree method based on the peridynamic model of solid mechanics. *Computers & Structures, 83*(17), 1526-1535.

Silling, S. A., & Askari, A. (2014). Peridynamic model for fatigue cracking. *SAND2014-18590. Albuquerque: Sandia National Laboratories*.

Sim, H.-B., & Uang, C.-M. (2012). Stress analyses and parametric study on full-scale fatigue tests of rib-to-deck welded joints in steel orthotropic decks. *Journal of Bridge Engineering, 17*(5), 765-773.

Sim, H.-B., Uang, C.-M., & Sikorsky, C. (2009). Effects of fabrication procedures on fatigue resistance of welded joints in steel orthotropic decks. *Journal of Bridge Engineering, 14*(5), 366-373. doi: doi:10.1061/(ASCE)1084-0702(2009)14:5(366)

Sivakumar, B., Ghosn, M., & Moses, F. (2011). *Protocols for collecting and using traffic data in bridge design* (Vol. 683): Transportation Research Board.

Sonsino C.M. (2007a) Course of SN-curves especially in the high-cycle fatigue regime with regard to component design and safety. *International Journal of Fatigue*, 29(12), 2246 - 2258.

Sonsino, C. M. (2007b). Fatigue testing under variable amplitude loading. *International Journal of Fatigue, 29*(6), 1080-1089. doi: http://dx.doi.org/10.1016/j.ijfatigue.2006.10.011

Sonsino, C. M. (2009). Effect of residual stresses on the fatigue behaviour of welded joints depending on loading conditions and weld geometry. *International Journal of Fatigue, 31*(1), 88-101. doi: http://dx.doi.org/10.1016/j.ijfatigue.2008.02.015

Stolarska, M., Chopp, D. L., Moës, N., & Belytschko, T. (2001). Modelling crack growth by level sets in the extended finite element method. *International Journal for Numerical Methods in Engineering, 51*(8), 943-960.

Sugioka, K. (2009). Life cycle evaluation of fatigue mitigation for orthotropic steel bridge decks.

Sukumar, N., Chopp, D. L., Moës, N., & Belytschko, T. (2001). Modeling holes and inclusions by level sets in the extended finite-element method. *Computer methods in applied mechanics and engineering, 190*(46), 6183-6200.

Sukumar, N., & Prévost, J. H. (2003). Modeling quasi-static crack growth with the extended finite element method part i: Computer implementation. *International Journal of Solids and Structures, 40*(26), 7513-7537. doi: http://dx.doi.org/10.1016/j.ijsolstr.2003.08.002

Sumi, Y., & Inoue, T. (2011). Multi-scale modeling of fatigue crack propagation applied to random sequence of clustered loading. *Marine Structures, 24*(2), 117-131. doi: http://dx.doi.org/10.1016/j.marstruc.2011.02.003

Sun, B., & Li, Z. (2014). A multi-scale damage model for fatigue accumulation due to short cracks nucleation and growth. *Engineering Fracture Mechanics, 127*, 280-295. doi: http://dx.doi.org/10.1016/j.engfracmech.2014.06.014

Sun, B., Xu, Y.-L., & Li, Z. (2016). Multi-scale model for linking collective behavior of short and long cracks to continuous average fatigue damage. *Engineering Fracture Mechanics, 157*, 141-153. doi: http://dx.doi.org/10.1016/j.engfracmech.2016.02.013

Susmel, L., Sonsino, C. M., & Tovo, R. (2011). Accuracy of the modified wöhler curve method applied along with the r_{ref} = 1 mm concept in estimating lifetime of welded joints subjected to multiaxial fatigue loading. *International Journal of Fatigue, 33*(8), 1075-1091. doi: http://dx.doi.org/10.1016/j.ijfatigue.2010.09.010

Susmel, L., & Taylor, D. (2007). A novel formulation of the theory of critical distances to estimate lifetime of notched components in the medium-cycle fatigue regime. *Fatigue & Fracture of Engineering Materials & Structures, 30*(7), 567-581.

Susmel, L., & Taylor, D. (2010). The theory of critical distances as an alternative experimental strategy for the determination of k ic and δk th. *Engineering Fracture Mechanics, 77*(9), 1492-1501.

Susmel, L., & Taylor, D. (2012). A critical distance/plane method to estimate finite life of notched components under variable amplitude uniaxial/multiaxial fatigue loading. *International Journal of Fatigue, 38*, 7-24. doi: http://dx.doi.org/10.1016/j.ijfatigue.2011.11.015

Susmel, L., Tovo, R., & Lazzarin, P. (2005). The mean stress effect on the high-cycle fatigue strength from a multiaxial fatigue point of view. *International Journal of Fatigue, 27*(8), 928-943. doi: http://dx.doi.org/10.1016/j.ijfatigue.2004.11.012

Suresh, S. (1998). *Fatigue of materials*: Cambridge university press.

Tabatabaeipour, M., Hettler, J., Delrue, S., & Van Den Abeele, K. (2016). Non-destructive ultrasonic examination of root defects in friction stir welded butt-joints. *NDT & E International, 80*, 23-34. doi: http://dx.doi.org/10.1016/j.ndteint.2016.02.007

Tanaka, K. (1974). Fatigue crack propagation from a crack inclined to the cyclic tensile axis. *Engineering Fracture Mechanics, 6*(3), 493-507.

Tang, K. K., Li, Z. X., He, D. D., & Zhang, Z. H. (2010). Evolution of plastic damage in welded joint of steel truss with pre-existing defects. *Theoretical and Applied Fracture Mechanics, 54*(2), 117-126. doi: http://dx.doi.org/10.1016/j.tafmec.2010.10.007

Taylor, D. (2010). *The theory of critical distances: A new perspective in fracture mechanics*: Elsevier.

Tebedge, N., Alpsten, G., & Tall, L. (1973). Residual-stress measurement by the sectioning method. *Experimental Mechanics, 13*(2), 88-96.

Tong, L., & Shen, Z. (1998). Fatigue behavior of field-butt-welded rib joints in orthotropic steel bridge decks *(in Chinese). Journal of Tongji University,* 26(2), 130-133.

Tong, L., & Shen, Z. (2000). Fatigue assessment of orthotropic steel bridge decks *(in Chinese). China Civil Engineering Journal,* 33(3), 16-21.

Tovo, R., & Lazzarin, P. (1999). Relationships between local and structural stress in the evaluation of the weld toe stress distribution. *International Journal of Fatigue, 21*(10), 1063-1078. doi: http://dx.doi.org/10.1016/S0142-1123(99)00089-4

Tsakopoulos, P. A., & Fisher, J. W. (2003). Full-scale fatigue tests of steel orthotropic decks for the williamsburg bridge. *Journal of Bridge Engineering, 8*(5), 323-333.

Villanueva, C. H., & Maute, K. (2014). Density and level set-xfem schemes for topology optimization of 3-d structures. *Computational Mechanics, 54*(1), 133-150. doi: 10.1007/s00466-014-1027-z

Vogt, M., Dilger, K., & Kassner, M. (2012). Investigations on different fatigue design concepts using the example of a welded crossbeam connection from the underframe of a steel railcar body. *International Journal of Fatigue, 34*(1), 47-56. doi: http://dx.doi.org/10.1016/j.ijfatigue.2011.01.017

Wang, B., De Backer, H., & Chen, A. (2016). An xfem based uncertainty study on crack growth in welded joints with defects. *Theoretical and Applied Fracture Mechanics, 86, Part B*, 125-142. doi: http://dx.doi.org/10.1016/j.tafmec.2016.06.005

Wang, B., Zhou, X.Y., De Backer, H., Chen, A., & Schmidt, F. (2017). Macro crack initiation life for orthotropic steel decks considering weld

heterogeneity and random traffic loading. *Structure and Infrastructure Engineering (accepted).* doi: 10.1080/15732479.2017.1315733

Wang, C., & Feng, Y. (2009). Review of fatigue research for orthotropic steel bridge decks *(in Chinese)*. *Steel Structures,* 24(9), 10-13

Wang, M.C. (1997). *Basic principles of the finite element method and numerical method (in Chinese)*: Tsinghua University Press, Beijing, China.

Wang, M. Y., Wang, X., & Guo, D. (2003). A level set method for structural topology optimization. *Computer methods in applied mechanics and engineering, 192*(1–2), 227-246. doi: http://dx.doi.org/10.1016/S0045-7825(02)00559-5

Wang, T.-L., Liu, C., Huang, D., & Shahawy, M. (2005). Truck loading and fatigue damage analysis for girder bridges based on weigh-in-motion data. *Journal of Bridge Engineering, 10*(1), 12-20. doi: doi:10.1061/(ASCE)1084-0702(2005)10:1(12)

Wang, Y., Li, Z. X., & Li, A. Q. (2011). Fatigue crack growth model for assessing reliability of box-girders for cable-stayed bridge combining shms with strain data. *Theoretical and Applied Fracture Mechanics, 55*(1), 60-67. doi: http://dx.doi.org/10.1016/j.tafmec.2011.01.006

Wang, Z.Q., & Chen, S.H. (2009). *Advanced fracture mechanics (in Chinese)*: Science Press, Beijing, China.

Wei, P., Wang, M. Y., & Xing, X. (2010). A study on x-fem in continuum structural optimization using a level set model. *Comput. Aided Des., 42*(8), 708-719. doi: 10.1016/j.cad.2009.12.001

Witek, L. (2009). Experimental crack propagation and failure analysis of the first stage compressor blade subjected to vibration. *Engineering Failure Analysis, 16*(7), 2163-2170. doi: http://dx.doi.org/10.1016/j.engfailanal.2009.02.014

Wolchuk, R. (1990). Lessons from weld cracks in orthotropic decks on three european bridges. *Journal of Structural Engineering, 116*(1), 75-84. doi: 10.1061/(ASCE)0733-9445(1990)116:1(75)

Wolf, E. (1970). Fatigue crack closure under cyclic tension. *Engineering Fracture Mechanics, 2*(1), 37-45. doi: http://dx.doi.org/10.1016/0013-7944(70)90028-7

Xiao, Z.-G., Chen, T., & Zhao, X.-L. (2012). Fatigue strength evaluation of transverse fillet welded joints subjected to bending loads. *International*

Journal of Fatigue, 38, 57-64. doi: http://dx.doi.org/10.1016/j.ijfatigue.2011.11.013

Xiao, Z.-G., Yamada, K., Inoue, J., & Yamaguchi, K. (2006). Fatigue cracks in longitudinal ribs of steel orthotropic deck. *International Journal of Fatigue, 28*(4), 409-416.

Xiao, Z.-G., Yamada, K., Ya, S., & Zhao, X.-L. (2008). Stress analyses and fatigue evaluation of rib-to-deck joints in steel orthotropic decks. *International Journal of Fatigue, 30*(8), 1387-1397. doi: http://dx.doi.org/10.1016/j.ijfatigue.2007.10.008

Ya, S., & Yamada, K. (2008). Fatigue durability evaluation of trough to deck plate welded joint of orthotropic steel deck. *Doboku Gakkai Ronbunshuu A, 64*(3), 603-616. doi: 10.2208/jsceja.64.603

Ya, S., Yamada, K., & Ishikawa, T. (2011). Fatigue evaluation of rib-to-deck welded joints of orthotropic steel bridge deck. *Journal of Bridge Engineering, 16*(4), 492-499. doi: doi:10.1061/(ASCE)BE.1943-5592.0000181

Yang, X., Li, N., Jin, Z., & Wang, T. (1997). A continuous low cycle fatigue damage model and its application in engineering materials. *International Journal of Fatigue, 19*(10), 687-692.

Yu, T., & Shi, L. (2012). Determination of sharp v-notch stress intensity factors using the extended finite element method. *The Journal of Strain Analysis for Engineering Design, 47*(2), 95-103.

Yu, T.T. (2014). *The extended finite element method: Theory, application and program (in Chinese)*: Science Press, Beijing, China.

Zerbst, U., Ainsworth, R., Beier, H. T., Pisarski, H., Zhang, Z., Nikbin, K., Nitschke-Pagel, T., Münstermann, S., Kucharczyk, P., & Klingbeil, D. (2014). Review on fracture and crack propagation in weldments–a fracture mechanics perspective. *Engineering Fracture Mechanics, 132*, 200-276.

Zerbst, U., Madia, M., & Hellmann, D. (2012). An analytical fracture mechanics model for estimation of s–n curves of metallic alloys containing large second phase particles. *Engineering Fracture Mechanics, 82*(0), 115-134. doi: http://dx.doi.org/10.1016/j.engfracmech.2011.12.001

Zeng, Z.B. (2011). Classification and reasons of typical fatigue cracks in orthotropic steel deck *(in Chinese)*. *Steel Structures*, 26(2), 9-15.

Zhang, Q.-H., Cui, C., Bu, Y.-Z., Liu, Y.-M., & Ye, H.-W. (2015). Fatigue tests and fatigue assessment approaches for rib-to-diaphragm in steel orthotropic decks. *Journal of Constructional Steel Research, 114*, 110-118. doi: http://dx.doi.org/10.1016/j.jcsr.2015.07.014

Zhang, Y.-H., & Maddox, S. J. (2009). Investigation of fatigue damage to welded joints under variable amplitude loading spectra. *International Journal of Fatigue, 31*(1), 138-152. doi: http://dx.doi.org/10.1016/j.ijfatigue.2008.04.006

Zhao, Y. X., Wang, J. N., & Gao, Q. (1999). Statistical evolution of small fatigue crack in 1cr18ni9ti weld metal. *Theoretical and Applied Fracture Mechanics, 32*(1), 55-64. doi: http://dx.doi.org/10.1016/S0167-8442(99)00026-9

Zhao, X.X. (2011). *Research on fatigue design parameter and structural details for orthotropic deck (in Chinese).* (Doctor), China Academy of Railway Sciences, Beijing, China.

Zheng, C. (2013). *Research on fatigue reliability evaluation of highway steel bridges based on fracture mechanics (in Chinese).* (Doctor), South China University of Technology, Guangzhou, China.

Zhou, T.Q. (2003). *Hot spot stress analysis of steel bridge components and numerical simulation of fatigue damage accumulation (in Chinese).* (Doctor), Southeast University, Nanjing, China.

Zhou, Y.B. (2010). *Crack study and local fatigue analysis of orthotropic steel decks on bridges (in Chinese).* (Master), Tsinghua University, Beijing, China.

Zhou, H., Shi, G., Wang, Y., Chen, H., & De Roeck, G. (2016). Fatigue evaluation of a composite railway bridge based on fracture mechanics through global–local dynamic analysis. *Journal of Constructional Steel Research, 122*, 1-13. doi: http://dx.doi.org/10.1016/j.jcsr.2016.01.014

Zhou, X.-Y., Treacy, M., Schmidt, F., Brühwiler, E., Toutlemonde, F., & Jacob, B. (2015). Effect on bridge load effects of vehicle transverse in-lane position: A case study. *Journal of Bridge Engineering*, 20(12), 04015020. doi: doi:10.1061/(ASCE)BE.1943-5592.0000763

Zhou, X.-Y., Schmidt, F., Toutlemonde, F., & Jacob, B. (2016). A mixture peaks over threshold approach for predicting extreme bridge traffic load effects. *Probabilistic Engineering Mechanics, 43*, 121-131. doi: http://dx.doi.org/10.1016/j.probengmech.2015.12.004

Zhu, J., & Guo, Y. (2014). Numerical simulation on fatigue crack growth of orthotropic steel highway bridge deck *(in Chinese)*. *Journal of Vibration and Shock*, 33(14), 40-47.

Zhu, S.Z. (2006). *Study on fatigue crack growth of 14MnNbq steel and welds(in Chinese).* (Master), Huazhong University of Science and Technology, Wuhan, China.